

UCLA

UCLA Electronic Theses and Dissertations

Title

The Hubble Constant and the Λ CDM Cosmology: A Magnified View using Strong Lensing

Permalink

<https://escholarship.org/uc/item/1bf2m1xr>

Author

Shajib, Anowar Jaman

Publication Date

2020

Peer reviewed|Thesis/dissertation

UNIVERSITY OF CALIFORNIA

Los Angeles

The Hubble Constant and the Λ CDM Cosmology:

A Magnified View

using Strong Lensing

A dissertation submitted in partial satisfaction

of the requirements for the degree

Doctor of Philosophy in Astronomy and Astrophysics

by

Anowar Jaman Shajib

2020

© Copyright by
Anowar Jaman Shajib
2020

ABSTRACT OF THE DISSERTATION

The Hubble Constant and the Λ CDM Cosmology:
A Magnified View
using Strong Lensing

by

Anowar Jaman Shajib

Doctor of Philosophy in Astronomy and Astrophysics

University of California, Los Angeles, 2020

Professor Tommaso Treu, Chair

Recently, a significant tension has been reported between two measurements of the Hubble constant (H_0) from early-Universe (e.g., cosmic microwave background) and late-Universe probes (e.g., cosmic distance ladder). If systematic errors are ruled out in these measurements, then new physics extending the Λ CDM model will be required to resolve the tension. Therefore, different independent probes of H_0 – such as the strong-lensing time-delay – are essential to confirm or resolve the tension. The measured time-delays between the lensed images of a background quasar constrain H_0 , as they depend on the absolute physical distances in the lens configuration. I led a team from the STRong-lensing Insights into the Dark Energy Survey (STRIDES) collaboration to analyze the lens DES J0408-5354. I modeled the mass distribution of this lens using Hubble Space Telescope imaging, and combined it with analyses from my collaborators to infer $H_0 = 74.2^{+2.7}_{-3.0}$ km s⁻¹ Mpc⁻¹ with the highest precision (3.9 per cent) from a single lens to date. This measurement agrees well with both the previous sample of six lenses from the H0LiCOW collaboration and other late-Universe

probes, thus it increases the aforementioned tension. To confirm or resolve this tension at the 5σ level – the gold standard of detecting new physics – we need to increase the sample size and improve precision per system while keeping the systematics under control. The large amount of required investigator time (~ 1 year per lens) is currently the main bottleneck to increase the sample size. I present an automated lens-modeling framework that will enable rapid increment of the sample size in the near future. I also show, through simulation, that incorporating the spatially resolved kinematics of the lensing galaxy improves the precision of H_0 per system. Additionally, I develop the first general method to efficiently compute the lensing properties of any given elliptical mass distribution. By allowing any radial shape of mass profile, this method helps to avoid any systematic that may potentially arise from adopting only a few specific parameterizations. I forecast that a sample of ~ 40 lenses with spatially resolved kinematics will provide sub-per-cent precision in H_0 within the next decade.

The dissertation of Anowar Jaman Shajib is approved.

Edward L. Wright

James Larkin

Andrea Ghez

Tommaso Treu, Committee Chair

University of California, Los Angeles

2020

To my parents, Anowara Sarker and Abu Naser

TABLE OF CONTENTS

1	Introduction	1
1.1	The Λ cold dark matter model of cosmology: concordance and tensions . . .	1
1.2	Strong gravitational lensing time delays as a cosmological probe	3
1.3	Overview of this dissertation	6
2	An evidence for the ΛCDM cosmology: measuring the integrated Sachs–Wolfe effect	8
2.1	Background	8
2.2	The ISW Effect	10
2.3	Data and Methods	14
2.3.1	CMB Map	14
2.3.2	<i>WISE</i> Data	15
2.3.3	Mask	16
2.3.4	Theoretical Computation	16
2.4	Results	17
2.4.1	Redshift Distribution	17
2.4.2	Bias Measurement	18
2.4.3	Cross-correlation Measurement	25
2.5	Discussion and Conclusions	30
3	Measurement of the Hubble constant from the strong lens system DES J0408–5354	34

3.1	Background	35
3.2	Framework of the cosmographic analysis	40
3.2.1	Strong-lensing time delay	40
3.2.2	Mass-sheet degeneracy	42
3.2.3	Kinematic analysis	44
3.2.4	Cosmological distances	45
3.2.5	Bayesian inference framework	46
3.3	The Lens System and Data Sets	52
3.3.1	<i>HST</i> imaging of the lens system	53
3.3.2	Spectroscopic observations of the lens components	54
3.3.3	Time delays	55
3.3.4	Velocity dispersion of the central deflector	58
3.3.5	Estimate of the external convergence	60
3.4	Lens model ingredients	60
3.4.1	Central deflector’s mass profiles	60
3.4.2	Central deflector’s light profile	62
3.4.3	Quasar host galaxy’s light profile	62
3.5	Lens model setups	63
3.5.1	Baseline models	63
3.5.2	Central deflector G1’s mass and light profiles	64
3.5.3	Satellite G2’s mass and light profile	66
3.5.4	Nearby line-of-sight galaxies	67
3.5.5	Galaxy group containing G1	74

3.5.6	Source component light profiles	74
3.5.7	Potential additional image C2 split from the image C	76
3.5.8	<i>HST</i> image region for likelihood computation	76
3.5.9	Dust extinction by the satellite G2	76
3.5.10	Requirement for astrometric precision	77
3.5.11	Model choice combinations	77
3.6	Lens modelling and cosmographic inference	79
3.6.1	Modelling workflow and results	79
3.6.2	Combining the time delays, kinematics, and external convergence in- formation	85
3.6.3	Inference of H_0	96
3.7	Discussion and summary	97
3.A	Impact of fiducial cosmology in the lens modelling	102
3.B	Impact of likelihood computation region choice	103
3.C	Impact of the convergence from the group containing G1	103
3.D	Checking for the existence and impact of a dark substructure	107
3.E	Nested sampling settings	110
3.F	Summary of uncertainty budget and systematic checks	112
3.G	Model summary and parameter priors	112
4	Improving time-delay cosmography with spatially resolved kinematics .	121
4.1	Background	121
4.2	Model ingredients	125
4.2.1	Strong gravitational lensing	125

4.2.2	Deflector mass model	127
4.3	Creating mock data	129
4.3.1	Mimicking extended source reconstruction with conjugate points . . .	132
4.3.2	Mock lensing data with spatially resolved velocity dispersion	135
4.4	Precision on Cosmological Distance Measurements	140
4.5	Cosmological inference	147
4.5.1	Cosmology from strong lensing alone	147
4.5.2	Joint analysis with <i>Planck</i>	156
4.6	Discussion and Comparison with Previous Work	157
4.7	Limitation of this present work	160
4.8	Summary	162
5	Automated and uniform modelling of lensed quasars	165
5.1	Background	165
5.2	<i>HST</i> sample	170
5.2.1	Data	171
5.2.2	Quads in the sample	171
5.3	Lens modelling	175
5.3.1	Mass profile parameterization	178
5.3.2	Light profile parameterization	178
5.3.3	Modelling procedure	179
5.3.4	Systematics	184
5.4	Results	184
5.4.1	Efficiency of the uniform framework	184

5.4.2	Lens models	185
5.4.3	Alignment between mass and light distributions	190
5.4.4	Deviation of flux ratios from macro-model	196
5.5	Summary and Discussion	198
5.A	Lens light parameters	204
5.B	Convergence, shear and stellar convergence	205
5.C	Time delays	205
5.D	Lens models	205
6	Unified lensing and kinematic analysis of elliptical mass profiles	212
6.1	Background	212
6.2	Decomposing an elliptical profile into concentric Gaussian components	217
6.2.1	An integral transform for fast Gaussian decomposition	219
6.2.2	Decomposing a two-dimensional elliptical profile with the one-dimensional transform	225
6.3	Kinematics of Gaussian components	227
6.3.1	Axisymmetric case	228
6.3.2	Spherical case	229
6.4	Lensing by Gaussian components	231
6.4.1	Complex formulation of lensing	232
6.4.2	Lensing by elliptical Gaussian convergence	233
6.5	Adding it all together: proof of concept	237
6.6	Conclusion: precision is feasible.	239
6.A	Properties of the Integral transform with a Gaussian Kernel	244

6.B	Efficient algorithm to compute the Faddeeva function	249
7	Conclusion	251
7.1	Summaries	251
7.1.1	Chapter 2: An evidence of the Λ CDM cosmology: measuring the integrated Sachs–Wolfe effect	251
7.1.2	Chapter 3: Measurement of the Hubble constant from the strong lens system DES J0408–5354	252
7.1.3	Chapter 4: Improving time-delay cosmography with spatially resolved kinematics	253
7.1.4	Chapter 5: Automated and uniform modelling of lensed quasars . . .	253
7.1.5	Chapter 6: Unified lensing and kinematic analysis of elliptical mass profiles	254
7.2	Final remarks	255

LIST OF FIGURES

2.1	Large-scale gravitational potential	12
2.2	Overdensity maps in galactic coordinate	14
2.3	Redshift distribution of AllWISE galaxy	19
2.4	Matching fraction of the <i>WISE</i> galaxies	20
2.5	Cross-correlation between <i>Planck</i> and <i>WISE</i>	21
2.6	Examples of simulated <i>WMAP</i> CMB maps	26
2.7	Monte Carlo covariance matrices	27
2.8	Power spectra of the cross-correlation	28
3.1	RGB color composite of the lens systems DES J0408–5354	57
3.2	Impact of varying Ω_m on the angular diameter distance ratios	70
3.3	Properties of the line-of-sight galaxies	71
3.4	Lens model and reconstructed image for power-law model	86
3.5	Lens model and reconstructed image for composite model	87
3.6	Comparison of the lensing properties	88
3.7	Distribution of external convergence	90
3.8	Comparison of the distance posteriors	91
3.9	Cosmological distance posteriors	92
3.10	Microlensing time-delay maps	95
3.11	Posterior probability distribution functions of H_0	98
3.12	Impact of Ω_m on H_0	104
3.13	Impact of w on H_0	105

3.14	Impact of mask choice on the distance posterior	106
3.15	External convergence impact from the nearby galaxy group	108
3.16	Constraints on the position and NFW halo properties of the dark substructure .	111
3.17	NESTCHECK diagnostic plot for our sampling settings	113
4.1	Posterior PDF of the model parameters for a power-law mass profile	130
4.2	Line-of-sight velocity dispersion for a combination of NFW and Jaffe profiles . .	131
4.3	Priors for the anisotropy radius	137
4.4	Posterior PDF of the model parameters from joint analysis	138
4.5	Posterior PDF of the model parameters from joint analysis	139
4.6	Distribution of deflector and source redshifts of the lenses	151
4.7	Posterior PDF of cosmological parameters for the flat Λ CDM model	152
4.8	Posterior PDF for ϕ CDM, w CDM, and N_{eff} CDM models	153
4.9	Posterior PDF for ow CDM model	154
4.10	Cosmological parameters obtained from lensing and in combination with <i>Planck</i>	158
4.11	Confidence regions of the dark energy equation of state parameters	159
5.1	Comparison between the observed and reconstructed strong-lens systems	172
5.2	Flowchart showing the decision-tree for uniform modelling of quads	176
5.3	Best fit models for J0248+1913, J0408-5354, J1251+2935, and J1433+6007 . . .	192
5.4	Stability of lens model parameters with increasing model complexity	193
5.5	Mass and light alignments in the deflector galaxies	195
5.6	Distribution of χ_f^2 for flux-ratio anomalies	197
5.7	Best fit models J0147+4630, J0259-1635, J0405-3308, J0420-4037	209
5.8	Best fit models for J0630-1201, J1330+1810, J1606-2333, J2038-4008	210

5.9	Best fit models for J2344-3056	211
6.1	Elliptical deflection potential producing dumbbell-shaped surface-density	214
6.2	“Divide and conquer” strategy to compute lensing quantities	217
6.3	Decomposing the Sérsic and the projected NFW profile into Gaussian components	222
6.4	Comparison between our method and the multi-Gaussian expansion (MGE) method	223
6.5	Lensing quantities for an elliptical Gaussian convergence profile	236
6.6	Fitting synthetic lensing data with concentric Gaussian components of an elliptical Sérsic profile	240
6.7	Region of convergence	246

LIST OF TABLES

2.1	Best fit parameters for different bias models	24
2.2	Statistical properties of <i>WISE</i> –CMB cross-correlation amplitudes.	29
3.1	Redshift and stellar velocity dispersion	56
3.2	Measurements of velocity dispersion	59
3.3	Evidence for different power-law model setups	83
3.4	Evidence for different composite model setups	84
3.5	Lensing quantities used to create the microlensing time-delay map	94
3.6	Accretion disc properties used to compute the microlensing time-delay maps . .	96
3.7	Uncertainty contributions from different parts of the cosmographic analysis . . .	112
3.8	Summary of systematic checks	114
3.9	Prior for the model parameters	116
4.1	Priors for joint analysis with power-law mass profile	134
4.2	Priors for joint analysis with composite mass model	141
4.3	Parameters for different observational setups.	144
4.4	Uncertainties of D_d and $D_{\Delta t}$ for a single lens with different observational setups.	145
4.5	Cosmological models and parameter priors.	146
4.6	Uncertainties of D_d and $D_{\Delta t}$ for different lens systems.	148
4.7	Uncertainties on cosmological parameters.	150
5.1	Observation information and references for the lens systems.	170
5.2	Lens model profiles.	187

5.3	Lens model parameters	188
5.4	Astrometric positions of the deflector and quasar images	189
5.5	Photometry of the deflector and quasar images	191
5.6	Continued from Table 5.5.	194
5.7	Lens light parameters	204
5.8	Convergence, shear, and stellar convergence at the image positions	206
5.9	Continued from Table 5.8.	207
5.10	Predicted time-delays between the quasar images	208
6.1	Fidelity of our lens modelling method	241

ACKNOWLEDGMENTS

I deeply thank my research advisors Professor Tommaso Treu and Professor Edward Wright for guiding me through my PhD research. Their wise guidance enabled me to acquire scientific insights throughout my research projects and critically helped me bring this dissertation into fruition.

I also thank Dr. Simon Birrer, who was a post-doctoral researcher at UCLA, and also a very helpful research mentor for me. A large part of this dissertation was completed in close collaboration with Dr. Birrer. Many of my research projects also benefitted from the inputs from my collaborators in the H0LiCOW and STRIDES collaborations, to whom I express my gratitude.

I am also deeply grateful to the UCLA Astronomy division and the graduate student community for cultivating a supportive social and work environment. The PhD program can be stressful at times, but the support I received from my cohorts greatly helped me push through the stressful periods.

Last but not the least, I am deeply grateful to my parents, for their uncountable sacrifices and unwavering support for me pursuing a PhD degree on the other side of the globe and in a subject uncommon in my home country.

VITA

- 2014 B.S. (Physics), The University of Tokyo, Japan.
- 2016 M.S. (Astronomy), UCLA, Los Angeles, California.

PUBLICATIONS

Shajib, A. J., Treu, T., and Birrer, S. Revisiting SLACS: elliptical galaxies are well described by stars and Navarro–Frenk–White dark matter halo. To be submitted.

Shajib, A. J. et al. High-resolution imaging follow-up of doubly imaged quasars. Submitted to MNRAS (March 2020), under review.

Shajib, A. J., et al. STRIDES: A 3.9 per cent measurement of the Hubble constant from the strong lens system DES J0408–5354. MNRAS, staa828, 2020.

Shajib, A. J. Unified lensing and kinematic analysis for *any* elliptical mass profile. MNRAS, 488, 1387–1400, 2019.

Shajib, A. J., et al. Is every strong lens model unhappy in its own way? Uniform modelling of a sample of 13 quadruply+ imaged quasars. MNRAS, 483, 5649–5671, 2019.

Shajib, A. J., Treu, T., and Agnello, A. Improving time-delay cosmography with spatially resolved kinematics. MNRAS, 473, 210–226, 2018.

Shajib, A. J. and Wright, E. L. Measurement of the integrated Sachs-Wolfe effect using the AllWISE data release. *ApJ*, 827:116 (9pp), 2016.

CHAPTER 1

Introduction

1.1 The Λ cold dark matter model of cosmology: concordance and tensions

Our current understanding of the Universe is described by the Λ cold dark matter (Λ CDM) cosmology. In this model, approximately 5 per cent of the Universe’s total energy budget can be attributed to the baryonic matter and radiation (Planck Collaboration 2018). The remaining 95 per cent of the energy budget is attributed to two components: dark matter and dark energy. The dark matter is a form of matter that interacts with other massive particles only through gravitation, but it does not interact with the electromagnetic wave. It accounts for approximately 25 per cent of the Universe’s energy budget. The dark energy – amounting to the remaining 70 per cent of the energy budget approximately – drives the accelerated expansion of the Universe, which can be interpreted as a non-zero cosmological constant Λ (Riess et al. 1998; Perlmutter et al. 1999).

The Λ CDM model is highly successful in predicting observations over a large range of cosmological scales. On the largest scale up to the sound horizon at the recombination epoch, the Λ CDM model explains the anisotropy in the temperature fluctuation of the cosmic microwave background (CMB; e.g., Bennett et al. 2013; Planck Collaboration 2018). On the smaller end of the scales, the Λ CDM model successfully explains galaxy clustering statistics upto ~ 1 Mpc (e.g., Dawson et al. 2013; Alam et al. 2017). Additionally, the existence of the dark matter is evident from observations of galaxy rotation curves, strong and weak

lensing by galaxies and galaxy clusters, galaxy clustering etc. (e.g., Treu & Koopmans 2004; Clowe et al. 2004; de Blok et al. 2008; Heymans et al. 2013; Abbott et al. 2018b). The existence of the dark energy is strongly demonstrated by cosmic distance ladder based on the type Ia supernova, galaxy clustering, and the integrated Sachs–Wolfe effect (e.g., Boughn & Crittenden 2004; Vikhlinin et al. 2009; Riess et al. 2009; Scolnic et al. 2018).

Despite the multitude of evidences in support of the Λ CDM model, some open questions and observational disagreements still remain. The origin and physical properties of the dark matter and dark energy are yet unknown. The cold dark matter paradigm faces observational challenges on the sub-galactic scale, namely the missing satellite problem and the “too big to fail” problem (e.g., Klypin et al. 1999; Boylan-Kolchin et al. 2011). More recently, several observations have reported a significant tension ($\sim 5\sigma$) in the measured values of the Hubble constant H_0 , a central parameter in cosmology. This tension is between two classes of measurements: those that depend on the early-Universe physics and those that depend on local or late-Universe probes of the Hubble constant.

The strongest early-Universe constraint $H_0 = 67.4 \pm 1.2 \text{ km s}^{-1} \text{ Mpc}^{-1}$ is given by the CMB observation, which requires extrapolating from $H(z = 1100)$ to the current epoch ($z = 0$) assuming the Λ CDM cosmology (Planck Collaboration 2018). Baryon acoustic oscillation (BAO) is another probe that depends on the early-Universe physics. Combining BAO with galaxy clustering, weak lensing measurements, and Big Bang nucleosynthesis (BBN) provides $H_0 = 67.4 \pm 1.2 \text{ km s}^{-1} \text{ Mpc}^{-1}$ (Abbott et al. 2018a).

Among the local measurements in contrast, the cosmic distance ladder – based on type Ia supernova (SNIa) and calibrated using Cepheids – measures $H_0 = 74.0 \pm 1.4 \text{ km s}^{-1} \text{ Mpc}^{-1}$ (Riess et al. 2019). Strong-lensing time delays provide another local measurement of the Hubble constant at $H_0 = 73.3^{+1.7}_{-1.8} \text{ km s}^{-1} \text{ Mpc}^{-1}$ (Wong et al. 2017). As these two local measurements are independent, a combination of them is in 5.3σ tension with the early-Universe measurements. Several other local measurements of H_0 are also consistent with the SNIa+Cepheids measurement – for example, $H_0 = 73.9 \pm 3.0 \text{ km s}^{-1} \text{ Mpc}^{-1}$ from the

Megamaser Cosmology Project (Pesce et al. 2020), $H_0 = 69.6 \pm 1.9 \text{ km s}^{-1} \text{ Mpc}^{-1}$ from SNIa luminosity distances calibrated with tip of the red giant branch stars (Freedman et al. 2019), $H_0 = 73.3 \pm 4.0 \text{ km s}^{-1} \text{ Mpc}^{-1}$ SNIa luminosity distances calibrated with Mira variables (Huang et al. 2020).

This tension in H_0 can be a result of unknown systematics in one or several of the measurements mentioned above. However, if systematics can be ruled out in these measurements, then the tension will point to new physics beyond the Λ CDM model. To identify potential unknown systematics or the lack thereof, independent and precise ($\lesssim 1$ per cent) probes of H_0 is essential. Among the aforementioned H_0 probes, time-delay cosmography based on strong-lensing time delays holds the promise to provide a third and precise perspective to resolve the tension between the CMB-based and SNIa+Cepheids-based measurements. In the next section, I provide a general overview of the time-delay cosmography.

1.2 Strong gravitational lensing time delays as a cosmological probe

Strong gravitational lensing is the phenomenon when multiple images of a background source are produced by the gravitational lensing effect of a foreground deflector, typically a massive galaxy or galaxy cluster. In the regime of thin-lens approximation, the mass distribution of the foreground object is confined within the lens plane. This approximation is justified because the line-of-sight thickness of the deflector's mass distribution is negligible compared to the large cosmological distances between the observer and the source. For the projected surface density $\Sigma(\boldsymbol{\theta})$ of the foreground deflector at the lens plane, the deflection angle $\tilde{\boldsymbol{\alpha}}$ for a photon penetrating the lens plane at the position $\boldsymbol{\theta}$ is given by

$$\tilde{\boldsymbol{\alpha}}(\boldsymbol{\theta}) = \frac{4G}{c^2} \int \frac{(\boldsymbol{\theta} - \boldsymbol{\theta}') \Sigma(\boldsymbol{\theta}')}{|\boldsymbol{\theta} - \boldsymbol{\theta}'|^2} d^2\boldsymbol{\theta}' \quad (1.1)$$

(Blandford & Narayan 1986). The source position $\boldsymbol{\beta}$ and the image positions $\boldsymbol{\theta}$ are related by the lens equation

$$\boldsymbol{\beta} = \boldsymbol{\theta} - \frac{D_{\text{ds}}}{D_{\text{s}}} \tilde{\boldsymbol{\alpha}}(\boldsymbol{\theta}) = \boldsymbol{\theta} - \boldsymbol{\alpha}(\boldsymbol{\theta}), \quad (1.2)$$

where D_{ds} is the angular diameter distance between the deflector and the source, D_{s} is the angular diameter distance between the observer and the source, and $\boldsymbol{\alpha} \equiv \frac{D_{\text{ds}}}{D_{\text{s}}} \tilde{\boldsymbol{\alpha}}$ is the scaled deflection angle.

The photons that are emitted at the same time from the source arrive at the observer with a time delay, because they travel different cosmological distances and through different gravitational potentials while going around different sides of the foreground deflector. As a result, this time delay contains cosmological information. The time delay Δt_{AB} between two images labelled as A and B are given by

$$\Delta t_{\text{AB}} = \frac{1 + z_{\text{d}}}{c} \frac{D_{\text{d}} D_{\text{s}}}{D_{\text{ds}}} \left[\frac{(\boldsymbol{\theta}_{\text{A}} - \boldsymbol{\beta})^2}{2} - \frac{(\boldsymbol{\theta}_{\text{B}} - \boldsymbol{\beta})^2}{2} - \psi(\boldsymbol{\theta}_{\text{A}}) + \psi(\boldsymbol{\theta}_{\text{B}}) \right]. \quad (1.3)$$

Here, z_{d} is the deflector redshift, D_{d} is the angular diameter distance to the deflector, and $\psi(\boldsymbol{\theta})$ is the deflection potential that relates to the deflection angle as $\boldsymbol{\alpha} \equiv \nabla \psi$. The combination of the three angular diameter distances, that Δt depends on, is referred to as the “time-delay distance”:

$$D_{\Delta t} \equiv (1 + z_{\text{d}}) \frac{D_{\text{d}} D_{\text{s}}}{D_{\text{ds}}} \propto \frac{1}{H_0}. \quad (1.4)$$

As a result, measuring the time delay leads to the time-delay distance, and thus directly constrains the Hubble constant. Other cosmological parameters can also be measured from the time-delay distance, but the time-delay distance is weakly dependent on them. Therefore, combining multiple time-delay distance measurements from a large sample is necessary to achieve strong constraints on the other cosmological parameters (Shajib et al. 2018).

To measure the time delay, the background object needs to vary in luminosity. Refsdal (1964) first proposed to use time delays measured from strongly lensed supernova to measure the Hubble constant. However, strongly lensed supernova are rare phenomena with only a handful observed so far (Kelly et al. 2015; Goobar et al. 2017; Grillo et al. 2018). Strongly

lensed quasars have provided variable sources suitable for time-delay cosmography in larger numbers.

Early measurements of the Hubble constant from lensed quasars in the nineties and early 2000s suffered from large systematics in the methodology and/or from poor data quality. However, over the last decade, the status of time-delay cosmography has improved by a large margin (Treu & Marshall 2016). The key breakthroughs in this field from the past two decades are:

1. improved measurement of the time delay from high-cadence monitoring (Fassnacht et al. 2002; Tewes et al. 2013),
2. pixel-based lens modelling of the lensed arcs up to the noise level from high-resolution images (Suyu & Halkola 2010),
3. combining stellar kinematics of the deflector to alleviate lensing degeneracies (Treu & Koopmans 2002b), and
4. statistical constraint on the lensing effect from the line-of-sight structures (Suyu et al. 2010; Greene et al. 2013; Rusu et al. 2017).

Thanks to these breakthroughs, recent measurements of the time-delay distances have been more precise and robust. The H_0 Lenses in the COSMOGRAIL’s Wellspring (H0LiCOW Suyu et al. 2017) collaboration has led this field by analyzing six lensed quasar systems, five of which were done blindly (Suyu et al. 2010, 2013; Wong et al. 2017; Bonvin et al. 2017; Birrer et al. 2019; Chen et al. 2019; Rusu et al. 2019). Combination of these six systems has provided a highly precise measurement of the Hubble constant at $H_0 = 73.3^{+1.7}_{-1.8}$ km s⁻¹ Mpc⁻¹. To make further progress in this field with the goal of achieving a sub-per-cent precision in H_0 , we need to increase the sample size of analysed systems and simultaneously improve current methodologies to keep the systematics under control as statistical uncertainty shrinks.

1.3 Overview of this dissertation

In this dissertation, I first provide a significant (3.4σ) evidence for the existence of the dark energy – i.e., the Λ CDM cosmology – by detecting the integrated Sachs–Wolfe (ISW) effect (Chapter 2). This was the highest detection of the ISW effect from a single dataset at the time of publishing the result (Shajib & Wright 2016).

Next in Chapter 3, I perform a state-of-the-art measurement of the Hubble constant using time-delay cosmography. This measurement at $H_0 = 74.2^{+2.7}_{-3.0}$ km s^{−1} Mpc^{−1} is the most precise measurement of H_0 from a single lensed quasar system to date. This relatively high precision was achievable by extracting the rich information contained in the atypically complex lensed quasar system DES J0408–5354, which required improving the numerical techniques of time-delay lens modelling at multiple fronts. Combining this new analysis with the previous sample of six H0LiCOW lenses increases the precision of H_0 from time-delay cosmography to 2 per cent, and further strengthens the H_0 tension between the early-Universe and the late-Universe probes.

In the next chapters, I develop several methodologies that will enable rapid progress in time-delay cosmography in the near future. There are two ways to improve the precision in H_0 : (i) improve precision per system with higher quality or more informative data, and (ii) increase the sample size by analyzing more systems. In Chapter 4, I develop a novel method to combine spatially resolved kinematics with the lensing observables to vastly increase the H_0 precision per system. Using simulated data I forecast that we will require a sample of ~ 40 lens systems to achieve a sub-per-cent precision in H_0 . However, our current methodology to model lensed quasars requires a large amount of investigator time (typically 6 months to 1 year). To rapidly increase the sample size of analyzed systems, automating the modelling procedure is key to decrease the required investigator time. In Chapter 5, I provide one of the first automated algorithms to uniformly model large samples of lensed quasars. I apply my algorithm to model a sample of 13 quadruply lensed quasar systems (hereafter, quads),

which is the largest sample of uniformly modelled quads to date having nearly doubled the sample of known quads with available high-resolution imaging.

One of the major systematics in lens modelling is the adopted mass model for the deflector galaxies of the lens systems, which are typically massive ellipticals. Previous studies have shown that the total mass distribution in the massive elliptical galaxies resembles a power law close to an isothermal profile (e.g., Treu & Koopmans 2004; Gavazzi et al. 2007). These observations motivated the use of elliptical power-law mass models to describe the deflector galaxies for time-delay lens modelling, and such models are currently not the dominant source of systematics (Millon et al. 2019). However, with increasing sample size of time-delay lenses and shrinking statistical uncertainty, we need to study the internal structure of elliptical lens galaxies more closely to revalidate our mass model assumptions. To identify potential departure from the power-law at various scale sizes, we need to adopt more complex and empirically motivated mass models, e.g., generalized Navarro–Frenk–White profile for the dark matter distribution, mass-to-light ratio gradient in the baryonic distribution. However, such complex mass profiles have been numerically intractable to implement in lens modelling. In Chapter 6, I provide a novel method for efficient lens modelling of elliptical mass profiles with any radial shape, however complex. Moreover, this framework self-consistently unifies lens modelling with kinematics modelling, enabling joint analysis of lensing and spatially resolved kinematics as introduced in Chapter 4.

Finally in Chapter 7, I summarize the main results from each chapter and conclude this dissertation.

CHAPTER 2

An evidence for the Λ CDM cosmology: measuring the integrated Sachs–Wolfe effect

This chapter was published as Shajib, A. J. & E. L. Wright. 2016, ApJ, 827, 116, and reproduced here with minor formatting changes.

2.1 Background

After the discovery of dark energy in the late nineties (Perlmutter et al. 1999; Riess et al. 1998), it became one of the most elusive mysteries in the current-era physics. The existence of dark energy is overwhelmingly, albeit indirectly, evidenced by the measurements of low-redshift Type Ia supernovae, baryon acoustic oscillation, galaxy clustering, and strong lensing (e.g., Riess et al. 2009; Reid et al. 2010; Vikhlinin et al. 2009; Suyu et al. 2013), combined with the measurement of cosmic microwave background (CMB) anisotropies by the *Wilkinson Microwave Anisotropy Probe* (WMAP) (Hinshaw et al. 2013) and *Planck* (Planck Collaboration 2016a) missions. All these observations suggest our universe to be flat, expanding at an accelerated rate, and dominated by dark energy with approximately 70% of the energy density of the universe accounted by it.

The integrated Sachs-Wolfe (ISW) effect (Sachs & Wolfe 1967; Rees & Sciama 1968) provides us a method to directly detect the effect of dark energy on CMB photons. When CMB photons cross a gravitational potential well, they experience blueshift while falling in and redshift while going out. The large-scale gravitational potential well is frozen for a matter-

dominated, dark-energy-free, flat universe. As a result, the net shift in energy experienced by the CMB photons amounts to zero. However, for a dark-energy-dominated universe the large-scale gravitational potential well decays while the CMB photons are crossing the potential well. Consequently, the photons gain a little amount of energy as the redshift fail to completely compensate the blueshift. This energy shift is approximately one order of magnitude smaller than the primary CMB anisotropies, therefore a direct measurement of the ISW effect is not possible. However, the ISW effect results a correlation between hotter regions in CMB with the large-scale structure (LSS), which can be used as an indirect probe to detect this effect.

Several studies have been performed to detect the ISW effect signal by cross-correlating *WMAP* CMB temperature maps with various survey catalogs and radiation backgrounds, e.g., Sloan Digital Sky Survey (SDSS) luminous red galaxies (Fosalba et al. 2003; Padmanabhan et al. 2005; Granett et al. 2009; Pápai et al. 2011), 2MASS galaxies (Afshordi et al. 2004; Rassat et al. 2007; Francis & Peacock 2010), APM galaxies (Fosalba & Gaztañaga 2004), radio galaxies (Nolta et al. 2004; Raccanelli et al. 2008), and hard X-ray background (Boughn & Crittenden 2004). The typical confidence level for the ISW effect detection in the above studies is $2\text{--}3\sigma$. Comprehensive analyses combining different data-sets were carried out by Ho et al. (2008) to detect a 3.5σ ISW effect signal and by Giannantonio et al. (2008) to achieve the strongest detection to date at 4.5σ . Planck Collaboration (2015) detected a 4σ ISW effect cross-correlation between the *Planck* CMB data and a combination of various data-sets. Using the *Planck* 2015 data release alone, Cabass et al. (2015) measured an upper limit for the ISW effect signal amplitude to be $A < 1.1$ at 95% confidence level relative to the Λ CDM expectation of $A = 1$.

The *Wide-field Infrared Survey Explorer* (*WISE*; Wright et al. 2010) conducted an all-sky survey in four mid-infrared frequency bands spanning from 3.4 to 22 μm . This survey, with millions of galaxies and active galactic nuclei (AGNs), provides one of the most lucrative data-sets to carry out ISW effect studies. Some earlier studies have been conducted using

WISE data to detect the ISW effect signal: using *WISE* preliminary release and *WMAP* 7-year data to find a 3.1σ detection with the best fit being 2.2σ higher than the Λ CDM prediction (Goto et al. 2012); using *WISE* all-sky data and *WMAP* 7-year data to find an 1σ detection consistent with the Λ CDM prediction (Kovács et al. 2013); using *WISE* all-sky data and *WMAP* 9-year data to find a combined 3σ ISW effect detection for galaxies and AGNs (Ferraro et al. 2015).

Whereas some of the above mentioned studies reported the signal amplitude of the ISW effect to be in good agreement to the Λ CDM model (e.g., Kovács et al. 2013; Ferraro et al. 2015), some other studies found the ISW effect amplitude to be higher (by $1-2\sigma$) than that predicted by the Λ CDM model (e.g., Ho et al. 2008; Granett et al. 2009; Goto et al. 2012). *WISE* has detected a large number of point sources over the whole sky and the final AllWISE data release goes roughly twice as deep into the redshift space than the previous all-sky data release according to the AllWISE Explanatory Supplement¹. This makes AllWISE data very well-suited to carry out an ISW effect study as the detected objects span a wide range in redshift space that includes where the ISW effect is maximized. In this study, we used the AllWISE and *WMAP* 9-year data-sets to detect the ISW effect signal.

The organization of the chapter is as follows. In section 2.2, we briefly review the ISW effect. In section 2.3, we describe the data-sets and methods. We present our results in section 2.4, followed by discussion and conclusions in section 2.5. Throughout this chapter, we use *Planck* 2015 results (Planck Collaboration 2016a): $H_0 = 67.74 \text{ km s}^{-1}\text{Mpc}^{-1}$, $\Omega_m = 0.31$ and $\Omega_V = 0.69$ for our fiducial cosmology.

2.2 The ISW Effect

The primary anisotropy in the CMB was created during the last scattering at redshift $z \sim 1100$ due to fluctuations of potential energy, photon density, and velocity. The ISW effect is a

¹<http://wise2.ipac.caltech.edu/docs/release/allwise/expsup/index.html>

secondary CMB anisotropy created by the time variation of gravitational potential along the line of sight (Figure 2.1). This can be expressed as an integral from the last scattering surface to present day as

$$\begin{aligned} \left(\frac{\delta T}{T}\right)_{ISW}(\hat{\mathbf{n}}) &= -\frac{1}{c^2} \int \left(\dot{\Phi} + \dot{\Psi}\right) [\eta, \hat{\mathbf{n}}(\eta_0 - \eta)] \times e^{-\tau(z)} d\eta \\ &\approx -\frac{2}{c^2} \int \dot{\Phi} [\eta, \hat{\mathbf{n}}(\eta_0 - \eta)] d\eta, \end{aligned} \quad (2.1)$$

where η is the conformal time given by $\eta = \int dt/a(t)$, $a(t)$ is the scale factor, $\dot{\Phi}$ and $\dot{\Psi}$ are the conformal time derivatives of the gravitational potentials Φ and Ψ , τ is the optical depth, and $e^{-\tau(z)}$ is the visibility function for CMB photons. Here on the second line, we approximated $\tau \ll 1$ over the period when $\dot{\Phi} \neq 0$ to take $e^{-\tau} \approx 1$. We also assumed that anisotropic stresses are negligible, thus we have $\Phi = \Psi$.

As mentioned before, the ISW effect signal is roughly 10 times smaller than the primary CMB anisotropies, thus cleanly separating the ISW effect from the primary anisotropy is not possible. Moreover, the total ISW effect signal includes both positive and negative contributions due to all the small-scale potential fluctuations along the line of sight. We can assume that the ISW effect contributions from the small-scale potential wells and hills cancel each other out within a large enough scale. Then, the significant contribution on the ISW effect signal comes from the LSS. In addition to the ISW effect, the Sunyaev-Zeldovich effect (Sunyaev & Zeldovich 1972) and lensing of CMB photons by matter distribution can also induce a secondary anisotropy that correlates with matter overdensity. However, these anisotropies are only important in small angular scales with multipole $l \gtrsim 100$. We can assume the ISW effect to be the dominant source of secondary anisotropy in the multipole range $l \leq 100$.

To detect the ISW effect signal, we can take a cross-correlation between the CMB temperature anisotropy and the overdensity of a tracer for matter distribution, e.g., galaxies and AGNs. For simplicity we only use subscript or superscript “ g ” to denote terms related

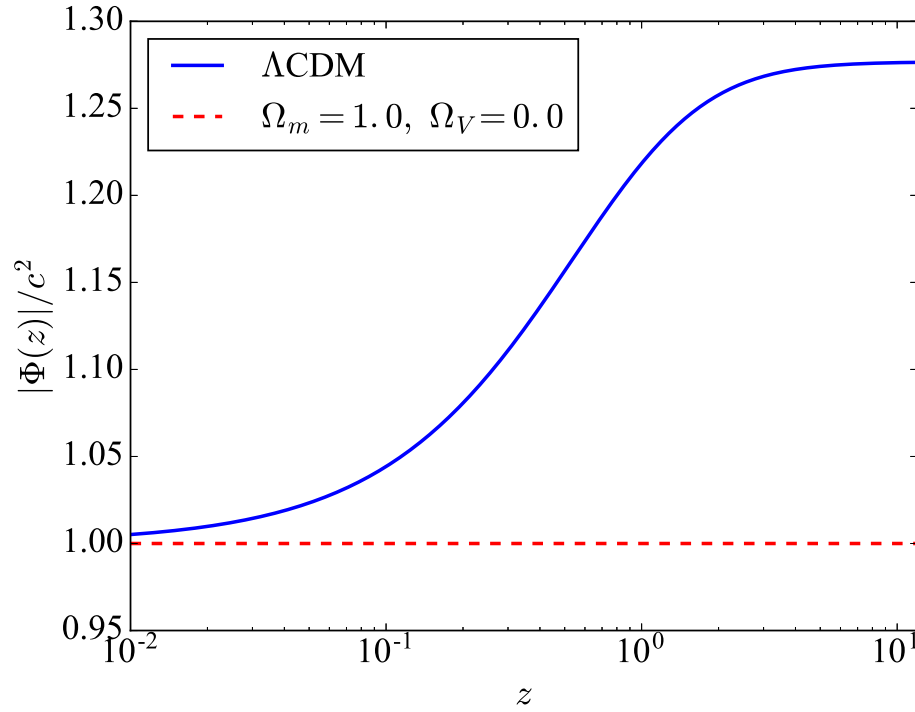


Figure 2.1: Large-scale gravitational potential as a function of redshift. The potential has been normalized so that $|\Phi(0)|/c^2 = 1$. Blue solid line is for the Λ CDM universe with our fiducial cosmology and red dashed line is for a matter-only flat universe.

to the tracer distribution, which are equally applicable for galaxies and AGNs. The tracer overdensity along a given direction $\hat{\mathbf{n}}$ is given by

$$\delta_g(\hat{\mathbf{n}}) = \int b_g(z) \frac{dN}{dz} \delta_m(\hat{\mathbf{n}}, z) dz, \quad (2.2)$$

where dN/dz is the selection function of the survey normalized so that $\int dN/dz dz = 1$, $b_g(z)$ is the tracer bias function relating visible matter and dark matter distributions, and δ_m is the matter density perturbation.

Then, the overdensity-CMB cross-power spectrum is given by

$$C_l^{Tg} = C_l^{\Phi g} = 4\pi T_{CMB} \int \Delta_m^2(k) I_l^\Phi(k) I_l^g(k) \frac{dk}{k}, \quad (2.3)$$

where $\Delta_m^2(k)$ is the dimensionless matter power spectrum at redshift $z = 0$ given by $\Delta_m^2(k) = k^3 P(k, z = 0)/2\pi^2$ (Cooray 2002). The weight functions for the tracer overdensity and the ISW effect are given by

$$I_l^g(k) = \int b_g(z) \frac{dN}{dz} D(z) j_l(k\chi(z)) dz, \quad (2.4)$$

$$I_l^\Phi(k) = \frac{3\Omega_m H_0^2}{c^2 k^2} \int \frac{d}{dz} [(1+z)D(z)] j_l(k\chi(z)) dz, \quad (2.5)$$

where j_l is the spherical Bessel function, $\chi(z)$ is the comoving distance to redshift z given by $\chi(z) = c[\eta_0 - \eta(z)]$, and $D(z)$ is the linear growth factor normalized so that $D(z = 0) = 1$.

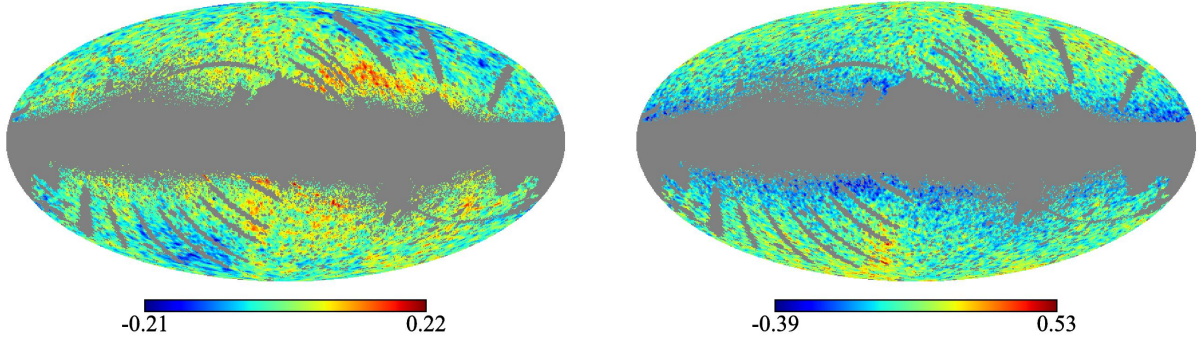


Figure 2.2: Overdensity maps in galactic coordinate with healpix resolution parameter $n_{\text{side}} = 128$ for galaxies (left) and AGNs (right). These maps are smoothed with a Gaussian window of standard deviation $\sigma = 0.5$ deg. The grey area is the mask where the overdensity is zero. The mask leaves the unmasked sky fraction $f_{\text{sky}} = 0.46$.

2.3 Data and Methods

2.3.1 CMB Map

We used the 9-year foreground reduced *WMAP* temperature data provided by the LAMBDA website² (Bennett et al. 2013). We only used Q, V, and W bands (41, 61, and 94 GHz respectively) as they have the least amount of galactic contamination. As we are only interested in $l \leq 100$, the maps were re-binned into HEALPIX (Hierarchical Equal Area isoLatitude Pixelization; Górski et al. 2005) maps with resolution parameter $n_{\text{side}} = 128$. We have used the KQ75y9 extended temperature analysis mask with $f_{\text{sky}} = 0.65$, which excludes point sources detected by *WMAP*. The final mask is the combination of the *WMAP* mask and a mask for the *WISE* data described in subsection 2.3.3. This final mask was applied to both of the maps before taking the cross-correlation.

²<http://lambda.gsfc.nasa.gov/>

2.3.2 *WISE* Data

The *WISE* mission surveyed the whole sky in four bands: 3.4 (W1), 4.6 (W2), 12 (W4), and 22 μm (W4). In this study, we used the AllWISE data release, which combines the 4-band cryogenic phase with the NEOWISE post-cryo phase (Mainzer et al. 2011). This data release is deeper than the previous all-sky data release by roughly a factor of two in W1 and W2 bands as the NEOWISE post-cryo phase only used these two bands. The AllWISE source catalog has over 747 million objects with $\text{SNR} \geq 5$ for profile-fit flux measurement in at least one band. We only select sources from the catalog using W1 and W2 magnitudes with $\text{SNR} \geq 5$ for W1 band and $\text{SNR} \geq 3$ for W2 band.

The coverage of *WISE* is not uniform throughout the sky. The median number of exposures for the AllWISE data release is 30.17 ± 0.02 in W1 and 30.00 ± 0.03 in W2 with each exposure being 7.7 s long for both bands. According to the AllWISE Explanatory Supplement, the catalog is 95% complete for $W1 < 17.1$. Therefore, we applied this magnitude cut to ensure uniformity and completeness for our galaxy sample.

In this study, galaxies are defined as sources in the AllWISE catalog that are not classified as stars or AGNs. To remove stars from the object catalog, we used the color cut: $[W1 - W2 < 0.4 \ \& \ W1 < 10.5]$ (Jarrett et al. 2011). We also removed any object with $W1 - W2 < 0$ to effectively remove galactic stars (Ferraro et al. 2015; Goto et al. 2012). To select AGNs from the catalog, we used the color cut criterion

$$W1 - W2 > 0.662 \exp [0.232(W2 - 13.97)^2] \quad (2.6)$$

(Assef et al. 2013).

For some of the objects in the AllWISE catalog, the W1 source flux uncertainty could not be measured because of the presence of a large number of saturated pixels in 3-band cryo frames containing the source. These sources lie along a narrow strip of ecliptic longitude and they are marked by *null* values for `w1sigmpro`. These objects are removed from the sample. We also discarded any object with `cc_flags` $\neq 0$ in W1 or W2, as a non-zero value

for `cc_flags` indicates a spurious detection (diffraction spike, persistence, halo, or optical ghost). After applying the SNR and magnitude cuts, we are left with approximately 383 million objects. Out of these, roughly 192 million (50.0%) are classified as galaxies, 189 million as stars (49.3%), and 2.6 million (0.7%) as AGNs according to the adopted color cut criteria.

2.3.3 Mask

We constructed the mask for the overdensity-CMB cross-correlation analysis with HEALPIX resolution parameter $n_{\text{side}} = 128$. The `moon_lev` flag in the AllWISE catalog indicates the fraction of frames contaminated by moonlight among the number of frames where the flux from a source was measured. We added HEALPIX pixels with more than 20% sources with `moon_lev` > 2 to the mask. HEALPIX pixels with more than 10% sources with `cc_flags` $\neq 0$ out of the total source count within the pixel are also added to the mask. As mentioned in subsection 2.3.2, some objects in the AllWISE catalog with *null* values for `w1msigpro` were removed from the sample and we excluded regions with more than 1% of such sources. We also excluded regions with galactic latitude $|b| < 10^\circ$ to effectively remove areas of galactic contamination. For the AGN overdensity map, some HEALPIX pixels ($< 0.2\%$) had abnormally high source count and we added these pixels to the mask for the AGN overdensity map. After applying the combined final mask, the unmasked sky fraction becomes $f_{\text{sky}} = 0.46$ (Figure 2.2). This unmasked region contains approximately 106 million galaxies and 1.5 million AGNs.

2.3.4 Theoretical Computation

It is computationally difficult to evaluate the spherical Bessel integrals in equations (2.4) and (2.5) through brute force. For efficient computation, we reformulated these integrals as logarithmically discretized Hankel transform following Hamilton (2000). In this form,

the integrals can be evaluated through fast-Fourier-transform (FFT) convolutions using the FFTLOG algorithm (Talman 1978).

Lastly, we used CAMB with HALOFIT (Lewis et al. 2000; Smith et al. 2003) to generate the non-linear matter power spectra for our fiducial cosmology.

2.4 Results

2.4.1 Redshift Distribution

We performed source matching between SDSS DR12 (Alam et al. 2015) galaxy sample and our AllWISE galaxy sample with a matching radius of $3''$. The matching radius was chosen based on the angular resolutions for *WISE* W1 and W2 bands, which are $6.1''$ and $6.4''$ respectively. We only chose approximately 82 million galaxies with $r > 22.2$ (95% completeness limit, Abazajian et al. 2004) from the SDSS DR12 *Photoz* catalog.³ The common sky fraction for our mask and SDSS coverage region is $f_{\text{sky}} = 0.24$ and it contains approximately 56 million AllWISE galaxies. We find matching pairs for roughly 29% of the AllWISE galaxy sample. The redshift distribution was then inferred from the SDSS photometric redshift of the matched galaxies (Figure 2.3). The low matching percentage of the AllWISE galaxies with SDSS is expected, because high redshift galaxies are optically fainter with redder $r-W1$ color and the majority of the unmatched AllWISE galaxies can be massive ellipticals at $z \gtrsim 1$ (Yan et al. 2013). As the 95% completeness magnitude limit for *WISE*, $W1 < 17.1$, goes quite deep in the redshift space, many high redshift *WISE* selected galaxies fall beyond the SDSS 95% completeness limit of $r < 22.2$ (Figure 2.4).

To obtain the redshift distribution of the AGN sample, we executed source matching with approximately 750 thousand objects flagged as ‘QSO’ in the SDSS DR12 *SpecObjA11* catalog, which has spectroscopic redshifts for roughly 4.4 million objects. The matching

³RA and dec for corresponding sources in the *Photoz* table are taken from the *GalaxyTag* table.

radius was also taken as $3''$. Out of roughly 848,000 *WISE* selected AGNs in the common coverage region, we found matching pairs for approximately 15% of them.

It should be noted that SDSS had an uneven target selection strategy over different redshifts leading to a bias in the redshift distribution of the SDSS objects. Therefore, the redshift distribution obtained by source matching with SDSS objects would also be similarly biased. However, the ISW effect sensitivity function is widespread over a broad range of redshift peaking at $z_{peak} \approx 0.66$ (Figure 2.3) and the ISW effect measurement by cross-correlation is not largely sensitive to errors in the estimation of redshift distribution (Afshordi 2004).

2.4.2 Bias Measurement

Following Ferraro et al. (2015), we used weak lensing of CMB by our tracers of matter overdensity to measure the bias. This method has two advantages over measuring the bias from auto-correlation of the tracers: (1) it takes into account contamination by stars or artifacts, (2) it is less prone to systematic errors giving a more robust estimation of the bias. The observed CMB temperature $T(\hat{\mathbf{n}})$ is the lensed remapping of the original CMB temperature field $T_0(\hat{\mathbf{n}} + \mathbf{d}) = T(\hat{\mathbf{n}})$, where \mathbf{d} is the deflection field. Then, CMB lensing convergence is defined as $\kappa \equiv -\nabla \cdot \mathbf{d}/2 = -\nabla^2 \phi/2$, where ϕ is the lensing potential. The lensing convergence can be expressed as the line-of-sight integral of matter fluctuation as

$$\kappa(\hat{\mathbf{n}}) = \int \delta(\chi \hat{\mathbf{n}}, z(\chi)) W^\kappa(\chi) d\chi, \quad (2.7)$$

where W^κ is the lensing window function given by

$$W^\kappa(\chi) = \frac{3\Omega_m H_0^2}{2c^2} \frac{\chi}{a(\chi)} \frac{\chi_{ls} - \chi}{\chi_{ls}} \quad (2.8)$$

(Cooray & Hu 2000). Here, $a(\chi)$ is the scale factor and $\chi_{ls} \approx 14$ Gpc is the comoving distance to the last-scattering surface.

The cross-correlation between the lensing convergence and matter overdensity field can be calculated using the Limber approximation (Limber 1953; Kaiser 1992), which works well

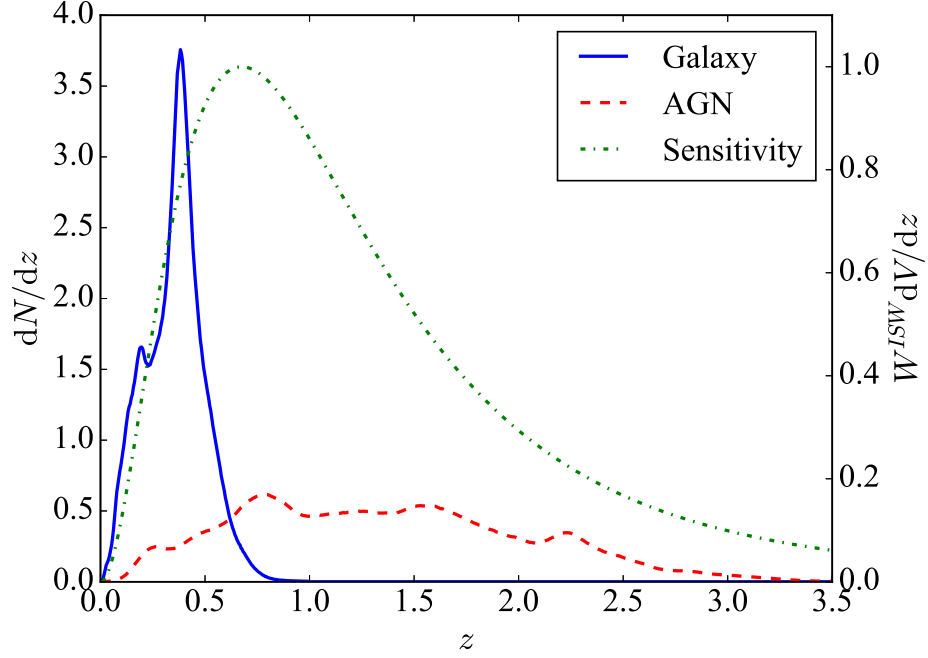


Figure 2.3: Redshift distribution of AllWISE galaxy (blue solid line) and AGN (red dashed line) samples along with the sensitivity function for the ISW effect cross-correlation (green dotted line). The redshift distribution for galaxies was obtained by cross-matching with SDSS galaxy `Photoz` catalog and the redshift distribution for AGNs was obtained by cross-matching with SDSS `SpecObjAll` catalog, with $3''$ matching radius for both cases. The distributions are normalized so that $\int (dN/dz) dz = 1$. The sensitivity function for the ISW effect cross-correlation given by $W^{ISW} dV/dz$ is shown with green dashed line, where $W^{ISW} = d[(1+z)D(z)]/dz$ is the ISW effect window function and V is the comoving volume. The sensitivity function is normalized to have a peak value of 1.

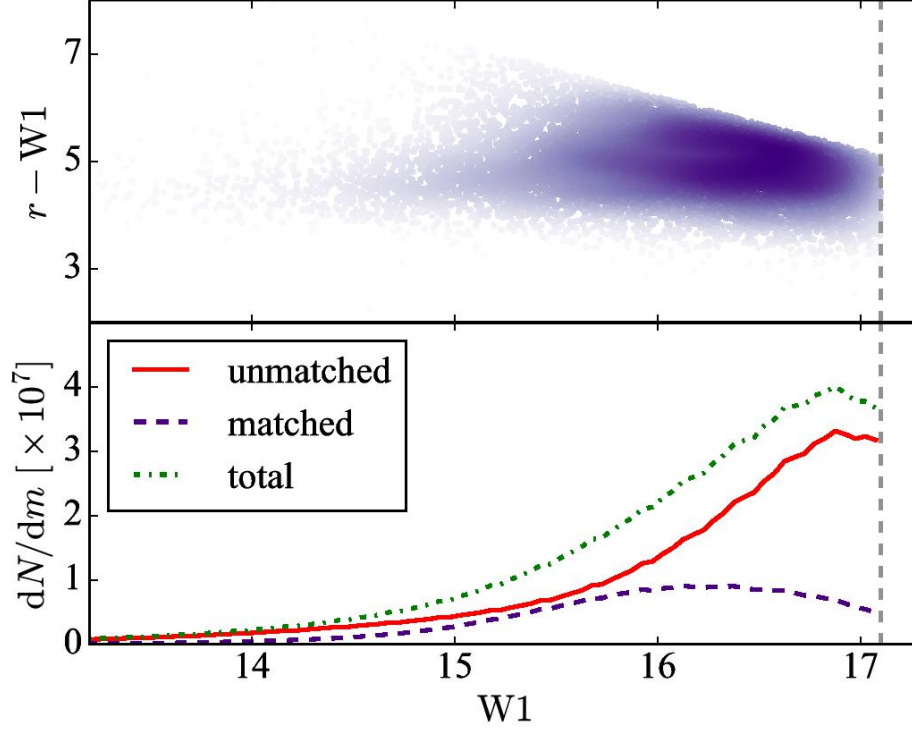


Figure 2.4: Matching fraction of the *WISE* galaxies with SDSS galaxies for different magnitudes and colors. The top panel shows $r-W1$ vs $W1$ color distribution of the matched galaxies. Darker area denotes higher density of galaxies and lighter area represents lower density of galaxies in this color-magnitude plot. The bottom panel shows the numbers of SDSS-matched (purple dashed line), unmatched (red solid line), and total (green dotted line) *WISE* galaxies per magnitude bin. The vertical grey dashed line shows the $W1 < 17.1$ magnitude cut for 95% completeness. Most of the unmatched galaxies are fainter in $W1$ and falls behind $r < 22.2$ (95% completeness cut for SDSS).

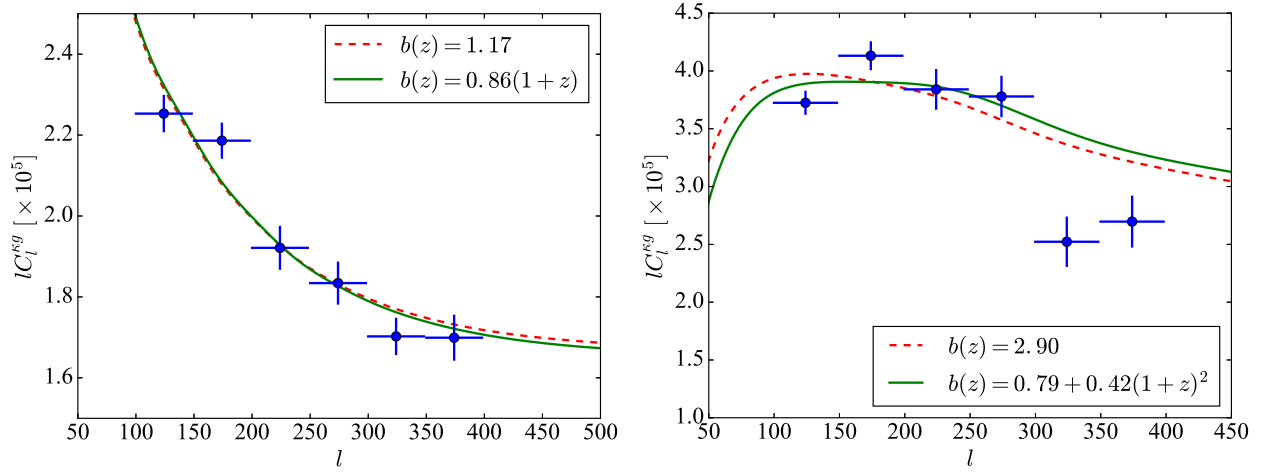


Figure 2.5: Cross-correlation between *Planck* lensing convergence and *WISE* galaxies (left) and AGNs (right). Vertical error bars are obtained from 100 simulated lensing convergence maps provided in the *Planck* lensing package and the horizontal error bars show bin widths for the bandpowers. The different bias models used for fitting are shown using lines and described in the corresponding legends. See Table 2.1 for the errors of the best fit parameters for different models.

for our angular scale of interest $l \gtrsim 100$, as

$$C_l^{\kappa g} \approx \int \frac{1}{\chi^2} W^\kappa(\chi) W^g(\chi) P\left(k = \frac{l+1/2}{\chi}, z\right) \frac{d\chi}{dz} dz, \quad (2.9)$$

where $P(k, z)$ is the non-linear matter power spectrum at redshift z for our fiducial cosmology and W^g is the tracer distribution window function given by

$$W^g(\chi) = \frac{dz}{d\chi} \frac{dN}{dz} b(\chi). \quad (2.10)$$

We used the lensing convergence map provided by *Planck* data release⁴ 2 (Planck Collaboration 2016b) to cross-correlate it with the overdensity maps of our LSS tracers to measure their effective biases. The correlation between *WISE* and *Planck* lensing convergence was investigated by Geach et al. (2013) and Planck Collaboration (2014), where these authors found $\sim 7\sigma$ detection for both galaxies and AGNs. Here, we repeated a similar analysis. We converted the lensing convergence and overdensity maps to HEALPIX resolution $n_{\text{side}} = 512$. The mask for this analysis was taken to be a combination of the mask for the ISW effect analysis and the lensing convergence mask provided in the *Planck* lensing package. The unmasked sky fraction for this combined mask is $f_{\text{sky}} = 0.45$. We obtained the pseudo-power spectrum $\tilde{C}_l^{\kappa g}$ of lensing-overdensity cross-correlation using the ANAFast facility of the HEALPIX package. We deconvolved the effect of masking and pixelization using the MASTER approach (Hivon et al. 2002) as

$$C_{l'}^{\kappa g} = \frac{1}{B_{l'}} \sum_l M_{ll'}^{-1} \tilde{C}_l^{\kappa g}, \quad (2.11)$$

where $M_{ll'}$ is the mode-mode coupling kernel for the applied mask and B_l is the pixel window function for $n_{\text{side}} = 512$. We binned the power spectra into six bins (bandpowers) in the multipole range $100 \leq l \leq 400$ as $C_b^{\kappa g} = \sum_l P_{bl} C_l^{\kappa g}$, where P_{bl} is the binning operator

$$P_{bl} = \begin{cases} \frac{l}{l_{\text{low}}^{(b+1)} - l_{\text{low}}^{(b)}}, & \text{if } l_{\text{low}}^{(b)} \leq l < l_{\text{low}}^{(b+1)}, \\ 0, & \text{otherwise.} \end{cases} \quad (2.12)$$

⁴<https://irsa.ipac.caltech.edu/Missions/planck.html>

Here, $l_{low}^{(b)}$ is the lower boundary of the b -th bin.

We used 100 simulated lensing convergence maps provided in the *Planck* lensing package to calculate the covariance matrix C as

$$C_{bb'} = \langle (\mathcal{C}_b^{\kappa g} - \langle \mathcal{C}_b^{\kappa g} \rangle_{sim}) (\mathcal{C}_{b'}^{\kappa g} - \langle \mathcal{C}_{b'}^{\kappa g} \rangle_{sim}) \rangle_{sim}, \quad (2.13)$$

where $\langle \rangle_{sim}$ denotes an average over the simulated maps.

We fit the estimated cross-correlation bandpowers to different bias models for both galaxies and AGNs. Several bias models have been proposed in the literature, e.g., constant bias model $b(z) = b_0$ (Peacock & Dodds 1994), linear redshift evolution model $b(z) = b_0(1 + z)$ (Ferraro et al. 2015), fitting function for AGNs $b(z) = b_0(0.55 + 0.289(1 + z)^2)$ (Croom et al. 2005) etc. We fit for the constant and linear evolution bias models in the lensing-overdensity cross-correlation analysis for galaxies, and the constant and fitting function bias models in the lensing-overdensity cross-correlation analysis for AGNs (Figure 2.5).

We obtained the best fit for each model by maximizing the likelihood function

$$\mathcal{L}(\mathbf{d}; \mathbf{t}, C) \propto \exp \left[-\frac{1}{2} (\mathbf{d} - \mathbf{t})^T C^{-1} (\mathbf{d} - \mathbf{t}) \right], \quad (2.14)$$

where \mathbf{d} is the vector containing measured bandpowers, \mathbf{t} is the vector containing expected bandpowers of the cross-correlation for each bias model, which depend on the model parameters, and C is the covariance matrix. Here, we have assumed that individual data points are Gaussian distributed. Maximizing the likelihood function is equivalent to minimizing $\chi^2 = (\mathbf{d} - \mathbf{t})^T C^{-1} (\mathbf{d} - \mathbf{t})$ and the likelihood ratio between two models are given by $-2 \ln(\mathcal{L}_1/\mathcal{L}_2) = \Delta\chi^2$. The best fit parameters for each model are given in Table 2.1. We used the best fit bias models, linear evolution model for galaxies and constant bias model for AGNs, in the CMB temperature-overdensity cross-correlation analysis.

Table 2.1. Best fit parameters for different bias models

LSS tracer	bias model $b(z)$	b_0	χ^2
Galaxy sample	b_0	1.17 ± 0.02^a	10.6
	$b_0(1+z)$	0.86 ± 0.01^a	9.7
AGN sample	b_0	2.90 ± 0.07^a	36.3
	$b_0(0.55 + 0.289(1+z)^2)$	1.44 ± 0.04^a	37.0

^aThe errors are computed by fitting the likelihood function $\mathcal{L}(\mathbf{d}; \mathbf{t}(b_0), \mathbf{C}) \propto \exp [(\mathbf{d} - \mathbf{t})^T \mathbf{C}^{-1} (\mathbf{d} - \mathbf{t})]$ to a Gaussian distribution and taking the standard deviation σ of the fit as the error. Here, \mathbf{d} is the vector containing measured bandpowers, \mathbf{t} is the vector containing expected bandpowers for a given bias model, and \mathbf{C} is the covariance matrix.

2.4.3 Cross-correlation Measurement

We measured the cross-correlation of *WMAP* CMB maps in Q, V, and W bands and the AllWISE galaxy and AGN overdensity maps. The complex geometry of the mask induces off diagonal correlations between the multipoles. We deconvolved the effect of masking and pixelization from the pseudo-power spectrum \tilde{C}_l^{Tg} , which is obtained through ANAFast, as

$$C_{l'}^{Tg} = \frac{1}{B_{l'} F_{l'}} \sum_l M_{ll'}^{-1} \tilde{C}_l^{Tg}, \quad (2.15)$$

where $M_{ll'}$ is the mode-mode coupling kernel for our adopted mask, B_l is the pixel window function for $n_{\text{side}} = 128$, and F_l is the *WMAP* beam transfer function. *WMAP* provides beam transfer functions for each differencing assembly in a band. We took an average of the beam transfer functions for all the differencing assemblies in a given band to obtain the beam transfer function for each band as $F_l^2 = \sum_i^N (F_l^{(i)})^2 / N$, where N is the number of differencing assemblies in each *WMAP* band and the index i goes over all the differencing assemblies. We binned the deconvolved power spectra into eight logarithmic bins (bandpowers) using a binning operator P_{bl} given by

$$P_{bl} = \begin{cases} \frac{1}{2\pi} \frac{l(l+1)}{l_{low}^{(b+1)} - l_{low}^{(b)}}, & \text{if } l_{low}^{(b)} \leq l < l_{low}^{(b+1)}, \\ 0, & \text{otherwise,} \end{cases} \quad (2.16)$$

where $l_{low}^{(b)}$ denotes the lower boundary of the b -th bin. We took the bin boundaries as $l = 2, 5, 8, 12, 17, 26, 41, 64, 100$; thus the first band includes $l = 2, 3, 4$ etc. We avoided $l \geq 100$ as the ISW effect is not sensitive to these small scales.

To estimate the Monte Carlo error bars and covariance matrices, we ran 5000 simulations for each *WMAP* band. We used our fiducial cosmological parameters and *WMAP* beam transfer function to obtain the simulated CMB maps using SYNFAST included in the HEALPIX package. Then, we added noise to each pixel by adding a random value from a Gaussian distribution with zero mean and standard deviation given by $\sigma = \sigma_0 / \sqrt{N_{obs}}$, where σ_0 is 2.188, 3.131, and 6.544 mK for Q, V, and W bands respectively and N_{obs} is the effective

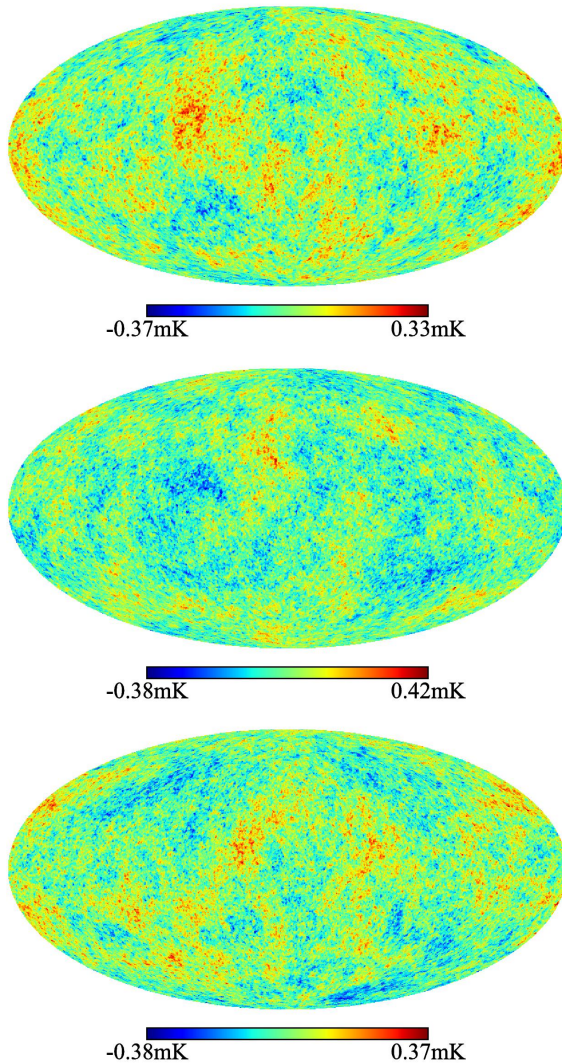


Figure 2.6: Examples of simulated *WMAP* CMB maps in Q band (top), V band (middle), and W band (bottom) using our fiducial cosmology and *WMAP* beam transfer function. They used different random a_{lm} 's, but the same C_l generated using CAMB for our fiducial cosmology.

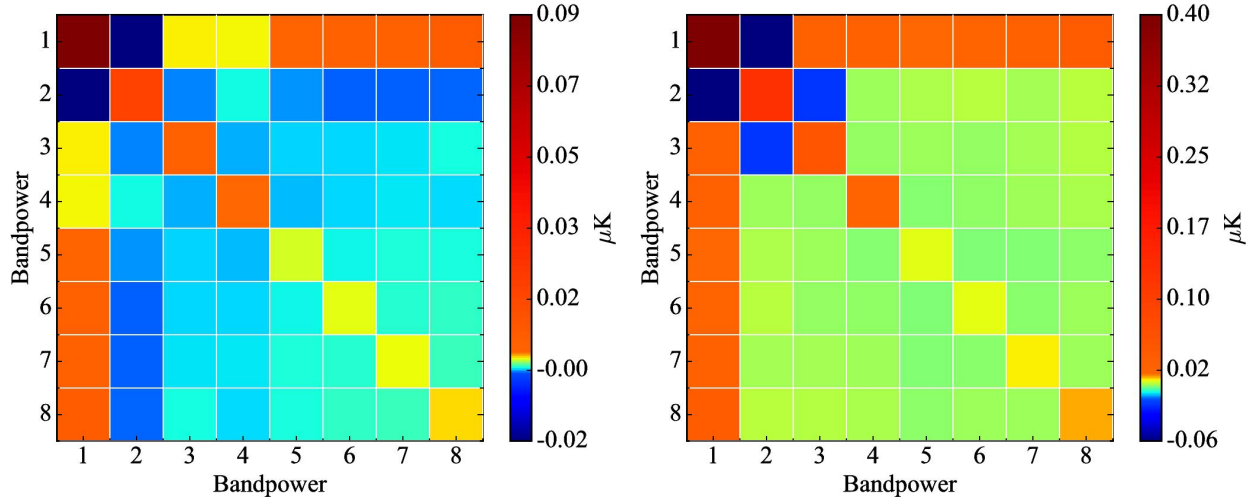


Figure 2.7: Monte Carlo covariance matrices for galaxy-CMB (left) and AGN-CMB (right) cross-correlation bandpowers in Q band. Covariance matrices for V and W bands are not included as they are similar.

number of observations for the corresponding pixel in the *WMAP* survey. Some examples of the simulated CMB maps for different *WMAP* bands are shown in Figure 2.6. We cross-correlated these simulated maps with AllWISE galaxy and AGN overdensity maps to obtain the covariance matrices according to equation (2.13). The error bars are taken to be the square roots of diagonal elements of the covariance matrix. The neighboring bins are anti-correlated by 3-20% in the lower multipole range and correlated by roughly 20-30% in the higher end of the multipole range (Figure 2.7).

We find that the band powers are consistent across different *WMAP* bands (Figure 2.8). This indicates that the CMB maps are not likely to have significant foreground contamination.

We obtained the amplitude A of the signal by minimizing $\chi^2 = (\mathbf{d} - A\mathbf{t})^T C^{-1}(\mathbf{d} - A\mathbf{t})$, where \mathbf{d} is the vector containing the measured bandpowers, \mathbf{t} is the vector containing corresponding bandpowers of the theoretically predicted power spectra for the Λ CDM model, and C is the Monte Carlo covariance matrix. Then, the signal amplitude and its error are

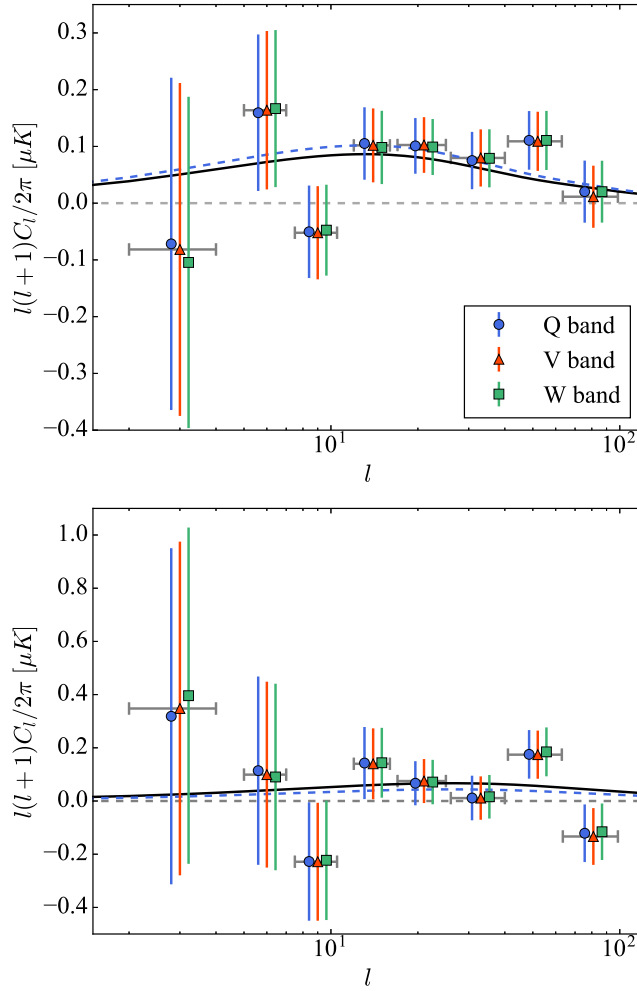


Figure 2.8: Power spectra of the cross-correlation between *WMAP* CMB maps and AllWISE overdensity maps for galaxies (top) and AGNs (bottom). The power spectra for $2 \leq l \leq 100$ in three *WMAP* bands, Q(blue circle), V(red triangle), and W(green rectangle), are binned into eight logarithmic bins. The points for Q and W bands are slightly shifted negatively and positively along l axis for better visual clarity. The vertical error bars are Monte Carlo error bars computed using 5000 simulated CMB maps for each *WMAP* band. The grey horizontal error bars for each group of points show the bin widths. The black solid line shows the theoretical prediction from the Λ CDM model and the blue dashed line is the best fit for Q band. For both galaxies and AGNs, the measured cross-correlation amplitude agrees very well with the Λ CDM prediction.

Table 2.2. Statistical properties of *WISE*–CMB
cross-correlation amplitudes.

LSS tracer	<i>WMAP</i> Band	A	S/N	χ^2	d.o.f.	$\Delta\chi^2_{\Lambda\text{CDM}}$	$\Delta\chi^2_{null}$
Galaxy sample	Q	1.18 ± 0.35	3.3	6.09	7	0.26	11.17
	V	1.19 ± 0.36	3.3	6.40	7	0.32	11.31
	W	1.17 ± 0.36	3.3	6.52	7	0.21	10.58
AGN sample	Q	0.65 ± 0.74	0.9	9.12	7	0.21	0.77
	V	0.62 ± 0.74	0.8	9.86	7	0.28	0.70
	W	0.65 ± 0.74	0.9	9.32	7	0.22	0.79

Note. — The “d.o.f.” column refers to the degrees of freedom of the χ^2 -distribution. $\Delta\chi^2_{null}$ shows $\Delta\chi^2$ of the best fit from the null hypothesis $\mathbf{t} = \mathbf{0}$ and $\Delta\chi^2_{\Lambda\text{CDM}}$ shows $\Delta\chi^2$ of the best fit from the ΛCDM prediction.

given by

$$\begin{aligned} A &= \mathbf{d}^T \mathbf{C}^{-1} \mathbf{t} [\mathbf{t}^T \mathbf{C}^{-1} \mathbf{t}]^{-1}, \\ \sigma_A &= [\mathbf{t}^T \mathbf{C}^{-1} \mathbf{t}]^{-1/2}. \end{aligned} \quad (2.17)$$

We calculated the significance of the detection from

$$\begin{aligned} \text{S/N} &= \sqrt{\chi_{null}^2 - \chi_{fit}^2} \\ &= \mathbf{d}^T \mathbf{C}^{-1} \mathbf{t} [\mathbf{t}^T \mathbf{C}^{-1} \mathbf{t}]^{-1/2} = \frac{A}{\sigma_A}, \end{aligned} \quad (2.18)$$

where χ_{fit}^2 is for the best fit and χ_{null}^2 is for the null hypothesis with $\mathbf{t} = \mathbf{0}$.

We detected the ISW effect signal for AllWISE galaxies with 3.3σ significance for all three *WMAP* bands. The combined ISW effect signal amplitude for the three *WMAP* bands is $A = 1.18 \pm 0.36$, which agrees very well with the Λ CDM prediction of $A = 1$. For AGNs, the ISW effect amplitude is $A = 0.64 \pm 0.74$ with 0.9σ significance, which is also in agreement with the Λ CDM model. The signal amplitude and some basic statistical properties for each *WMAP* band are given in Figure 2.4.3.

2.5 Discussion and Conclusions

In this study, we detected the ISW effect signal from the cross-correlation between the *WMAP* CMB temperature map and the matter overdensity map using AllWISE galaxies and AGNs as tracers for matter distribution. The ISW effect detection significances for galaxies and AGNs are 3.3σ and 0.9σ respectively with a combined significance of 3.4σ , with good agreement to the Λ CDM model for both tracers.

Among other ISW effect studies using *WISE* data, Goto et al. (2012) detected the ISW effect amplitude to be 2.2σ higher than that for the Λ CDM model, where these authors used *WISE* preliminary release and *WMAP* 7-year data. Ferraro et al. (2015) used *WISE* all-sky release and *WMAP* 9-year data to detect the ISW effect signal at 3σ and in good agreement with the Λ CDM cosmology. Our result fully agrees with the finding of Ferraro et al. (2015).

The measured biases of the tracers in our study for constant and linear redshift evolution bias models are lower than those calculated by Ferraro et al. (2015) by approximately 13-20%. Ferraro et al. (2015) used the lensing potential map from *Planck* data release 1 (2013), whereas we used the lensing convergence map provided by *Planck* data release 2 (2015). The 2013 lensing potential map was obtained by combining only the 143 and 247 GHz channels, whereas the 2015 lensing convergence map was constructed by applying a quadratic estimator to all nine frequency bands. Kuntz (2015) used both of the *Planck* data releases to measure the cross-correlation between CMB lensing and Canada-France-Hawaii Telescope Lensing Survey (CFHTLenS) galaxy catalog and found that the cross-correlation amplitude measured using the 2015 data is roughly 19% lower than that measured using the 2013 data. This result is consistent with the discrepancy in the bias measurement between Ferraro et al. (2015)’s and our studies.

The redshift distribution of the AllWISE galaxies might have missed a large fraction ($\sim 70\%$) at the higher redshift end of the distribution due to the shallower depth of SDSS galaxies. However, this missing fraction does not significantly effect our final amplitude measurement. We checked the robustness of our measurement against errors in redshift distribution estimation by using the redshift distribution of W1 selected galaxies from *WISE* all-sky release given by Yan et al. (2013) (as used by Ferraro et al. (2015)) instead of our own estimation. This distribution spans a wide range of redshift up to $z \sim 0.9$. We found the ISW effect amplitude for the galaxy sample to be $A = 1.28 \pm 0.39$ for this galaxy redshift distribution, which is very close (within 0.3σ) to the original measurement.

Contamination due to foreground emission in the CMB maps might lead to systematic error in the ISW effect detection in the form of spurious correlation with LSS tracers. However, the amount of foreground contamination would be different across the frequency bands. In our measurement, we find the cross-correlations between the LSS tracers and the CMB maps in three *WMAP* bands to be consistent with each other. This consistency rules out any significant contamination by foreground emission in the CMB maps.

The significance of the ISW effect signal amplitude for our AGN sample is low (0.9σ). This low significance is partially because the AGN sample mostly spans redshift range $z \geq 1$ where the universe is not yet dominated by dark energy. As a result, the ISW effect is less sensitive to this redshift range and the expected signal becomes low. On the other hand, due to the much smaller sample size of the AllWISE AGNs, the shot noise is higher than that for the galaxy sample. This high shot noise limits the detection significance, especially in higher multipoles.

Dark energy is one of the most active fields in modern cosmology as many of its properties still remain unknown. Although the existence of dark energy is highly evidenced by various indirect measurements, the ISW effect is one of the only few direct observational probes to study dark energy. In this study, we detected the ISW effect signal by cross-correlating *WMAP* CMB temperature maps with AllWISE galaxies and AGNs. These detections rule out a matter-dominated, dark-energy-free universe by a combined significance of 3.4σ . Future surveys, covering a large portion of the sky with extensive redshift coverage and sufficient number of frequency bands for photometric redshift estimation, can push this detection significance to 5σ level and attain the precision necessary to pinpoint the physical properties of dark energy.

Acknowledgements

We thank Alice E. Shapley, Xinnan Du, Daniel Cohen, Emily Martin, and Anson Lam for valuable comments to make this chapter clearer. AJS was partially supported by the National Aeronautics and Space Administration (NASA) grant 4-443820-WR-79063-02. This publication makes use of data products from the *WISE*, which is a joint project of the University of California, Los Angeles, and the Jet Propulsion Laboratory (JPL), California Institute of Technology, and NEOWISE, which is a project of the JPL, California Institute of Technology. *WISE* and NEOWISE are funded by the NASA. This research made use

of NASA's Astrophysics Data System; the NASA/IPAC Infrared Science Archive, which is operated by the JPL, California Institute of Technology, under contract with the NASA; matplotlib, a Python library for publication quality graphics (Hunter 2007); SciPy (Jones et al. 2001). We acknowledge the use of the Legacy Archive for Microwave Background Data Analysis (LAMBDA), part of the High Energy Astrophysics Science Archive Center (HEASARC). HEASARC/LAMBDA is a service of the Astrophysics Science Division at the NASA Goddard Space Flight Center. Funding for SDSS-III has been provided by the Alfred P. Sloan Foundation, the Participating Institutions, the National Science Foundation, and the U.S. Department of Energy Office of Science. The SDSS-III web site is <http://www.sdss3.org>. SDSS-III is managed by the Astrophysical Research Consortium for the Participating Institutions of the SDSS-III Collaboration.

CHAPTER 3

Measurement of the Hubble constant from the strong lens system DES J0408–5354

This chapter was published as Shajib, A. J., S. Birrer, T. Treu, A. Agnello, E. J. Buckley-Geer, J. H. H. Chan, L. Christensen, C. Lemon, H. Lin, M. Millon, J. Poh, C. E. Rusu, D. Sluse, C. Spiniello, G. C. F. Chen, T. Collett, F. Courbin, C. D. Fassnacht, J. Frieman, A. Galan, D. Gilman, A. More, T. Anguita, M. W. Auger, V. Bonvin, R. McMahon, G. Meylan, K. C. Wong, T. M. C. Abbott, J. Annis, S. Avila, K. Bechtol, D. Brooks, D. Brout, D. L. Burke, A. Carnero Rosell, M. Carrasco Kind, J. Carretero, F. J. Castander, M. Costanzi, L. N. da Costa, J. De Vicente, S. Desai, J. P. Dietrich, P. Doel, A. Drlica-Wagner, A. E. Evrard, D. A. Finley, B. Flaugher, P. Fosalba, J. García-Bellido, D. W. Gerdes, D. Gruen, R. A. Gruendl, J. Gschwend, G. Gutierrez, D. L. Hollowood, K. Honscheid, D. Huterer, D. J. James, T. Jeltema, E. Krause, N. Kuropatkin, T. S. Li, M. Lima, N. MacCrann, M. A. G. Maia, J. L. Marshall, P. Melchior, R. Miquel, R. L. C. Ogando, A. Palmese, F. Paz-Chinchón, A. A. Plazas, A. K. Romer, A. Roodman, M. Sako, E. Sanchez, B. Santiago, V. Scarpine, M. Schubnell, D. Scolnic, S. Serrano, I. Sevilla-Noarbe, M. Smith, M. Soares-Santos, E. Suchyta, G. Tarle, D. Thomas, A. R. Walker, & Y. Zhang. 2020, MNRAS, 494, 6072, and reproduced here with minor formatting changes.

3.1 Background

The concordance Λ cold dark matter (Λ CDM) cosmology explains the accelerated expansion of the Universe by incorporating the cosmological constant Λ (Riess et al. 1998; Perlmutter et al. 1999). The Λ CDM model is very successful in predicting observations covering a large range of physical scales – from the scale of sound horizon at the recombination epoch, down to the structure formation at the megaparsec scale (e.g. Alam et al. 2017; Planck Collaboration 2018; Abbott et al. 2018b). The Hubble constant, H_0 , plays a central role in cosmology, including in the Λ CDM model. The Hubble constant is not only crucial to determine the age of the Universe, it also normalizes the distances to distant galaxies. As a result, a precise understanding of the galaxy formation and evolution, and the Universe as a whole, closely depends on the precise knowledge of the Hubble constant.

Recently, a significant tension has been reported between the measurements of the Hubble constant using early-Universe and late-Universe probes (e.g. Planck Collaboration 2018; Riess et al. 2019; Wong et al. 2019). Among others, the most precise constraints on the Hubble constant come from extrapolating the cosmic microwave background (CMB) observation at the early-Universe, and from the measurement based on the cosmic distance ladder calibrated with parallax distances, Cepheids, and type Ia supernovae (SNIae). Assuming a Λ CDM cosmology, the *Planck* measurement gives $H_0 = 67.4 \pm 0.5 \text{ km s}^{-1} \text{ Mpc}^{-1}$ (Planck Collaboration 2018). The Supernovae, H_0 , for the Equation of State of dark energy (SH0ES) team measures $H_0 = 74.03 \pm 1.42 \text{ km s}^{-1} \text{ Mpc}^{-1}$ by calibrating the SNIa distance ladder using Cepheids and parallax distances (Riess et al. 2019). These two measurements are at 4.4σ tension. A cosmic distance ladder measurement from the Carnegie–Chicago Hubble project calibrated by the tip of the red giant branch (TRGB) stars reports $H_0 = 69.8 \pm 1.9 \text{ km s}^{-1} \text{ Mpc}^{-1}$, consistent with both of the above values on opposite sides (Freedman et al. 2019). However, the SH0ES team finds $H_0 = 72.4 \pm 1.9 \text{ km s}^{-1} \text{ Mpc}^{-1}$ using the TRGB stars to calibrate the SNIae distance ladder (Yuan et al. 2019). Additional probes, all con-

sistent with the tension at varying degrees of significance are summarized by Verde et al. (2019). This tension between the early-Universe and the late-Universe probes can be due to unknown systematics in any or all of the probes. However, if systematics can be ruled out as the source of this tension, then this tension would require extension of the Λ CDM model. In order to reach a conclusion on the tension and whether new physics is needed, it is paramount to have multiple independent measurements of the Hubble constant, each with sufficient precision on its own to resolve the discrepancy (< 2 per cent). In parallel it is also crucial to investigate in detail all possible sources of systematic uncertainties in each method.

Time-delay cosmography measures H_0 and other cosmological parameters independently of both the CMB or other high-redshift observations and the local probes such as the ones using the cosmic distance ladder (Refsdal 1964). The time-delay between the arrival time of photons at multiple images of a strong-lensing system (hereafter, lens) depends on the three angular diameter distances – between the observer and the deflector, between the deflector and the source, and between the observer and the source. A combination of these three angular diameter distances gives the so-called “time-delay distance” (Suyu et al. 2010). This time-delay distance is inversely proportional to H_0 and thus measuring this distance directly constrains H_0 .

To measure the time delay between the arrivals of photon at different lensed images that were emitted at the same time, we require a time-variable source. Although Refsdal (1964) originally proposed using strongly lensed supernovae as a time-variable source to measure the time-delay, only a few such supernovae have been discovered so far (e.g. Kelly et al. 2015; Goobar et al. 2017; Grillo et al. 2018). Even though the number of lensed supernova is still too small to be a competitive cosmological probe, the re-appearance of supernova Refsdal as predicted provides an important validation of the method (Treu et al. 2016).

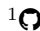
Strongly lensed quasars have provided time-variable sources in larger numbers. As a result, these objects have been predominantly used to measure H_0 from their time-delays

(e.g. Schechter et al. 1997; Treu & Koopmans 2002b; Suyu et al. 2010). Although some of the early measurements had shortcomings in the data quality or the analysis technique, both of these aspects have tremendously improved over the past decade (for a review with historical perspective, see Treu & Marshall 2016). The key breakthroughs in the past two decades have been: **(i)** high cadence monitoring to determine the time delays (e.g. Fassnacht et al. 2002; Tewes et al. 2013), **(ii)** high resolution images of the lensed arcs from the quasar host galaxy and pixel-based lens modelling to constrain the lens mass distribution (Suyu et al. 2010), **(iii)** adding stellar kinematics of the deflector (Treu & Koopmans 2002b), and **(iv)** statistical analysis of the line of sight to constrain the external convergence (Suyu et al. 2010; Greene et al. 2013; Rusu et al. 2017). Implementing these improvements, the H_0 Lenses in COSMOGRAIL’s Wellspring (H0LiCOW) collaboration measure $H_0 = 73.3^{+1.7}_{-1.8}$ km s $^{-1}$ Mpc $^{-1}$ using six lens systems (Suyu et al. 2010, 2013, 2014; Wong et al. 2017; Bonvin et al. 2017; Birrer et al. 2019; Rusu et al. 2019; Chen et al. 2019; Wong et al. 2019).

To reach 1 per cent precision in the Hubble constant with time-delay cosmography, a sample of ~ 40 lenses is necessary (Shajib et al. 2018). To have such a large sample of strongly lensed quasars available in the first place, the STRong-lensing Insights into Dark Energy Survey collaboration (STRIDES; Treu et al. 2018) has discovered numerous new lenses from the Dark Energy Survey (DES) footprint, in cases combining data from other large-area sky surveys (e.g. Agnello et al. 2015b; Nord et al. 2016; Ostrovski et al. 2017; Agnello et al. 2018b; Anguita et al. 2018; Lemon et al. 2019). The STRIDES is an external collaboration of the DES. The DES data are particularly useful in discovering new lenses due to its combination of uniform depth and coverage of area in the Southern hemisphere that is not covered by the Sloan Digital Sky Survey (SDSS). Additionally, thanks to new data mining and machine learning based techniques, new lenses have been discovered also from other photometric surveys – such as the VLT Survey Telescope-ATLAS (VST-ATLAS), Kilo-Degree Survey Strongly lensed Quasar Detection project (KiDS-SQuaD) (e.g., Agnello et al. 2015a, 2018d; Spiniello et al. 2018).

In this chapter, we present a blind analysis of the lens system DES J0408–5354 and infer H_0 from its time delays (Courbin et al. 2018). This lens was discovered in the DES footprint (Lin et al. 2017; Diehl et al. 2017). This chapter sets down two goals underlying our analysis. First, we aim to increase the statistical precision of the H_0 determination by presenting results from the analysis of a new lens system. Second, this system is being analysed independently and in parallel by two teams using two different codes in order to estimate potential systematics arising from modelling choices and software. This chapter presents the first of these two independent and blind analyses for DES J0408–5354. To facilitate meaningful comparison between independent modelling teams, the participating teams agreed beforehand on a set of baseline models with minimal but sufficient specifications. The teams are free to extend on the baseline models for exploring different sources of systematics as they see fit. This additional exploration by a team proceeds independently while keeping the cosmographic inferences blind. In this way, we aim to check on systematics that can potentially arise from different codes through comparison of the baseline models from different teams, and also from different model choices within one team’s analysis. In this chapter, we infer H_0 using the lens modelling software LENSTRONOMY, which is publicly available online at Github¹ (Birrer et al. 2015; Birrer & Amara 2018). A second independent team uses the software GLEE to analyse the same lens system (Suyu & Halkola 2010). In a future paper, cosmographic inference based on this second analysis and a comparison between the two analyses will be presented (Yıldırım et al., in preparation). Both of the independent modelling works use the results from a companion paper, which analyses the lens environment to detect galaxy groups and estimate the external convergence using the DES data, and measure the stellar kinematics of the central deflector galaxy from spectroscopic observations (Buckley-Geer et al. 2020).

Our concerted effort to analyse a system independently but based on the same data, and with some overlap in modelling choices, is an important step forward in estimating the

¹ <https://github.com/sibirrer/lenstronomy>

modelling errors with respect to previous works. Previous efforts by the H0LiCOW and Strong-lensing High Angular Resolution Programme (SHARP) collaborations took some step in this direction by assigning different lead investigators and softwares to the analysis of the six lenses (Lagattuta et al. 2012; Suyu et al. 2017). The lens systems B1608+656, RXJ1131–1231, HE 0435–1223, WFI2033–4723, and PG 1115+080 were analysed using the lens modelling software GLEE, whereas the systems RXJ1131–1231 and SDSS 1206+4332 were analysed using the software LENSTRONOMY (Suyu et al. 2010, 2013; Birrer et al. 2016, 2019; Wong et al. 2017; Rusu et al. 2019; Chen et al. 2019). In total, four different lead investigators modelled these six lenses, even though there was overlap between the team members. The two softwares used in the modelling differ in various aspects. For example, LENSTRONOMY performs source-reconstruction using a basis set of shapelets, whereas GLEE performs a pixelized source-reconstruction with regularization. LENSTRONOMY is a publicly available open-source software, whereas GLEE is not.

In order to preserve the blindness of the analysis, this chapter and the companion describing the analysis of the environment and line of sight used to compute the external convergence were internally reviewed by the STRIDES collaboration and the DES strong-lensing working group before unblinding. Once both the analyses and manuscripts met the approval of the internal reviewers and co-authors, unblinding happened on 2019 September 25. After unblinding, the only changes to the manuscript were the addition of the unblinded measurements, discussion on the unblinded results in Section 3.7, minor editing for clarity, grammar, and typos after the DES collaboration-wide review, and the addition of the plot showing the galaxy group’s convergence described in Appendix 3.C.

This chapter is organized as follows. In Section 3.2, we lay out the necessary formalism and describe the analysis framework. We present the data sets used in our analysis in Section 3.3. Next in Section 3.4, we describe the different mass and light profiles that are used in the lens modelling. We present the various lens model choices in Section 3.5. We report the results from the lens modelling and the cosmographic inference in Section 3.6. Finally, we

discuss the results and summarize the chapter in Section 3.7. We provide summaries of the uncertainty budget in our inferred H_0 , systematic checks, adopted models and parameter priors in Appendices 3.F and 3.G. The reported uncertainties in this chapter are computed from 16th and 84th percentiles of the posterior probability distribution.

3.2 Framework of the cosmographic analysis

In this section, we outline our cosmographic analysis using strong-lensing time delays. We briefly lay out the strong-lensing time-delay formalism in Section 3.2.1, discuss the lensing degeneracies in Section 3.2.2, present an overview of the kinematic analysis in Section 3.2.3, describe the cosmological analysis in Section 3.2.4, and formalize the underlying Bayesian inference framework of our analysis in Section 3.2.5.

3.2.1 Strong-lensing time delay

The framework described in this subsection was developed in previous studies – e.g., see Schneider et al. (1992); Blandford & Narayan (1992) – and was applied in previous studies to the measure H_0 from time delays (e.g., Suyu et al. 2010; Wong et al. 2017; Birrer et al. 2019).

The time delay Δt_{XY} between arrival of photons at two images, indexed with X and Y, of a multiply-imaged quasar by a single deflector is given by

$$\Delta t_{XY} = \frac{1 + z_d}{c} \frac{D_d D_s}{D_{ds}} \left[\frac{(\boldsymbol{\theta}_X - \boldsymbol{\beta})^2}{2} - \frac{(\boldsymbol{\theta}_Y - \boldsymbol{\beta})^2}{2} - \psi(\boldsymbol{\theta}_X) + \psi(\boldsymbol{\theta}_Y) \right]. \quad (3.1)$$

Here, the three angular diameter distances are D_d : between the observer and the deflector, D_s : between the observer and the source, and D_{ds} : between the deflector and the source. Additionally, z_d is the deflector redshift, c is the speed of light, $\boldsymbol{\theta}$ is the image position, $\boldsymbol{\beta}$ is the source position, and ψ is the deflection potential. The deflection potential is defined such that its gradient gives the deflection field $\boldsymbol{\alpha} \equiv \nabla \psi$. Then, the deflection potential relates to

the convergence κ as $\kappa = \nabla^2\psi/2$. We define the Fermat potential ϕ as

$$\phi(\boldsymbol{\theta}) \equiv \frac{(\boldsymbol{\theta} - \boldsymbol{\beta})^2}{2} - \psi(\boldsymbol{\theta}), \quad (3.2)$$

and the time-delay distance as

$$D_{\Delta t} \equiv (1 + z_d) \frac{D_d D_s}{D_{ds}}. \quad (3.3)$$

Then, we can express equation (3.1) in a more compact form as

$$\Delta t_{XY} = \frac{D_{\Delta t}}{c} (\phi(\boldsymbol{\theta}_X) - \phi(\boldsymbol{\theta}_Y)) \equiv \frac{D_{\Delta t}}{c} \Delta\phi_{XY}. \quad (3.4)$$

If multiple deflectors are present at close angular proximity at different redshifts, then we need to use the multilens-plane formalism to describe the lensing effect with sufficient accuracy. The time delay between two images for the case of lensing with P lens planes can be obtained by tracing the lensed light-ray backward from the image plane to the source plane as

$$\Delta t_{XY} = \sum_{i=1}^P \frac{D_{\Delta t, i, i+1}}{c} \left[\frac{(\boldsymbol{\theta}_{X, i} - \boldsymbol{\theta}_{X, i+1})^2}{2} - \frac{(\boldsymbol{\theta}_{Y, i} - \boldsymbol{\theta}_{Y, i+1})^2}{2} - \zeta_{i, i+1} \{ \psi_i(\boldsymbol{\theta}_{X, i}) - \psi_i(\boldsymbol{\theta}_{Y, i}) \} \right] \quad (3.5)$$

(cf. equation 9.17 of Schneider et al. 1992). Here, the first lens plane is the nearest to the observer and the $(P+1)$ -th plane refers to the source plane. The time-delay distance $D_{\Delta t, i, j}$ between a pair of planes is defined as

$$D_{\Delta t, i, j} \equiv \frac{1 + z_i}{c} \frac{D_i D_j}{D_{ij}}, \quad i < j, \quad (3.6)$$

where D_i is the angular diameter distance from the observer to the i th plane and D_{ij} is the angular diameter distance between the i th and j th planes. The rescaling factor $\zeta_{i, j}$ is defined as

$$\zeta_{i, j} \equiv \frac{D_{ij} D_s}{D_j D_{is}}, \quad i < j. \quad (3.7)$$

In this multilens-plane case, we can define the time-delay distance between the central deflector plane and the source plane as the effective time-delay distance $D_{\Delta t}^{\text{eff}} \equiv D_{\Delta t, d, s}$ that

normalizes the multilens-plane time delay as

$$\begin{aligned}
\Delta t_{XY} &= \frac{D_{\Delta t}^{\text{eff}}}{c} \sum_{i=1}^P \frac{1+z_i}{1+z_d} \frac{D_i D_{i+1} D_{\text{ds}}}{D_d D_s D_{i+1}} \left[\frac{(\boldsymbol{\theta}_{X,i} - \boldsymbol{\theta}_{X,i+1})^2}{2} \right. \\
&\quad \left. - \frac{(\boldsymbol{\theta}_{Y,i} - \boldsymbol{\theta}_{Y,i+1})^2}{2} \right. \\
&\quad \left. - \zeta_{i,i+1} \{ \psi_i(\boldsymbol{\theta}_{X,i}) - \psi_i(\boldsymbol{\theta}_{Y,i}) \} \right] \\
&= \frac{D_{\Delta t}^{\text{eff}}}{c} \Delta \phi_{XY}^{\text{eff}}.
\end{aligned} \tag{3.8}$$

Here, we defined the effective Fermat potential for the multilens-plane case as

$$\phi^{\text{eff}}(\boldsymbol{\theta}) \equiv \sum_{i=1}^P \frac{1+z_i}{1+z_d} \frac{D_i D_{i+1} D_{\text{ds}}}{D_d D_s D_{i+1}} \left[\frac{(\boldsymbol{\theta}_i - \boldsymbol{\theta}_{i+1})^2}{2} - \zeta_{i,i+1} \psi_i(\boldsymbol{\theta}_i) \right]. \tag{3.9}$$

In equation (3.8), the effective Fermat potential difference $\Delta \phi_{XY}^{\text{eff}}$ only contains the distance ratios. Thus, this term does not depend on H_0 . However, the distance ratios weakly depend on the relative expansion history, thus on the density parameter Ω in the context of Λ CDM. Only the effective time-delay distance $D_{\Delta t}^{\text{eff}}$ depends on H_0 in equation (3.8). For the single lens plane case with $P = 1$, the effective Fermat potential ϕ^{eff} and the effective time-delay distance $D_{\Delta t}^{\text{eff}}$ naturally take the form of their single-lens-plane equivalents ϕ and $D_{\Delta t}$ from equations (3.2) and (3.3), respectively.

3.2.2 Mass-sheet degeneracy

For lensing, the imaging observables such as the flux ratios and the relative astrometry are invariant with respect to the mass-sheet transformation (MST; Falco et al. 1985). If we transform the convergence and the source plane as

$$\begin{aligned}
\kappa(\boldsymbol{\theta}) &\rightarrow \kappa_{\vartheta}(\boldsymbol{\theta}) = \vartheta \kappa(\boldsymbol{\theta}) + 1 - \vartheta, \\
\boldsymbol{\beta} &\rightarrow \boldsymbol{\beta}' = \vartheta \boldsymbol{\beta},
\end{aligned} \tag{3.10}$$

then the lensing observables except the time delay remain invariant. This invariance under the MST is called the mass-sheet degeneracy (MSD). Notably, the MST also rescales the

magnification, thus the MSD can be broken with standard candles (Bertin & Lombardi 2006).

We can express the physically existent “true” mass distribution as

$$\kappa_{\text{true}} = \kappa_{\text{lens}} + \kappa_{\text{ext}}, \quad (3.11)$$

where, κ_{lens} is the convergence of the central deflector including nearby satellites and perturbers, and κ_{ext} is the convergence from projecting all the line-of-sight inhomogeneities onto the lens plane. If we impose the condition $\lim_{\theta \rightarrow \infty} \kappa_{\text{lens}} = 0$, then we have $\lim_{\theta \rightarrow \infty} \kappa_{\text{true}} = \kappa_{\text{ext}}$. As a result, we can interpret the external convergence κ_{ext} as the convergence far from or “external” to the central deflector. However, as we cannot constrain κ_{ext} only from the lensing observables due to the MSD, we aim to constrain a model κ'_{model} that captures all the lensing effects of κ_{true} . By taking $\vartheta = 1/(1 - \kappa_{\text{ext}})$ in equation (4.7), we can obtain an MST of κ_{true} as

$$\kappa_{\vartheta} = \frac{1}{1 - \kappa_{\text{ext}}}(\kappa_{\text{lens}} + \kappa_{\text{ext}}) - \frac{\kappa_{\text{ext}}}{1 - \kappa_{\text{ext}}} = \frac{\kappa_{\text{lens}}}{1 - \kappa_{\text{ext}}} = \kappa'_{\text{model}}. \quad (3.12)$$

Here, we name this κ_{ϑ} as κ'_{model} because it captures all the lensing effect of κ_{true} by the virtue of MST. If we can constrain κ'_{model} , then we can obtain κ_{true} simply through a MST with $\vartheta = 1 - \kappa_{\text{ext}}$ where κ_{ext} is separately constrained by studying the lens environment. However, the lens model κ_{model} that we actually constrain can potentially be an internal MST of κ'_{model} given by

$$\kappa'_{\text{model}} = \vartheta_{\text{int}} \kappa_{\text{model}} + 1 - \vartheta_{\text{int}}. \quad (3.13)$$

The internal MST factor ϑ_{int} only changes the shape of the mass profile, but it does not add any physical mass to the model within the Einstein radius. Note that both κ_{model} and κ'_{model} can satisfy $\lim_{\theta \rightarrow \infty} \kappa = 0$ by construction. In that case, ϑ_{int} is not a constant over the whole plane and we have the condition $\lim_{\theta \rightarrow \infty} \vartheta_{\text{int}} = 1$ (Schneider & Sluse 2014). This condition implies that ϑ_{int} does not physically add an infinite background-mass-sheet. With such a ϑ_{int} , both models κ_{model} and κ'_{model} can reproduce the lensing observables that are indistinguishable within the noise level in the data. Finally, combining equations (3.11), (3.12),

and (3.13), we write the relation between the “true” convergence κ_{true} and the modelled convergence κ_{model} as

$$\kappa_{\text{true}} = (1 - \kappa_{\text{ext}}) [\vartheta_{\text{int}} \kappa_{\text{model}} + 1 - \vartheta_{\text{int}}] + \kappa_{\text{ext}}. \quad (3.14)$$

Using different but equally plausible model parametrizations – e.g. power-law profile, composite profile – we explore different model families related by equation (3.13). To alleviate the MSD within a model family by constraining ϑ_{int} , we utilize non-lensing observables, e.g. kinematics of the deflector galaxy. Kinematics probes the 3D deprojection of κ_{lens} for a given combination of κ_{model} and κ_{ext} . Moreover, the addition of the kinematic information also constrains the angular diameter distance to the deflector D_{d} (Paraficz & Hjorth 2009; Jee et al. 2015). As a result, the uncertainty on the estimated H_0 is improved by kinematics in two ways:

1. by alleviating the MSD, and
2. by adding extra constraint on cosmology through D_{d}

(Birrer et al. 2016; Jee et al. 2016; Shajib et al. 2018). In the next subsection, we outline the kinematic analysis framework.

3.2.3 Kinematic analysis

The kinematic observable is the luminosity-weighted line-of-sight stellar velocity dispersion σ_{los} . To model the 3D mass distribution consistent with the observed velocity dispersion, we adopt the spherical solution of the Jeans equations. Although the true mass distribution is non-spherical, the assumption of spherical symmetry is sufficient given the 10–25 per cent uncertainty in our kinematic data (Section 3.3.4; Sonnenfeld et al. 2012). We can express the spherical Jeans equation as

$$\frac{d(l(r) \sigma_{\text{r}}^2)}{dr} + \frac{2\beta_{\text{ani}} l(r) \sigma_{\text{r}}^2}{r} = -l(r) \frac{d\Phi}{dr}. \quad (3.15)$$

Here, $l(r)$ is the 3D luminosity density of the stars, σ_r is the intrinsic radial velocity dispersion, and $\beta_{\text{ani}}(r)$ is the anisotropy parameter relating σ_r with the tangential velocity dispersion σ_t as

$$\beta(r) \equiv 1 - \frac{\sigma_t^2}{\sigma_r^2}. \quad (3.16)$$

By solving equation (3.15), we can obtain the luminosity-weighted, line-of-sight velocity dispersion as

$$\sigma_{\text{los}}^2(R) = \frac{2G}{I(R)} \int_R^\infty \mathcal{K}_\beta \left(\frac{r}{R} \right) \frac{l(r) M(r)}{r} dr, \quad (3.17)$$

where $M(r)$ is the enclosed mass within radius r (equation (A15)–(A16) of Mamon & Lokas 2005). Here, the function $\mathcal{K}_\beta(\varrho)$ depends on the parametrization of $\beta(r)$. We adopt the Osipkov–Merritt parametrization of the anisotropy parameter given by

$$\beta_{\text{ani}}(r) = \frac{r^2}{r^2 + r_{\text{ani}}^2}, \quad (3.18)$$

where r_{ani} is the anisotropy scale radius (Osipkov 1979; Merritt 1985b,a). For this parametrization, the function \mathcal{K}_β takes the form

$$\begin{aligned} \mathcal{K}_\beta(u) = & \frac{u_{\text{ani}}^2 + 1/2}{(u_{\text{ani}} + 1)^{3/2}} \left(\frac{u^2 + u_{\text{ani}}^2}{u} \right) \tan^{-1} \left(\sqrt{\frac{u^2 - 1}{u_{\text{ani}}^2 + 1}} \right) \\ & - \frac{1/2}{u_{\text{ani}}^2 + 1} \sqrt{1 - \frac{1}{u^2}}, \end{aligned} \quad (3.19)$$

where $u_{\text{ani}} = r_{\text{ani}}/R$ (Mamon & Lokas 2005).

The enclosed mass $M(r)$ is computed from the 3D mass profile. For the convergence and surface brightness profiles that cannot be straightforwardly deprojected into three dimension, we decompose them into concentric Gaussian components (Bandinelli 1991; Emsellem et al. 1994; Cappellari 2002; Shajib 2019). We then deproject the Gaussian components into 3D Gaussians to compute the enclosed mass $M(r)$ and 3D light density profile $l(r)$.

3.2.4 Cosmological distances

In this section, we effectively follow Birrer et al. (2016, 2019) to jointly infer $D_{\Delta t}$ and D_d . From the modelled convergence profile κ'_{model} of the deflector, we derive the time-delay dis-

tance $D'_{\Delta t}$ particular to the deflector's line of sight. We need to correct $D'_{\Delta t}$ for the external convergence κ_{ext} to obtain the true time-delay distance $D_{\Delta t}$. From equations (3.1) and (3.12), we can express the true time-delay distance $D_{\Delta t}$ as

$$D_{\Delta t} = \frac{D'_{\Delta t}}{1 - \kappa_{\text{ext}}}. \quad (3.20)$$

We can express σ_{los} in terms of parameters characterizing the 2D mass and light distributions and relevant angular diameter distances as

$$\sigma_{\text{los}}^2 = \frac{D_s}{D_{\text{ds}}} c^2 J(\xi_{\text{lens}}, \xi_{\text{light}}, \beta_{\text{ani}}), \quad (3.21)$$

where ξ_{lens} is the set of mass parameters, ξ_{light} is the set of light distribution parameters, c is the speed of light, and the function J captures all the dependencies from the mass profile, the light profile, and the orbital anisotropy (Birrer et al. 2016). The parameters in the argument of the function J are expressed in angular units, thus they do not depend on the cosmology. Then from equation (3.1), we have

$$\frac{D_d D_s}{D_{\text{ds}}} = \frac{c \Delta t_{\text{XY}}}{(1 + z_d) \Delta \phi_{\text{XY}}^{\text{eff}}(\xi_{\text{lens}})}. \quad (3.22)$$

Combining this equation with equation (3.21), we can write

$$D_d = \frac{c^3 \Delta t_{\text{XY}} J(\xi_{\text{lens}}, \xi_{\text{light}}, \beta_{\text{ani}})}{(1 + z_d) \sigma_{\text{los}}^2 \Delta \phi_{\text{XY}}^{\text{eff}}(\xi_{\text{lens}})} \quad (3.23)$$

(Birrer et al. 2016). As a result, we can estimate the angular diameter distance D_d to the deflector by combining the kinematics with the lensing observables. Therefore, we can infer two cosmological distances, $D_{\Delta t}$ and D_d , at specific redshifts relevant to the lens system. Thus, we can constrain the Hubble constant and other cosmological parameters from the distance–redshift relation for a given cosmology. In the next section, we describe the combined Bayesian framework to infer the Hubble constant from the observables.

3.2.5 Bayesian inference framework

At the top level, the two cosmological distances $D_{\Delta t}$ and D_d contain all the cosmographic information. We express the set of cosmological distances using the notation D , which is a

function $D(\omega; C)$ of the set of cosmological parameters ω for a given cosmology C . We denote the set containing all the observables as $O \equiv \{O_{\text{img}}, O_{\Delta t}, O_{\text{kin}}, O_{\text{env}}\}$, where O_{img} contains the imaging data of the lens system, $O_{\Delta t}$ contains the observed time delays, O_{kin} contains the spectra the of the deflector to estimate the kinematics, and O_{env} contains photometric and spectroscopic survey data of the lens environment to estimate the external convergence. Then from Bayes' theorem, we can write

$$\begin{aligned} p(\omega | O, C) &\propto p(O | \omega, C) p(\omega | C) \\ &= p(O | D(\omega; C)) p(\omega | C), \end{aligned} \quad (3.24)$$

where the probability density $p(\omega | O, C)$ is called the posterior of ω , the probability density $p(O | \omega, C)$ is called the likelihood of O given $\{\omega, C\}$, and the probability density $p(\omega | C)$ is called the prior for ω . In the last line of the above equation, we have changed $\{\omega, C\}$ into $D(\omega; C)$ in the likelihood term, as it allows us to break down the computation of the likelihood into two steps. First, we compute the likelihood $p(O | D)$ of the observed data for given cosmological distances marginalizing over various model choices and their respective parameters. Then, we can fold in the prior of the cosmological parameters $p(\omega | C)$ to obtain the posterior $p(\omega | O, C)$. As the different pieces of the data in O are independent, we can break up the likelihood into likelihoods of each observable type as

$$p(O | D) = p(O_{\text{img}} | D) p(O_{\Delta t} | D) p(O_{\text{kin}} | D) P(O_{\text{env}} | D). \quad (3.25)$$

When computing these likelihood functions, we adopt a combination of model choices. We denote the model choice containing the mass model parameters ξ_{lens} and deflector light model parameters ξ_{light} as M . In addition, we have to make specific choices for the parametrization ξ_{source} of the source light distribution and the parametrization ξ_{pert} of the mass profiles of the line-of-sight perturbers. We denote the model choice encompassing ξ_{source} and ξ_{pert} as S . We also marginalize over the external convergence κ_{ext} and the parameters ξ_{β} characterizing β_{ani} . Adding it all together, we can marginalize all the specific model parameters to express

the total likelihood given the distances as

$$\begin{aligned}
p(O \mid D, M) = & \int p(O_{\text{img}} \mid \xi_{\text{lens}}, \xi_{\text{light}}, \xi_{\text{source}}, \xi_{\text{pert}}, M, S) \\
& \times p(O_{\Delta t} \mid \Delta t(\xi_{\text{lens}}, \xi_{\text{light}}, \xi_{\text{pert}}, \kappa_{\text{ext}}; M, S)) \\
& \times p(\xi_{\text{source}}, \xi_{\text{pert}} \mid S) p(S) \\
& \times p(O_{\text{kin}} \mid \sigma_{\text{los}}(\xi_{\text{lens}}, \xi_{\text{light}}, \kappa_{\text{ext}}, \xi_{\beta}; M)) p(\xi_{\beta} \mid \xi_{\text{lens}}, \xi_{\text{light}}, M) \\
& \times p(O_{\text{env}} \mid \kappa_{\text{ext}}) p(\kappa_{\text{ext}}) \\
& \times p(\xi_{\text{lens}}, \xi_{\text{light}} \mid M) \\
& \times d\xi_{\text{source}} d\xi_{\text{pert}} dS d\xi_{\beta} d\kappa_{\text{ext}} d\xi_{\text{lens}} d\xi_{\text{light}}.
\end{aligned} \tag{3.26}$$

Here, we omitted some model parameters and model specifications in the conditional statements of the likelihoods where the corresponding likelihood does not depend on them. Breaking up the likelihood as above allows us to partially separate the computation of the likelihoods for different observable types before marginalizing over the model parameters. We first describe the imaging likelihood and marginalization over relevant models and model parameters in Section 3.2.5.1, then we explain the derivation of the joint posterior combining time delay and kinematics likelihoods with the lens model posterior in Section 3.2.5.2.

3.2.5.1 Lens model posterior and evidence from imaging likelihood

We can first obtain the posterior of the lens model parameters $\Xi \equiv \{\xi_{\text{lens}}, \xi_{\text{light}}, \xi_{\text{source}}, \xi_{\text{pert}}\}$ as

$$p(\Xi \mid O_{\text{img}}, M, S) = \frac{p(O_{\text{img}} \mid \Xi, M, S) p(\Xi \mid M, S)}{p(O_{\text{img}} \mid M, S)}. \tag{3.27}$$

Here, the term in the denominator $\mathcal{Z} \equiv p(O_{\text{img}} \mid M, S)$ is the evidence for the imaging data O_{img} given the model $\{M, S\}$. We first change the variables $\{\xi_{\text{lens}}, \xi_{\text{pert}}\} \rightarrow \{\xi_{\text{lens}}, \Delta\phi_{\text{XY}}^{\text{eff}}\}$ in equation (3.27) to be able to marginalize over parameters related to the line-of-sight galaxies while retaining their effect on the Fermat potential difference $\Delta\phi_{\text{XY}}$. As the Jacobian

determinant $|\mathrm{d}\{\xi_{\text{lens}}, \Delta\phi_{\text{XY}}^{\text{eff}}\}/\mathrm{d}\{\xi_{\text{lens}}, \xi_{\text{pert}}\}|$ cancels out from both sides, we have

$$\begin{aligned}
& p(\xi_{\text{lens}}, \xi_{\text{light}}, \xi_{\text{source}}, \Delta\phi_{\text{XY}}^{\text{eff}} \mid O_{\text{img}}, M, S) \\
&= p(O_{\text{img}} \mid \xi_{\text{lens}}, \xi_{\text{light}}, \xi_{\text{source}}, \Delta\phi_{\text{XY}}^{\text{eff}}, M, S) \\
&\quad \times \frac{p(\xi_{\text{lens}}, \xi_{\text{light}}, \xi_{\text{source}}, \Delta\phi_{\text{XY}}^{\text{eff}} \mid M, S)}{p(O_{\text{img}} \mid M, S)}.
\end{aligned} \tag{3.28}$$

We can marginalize this posterior over ξ_{source} and S as

$$\begin{aligned}
& p(\xi_{\text{lens}}, \xi_{\text{light}}, \Delta\phi_{\text{XY}}^{\text{eff}} \mid O_{\text{img}}, M) \\
&= \int p(\xi_{\text{lens}}, \xi_{\text{light}}, \xi_{\text{source}}, \Delta\phi_{\text{XY}}^{\text{eff}} \mid O_{\text{img}}, S, M) \\
&\quad \times p(S) \, \mathrm{d}\xi_{\text{source}} \, \mathrm{d}S.
\end{aligned} \tag{3.29}$$

Since the term inside the integral contains the evidence term \mathcal{Z} , the integral over the model space S automatically weights the models $\{S\}$ according to their evidence ratios. As we can only discretely sample models $\{S_n\}$ from the model space S , the integral in equation (3.27) becomes a discrete sum as

$$\begin{aligned}
& p(\xi_{\text{lens}}, \xi_{\text{light}}, \Delta\phi_{\text{XY}}^{\text{eff}} \mid O_{\text{img}}, M) \\
&= \sum_n \Delta S_n \int p(\xi_{\text{lens}}, \xi_{\text{light}}, \xi_{\text{source}}, \Delta\phi_{\text{XY}}^{\text{eff}} \mid O_{\text{img}}, S_n, M) \\
&\quad \times p(S_n) \, \mathrm{d}\xi_{\text{source}}.
\end{aligned} \tag{3.30}$$

Here, the term ΔS_n can be interpreted as the model space volume represented by the model S_n , thus it can account for sparse sampling from the model space.

In our model, we have both linear and non-linear parameters. The linear parameters are the amplitudes of the surface brightness profiles that we treat with a basis set in our model (Birrer et al. 2015). We denote the linear parameters using the vector $\boldsymbol{\lambda}$ and non-linear parameters using the set ν . Hence, the lens model parameters can alternatively be expressed as $\Xi \equiv \{\nu, \boldsymbol{\lambda}\}$. We can write the evidence integral as

$$\mathcal{Z} = \int p(O_{\text{img}} \mid \nu, \boldsymbol{\lambda}, M, S) p(\boldsymbol{\lambda} \mid M, S) p(\nu \mid M, S) \, \mathrm{d}\boldsymbol{\lambda} \, \mathrm{d}\nu. \tag{3.31}$$

We can first marginalize over the linear parameters to get the likelihood $P(O_{\text{img}} \mid \nu, M, S)$ in terms of only the non-linear parameters as

$$p(O_{\text{img}} \mid \nu, M, S) = \int p(O_{\text{img}} \mid \nu, \boldsymbol{\lambda}, M, S) p(\boldsymbol{\lambda} \mid M, S) d\boldsymbol{\lambda}. \quad (3.32)$$

If $\hat{\boldsymbol{\lambda}}$ is the maximum-likelihood estimator of $P(O_{\text{img}} \mid \nu, \boldsymbol{\lambda}, M, S)$ for given $\{\nu, M, S\}$, then we can approximate the likelihood using up to the second-order terms in the Taylor expansion in the vicinity of $\hat{\boldsymbol{\lambda}}$ as

$$p(O_{\text{img}} \mid \nu, \boldsymbol{\lambda}, M, S) \approx p(O_{\text{img}} \mid \nu, \hat{\boldsymbol{\lambda}}, M, S) \times \exp \left[-\frac{1}{2} \Delta \boldsymbol{\lambda}^\top \mathbf{K}_{\lambda\lambda}^{-1} \Delta \boldsymbol{\lambda} \right], \quad (3.33)$$

where $\Delta \boldsymbol{\lambda} = \boldsymbol{\lambda} - \hat{\boldsymbol{\lambda}}$, and $\mathbf{K}_{\lambda\lambda}$ is the covariance matrix of $\boldsymbol{\lambda}$ (equation [12] of Birrer et al. 2015). We can directly obtain $\hat{\boldsymbol{\lambda}}$ given the set of non-linear parameters ν by solving a set of linear equations. If we take a uniform prior $U(-\mathbf{w}/2, \mathbf{w}/2)$ for $\boldsymbol{\lambda}$, then from equation (3.32) we have

$$p(O_{\text{img}} \mid \nu, M, S) \approx p(O_{\text{img}} \mid \nu, \hat{\boldsymbol{\lambda}}, M, S) \frac{[(2\pi)^n \det(\mathbf{K}_{\lambda\lambda})]^{1/2}}{\prod_i^n w_i}, \quad (3.34)$$

where $n = \dim(\boldsymbol{\lambda})$ is the number of linear parameters. Then, we can express the evidence as

$$\mathcal{Z} \approx \frac{[(2\pi)^n \det(\mathbf{K}_{\lambda\lambda})]^{1/2}}{\prod_i^n w_i} \int p(O_{\text{img}} \mid \nu, \hat{\boldsymbol{\lambda}}, M, S) p(\nu \mid M, S) d\nu. \quad (3.35)$$

3.2.5.2 Joint posterior combining time delay and kinematics likelihoods

Next, we can fold in the time-delay likelihood to update the posterior and marginalize over the Fermat potential $\Delta\phi_{\text{XY}}^{\text{eff}}$ as

$$\begin{aligned} & p(D, \xi_{\text{lens}}, \xi_{\text{light}}, \kappa_{\text{ext}} \mid O_{\text{img}}, O_{\Delta t}, O_{\text{env}}, M) \\ & \propto \int p(O_{\Delta t} \mid \Delta t(D, \xi_{\text{lens}}, \xi_{\text{light}}, \Delta\phi_{\text{XY}}^{\text{eff}}, \kappa_{\text{ext}}; O_{\text{img}}, O_{\text{env}}, M)) \\ & \quad \times p(\xi_{\text{lens}}, \xi_{\text{light}}, \Delta\phi_{\text{XY}}^{\text{eff}} \mid O_{\text{img}}, M) \\ & \quad \times p(\kappa_{\text{ext}} \mid O_{\text{env}}) p(D) d\Delta\phi_{\text{XY}}^{\text{eff}}. \end{aligned} \quad (3.36)$$

Tie & Kochanek (2018) introduce a possible microlensing time-delay effect due to the asymmetric magnification of a quasar accretion disc – assuming the lamppost model (Shakura & Sunyaev 1973) – due to microlensing by the foreground stars in the deflector galaxy. Note, the time-delay measurement from the quasar light curves accounts for the long-term variation in the microlensing magnification pattern. Tie & Kochanek (2018)’s microlensing time-delay effect is due to the non-uniform weighting of the quasar accretion disc brightness by the microlensing magnification pattern, thus this effect depends on the gradient of the magnification across the accretion disc. The long-term change in the magnification pattern is not necessarily correlated with the gradient of the magnification across the accretion disc. For the case that marginalizes over this microlensing time-delay effect, the above equation becomes

$$\begin{aligned}
& p(D, \xi_{\text{lens}}, \xi_{\text{light}}, \kappa_{\text{ext}} \mid O_{\text{img}}, O_{\Delta t}, O_{\text{env}}, M) \\
& \propto \int p(O_{\Delta t} \mid \Delta t(D, \xi_{\text{lens}}, \xi_{\text{light}}, \xi_{\text{micro}}, \kappa_{\text{ext}}, \Delta\phi_{\text{XY}}^{\text{eff}}; O_{\text{img}}, O_{\text{env}}, M)) \\
& \quad \times p(\xi_{\text{lens}}, \xi_{\text{light}}, \Delta\phi_{\text{XY}}^{\text{eff}} \mid O_{\text{img}}, M) \\
& \quad \times p(\kappa_{\text{ext}} \mid O_{\text{env}}) p(\xi_{\text{micro}}) p(D) d\Delta\phi_{\text{XY}}^{\text{eff}} d\xi_{\text{micro}},
\end{aligned} \tag{3.37}$$

where ξ_{micro} is the set of parameters relevant to the microlensing time-delay effect, e.g. parameters related to the properties of the black hole and the accretion disc (Chen et al. 2018, Section 3.6.2.3).

Then, we can update the posterior once again by folding in the kinematic likelihood as

$$\begin{aligned}
& p(D, \xi_{\text{lens}}, \xi_{\text{light}}, \kappa_{\text{ext}}, \xi_{\beta} \mid O_{\text{img}}, O_{\Delta t}, O_{\text{kin}}, O_{\text{env}}, M) \\
& = p(O_{\text{kin}} \mid \sigma_{\text{los}}(D, \xi_{\text{lens}}, \xi_{\text{light}}, \kappa_{\text{ext}}, \xi_{\beta}; M)) \\
& \quad \times p(\xi_{\beta} \mid \xi_{\text{lens}}, \xi_{\text{light}}, M) \\
& \quad \times p(D, \xi_{\text{lens}}, \xi_{\text{light}}, \kappa_{\text{ext}} \mid O_{\text{img}}, O_{\Delta t}, M).
\end{aligned} \tag{3.38}$$

Now, we can marginalize over the model parameters to obtain the posterior of the cos-

mological distances D as

$$\begin{aligned}
p(D \mid O, M) &= p(D \mid O_{\text{img}}, O_{\Delta t}, O_{\text{kin}}, O_{\text{env}}, M) \\
&= \int p(D, \xi_{\text{lens}}, \xi_{\text{light}}, \kappa_{\text{ext}}, \xi_{\beta} \mid O_{\text{img}}, O_{\Delta t}, O_{\text{kin}}, O_{\text{env}}, M) \\
&\quad \times d\xi_{\beta} d\kappa_{\text{ext}} d\xi_{\text{lens}} d\xi_{\text{light}}.
\end{aligned} \tag{3.39}$$

Finally, we can marginalize over the deflector mass model choices as

$$p(D \mid O) = \sum_M p(D \mid O, M) p(M \mid O). \tag{3.40}$$

A particular choice of mass model M breaks the MSD (Schneider & Sluse 2014). However, we cannot ascertain that our adopted mass model choice represents the true mass distribution. As a result, we cannot weigh different mass models according to their evidence ratios as a higher evidence value may just be a fluke from breaking the MSD near a better fit of the data. Therefore, we take $p(M \mid O) = 1$ to equally weight different deflector mass model choices.

As the likelihood $p(O \mid D)$ follows the proportionality relation

$$p(O \mid D) \propto \frac{p(D \mid O)}{p(D)}, \tag{3.41}$$

we can then use the distance posterior $p(D \mid O)$ to obtain the posterior of the cosmological parameters $p(\omega \mid O, C)$ from equation (3.24).

3.3 The Lens System and Data Sets

In this chapter, we perform cosmographic analyses of the lens systems DES J0408–5354. This lens was discovered and confirmed by Lin et al. (2017) from a large sample of potential galaxy–galaxy lenses in the DES footprint (Diehl et al. 2017). Agnello et al. (2017) acquired follow-up data and modelled the system presenting evidence for a faint perturber G2 near one of the quasar images, which was later confirmed by the deeper and higher resolution imaging from the *Hubble Space Telescope* (*HST*; Shajib et al. 2019).

The necessary data sets and ancillary measurements for cosmographic analysis are

1. high-resolution imaging of the lens system,
2. spectroscopy of the lens components to measure redshifts,
3. measured time-delays between the images,
4. LOS velocity dispersion of the central deflector galaxy, and
5. estimate of the external convergence.

Each type of data set or ancillary measurement is described in the following subsections.

3.3.1 *HST* imaging of the lens system

HST Wide-Field Camera 3 (WFC3) imaging was obtained under the program GO-15320 (PI: Treu; Shajib et al. 2019). The images were taken in three filters: F160W in infrared (IR), F814W and F475X in ultraviolet–visual (UVIS). For each filter, four exposures – two short and two long – were taken to cover the large dynamic range in brightness encompassing the bright quasar images and the fainter extended host galaxy. For the IR band, we chose a 4-point dither pattern and STEP100 readout sequence for the MULTIACCUM mode. For the UVIS bands, we adopted a 2-point dither pattern. The total exposure times for the three filters are 2196.9 s in F160W, 1428 s in F814W, and 1348 s in F475X.

The data in each band were reduced with the standard ASTRODRIZZLE package (Avila et al. 2015). The final pixel scale after drizzling is 0.08 arcsec in the IR band, and 0.04 arcsec in the UVIS band. We estimate the background level in the reduced image from each band using SEXTRACTOR and subtract it from the reduced image (Bertin & Arnouts 1996).

Fig. 3.1 shows the color-composite image for the lens system and its surrounding. The central deflector galaxy G1 has a visible satellite galaxy G2. The four prominent nearby

galaxies along the line of sight are marked with G3, G4, G5, and G6. Note that the naming convention of these galaxies is different in Lin et al. (2017) and Agnello et al. (2017).

The lens has multiple lensed arcs from additional source components, S2 and S3. The lensed arc S2 lies inside the Einstein radius and it has a noticeable counterimage on the North–West of image B. Another faint lensed arc S3 lies on the East of image D. We could not identify the counterimage of S3 from visual inspection.

3.3.2 Spectroscopic observations of the lens components

The central deflector G1 sits at the redshift $z_d = 0.597$ and the quasar sits at redshift $z_{\text{QSO}} = 2.375$ (Lin et al. 2017). Buckley-Geer et al. (2020) measure redshifts for the nearby line-of-sight galaxies G3–G6 from spectroscopic observations using the Magellan and the Gemini telescopes obtaining $z_{\text{G3}} = 0.769$, $z_{\text{G4}} = 0.771$, $z_{\text{G5}} = 1.032$, and $z_{\text{G6}} = 0.594$. The redshifts are precise up to the specified decimal point.

We measure the redshift of S2 $z_{\text{S2}} = 2.228$ from the integral-field spectroscopy observations of DES J0408–5354 with the Multi-Unit Spectroscopic Explorer (MUSE, on the ESO VLT UT4). The MUSE observations of the lens and its immediate neighbourhood, within approximately 45 arcsec, were carried out in Period 102 during two nights on 2019 January 11 and 13 [run 0102.A-0600(E), PI Agnello]. The observations were executed in wide-field mode with adaptive-optics (AO) corrections, so that the multiple images and galaxies in this lens could be properly deblended. The AO wide field mode of MUSE results in a wavelength coverage from 4700 to 5803 Å, and 5966–9350 Å at a spectral resolution of $R \sim 1700$ –3400. Each observation block contains four exposures, with the main target placed in four different quadrants of the instrument’s field of view. An approximately 15 arcsec \times 15 arcsec region centred on the lens was exposed for 4h, with a dither-and-rotation pattern that minimized artefacts due to the multiple instrument slicers and channels. We reduced the data cubes using the standard ESOREX pipeline recipes and flux calibrated them using observations of standard stars obtained on the two nights. Offsets between 20 individual exposures were

determined from cross-correlations of white light images created from individual data cubes. We cleaned strong sky-line residuals from the final combined data cube using ZAP (Soto et al. 2016). The setup results in a final data cube with a full field of view of $92 \text{ arcsec} \times 95 \text{ arcsec}$. For this work, we analysed a $8 \text{ arcsec} \times 8 \text{ arcsec}$ ‘mini-cube’ centred around the lens. We use three stars in the field as reference point source function (PSF) cubes. We decompose the ‘mini-cube’ as a superposition of four Moffat profiles for the quasar images, and a convolved de Vaucouleurs profile for the deflector light distribution. By means of this procedure, all component spectra could be reliably separated and the quasar shot noise on the deflector spectra was minimized. We use Mg II emission lines to measure S2’s redshift and velocity dispersion. As S2 and the quasar are at different redshift, the quasar’s Mg II contamination does not overlap with S2’s Mg II lines. Also, given the large systematic uncertainty on the velocity dispersion described in the next paragraph, residual AGN contamination is not a dominant source of bias.

We also measure the line-of-sight velocity dispersions of G3–G6 and S2 from the MUSE spectra (Table 3.1). We adopt an uncertainty of 20 km s^{-1} on the measured velocity dispersion to account for the typical systematic uncertainty for kinematics extracted from MUSE spectra (Guérou et al. 2017). The estimated PSF from the stars in the MUSE observation can be different than the PSF of the quasar due to different SED within a filter. However, the impact in the estimated velocity dispersion from this potential PSF mismatch is subdominant to this conservative estimate of the systematic uncertainty.

3.3.3 Time delays

Courbin et al. (2018) present the measured time delays between the images of DES J0408–5354. This system was monitored to obtain light-curves of the lensed images using the MPIA 2.2 m telescope at La Silla observatory between 2016 October 1 and 2017 April 8. The system was observed almost daily except for 14 consecutive nights between 2016 December 10 and 2016 December 24, and for one week in 2017 January due to bad weather and technical

Table 3.1: Redshift and stellar velocity dispersion for the line-of-sight galaxies G3–G6 and S2. The relative offsets of the observed centroids for G3–G6 are computed from the coordinate RA 04:08:21.71 and Dec $-53:53:59.34$. The tabulated uncertainties for the velocity dispersions are statistical uncertainties. However, we adopt a 20 km s^{-1} uncertainty for each measurement to account for the typical systematic uncertainty for kinematics obtained from MUSE spectra (Gu  rou et al. 2017). The redshifts are precise up to the specified decimal point.

Galaxy	ΔRA (arcsec)	ΔDec (arcsec)	Redshift	Stellar velocity dispersion (km s^{-1})
G3	1.08	-6.52	0.769	226 ± 7
G4	-0.40	-13.58	0.771	153 ± 10
G5	5.34	-0.78	1.032	56 ± 2
G6	10.90	5.53	0.594	63 ± 7
S2	–	–	2.228	46 ± 9

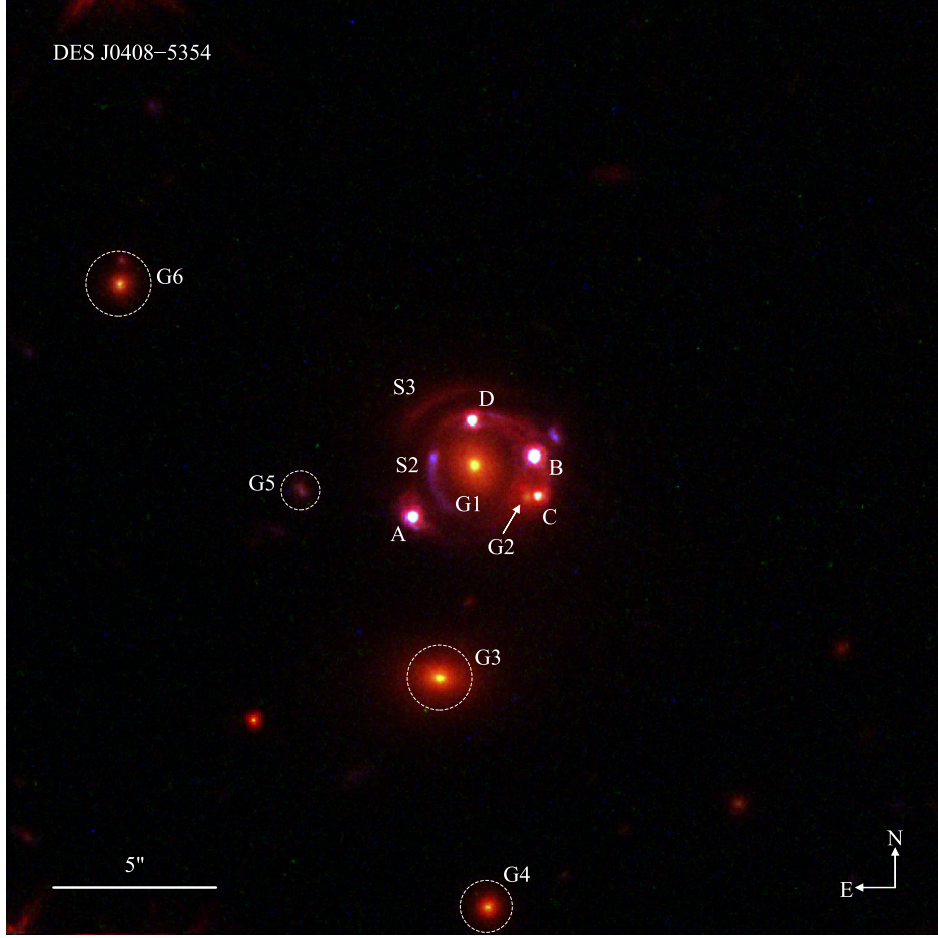


Figure 3.1: RGB color composite of the lens systems DES J0408–5354. The three *HST* filters used to create the RGB image are F160W (red), F814W (green), and F475X (blue). The relative amplitudes between the three filters are adjusted in this figure for better visualization by achieving a higher contrast. We label different components of the lens system. G1 is the main deflector galaxy and G2 is its satellite galaxy. In addition to the lensed arcs from the extended quasar host galaxy, this lens system has extra source components S2 and S3. The source component S2 is doubly imaged and forms an extended arc inside the Einstein radius. S3 forms another fainter extended arc on the North-East outside the Einstein radius without a noticeable counterimage. Four nearby perturbers G3–G6 along the line of sight are marked with the dashed, white circles.

problems. Additional monitoring was carried out using the 1.2 m the *Leonhard Euler* 1.2 m Swiss Telescope (*Euler*) between 2016 July and 2017 April. The mean observation cadence with *Euler* is 5 d. From these light-curves of the lensed images, the measured time delays are $\Delta t_{AB} = -112.1 \pm 2.1$ d, $\Delta t_{AD} = -155.5 \pm 12.8$ d, and $\Delta t_{BD} = -42.4 \pm 17.6$ d (see Fig. 3.1 for the naming of the images). The time delays relative to image C could not be measured due the close proximity of a satellite galaxy as it is difficult to deblend the quasar flux from the satellite’s in the ground-based monitoring data.

3.3.4 Velocity dispersion of the central deflector

Buckley-Geer et al. (2020) measure the velocity dispersion of G1. The velocity dispersion is measured with four different observing setups: two mask setups with the Magellan telescope, one with the Gemini telescope, and one with the MUSE spectra. The specifics and the measured values from these four setups are tabulated in Table 3.2. We estimate the systematic uncertainty $\sigma_{\sigma_{\text{los}}}^{\text{sys}}$ in the measured velocity dispersion to add the reported statistical uncertainty $\sigma_{\sigma_{\text{los}}}^{\text{stat}}$. We infer a systematic uncertainty of 17 km s^{-1} from the variance in the estimated velocity dispersions when different settings – e.g. the stellar population library, the stellar templates, the wavelength region – are varied in the kinematic fitting. We form a covariance matrix for the velocity dispersion measurements with $(\sigma_{\sigma_{\text{los}}}^{\text{sys}})^2 + (\sigma_{\sigma_{\text{los}}}^{\text{stat}})^2$ for the diagonal terms and $(\sigma_{\sigma_{\text{los}}}^{\text{sys}})^2$ for off-diagonal terms, as the source of the systematic in the kinematic fitting is common between all the measurements.

Table 3.2: Measurements of velocity dispersion from three different setups from Buckley-Geer et al. (2020). The quoted uncertainties are only statistical, see Section 3.3.4 for the estimated systematic uncertainty.

Instrument and setup	Aperture dimension (arcsec \times arcsec)	Aperture rotation (deg E of N)	Seeing (arcsec)	Moffat PSF exponent	Velocity dispersion (km s ⁻¹)
Magellan mask A	1 \times 1	99	0.68	-2.97	230 \pm 37
Magellan mask B	1 \times 1	99	0.76	-3.20	236 \pm 42
Gemini mask A2	0.75 \times 1	0	0.52	-3.06	220 \pm 21
MUSE	1 \times 1	0	0.61	-1.55	227 \pm 9

3.3.5 Estimate of the external convergence

Buckley-Geer et al. (2020) present the distribution of the external convergence κ_{ext} for DES J0408–5354. This analysis is based on the weighted galaxy number counts approach of Greene et al. (2013), which was further developed by Rusu et al. (2017), Birrer et al. (2019), and Rusu et al. (2019). In brief, weighted number counts are computed in 45 arcsec- and 120 arcsec-radii apertures centred on the lensing system, up to a depth of $I = 22.5$ mag, using simple physical weights robust to measurement errors, such as the inverse of the distance to the lens and photometric/spectroscopic redshifts. Analogous number counts are computed in a large number of same-size apertures and depth in a cosmological survey, in this case DES, so as to measure the over/underdensity of the DES J0408–5354 line of sight relative to the median line of sight through the Universe, in terms of weighted number count ratios. In this case, the line of sight was found to be underdense, and a combination of weighted number count ratios was used as constraint to select statistically similar lines of sight from the Millennium Simulation (Springel et al. 2005). Using the external convergence maps from Hilbert et al. (2009) corresponding to each Millennium Simulation line of sight, we construct a probability distribution function of κ_{ext} . This probability distribution function of κ_{ext} is provided in Section 3.6.2.2 (specifically in Fig. 3.7).

3.4 Lens model ingredients

In this section, we describe the mass and light profiles used to construct the lens model in our analysis.

3.4.1 Central deflector’s mass profiles

To model the main deflector’s mass distribution, we adopt two sets of profiles: (i) power-law, and (ii) composite mass profile.

3.4.1.1 Power-law mass profile

We adopt the power-law elliptical mass distribution (Barkana 1998). This profile is described by

$$\kappa_{\text{PL}}(\theta_1, \theta_2) = \frac{3 - \gamma}{2} \left[\frac{\theta_{\text{E}}}{\sqrt{q_{\text{m}}\theta_1^2 + \theta_2^2/q_{\text{m}}}} \right]^{\gamma-1}, \quad (3.42)$$

where γ is the power-law slope, θ_{E} is the Einstein radius, and q_{m} is the axis ratio. The coordinates (θ_1, θ_2) are in the frame that is aligned with the major and minor axes. This frame is rotated by a position angle φ_{m} from the frame of on-sky coordinates.

3.4.1.2 Composite mass profile

In the composite mass profile, we adopt separate mass profiles for the baryonic and the dark components of the mass distribution.

For the dark component, we choose a Navarro–Frenk–White (NFW) profile with ellipticity defined in the potential. The spherical NFW profile in 3D is given by

$$\rho_{\text{NFW}}(r) = \frac{\rho_{\text{s}}}{(r/r_{\text{s}})(1 + r/r_{\text{s}})^2}, \quad (3.43)$$

where r_{s} is the scale radius, and ρ_{s} is the normalization (Navarro et al. 1997).

For the baryonic mass profile, we adopt the Chameleon convergence profile. The Chameleon profile approximates the Sérsic profile within a few per cent in the range $0.5\text{--}3R_{\text{eff}}$, where R_{eff} is the effective or half-light radius of the Sérsic profile. The Chameleon profile is the difference between two non-singular isothermal ellipsoids given by

$$\kappa_{\text{Chm}}(\theta_1, \theta_2) = \frac{\kappa_0}{1 + q_{\text{m}}} \left[\frac{1}{\sqrt{\theta_1^2 + \theta_2^2/q_{\text{m}}^2 + 4w_{\text{c}}^2/(1 + q_{\text{m}}^2)}} - \frac{1}{\sqrt{\theta_1^2 + \theta_2^2/q_{\text{m}}^2 + 4w_{\text{t}}^2/(1 + q_{\text{m}}^2)}} \right] \quad (3.44)$$

(Dutton et al. 2011; Suyu et al. 2014). This profile is convenient to compute lensing properties using closed-form expressions.

With each of these models, we include an external shear profile parameterized with the shear magnitude γ_{ext} and shear angle φ_{ext} .

3.4.2 Central deflector's light profile

We use the Sérsic profile and the Chameleon profile to model different light components of the lens system.

3.4.2.1 Sérsic profile

The Sérsic profile is given by

$$I_{\text{Sérsic}}(\theta_1, \theta_2) = I_{\text{eff}} \exp \left[-b_n \left\{ \left(\frac{\sqrt{\theta_1^2 + \theta_2^2 / q_L^2}}{\theta_{\text{eff}}} \right)^{1/n_s} - 1 \right\} \right], \quad (3.45)$$

where θ_{eff} is the effective radius, I_{eff} is the amplitude at θ_{eff} , and n_s is the Sérsic index (Sérsic 1968). The factor b_n normalizes the profile such that half of the total luminosity is contained within θ_{eff} .

3.4.2.2 Chameleon profile

We use the same Chameleon profile from equation (3.44) to fit the central deflector's light profile by replacing the convergence amplitude κ_0 with flux amplitude I_0 .

3.4.3 Quasar host galaxy's light profile

We choose an elliptical Sérsic profile to model the smooth component of the quasar host galaxy's light distribution. Additionally, we use a basis set of shapelets to reconstruct the non-smooth features in the extended source light distribution (Refregier 2003; Birrer et al. 2015). The set of shapelets is characterized with a scale size ς and maximum polynomial order n_{max} . The order n_{max} determines the total number of shapelet components $n_{\text{shapelet}} =$

$$(n_{\text{max}} + 1)(n_{\text{max}} + 2)/2.$$

We model the quasar images as point-sources on the image plane convolved with the reconstructed point spread function (PSF). We let the amplitudes of each quasar image free.

3.5 Lens model setups

In this section, we present the specific model choices for DES J0408–5354. Extending on the baseline models, we choose different options – that we consider equally viable – for some particular components of the model. A combination of these options then make up our model settings S for each mass profile family M . To be specific, the model settings S include the model components describing the source and the line-of-sight galaxies, and the model settings M include the mass and light profiles of the central deflector galaxy G1. We marginalize over these model settings S to account for any possible source of systematics that may be introduced from adopting only one specific choice. We first state the baseline models in Section 3.5.1. Then, we elaborate on the different additional model choices in Sections 3.5.2–3.5.9, and we summarize the set of model settings S that we marginalize over in Section 3.5.11. A summary of the adopted models and the parameter priors are tabulated in Appendix 3.G.

3.5.1 Baseline models

The specifics of the baseline models agreed by the participating independent modelling teams are:

1. Central deflector G1’s mass profile: power-law profile and composite profile (elliptical NFW potential for the dark component, double Chameleon convergence for luminous component),
2. Central deflectors G1’s light profile:

- (1) *For models with power-law mass profile:* double Sérsic profile in all three bands,
- (2) *For models with composite mass profile:* double Chameleon light profile in the F160W band linked with the double Chameleon mass profile, double Sérsic profiles in UVIS bands,
- 3. Satellite G2’s mass profile: singular isothermal sphere (SIS) placed on G1’s lens plane,
- 4. External shear,
- 5. Explicit modelling of the line-of-sight galaxies G3–G6, multilens-plane treatment for G3,
- 6. Multisource-plane treatment for quasar host S1 and additional source component S2.

In the next sections, we explain these model settings and further extend on some of these settings as we see fit.

3.5.2 Central deflector G1’s mass and light profiles

We choose two sets of mass profile for the central deflector G1: power-law mass profile and composite mass profile.

For the corresponding light profile distribution of G1 with the power-law mass profile, we adopt a double Sérsic profile in the IR band, and a single Sérsic profile for each of the UVIS bands. Here, we deviated from the baseline model of double Sérsic profile for the UVIS bands, as we find a single Sérsic profile for each of the UVIS bands is sufficient and the posteriors of the lens model parameters are almost identical between the double Sérsic and single Sérsic profiles for the UVIS bands. Therefore, we adopt the single Sérsic profile for the UVIS bands to increase numerical efficiency by simplifying our model. However, we still use the double Sérsic profile in the IR band where the signal-to-noise ratio of the galaxy light is higher and thus more flexibility is needed to render it within the noise. The centroids are joint for all the Sérsic profiles between the bands. The axis ratio q_L , position angle φ_L ,

and the Sérsic index n_s are also joint between the UVIS bands. We let effective radius θ_{eff} and amplitude I_{eff} as free parameters independently for all bands to allow a color gradient.

For the composite mass profile, we model the dark matter distribution with a NFW profile with ellipticity parameterized in the potential. For the baryonic matter distribution, we adopt two concentric Chameleon profiles to model both the luminous mass distribution and the light distribution in the F160W band. We join the scaling and ellipticity parameters of each pairing of the Chameleon profiles between the baryonic mass distribution and the F160W light distribution. We do not fix the amplitude ratio between the two Chameleon profiles and this ratio is sampled as a non-linear parameter in our model. For each of the two UVIS bands, we adopt a single Sérsic profile. Similar to power-law profile, the Sérsic profile parameters except θ_{eff} and I_{eff} are joint between the UVIS bands and the centroids of the all the deflector light profiles are joint together. The amplitudes of the mass and light profiles are independent of each other, thus we allow the mass-to-light ratio (M/L) to be free. We adopt a Gaussian prior equivalent to 12.74 ± 1.71 arcsec for the NFW scale radius r_s based on the results of Gavazzi et al. (2007) for the Sloan Lens ACS (SLACS) survey lenses (Bolton et al. 2006). G1’s velocity dispersion and redshift are within the range of those from the SLACS lenses, thus SLACS is a representative sample of elliptical galaxies such as G1 (Treu et al. 2006). Similar priors were adopted in previous H0LiCOW analyses of time-delay lenses (e.g., Wong et al. 2017; Rusu et al. 2019).

We find the half-light radius θ_{eff} of the Sérsic profiles to be degenerate with the Sérsic index n_s in our models and the models tend to optimize towards large values of θ_{eff} that is inconsistent with our observational prior. To prevent θ_{eff} from converging towards abnormally large values, we impose an empirical prior on θ_{eff} . We derive a scaling relation from the distribution of the central velocity dispersion $\sigma_{e/2}$ measured within half of effective radius and R_{eff} in physical unit for the lenses in the SLACS sample (Auger et al. 2010a). We account for intrinsic scatter in the derived scaling relation as we are ignoring the average surface brightness $\bar{I}(R_{\text{eff}})$ in the relation between the three quantities along the fundamental plane.

Then, we derive a distribution for R_{eff} for DES J0408–5354 for the given central velocity dispersion measurements from Table 3.2. In practice, we simultaneously sample $R_{\text{eff}}^{\text{J0408}}$ and the parameters $\{m, b, \mathcal{S}\}$ – for the scaling relation

$$\log_{10}(\sigma_{\text{los}}/\text{km s}^{-1}) = m \log_{10}(R_{\text{eff}}/\text{kpc}) + b \quad (3.46)$$

with scatter \mathcal{S} – from a joint likelihood for the SLACS sample data and the measured velocity dispersions of DES J0408–5354. For each sampled $R_{\text{eff}}^{\text{J0408}}$, we transform the measured central velocity dispersions within each aperture into $\sigma_{e/2}$ using the aperture correction formulae given by Jorgensen et al. (1995). We include the intrinsic scatter in the likelihood term for DES J0408–5354’s velocity dispersions, thus the scatter in the scaling relation propagates into the $R_{\text{eff}}^{\text{J0408}}$ distribution. We estimate the scaling relation parameters as $m = 0.18^{+0.05}_{-0.04}$, $b = 2.2 \pm 0.04$, $\mathcal{S} = 1.53 \pm 0.05$. We convert the $R_{\text{eff}}^{\text{J0408}}$ distribution in physical unit into θ_{eff} distribution in angular unit using the angular diameter distance to DES J0408–5354 for our fiducial cosmology, however we add 10 per cent uncertainty to the distribution to remove any strong dependence on the choice of cosmology. We take a Gaussian prior with the same mean and standard deviation of the resultant θ_{eff} distribution from the SLACS lenses (Table 3.9). We adopt this prior only to prevent θ_{eff} from veering off to very large values. The adopted prior is broad enough not to bias the θ_{eff} posterior within the plausible range of values, including for the double Sérsic profile.

3.5.3 Satellite G2’s mass and light profile

In addition to the power-law or composite mass profile for the central deflector, we add a singular isothermal sphere (SIS) profile for G2’s mass distribution and a circular Sérsic profile for its light distribution. The Sérsic profile parameters except θ_{eff} are joint between all bands. We join the centroid between the SIS and Sérsic profiles. Although a deviation from the isothermal profile in G2’s mass can potentially change the deflection potential at image C, such a change will be negligible in our inference of H_0 as time-delays with respect to

image C are not used in our inference. The SIS profile is sufficient to capture the astrometric position of the image C in our modelling.

3.5.4 Nearby line-of-sight galaxies

We explicitly model the mass distributions of line-of-sight galaxies G3–6 to fully capture their higher than second-order lensing effects that cannot be accounted for by the external convergence and the external shear profiles. First in Section 3.5.4.1, we describe our selection criterion for the line-of-sight galaxies to explicitly include in our lens model. Then in Section 3.5.4.2, we explain the mutli-lens-plane treatment of the line-of-sight galaxies. Lastly in Sections 3.5.4.3 and 3.5.4.4, we describe the mass profiles we adopt to model these line-of-sight galaxies.

3.5.4.1 Selection criterion of the line-of-sight galaxies for explicit modelling

To select the line-of-sight galaxies for explicit modelling, we first estimate the contribution in time-delays between the images from higher than second-order derivatives of the deflection potential of these galaxies. To quantify this effect, we set a SIS profile for each perturber with its Einstein radius corresponding to the estimated central velocity dispersion. We infer the velocity dispersion for all the line-of-sight galaxies from their stellar masses using two scaling relations – one from Auger et al. (2010a) and the other from Zahid et al. (2016). To be conservative, we choose the upper limit of the 1σ confidence interval of the estimated stellar mass and choose the larger value of the velocity dispersions estimated from the two scaling relations (Buckley-Geer et al. 2020). We select the line-of-sight galaxies that may cause more than 1 per cent shift in the measured Hubble constant if higher than second-order derivatives of their deflection potential are ignored. The shift in the Hubble constant can be related to the relative astrometric shift $\delta\boldsymbol{\theta}_{\text{AB}}$ between image A and B as

$$\frac{\delta H_0}{H_0} \lesssim \frac{D_{\Delta t}}{c\Delta t_{\text{AB}}}(\boldsymbol{\theta}_{\text{A}} - \boldsymbol{\theta}_{\text{B}}) \cdot \delta\boldsymbol{\theta}_{\text{AB}} \quad (3.47)$$

(Birrer & Treu 2019). We take the relative astrometric shift $\delta\boldsymbol{\theta}_{AB} = \boldsymbol{\alpha}_A^{(3)} - \boldsymbol{\alpha}_B^{(3)}$, where the term on the right-hand side is the relative deflection angle for third and higher order lensing effects from the SIS profile corresponding to each line-of-sight galaxy. Thus, we set the selection criterion

$$\frac{D_{\Delta t}^{\text{fiducial}}}{c\Delta t_{AB}}(\boldsymbol{\theta}_A - \boldsymbol{\theta}_B) \cdot \left(\boldsymbol{\alpha}_A^{(3)} - \boldsymbol{\alpha}_B^{(3)}\right) \geq 0.01. \quad (3.48)$$

This criterion selects G3–G6 for explicit modelling. Note that the perturber selection criterion based on the “flexion shift” $\Delta_3 x > 10^{-4}$ also selects G3–G6 for explicit modelling (McCully et al. 2017; Sluse et al. 2019; Buckley-Geer et al. 2020).

3.5.4.2 Multilens-plane modelling of the line-of-sight galaxies

We model this lens system with a multilens-plane treatment by setting G3’s lens plane at its own redshift $z_{G3} = 0.769$, as G3 is close enough to G0 to cause more than 1 per cent deviation in the computed time-delays if we place it on G0’s lens plane. We place G4–G6 on G0’s lens plane as we assume that the deviation in computed time-delays due to this assumption is negligible given the combinations of their stellar masses and distances from G0.

Additionally, we model the mass profile of S2 at its redshift $z_{S2} = 2.228$. Therefore, we have three lens-planes in our model. We can express the effective Fermat potential for the triple-lens-plane case from equation (3.9) as

$$\begin{aligned} \phi^{\text{eff}}(\boldsymbol{\theta}) = & \left[\frac{D_{G3}D_{G1,S1}}{D_{S1}D_{G1,G3}} \frac{(\boldsymbol{\theta}_{G1} - \boldsymbol{\theta}_{G3})^2}{2} - \psi_{G1}(\boldsymbol{\theta}_{G1}) \right] \\ & + \frac{1 + z_{G3}}{1 + z_{G1}} \left[\frac{D_{G3}D_{S2}D_{G1,S1}}{D_{G1}D_{S1}D_{G3,S2}} \frac{(\boldsymbol{\theta}_{G3} - \boldsymbol{\theta}_{S2})^2}{2} \right. \\ & \quad \left. - \frac{D_{G3}D_{G1,S1}}{D_{G1}D_{G3,S1}} \psi_{G3}(\boldsymbol{\theta}_{G3}) \right] \\ & + \frac{1 + z_{S2}}{1 + z_{G1}} \frac{D_{S2}D_{G1,S1}}{D_{G1}D_{S2,S1}} \left[\frac{(\boldsymbol{\theta}_{S2} - \boldsymbol{\beta})^2}{2} - \psi_{S2}(\boldsymbol{\theta}_{S2}) \right]. \end{aligned} \quad (3.49)$$

Here, $\boldsymbol{\theta}_G$ is the quasar’s image position on G’s plane with $G \in \{G1, G3, S2\}$, ψ_G is the

deflection potential of G, and β is the quasar’s position on the source-plane. We fix the distance ratios in the above equation in our modelling. We adopt the Λ CDM cosmology with the cosmological density parameters $\Omega_m = 0.3$, $\Omega_\Lambda = 0.7$ to obtain these distance ratios. The relevant distance ratios change by less than 1 per cent within $0.25 \lesssim \Omega_m \lesssim 0.35$ and $-1.1 \lesssim w \lesssim -0.9$ (Fig. 3.2). Therefore, adopting this fiducial cosmology is only a weak assumption in our analysis. Fixing these distance ratios does not linearly affect our inference of H_0 , as the ratios do not depend on H_0 . However, there can potentially be a small non-linear shift in the inferred H_0 from our analysis had we adopted a different set of values for Ω_m and Ω_Λ . The non-linear effect on H_0 from fixing density parameters in the multilens-plane treatment was demonstrated to be less than 1 per cent for two previously analysed lens systems, HE 0435–1223 and WFI 2033–4723 (Wong et al. 2017; Rusu et al. 2019). In Appendix 3.A, we show that H_0 shifts by less than 1 per cent if we change the matter density parameter to $\Omega_m = 0.1$ and to $\Omega = 0.45$ within the Λ CDM cosmology. This range in Ω_m covers nearly the full range of our prior $\Omega_m \in [0.05, 0.5]$ for inferring H_0 for the Λ CDM cosmology. As a shift less than 1 per cent in H_0 is much smaller than the typical precision on H_0 (~ 5 –8 per cent) allowed by the current data quality, we consider that the impact of fixing the distance ratios using a fiducial Λ CDM cosmology has negligible impact in our analysis. However, we find that our inference of H_0 is sensitive to the dark energy equation of state parameter w in the w CDM cosmology. As we adopt a double source plane model – as described in Section 3.5.6 – the distance ratios or the ζ terms in equation (3.8) become sensitive to w (Gavazzi et al. 2008; Collett et al. 2012; Collett & Auger 2014). Therefore, the distance posteriors from this analysis should not be used to infer H_0 in extended cosmologies other than the Λ CDM model. We postpone the derivation of a distance posterior in more general cosmologies to future work.

We model G3 and S2 with SIS profiles. We place G3 at its “true” position on its own lens plane by tracing back from its observed position accounting for the foreground deflectors. As we also model the flux distribution from S2, we join the centroid of S2’s mass profile with

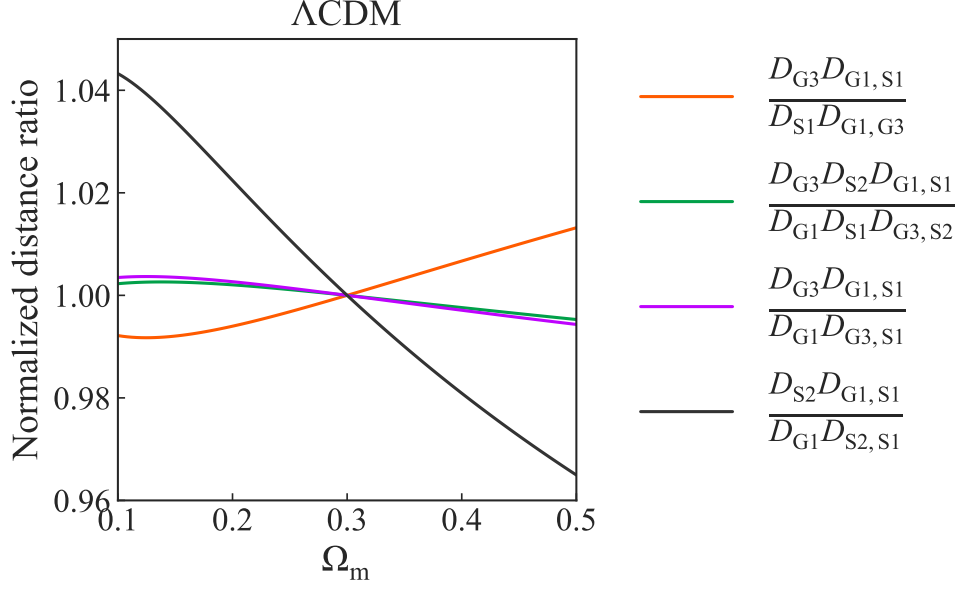


Figure 3.2: Impact of varying Ω_m in the Λ CDM cosmology on the angular diameter distance ratios between the lens and source planes. All the distance ratios except for the black line changes less than 1 per cent for a wide range of Ω_m . The black line corresponds to the distance ratio involving S2’s lens plane. As the S2’s Einstein radius is small (~ 0.002 arcsec), the change in the black line only has a small effect on the effective Fermat potential [cf. equation (3.49)]. Therefore, fixing the distance ratios for the fiducial cosmology with $\Omega_m = 0.3$ is not a strong assumption in our analysis. See Appendix 3.A for tests validating this point.

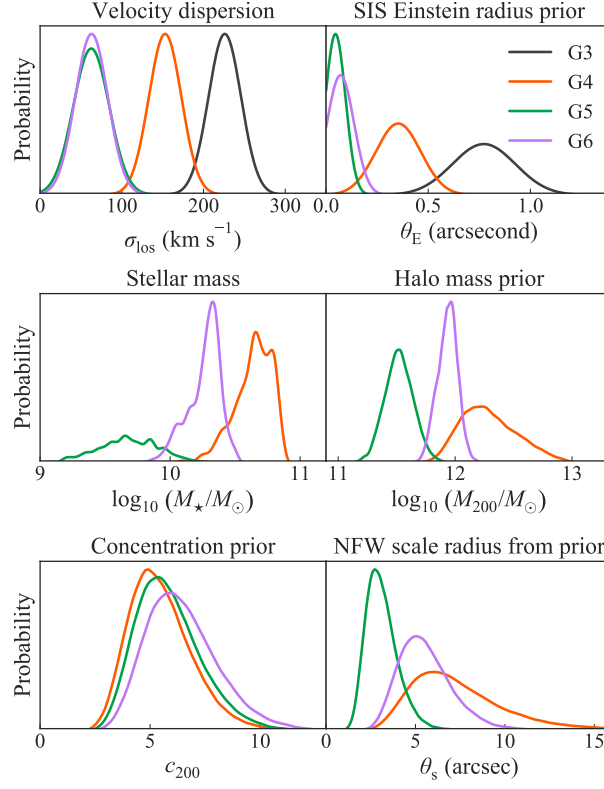


Figure 3.3: Observed and estimated properties of the line-of-sight galaxies G3–G6. **Top left:** velocity dispersions derived from the MUSE integral field spectra. **Top right:** SIS Einstein radius distributions obtained from the observed velocity dispersions. **Middle left:** estimated stellar masses from Buckley-Geer et al. (2020). **Middle right:** halo mass M_{200} inferred from the estimated stellar mass using the stellar mass–halo mass relation from Behroozi et al. (2019). **Bottom left:** halo concentration parameter c_{200} obtained using a halo mass–concentration relation for our fiducial cosmology (Diemer & Joyce 2019). **Bottom right:** scale radius of the NFW profile in angular unit for our fiducial cosmology from the M_{200} and c_{200} priors. The intrinsic scatter and uncertainties of the adopted scaling relations are accounted for at each conversion step. We use the SIS Einstein radius distributions as priors for the SIS model and the M_{200} and c_{200} distributions as priors for the NFW model for G4–G6.

its light centroid on its plane.

For G4–G6, we fix their centroids at their observed position on the lens plane of G1. For the mass profiles of G4–G6, we adopt two choices: the SIS profile and the spherical NFW profile. We choose the additional NFW model for G4–G6 as the NFW scale radius estimated from each of their stellar masses is smaller than the distance between the galaxy and G0 (Fig. 3.3, Section 3.5.4.4). Thus, their mass profile slopes can potentially be different from the isothermal profile at the centre of G0. In Sections 3.5.4.3 and 3.5.4.4, we describe the priors for the SIS and NFW profile parameters, respectively, of the line-of-sight galaxies.

3.5.4.3 SIS profile for the line-of-sight galaxies

We estimate the SIS Einstein radius distribution from each galaxy’s SIS velocity dispersion σ_{SIS} using the relation

$$\theta_{\text{E,SIS}} = 4\pi \left(\frac{\sigma_{\text{SIS}}}{c} \right)^2 \frac{D_{\text{G,S1}}}{D_{\text{S1}}}, \quad (3.50)$$

where $\theta_{\text{E,SIS}}$ is the Einstein radius for an SIS profile, and $D_{\text{G,S1}}$ is the angular diameter distance between a line-of-sight galaxy $G \in \{\text{G3, G4, G5, G6, S2}\}$ and S1. We calculate the distance ratio in the above equation using our fiducial cosmology. We do not need to add uncertainty to the fiducial cosmology used here as the distance ratios are independent of H_0 and a large shift (e.g., by 0.1) in Ω_{m} changes them by negligible amount relative to the 20 km s^{−1} uncertainty we adopted for the velocity dispersions.

G4 and G6’s observed morphologies indicate that they are elliptical galaxies. Therefore, we take their observed stellar velocity dispersions σ_{ap} as σ_{SIS} in equation (3.50) to obtain these galaxies’ Einstein radius prior distributions (Treu et al. 2006; Auger et al. 2010a). In contrast, G5’s spectra contains bright [O II] emission lines indicative of a star-forming galaxy. We also take S2 as a star-forming galaxy due to its blue color in the *HST* three-band imaging (Fig. 3.1). Therefore, we estimate the rotational velocities v_c of G5 and S2 from their observed ‘aperture-averaged’ velocity dispersions σ_{ap} using the scaling relation

between $v_c^2/\sigma_{\text{ap}}^2$ and Sérsic index n_s from Agnello et al. (2014). We obtain the Sérsic index of G5 $n_s = 4$ by fitting a Sérsic profile to its light distribution in the F814W band. From a preliminary lens model, we adopt S2’s Sérsic index as $n_s = 1.5$. For these Sérsic indices, the $v_c^2/\sigma_{\text{ap}}^2$ ratios are approximately 2.5 and 2.2, respectively, for G5 and S2. We adopt a Gaussian uncertainty with standard deviation 0.2 for these ratios to account for the scatter observed in the $v_c^2/\sigma_{\text{ap}}^2$ – n_s distribution (cf. fig. 6 of Agnello et al. 2014). Then, to convert the estimated rotational velocity v_c into the corresponding SIS velocity dispersion σ_{SIS} , we use the relation

$$\sigma_{\text{SIS}}^2 = \frac{GM(R)}{2R} = \frac{v_c(R)^2}{2}, \quad (3.51)$$

where $M(R)$ is the enclosed 3D mass within a radius R . The estimated SIS velocity dispersions are $\sigma_{\text{SIS}}^{\text{G5}} = 62 \pm 22 \text{ km s}^{-1}$ and $\sigma_{\text{SIS}}^{\text{S2}} = 48 \pm 11 \text{ km s}^{-1}$. We parameterize the SIS Einstein radius distributions derived from the velocity dispersions as Gaussian priors for the SIS mass profiles of G3–G6 and S2.

3.5.4.4 NFW profile for the line-of-sight galaxies

We parameterize the NFW profiles for G4–G6 with the halo mass M_{200} and concentration c_{200} . We obtain the priors on the NFW profile parameters from the estimated stellar masses of G4–G6 (Buckley-Geer et al. 2020). We derive the halo mass distribution from the stellar mass distribution using the stellar mass–halo mass relation from Behroozi et al. (2019) for the respective redshift of the line-of-sight galaxy. We weight the halo-mass distribution with the halo mass function for our fiducial cosmology and the relevant redshift from Tinker et al. (2008). We obtain the concentration distribution from the halo mass distribution for our fiducial cosmology using the M – c relation from Diemer & Joyce (2019). We propagate the uncertainties and scatters in these relations when deriving one quantity from another. The M_{200} priors and c_{200} priors for G4–G6 are shown in Fig. 3.3. We can also derive the NFW scale radius $r_s = R_{200}/c_{200}$ in physical unit, and convert it to the scale radius θ_s in angular unit given our fiducial cosmology (Fig. 3.3). We do not use these scale radii as prior, we only

show the distributions to motivate our choice of the NFW profile for the galaxies G4–G6.

3.5.5 Galaxy group containing G1

We do not explicitly model the galaxy group that contains the central deflector G1 [Group 5 in Buckley-Geer et al. (2020)]. The estimated flexion shift $\log_{10} \Delta x_3 = -3.86^{+0.97}_{-0.72}$ for this group is marginally above the conservative threshold $\Delta x_3 > 10^{-4}$ (Buckley-Geer et al. 2020). However, the larger end of the flexion shift is provided by the case where the group is centred near to the central deflector. In that case, the group’s halo coincides with the deflector’s halo, which is already accounted for in our lens models. However, if the group’s centroid is offset from the central deflector, then the flexion shift becomes smaller. Then, the group’s contribution can be considered only in the approximated convergence, as the external shear profile already captures the shear contribution from the group. In Appendix 3.C, we show that the impact of the group’s convergence, if explicitly accounted for, only shifts H_0 by 0.4 per cent. This small shift justifies our choice of not including the group in our lens model.

3.5.6 Source component light profiles

We use an elliptical Sérsic light profile and a set of shapelets to reconstruct the quasar host S1’s light profile. We join all the Sérsic profile parameters across the three bands. We join the shapelet scale size ς across the UVIS bands and leave ς in the IR band as a free parameter.

To reconstruct S2’s light profile, we take a basis set of one elliptical Sérsic profile and multiple shapelets. We join the Sérsic profile parameters and the shapelet scale size ς across bands. For S3’s light profile, we adopt only an elliptical Sérsic profile. All the profile parameters for this profile except the amplitude I_{eff} are joint across the three bands.

For each model setup, we choose three fixed values of n_{max} : S1’s n_{max} in the IR band, S1’s n_{max} in the UVIS band, and S2’s n_{max} common across the three bands. We adopt three different sets of $\{n_{\text{max}}^{\text{S1, IR}}, n_{\text{max}}^{\text{S1, UVIS}}, n_{\text{max}}^{\text{S2}}\}$: $\{6, 3, 2\}$, $\{7, 4, 2\}$, $\{8, 5, 3\}$. A minimum number

of shapelets is necessary to sufficiently capture the complex structures in the lensed arcs, however we would start to fit the noise in the data by adopting too many more shapelets than necessary. We choose these values for n_{max} so that we hit a balance between these two scenarios. As we show in Table 3.3, the model evidence peaks around these values leading to our choice of these n_{max} values. We check if the inferred H_0 value from our analysis depends on the particular range of n_{max} values adopted above. We find that a set of larger n_{max} values $\{12, 9, 9, 4\}$ and a set of smaller n_{max} values $\{2, 2, 2, 2\}$ both infer H_0 within the range spanned by the models with our adopted n_{max} values. Thus, our inference of H_0 is robust against the particular range of adopted n_{max} values.

We place the additional source component S2 at the source plane with redshift $z_{\text{S2}} = 2.228$. As we do not know the redshift of S3, we adopt two choices for its redshift: z_{QSO} and z_{S2} .

For the model where we place S3 on S2's plane, we ignore the mass distribution of S3. From our lens model, we find that S3 is approximately twice further away from the quasar position on S2's plane than S2. We run a lens model ignoring S2's mass profile as well and find that the time-delay distance shifts by 0.94 per cent. The total flux from the reconstructed source light distribution of S2 and S3 are comparable after accounting for lensing magnification. If S2 and S3 are at a similar redshift, then they have similar total mass. If we assume SIS profile for S2 and S3, then the convergence of S3 at the quasar position would be approximately half of that from S2. We estimate that the time-delay distance will shift by $\lesssim 0.5$ per cent due to ignoring S3's mass distribution, if it indeed lies at a similar redshift of S2. This shift is negligible compared to the typical uncertainty (5–8 per cent) on the estimated time-delay distance given the quality of the current data. Therefore, we do not include its mass distribution in our model as we do not know the true redshift of S3.

3.5.7 Potential additional image C2 split from the image C

A faint blob is noticeable on a few pixels toward North-East from the position of G2 in the F160W band. This blob can potentially be another quasar image C2 split off from the image C by the nearby satellite G2. This potential additional image is not noticeable in the UVIS bands, but this non-detection in the UVIS bands can be caused by differential extinction through G2. If such an additional image is predicted by the model, we allow the model to assign point-source-like flux at the position of the predicted additional image. Note that we do not impose the existence of this additional image in the model.

3.5.8 *HST* image region for likelihood computation

To compute the imaging likelihood, we choose a large enough circular region of the *HST* image centred on the deflector galaxy in each band so that it contains most of the flux from the lens system in that particular band. The radii of these regions are 4.3, 3.3, and 3.3 arcsec in the F160W, F814W, and F475X bands, respectively. We mask out some of the pixels around the faint blob visible between G1 and G3 to block its light that would otherwise be within the chosen apertures. See the “Normalized Residual” plots of Figs 3.4 or 3.5 for the shape of the likelihood computation regions. In Appendix 3.B, we show that this particular choice of likelihood computation regions is not a source of bias in our analysis.

3.5.9 Dust extinction by the satellite G2

The satellite G2 may cause differential dust extinction to the lensed light distribution near image C. Ignoring this differential extinction may produce poor fitting around image C in the modelling. To account for this effect, we multiply a differential extinction factor $\exp[-\tau_\lambda(\theta_1, \theta_2)]$ to the lensed light distribution from the quasar host galaxy in all three bands. Here, τ_λ is equivalent to an optical depth parameter. We set the differential extinction profile proportional to G2’s IR surface brightness with a wavelength-dependent

normalization. Therefore, we take $\tau_\lambda(\theta_1, \theta_2) = \tau_\lambda^0 I_{\text{G2}}(x, y)$, where $I_{\text{G2}}(\theta_1, \theta_2)$ is G2’s light distribution parameterized with a Sérsic profile as described in Section 3.5.3. Thus, we are only modelling the differential extinction effect by G2 and this extinction goes to zero far away from G2. We do not model the differential extinction effect for the central deflector G1 as elliptical galaxies like G1 are typically dust-poor. We connect the proportionality constant τ_λ^0 for each band using the differential extinction law of Cardelli et al. (1989) with $R_V = 3.1$. As a result, we only have τ_{F814W}^0 as a non-linear parameter in our model. As a check, we run a lens model with the proportionality constant τ_λ^0 in each band independent of each other and we find that the three constrained τ_λ^0 parameters follow the extinction law from Cardelli et al. (1989) for $R_V \sim 3\text{--}5$. The amplitudes of the quasar images are free parameters, therefore any possible differential extinction effect in the quasar image flux is already accounted for.

3.5.10 Requirement for astrometric precision

For the lens system DES J0408–5354, a precision of 6 mas is required in the estimated source position to match the precision of the most precise time delay, Δt_{AB} (Birrer & Treu 2019). Given the magnification and the multiplicity of the images, this precision in the source position translates to an astrometric precision of approximately 40 mas for each image position on the image plane under a fixed lens model. As we can constrain the image positions in our models within 10 mas, we meet the requirement for astrometric precision. We expect any non-accounted astrometric uncertainty on the level of 10 mas or below to be subdominant in the error budget and the systematic impact.

3.5.11 Model choice combinations

Assembling the different choices described above for various components in our models, we have the following options that we vary:

1. Central deflector G1’s mass profile: power-law, composite,
2. Source n_{max} : $\{6, 3, 2\}$, $\{7, 4, 2\}$, $\{8, 5, 3\}$,
3. S3 redshift: $z_{\text{QSO}} = 2.375$, $z_{\text{S2}} = 2.28$, and
4. G4–G6 mass profile: SIS, NFW.

Taking all possible combinations of these choices, we have 24 different models in total – 12 for the power-law and 12 for the composite mass profiles. All the light profiles for lens and source light distribution form a linear basis set, thus all the amplitude parameters are linear (Birrer et al. 2015; Birrer & Amara 2018). We have 85–137 linear parameters and 57–62 non-linear parameters in the 24 model setups with either power-law or composite mass profiles.

We can compare the number of chosen models in this study with the 128 model runs performed in the cosmographic analysis of SDSS 1206+4332 (Birrer et al. 2019). Since Birrer et al. (2019) performed two separate sampling runs for the same model, these authors adopt 64 different models in practice combining the power-law and composite mass profiles. As Birrer et al. (2019) find that explicitly accounting for the non-linear components of the foreground shear has negligible impact in the cosmographic analysis, we choose not to include it in our analysis. Note, the linear components of the foreground shear is already accounted by the adopted external shear profile. Moreover, Birrer et al. (2019) incorporate two different likelihood-computation region sizes in their model choices, whereas we do not vary it in our analysis as we show that our analysis is stable against different choices of the likelihood-computation region size (Appendix 3.B). As a result, the comparable number of models in Birrer et al. (2019) is 16 to contrast with our adopted model number of 24. These numbers, although not identical, are comparable and difference between the exact number of chosen models to check systematics can arise naturally due to different complexity in different lens systems.

3.6 Lens modelling and cosmographic inference

In this section, we first present the lens modelling results (Section 3.6.1), combine the time-delay and kinematics likelihoods with the lens model posterior to produce the cosmological distance posterior (Section 3.6.2), and infer H_0 from the distance posterior (Section 3.6.3).

3.6.1 Modelling workflow and results

We simultaneously model the images from all three *HST* bands. For each model choice from Section 3.5.11, we reconstruct the PSF for each *HST* band. Thus, a set of three reconstructed PSFs is part of the model choice S that we marginalize (cf. equation 3.27). To initiate the PSF reconstruction, we take an initial PSF estimate by taking the median of a few (~ 4 – 6) stars from each *HST* image and then re-centring the median PSF. At each iteration of the PSF reconstruction process, we first realign the IR band’s coordinate system with the UVIS bands’ coordinate system using the quasar image positions (Shajib et al. 2019). Then, we optimize the lens model given the PSF from the initial estimate or the previous iteration of PSF reconstruction. Finally, we subtract the extended host-galaxy and the lens-galaxy light from the image and optimize the PSF using the residual quasar images (see for details Birrer et al. 2019, and for similar procedure Chen et al. 2016). We use LENSTRONOMY for lens modelling and PSF reconstruction and the particle swarm optimization (PSO) routine of COSMOHAMMER for optimizing the model (Kennedy & Eberhart 1995; Akeret et al. 2013; Birrer & Amara 2018). We repeat the set of the following three steps five times in total to reconstruct the PSF:

1. IR band image re-alignment,
2. lens model optimization using PSO,
3. PSF reconstruction.

We check that the reconstructed PSF stabilizes after five such iterations as the PSFs from

additional iterations do not lead to higher imaging likelihood.

After the PSF reconstruction, we simultaneously sample from the lens model posterior and compute the model evidence \mathcal{Z} using the dynamic nested sampling algorithm (Skilling 2004; Higson et al. 2018). We use the nested sampling software DYPOLYCHORD (Handley et al. 2015; Higson et al. 2019). In Appendix 3.E, we describe the sampler settings, assess the numerical performance, and conclude that the chosen settings allow for sufficient exploration of the posterior space.

We perform our analysis while blinding H_0 and other model parameters and lensing quantities directly related to H_0 , i.e. the model-predicted time delays. We also blind the mass profile slope γ of the power-law model after the initial exploration stage to find a stable preliminary lens model. In practice, the mean of the blinded quantities are always subtracted from the distribution within the analysis software, so that the printed values or plotted distributions are centred at zero. After all the co-authors had agreed during a teleconference on 2019 September 25 that sufficient amount of checks for modelling systematics were carried out, the analysis was frozen and the actual posterior distribution of H_0 was revealed for the first time. We report this H_0 posterior in this chapter without any further alteration.

Figs. 3.4 and 3.5 display the most likely models for the power-law and composite profiles, respectively. In addition to the lensed complex structures in the Einstein ring from the extended quasar host galaxy, the lensed arcs S2 and S3 are also reproduced very accurately. Moreover, the models reproduce the additional split image C2 on the other side of G2 from image C.

Tables 3.3 and 3.4 tabulate the evidences for different model choices. We combine the model posteriors weighted by the evidence ratios within each lens model family – power-law or composite – to marginalize over the model choices. Previous studies – e.g. Birrer et al. (2019); Rusu et al. (2019); Chen et al. (2019) – use the Bayesian information criterion (BIC) as an estimate of the evidence for Bayesian model averaging (BMA; e.g. Madigan & Raftery 1994; Hoeting et al. 1999). Whereas BIC estimates the model evidence based on the maxima

of the likelihood function under certain assumptions, nested sampling directly computes the model evidence by integrating over the whole prior space. Hence, the evidence obtained from nested sampling is more robust.

We account for sparse sampling from the model space by down-weighting the evidence ratios between the models. Effectively, we want to estimate the factor ΔS_n in equation (3.30) to account for sparse sampling. We estimate the sparsity of the sampled models by taking the variance of $\Delta \log \mathcal{Z}$ between “neighbouring” model pairs that differ in only one model setting. In this way, we are being conservative by accepting more variance in our lens model posterior to avoid any bias due to sparse sampling from the model space. For 12 models within each mass profile family, we then have 20 such “neighbouring” models. We obtain $\sigma_{\Delta \log \mathcal{Z}}^{\text{model}} = 436$ for the power-law models and $\sigma_{\Delta \log \mathcal{Z}}^{\text{model}} = 1210$ for the composite models. We follow Birrer et al. (2019) to adjust the relative weights of the model by convolving the evidence ratios with a Gaussian kernel with standard deviation $\sigma_{\Delta \log \mathcal{Z}} = (\sigma_{\Delta \log \mathcal{Z}}^{\text{model}})^2 + \sigma_{\Delta \log \mathcal{Z}}^{\text{numeric}})^{1/2}$. Here, we take $\sigma_{\Delta \log \mathcal{Z}}^{\text{numeric}} = 34$ as explained in Appendix 3.E. Following Birrer et al. (2019), we first calculate the absolute weight $W_{n,\text{abs}}$ of the n^{th} model by convolving the evidence uncertainty with the evidence ratio function $f(x)$ as

$$W_{n,\text{abs}} = \frac{1}{\sqrt{2\pi}\sigma_{\Delta \log \mathcal{Z}}} \int_{-\infty}^{\infty} f(x) \exp \left[-\frac{(\log \mathcal{Z}_n - x)^2}{2\sigma_{\Delta \log \mathcal{Z}}^2} \right] dx, \quad (3.52)$$

where we define the evidence ratio function $f(x)$ as

$$f(x) \equiv \begin{cases} 1 & x \geq \log \mathcal{Z}_{\text{max}}, \\ \exp(x - \log \mathcal{Z}_{\text{max}}) & x < \log \mathcal{Z}_{\text{max}}. \end{cases} \quad (3.53)$$

We then obtain the relative weight $W_{n,\text{rel}}$ by simply normalizing the absolute weights by the maximum absolute weight as

$$W_{n,\text{rel}} = \frac{W_{n,\text{abs}}}{\max(\{W_{n,\text{abs}}\})}. \quad (3.54)$$

In the limit of $n \rightarrow \infty$, we would have a perfect sampling of models from the model space. In that case, we have $\sigma_{\Delta \log \mathcal{Z}}^{\text{model}} \rightarrow 0$ and $\sigma_{\Delta \log \mathcal{Z}} \rightarrow \sigma_{\Delta \log \mathcal{Z}}^{\text{numeric}}$. Furthermore, if the evidence

value is perfectly computed with $\sigma_{\Delta \log \mathcal{Z}}^{\text{numeric}} = 0$, then the exponential function inside equation (3.52) becomes a Dirac delta function. In that limit, the relative weight $W_{n,\text{rel}}$ approaches the evidence ratio as

$$\lim_{\sigma_{\Delta \log \mathcal{Z}} \rightarrow 0} W_{n,\text{rel}} = \frac{\mathcal{Z}_n}{\mathcal{Z}_{\text{max}}}. \quad (3.55)$$

In Fig. 3.6, we compare the posteriors of important lens parameters between power-law and composite mass profiles after marginalizing over the model space using the adjusted evidence ratios as described above.

Table 3.3: Evidence for different power-law model setups. The model setups are ordered from higher to lower evidence. The relative weights for each model are obtained from the evidence ratios adjusted for sparse sampling from the model space as described in Section 3.6.1.

Mass profile	Source n_{\max}	z_{S3}	G4–G6 mass profile	$\log \mathcal{Z}$ (± 24)	$\Delta \log \mathcal{Z}$ (± 34)	Relative weight, W_{rel}
Power law	{8, 5, 3}	2.375	SIS	−25087	0	1.00
Power law	{6, 3, 2}	2.375	SIS	−25215	128	0.77
Power law	{8, 5, 3}	2.228	SIS	−25232	145	0.74
Power law	{7, 4, 2}	2.375	SIS	−25317	230	0.60
Power law	{7, 4, 2}	2.228	SIS	−25421	333	0.45
Power law	{6, 3, 2}	2.228	SIS	−25450	363	0.41
Power law	{8, 5, 3}	2.375	NFW	−25578	490	0.26
Power law	{7, 4, 2}	2.228	NFW	−25624	537	0.22
Power law	{6, 3, 2}	2.228	NFW	−25656	569	0.19
Power law	{6, 3, 2}	2.375	NFW	−26432	1345	0.00
Power law	{8, 5, 3}	2.228	NFW	−26469	1382	0.00
Power law	{7, 4, 2}	2.375	NFW	−26551	1464	0.00

Table 3.4: Evidence for different composite model setups. The model setups are ordered from higher to lower evidence. The relative weights for each model are obtained from the evidence ratios adjusted for sparse sampling from the model space as described in Section 3.6.1.

Mass profile	Source n_{\max}	z_{S3}	G4–G6 mass profile	$\log \mathcal{Z}$ (± 24)	$\Delta \log \mathcal{Z}$ (± 34)	Relative weight, W_{rel}
Composite	{7, 4, 2}	2.228	SIS	−25055	0	1.00
Composite	{8, 5, 3}	2.228	SIS	−25121	66	0.96
Composite	{8, 5, 3}	2.375	SIS	−25147	92	0.94
Composite	{6, 3, 2}	2.228	SIS	−25155	100	0.94
Composite	{7, 4, 2}	2.375	SIS	−25155	100	0.93
Composite	{6, 3, 2}	2.375	NFW	−25252	197	0.87
Composite	{6, 3, 2}	2.375	SIS	−25292	237	0.85
Composite	{7, 4, 2}	2.375	NFW	−25482	427	0.72
Composite	{6, 3, 2}	2.228	NFW	−25985	930	0.44
Composite	{8, 5, 3}	2.375	NFW	−26541	1486	0.22
Composite	{8, 5, 3}	2.228	NFW	−27073	2018	0.09
Composite	{7, 4, 2}	2.228	NFW	−28979	3924	0.00

3.6.2 Combining the time delays, kinematics, and external convergence information

To combine the time-delay likelihood with the lens imaging likelihood, we importance sample from the lens model posterior weighted by the joint time-delay and kinematics likelihood (Lewis & Bridle 2002). In Section 3.6.2.1, we fold in the time-delay and kinematic likelihoods into the lens model posterior. Then in Section 3.6.2.2, we add the external convergence distribution to the cosmological distance posteriors. Finally in Section 3.6.2.3, we check the impact of microlensing time-delay on our inference of the effective time-delay distance.

3.6.2.1 Combining time-delay and kinematics likelihoods

The posterior samples from nested sampling carry weights proportional to their contribution to the posterior mass. We obtain 10000 equally weighted posterior samples through weighted random sampling from the nested sampling chain for each lens model setup. To combine distance posteriors from different lens model setups, we randomly sample a number of points from the lens model posterior for each setup within a mass-model family, where the sampled number is proportional to the relative weight computed from the adjusted evidence ratio (Tables 3.3 and 3.4). We then uniformly sample 4000 points of $(D_{\Delta t}^{\text{eff}}, D_s/D_{\text{ds}})$ for each lens model sample from $[0, 2.15]D_{\Delta t}^{\text{eff, fiducial}} \times [0.35, 1.35](D_s/D_{\text{ds}})^{\text{fiducial}}$. The chosen boundaries fully contain $(> 5\sigma)$ the distance posteriors and they also encompass the range allowed by the priors $H_0 \in [0, 150] \text{ km s}^{-1} \text{ Mpc}^{-1}$ and $\Omega_m \in [0.05, 0.5]$, given our fiducial cosmology. This procedure effectively gives us $4000 \times N_{\text{sample}}$ points from the joint space combining the lens model parameters and $(D_{\Delta t}^{\text{eff}}, D_s/D_{\text{ds}})$, where N_{sample} is the number of lens model samples. We then importance sample from these $4000 \times N_{\text{sample}}$ points weighted by the joint time-delay and kinematic likelihood to obtain the marginalized posterior distribution of $(D_{\Delta t}^{\text{eff}}, D_s/D_{\text{ds}})$. We only consider Δt_{AB} and Δt_{AD} in the time-delay likelihood as Δt_{BD} is not independent of the others. We then transform the $(D_{\Delta t}^{\text{eff}}, D_s/D_{\text{ds}})$ distribution into the

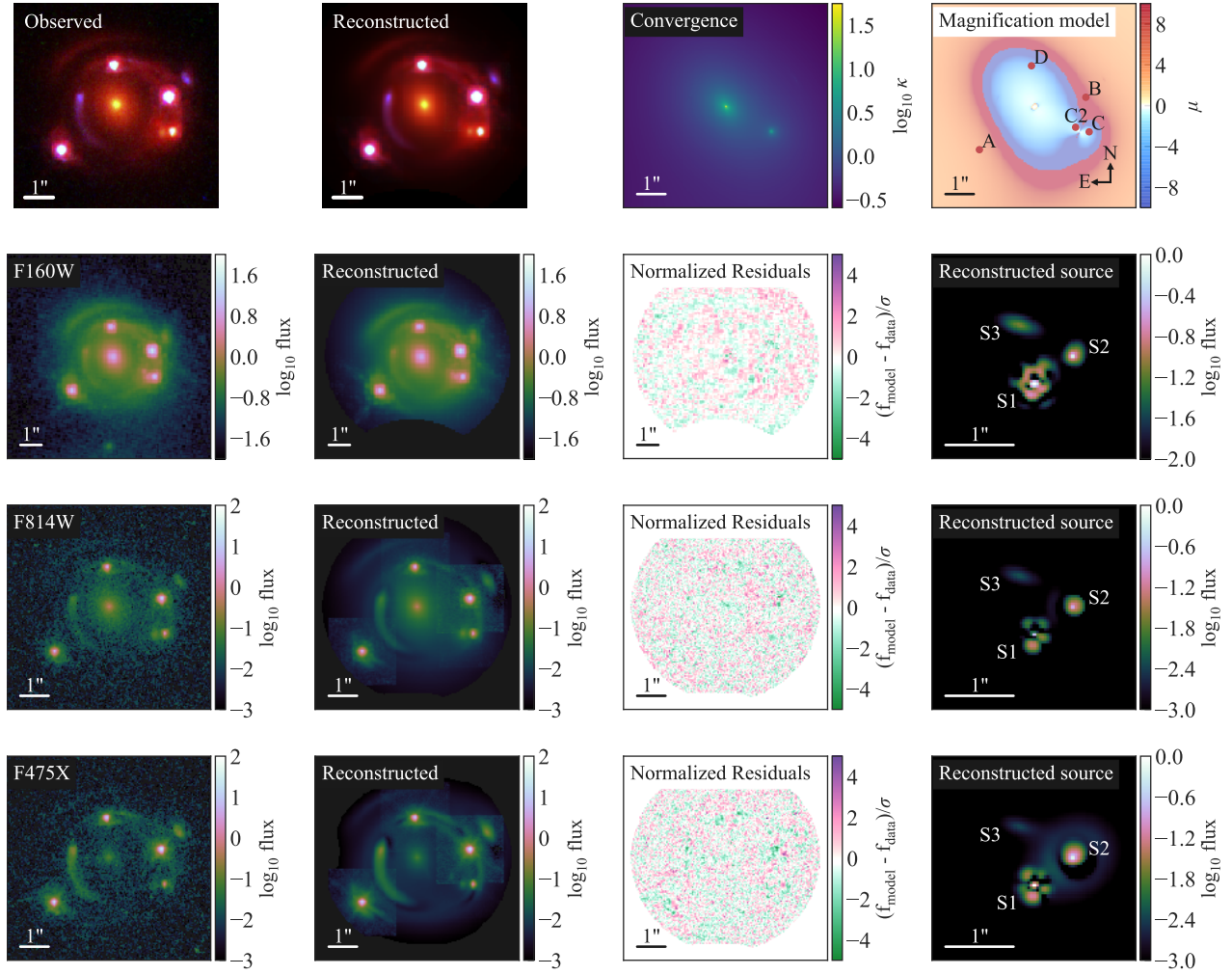


Figure 3.4: The most likely lens model and reconstructed image of DES J0408–5354 using the power-law model. The top row shows the observed RGB image, reconstructed RGB image, the convergence profile, and the magnification model in order from the left-hand side to the right-hand side. The next three rows show the observed image, the reconstructed image, the residual, the reconstructed source in order from the left-hand side to the right-hand side for each of the *HST* filters. The three filters are F160W (second row), F814W (third row), and F475X (fourth row). All the scale bars in each plot correspond to 1 arcsec. The patchy or ring-like artefacts in the source reconstruction translate to lensed features below the noise level in the image, thus they do not affect our lens model.

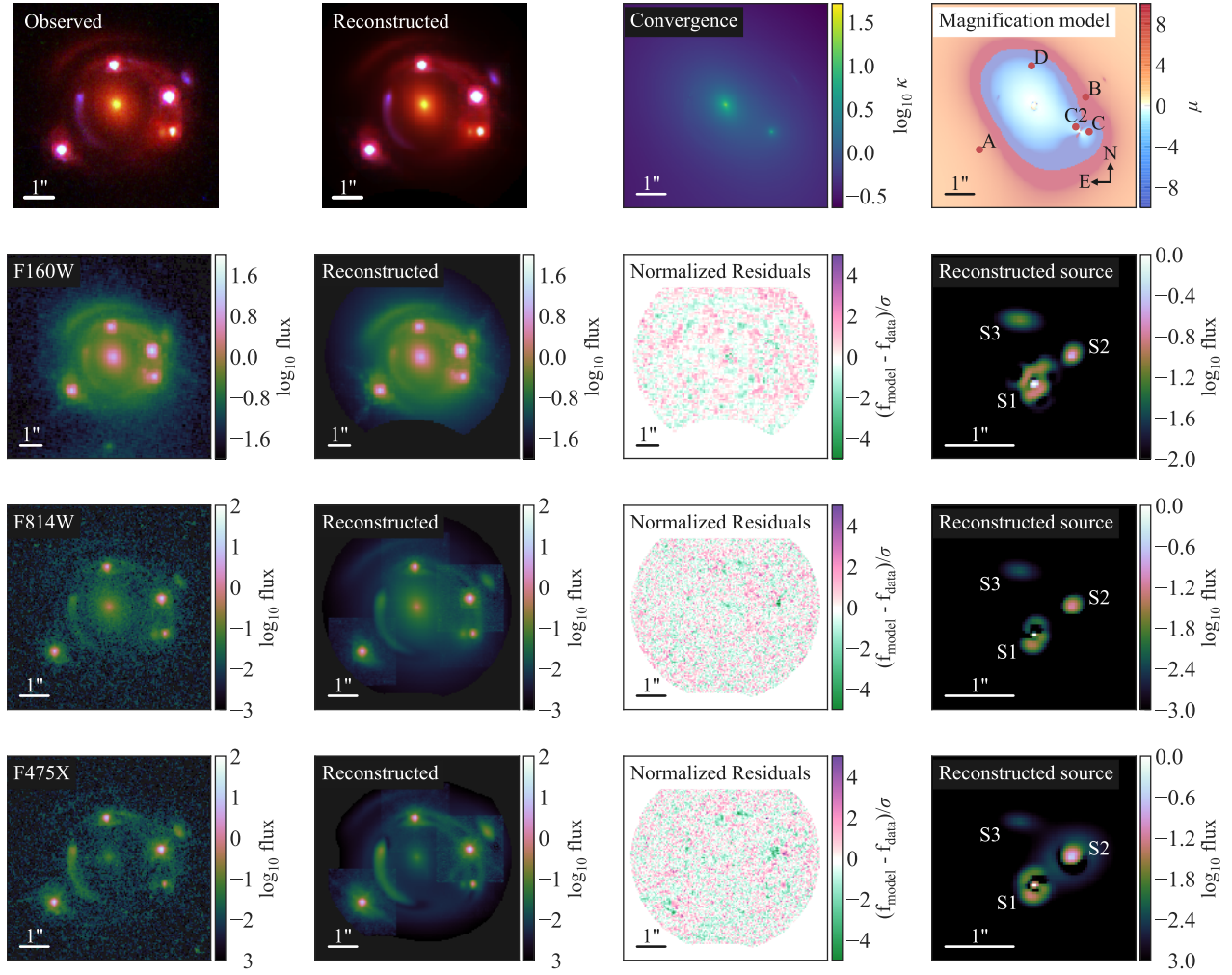


Figure 3.5: The most likely lens model and reconstructed image of DES J0408–5354 using the composite model. The top row shows the observed RGB image, reconstructed RGB image, the convergence profile, and the magnification model in order from the left-hand side to the right-hand side. The next three rows show the observed image, the reconstructed image, the residual, the reconstructed source in order from the left-hand side to the right-hand side for each of the *HST* filters. The three filters are F160W (second row), F814W (third row), and F475X (fourth row). All the scale bars in each plot correspond to 1 arcsec. The patchy or ring-like artefacts in the source reconstruction translate to lensed features below the noise level in the image, thus they do not affect our lens model.

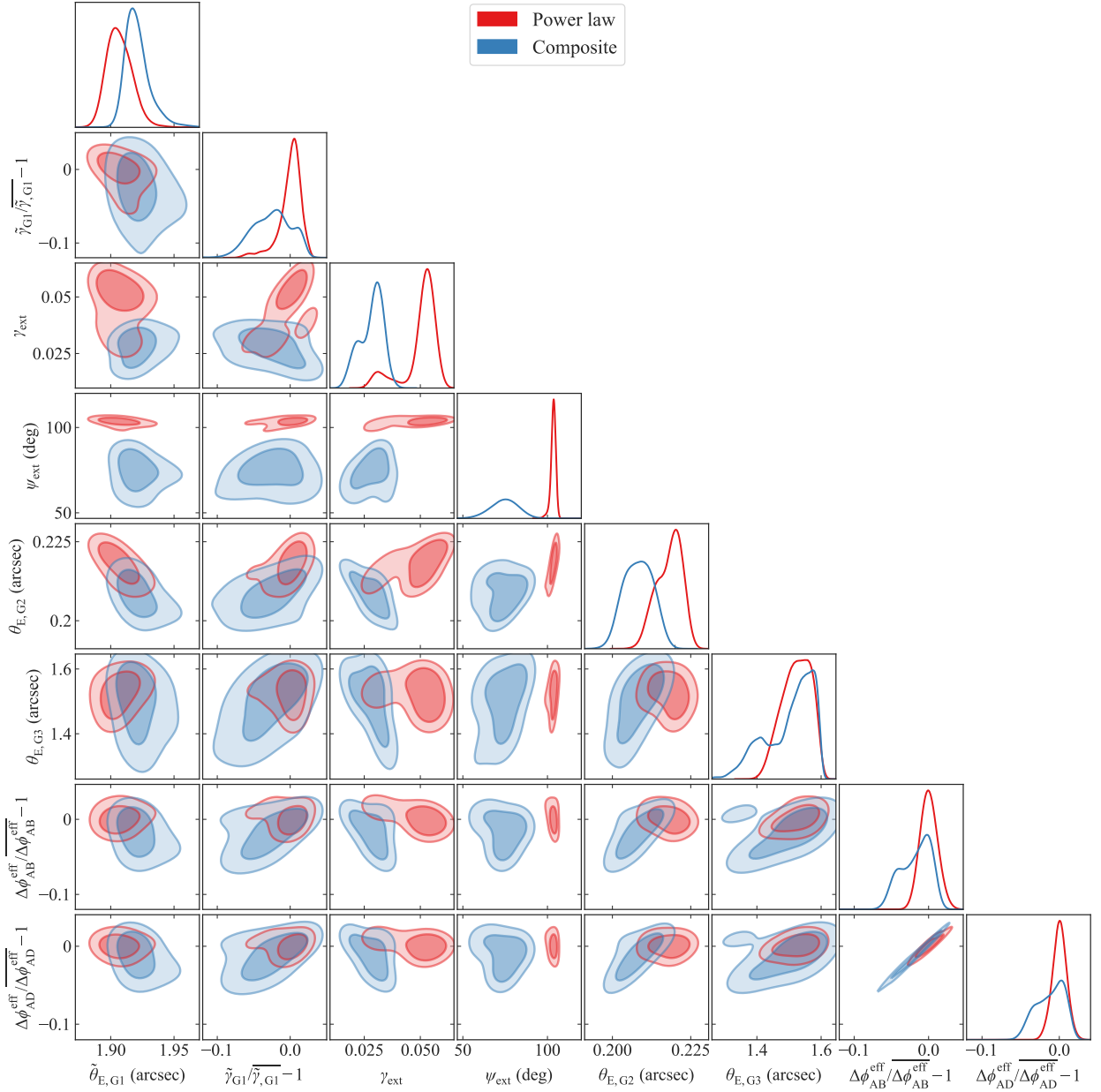


Figure 3.6: Comparison of the lensing properties between the power-law and composite mass models. The posteriors are weighted combinations of 12 models for each mass model family. Here, $\tilde{\theta}_E$ is the Einstein radius defined to contain mean convergence of 1, and the profile slope $\tilde{\gamma}$ is defined as the derivative of the convergence profile at $\tilde{\theta}_E$. We blind the profile-slope and the effective Fermat potential differences by subtracting the mean and then normalize it with the mean to show relative offsets in percentage.

$(D_{\Delta t}^{\text{eff}}, D_d)$ distribution.

Since there are four observing setup for G1’s central line-of-sight velocity dispersion, we compute four line-of-sight velocity dispersions for each sample from the lens model posterior. We account for covariance between these four measurements in the kinematic likelihood (see Section 3.3.4 for covariance matrix definition). We choose a uniform prior for the anisotropy scale radius as $r_{\text{ani}} \sim U(0.5\theta_{\text{hl}}, 5\theta_{\text{hl}})$, where θ_{hl} is the half-light radius in the F160W band. As we model the deflector light distribution using a double Sérsic profile, we numerically compute the radius of the circular aperture that contains half of the total flux from the double Sérsic profile.

3.6.2.2 Adding the external convergence distribution into the cosmological distance posterior

We apply a selection criterion on the $P(\kappa_{\text{ext}})$ estimated in Buckley-Geer et al. (2020) by requiring that the selected lines of sight also correspond to the external shear values predicted by our lens models. In Fig. 3.7, we show the probability distribution of κ_{ext} for the fiducial choice of constraints explored in Buckley-Geer et al. (2020), and the two κ_{ext} distributions consistent with the external shear values for the power-law and composite mass profiles [see Buckley-Geer et al. (2020) for further details].

We sample from the external convergence distribution corresponding to each mass profile. We correct the distance posterior using the sampled external convergence according to equation (3.20).

Fig. 3.8 shows the comparison of distance posteriors between the mass model families and between different settings within a mass model family. The distance posteriors are consistent between different model setups. From the combined distance posterior from all the models, we obtain the 1D marginalized constraints for the effective time delay distance $D_{\Delta t}^{\text{eff}} = 3382_{-115}^{+146}$ Mpc and the angular diameter distance $D_d = 1711_{-280}^{+376}$ Mpc (Fig. 3.9).

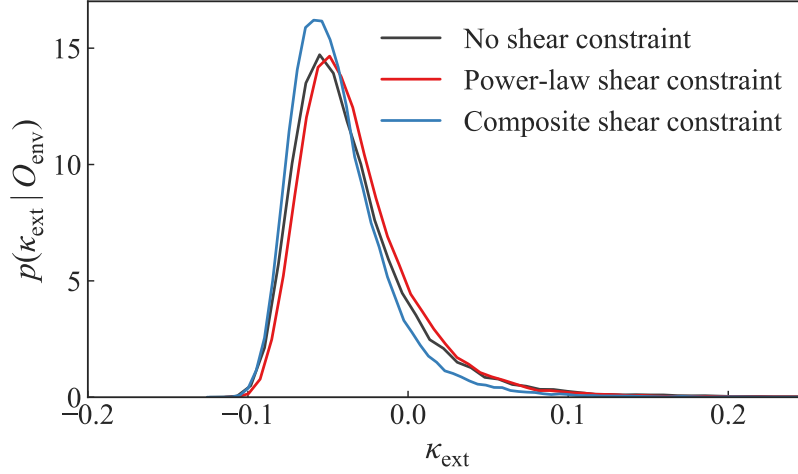


Figure 3.7: Distribution of external convergence κ_{ext} . The black line shows the κ_{ext} distribution from Buckley-Geer et al. (2020) without imposing any shear constraint. The red and blue lines show the distributions with shear constraints from the power-law and the composite mass models, respectively.

3.6.2.3 Microlensing time-delay effect

We check the impact of microlensing by the deflector galaxy’s stars on the measured time-delays in our analysis (Tie & Kochanek 2018). Note, this microlensing time-delay from Tie & Kochanek (2018) is based on the lamp-post model for the AGN accretion disc (Shakura & Sunyaev 1973). This effect will not necessarily exist for other disc models.

We generate the microlensing time-delay maps following Bonvin et al. (2018) and Chen et al. (2018). The estimated microlensing time-delay depends on the magnification of the lens model, on the stellar contribution at the image position, and on the properties of the black hole’s accretion disc.

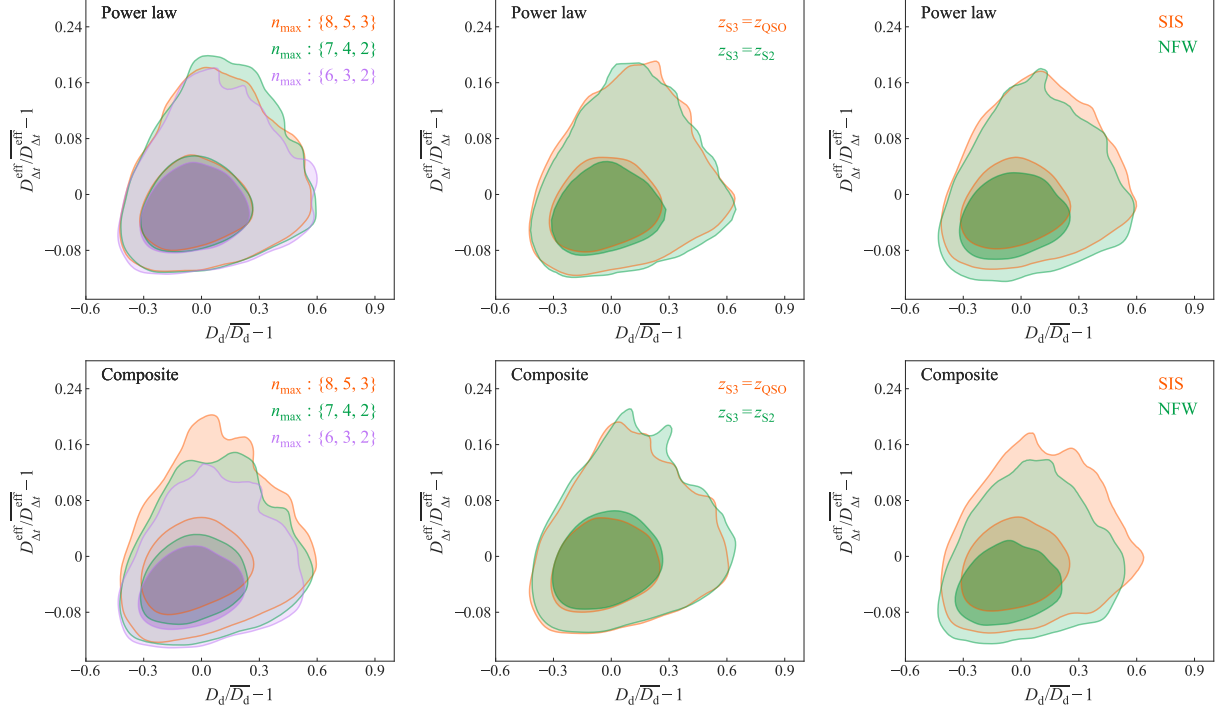


Figure 3.8: Comparison of the distance posteriors between choices of the lens model setups for the power-law models (top row) and the composite models (bottom row). The distance posteriors are weighted combinations of different runs with one common model setting as specified. One of the posteriors mean is subtracted from all them and then they are normalized by the mean to get the relative shifts in percentage. **Left-hand panel:** the distance posteriors for different settings of the source components' n_{\max} . **Centre:** the distance posteriors for different redshifts of S3. **Right-hand panel:** the distance posteriors for SIS and NFW mass profiles for the line-of-sight galaxies. The distance posteriors from different models are consistent.

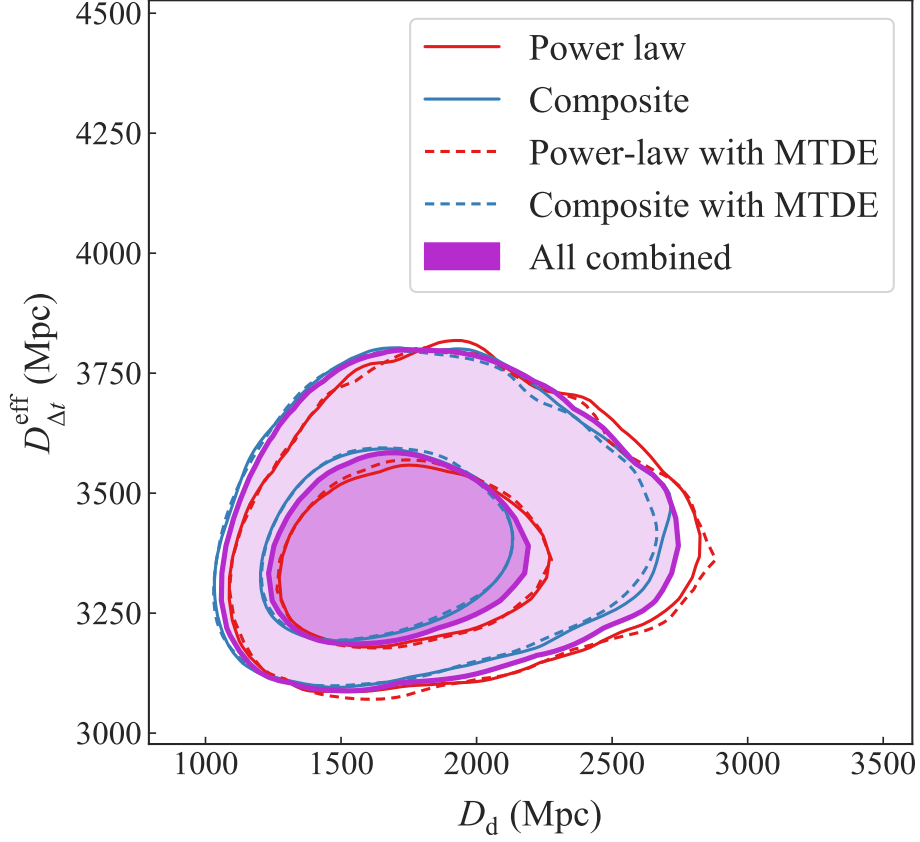


Figure 3.9: Cosmological distance posteriors for power-law (red) and composite mass-profile families (blue), and for all models combined (purple). All the models are combined within each categories weighted by their adjusted evidence ratios (Table 3.3). The solid contours for the power-law and composite mass profiles are without accounting for the microlensing time-delay effect (MTDE), and the corresponding dashed contours show the ones with the MTDE. The MTDE is negligible in our analysis and we do not incorporate this effect in the final distance posterior (purple contours) combining all the models.

We estimate the black hole mass using the scaling relation

$$\log_{10} \left(\frac{M_{\text{BH,Mg II}}}{M_{\odot}} \right) = b + m \log_{10} \left(\frac{\text{EW}_{\text{Mg II}}}{\text{\AA}} \right) + 2 \log_{10} \left(\frac{\text{FWHM}_{\text{Mg II}}}{\text{km s}^{-1}} \right) \quad (3.56)$$

between the black hole mass $M_{\text{BH,vir}}$, and the rest-frame full width at half-maximum (FWHM) and equivalent width (EW) of the Mg II broad line. This equation is equivalent to the $M_{\text{BH}} \propto R_{\text{BLR}} \sigma_{\text{BLR}}^2$, where R_{BLR} is the radius of the broad-line region and σ_{BLR} is the velocity dispersion of the broad-line region. Here, we used the EW as a proxy for R_{BLR} and the FWHM as a proxy for σ_{BLR} [cf. equation (2) of Shen et al. (2011)]. We estimate the parameters of this scaling relation using the SDSS quasars from the catalogue provided by Shen et al. (2011) as $b = 2.71$ and $m = -0.61$. We only take the quasars with non-zero entries for $M_{\text{BH,vir}}$, $\text{FWHM}_{\text{Mg II}}$, and $\text{EW}_{\text{Mg II}}$. Moreover, we only select the quasars within $1300 \text{ km s}^{-1} \leq \text{FWHM}_{\text{Mg II}} \leq 30000 \text{ km s}^{-1}$ to remove the quasars creating stripe-like features at the boundaries of the $M_{\text{BH,vir}}$ – $\text{FWHM}_{\text{Mg II}}$ scatter plot. As a result, we have 85038 selected quasars to fit the above scaling relation. We obtain the rest-frame FWHM and EW of the Mg II line from the quasar spectra at image B and image D from Agnello et al. (2017) as $\text{FWHM}_{\text{Mg II}}^{\text{B}} = 3413 \text{ km s}^{-1}$, $\text{EW}_{\text{Mg II}}^{\text{D}} = 37.3 \text{ \AA}$, $\text{FWHM}_{\text{Mg II}}^{\text{D}} = 2952 \text{ km s}^{-1}$, $\text{EW}_{\text{Mg II}}^{\text{B}} = 30.5 \text{ \AA}$. We apply a magnification correction to the estimated black hole mass from each image as

$$\log_{10} \left(\frac{M_{\text{BH}}}{M_{\odot}} \right) = \log_{10} \left(\frac{M_{\text{BH,Mg II}}}{M_{\odot}} \right) - g \log_{10} \mu, \quad (3.57)$$

where we take the calibration factor $g = 0.5$ (Vestergaard & Peterson 2006). We also add 0.25 dex uncertainty to the estimated black hole mass to account for the limitation of using Mg II to measure it (Woo et al. 2018). Averaging over the estimates from image B and D, we obtain the black hole mass of the quasar as $\log_{10} (M_{\text{BH,vir}}^{\text{J0408}}/M_{\odot}) = 8.41 \pm 0.27$. We also estimate the Eddington ratio using the scaling relation

$$\log_{10} \left(\frac{L'_{\text{bol}}}{L'_{\text{Edd}}} \right) = b + m \log_{10} \left(\frac{M_{\text{BH,Mg II}}}{M_{\odot}} \right). \quad (3.58)$$

Table 3.5: Lensing quantities at the image positions used to create the microlensing time-delay map. The total convergence κ , the stellar convergence κ_\star , the shear γ_{shear} , and the magnification μ are obtained from the best-fitting composite model. As the local slope of the composite model at the image positions can deviate from the 3D slope $\gamma = 2$ of an isothermal profile, κ and γ_{shear} are not necessarily identical.

TImage	κ	κ_\star	γ_{shear}	μ
A	0.46	0.03	0.19	3.9
B	0.59	0.06	0.32	15.5
D	0.70	0.13	0.69	-2.6

We estimate $m = -0.33$, $b = 2.2$ with an intrinsic scatter of 0.64 dex by fitting the relation to the same objects selected from Shen et al. (2011)’s catalogue. We also apply a magnification correction on the Eddington ratio obtained for each image as

$$\log_{10} \left(\frac{L_{\text{bol}}}{L_{\text{Edd}}} \right) = \log_{10} \left(\frac{L'_{\text{bol}}}{L'_{\text{Edd}}} \right) + (g - 1) \log_{10} \mu \quad (3.59)$$

(Birrer et al. 2019). As a result, we obtain $\log_{10} (L_{\text{bol}}/L_{\text{Edd}}) = -1.48 \pm 0.27$ after averaging over the estimates from images B and D. The accretion disc size R_0 is determined assuming a standard accretion disc model (Shakura & Sunyaev 1973). In Tables 3.5 and 3.6, we tabulate the values used to create the microlensing time delay maps shown in Fig. 3.10. We assumed Salpeter initial mass function (IMF) and ignored the uncertainty on the convergence and shear parameters. Shifting the stellar convergence κ_\star by the typical uncertainty of 10 per cent or changing the IMF has negligible impact on the estimated microlensing time-delay distribution in Fig. 3.10.

We account for the microlensing time-delay effect in the measured time delay by sampling from the microlensing time-delay distribution and adjusting the measured time delay as

$$\Delta t_{\text{XY,adjusted}} = \Delta t_{\text{XY,measured}} + t_{\text{X,micro}} - t_{\text{Y,micro}}. \quad (3.60)$$

The microlensing time-delay effects is small compared to the uncertainty on the measured

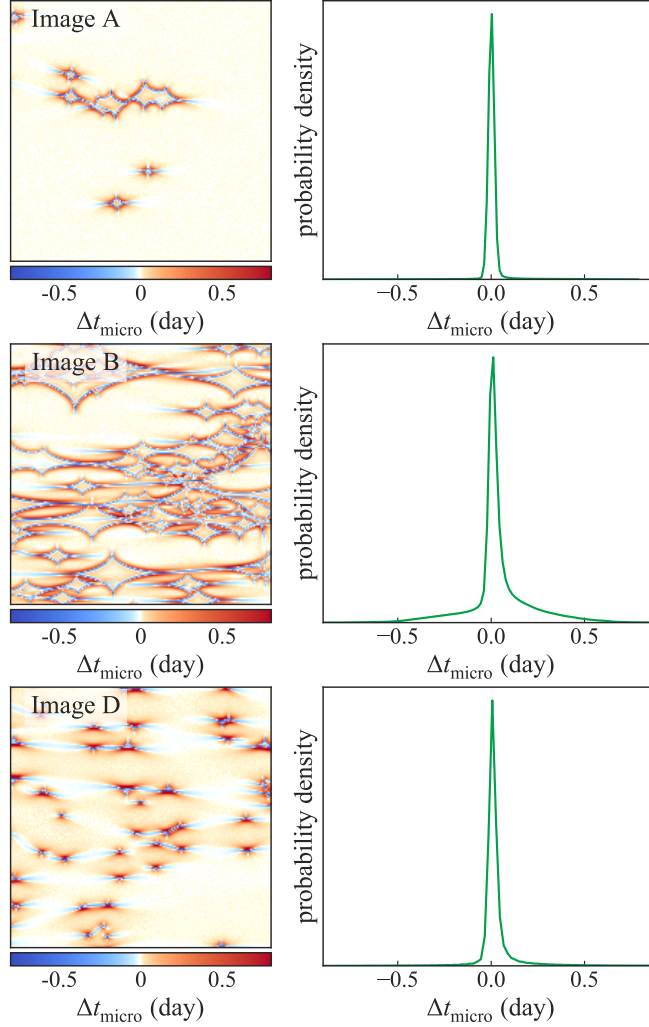


Figure 3.10: Microlensing time-delay maps and the probability of microlensing time-delays for images A, B, and D. Each microlensing time-delay map on the left-hand column is created from the relevant image magnification, stellar contribution to the convergence at the image position, and the accretion disc properties of the black hole. The probability density function of the microlensing time-delay at each image position is shown in the right-hand column. The expected fluctuation in the measured time-delays is small relative to the measurement uncertainty.

Table 3.6: Properties of the quasar accretion disc used to compute the microlensing time-delay maps.

Quantity	Value
Black hole mass, $\log_{10}(M_{\text{BH}}/M_{\odot})$	8.41 ± 0.27
Eddington ratio, $\log_{10}(L_{\text{bol}}/L_{\text{Edd}})$	-1.48 ± 0.27
Accretion disc size, R_0 (cm)	3.125×10^{14}
Accretion efficiency, η	0.1
Central wavelength for light curve observation, λ (μm)	0.668
Average foreground stellar mass, $\langle M_{\star}/M_{\odot} \rangle$	0.3

time delays. Thus, accounting for this microlensing time-delay effect does not shift the effective time-delay distance by more than 0.1 per cent (Fig. 3.9). We only perform this step as a check and we do not include this effect in our inference of H_0 .

3.6.3 Inference of H_0

The cosmological distance posterior contains all the cosmographic information. We infer H_0 from this distance posterior for a flat Λ CDM cosmology with priors $H_0 \in [0, 150]$ km s⁻¹ Mpc⁻¹ and $\Omega_{\text{m}} \in [0.05, 0.5]$. We take these priors for consistency with previous H0LiCOW analyses (Birrer et al. 2019; Rusu et al. 2019; Chen et al. 2019). The Ω_{m} prior is based on our knowledge from various observations that the Universe is neither empty nor closed. We take a kernel density estimate of the distance posterior as the likelihood function for cosmological parameters to retain the full covariance between $D_{\Delta t}^{\text{eff}}$ and D_{d} . Similar to Birrer et al. (2019), we take the bandwidth for the kernel density estimation to be sufficiently narrow so as to not affect the resultant posteriors of the cosmological parameters. We infer $H_0 = 74.2^{+2.7}_{-3.0}$ km s⁻¹ Mpc⁻¹ in the Λ CDM cosmology, which is a 3.9 per cent measurement (Fig. 3.11). In this 3.9 per cent uncertainty, we estimate that the time-delay measurement contributes

1.8 per cent, the external convergence contributes 3.3 per cent, and the lens modelling and other sources contribute the remaining 1 per cent uncertainty. As a systematic check on our model weighting scheme, we infer H_0 by combining all the models with equal weight as done in the first few analyses of the H0LiCOW lenses (e.g., Wong et al. 2017). For this most conservative weighting scheme, we find $H_0 = 74.8^{+2.7}_{-3.0}$ km s⁻¹ Mpc⁻¹, which is a 0.8 per cent deviation from our quoted H_0 above. We summarize the various systematic checks performed in this chapter and their corresponding impacts on the inferred H_0 in Appendix 3.F.

3.7 Discussion and summary

In this chapter, we analyse the lens system DES J0408–5354 to blindly infer the effective time-delay distance from the observed time delays. We model the mass profile of the lens system using high-resolution *HST* imaging from three bands. We combine the time-delay and kinematic likelihoods with the lens model posterior, and factor in the statistically inferred external convergence to obtain the cosmological distance posteriors in the $D_{\Delta t}^{\text{eff}}-D_d$ plane. We perform a thorough check for systematic effects arising from model choices, and we marginalize over them to account for this source of systematic uncertainties in our analysis. As a result, we constrain the 2D joint posterior of the effective time delay distance $D_{\Delta t}^{\text{eff}}$ and the angular diameter distance to the deflector D_d that fully incorporates their covariance. The marginalized estimates for these two distances are $D_{\Delta t}^{\text{eff}} = 3382^{+146}_{-115}$ with 3.9 per cent uncertainty, and $D_d = 1711^{+376}_{-280}$ with 19.2 per cent uncertainty. These constraints translate into $H_0 = 74.2^{+2.7}_{-3.0}$ km s⁻¹ Mpc⁻¹ with a precision of 3.9 per cent. This estimated value of H_0 is consistent with from the previously analysed sample of six lenses by the H0LiCOW collaboration, $H_0 = 73.3^{+1.7}_{-1.8}$ km s⁻¹ Mpc⁻¹ (Wong et al. 2019). It is also consistent with measurements of H_0 based on the local distance ladder (Riess et al. 2019; Freedman et al. 2019), reinforcing the tension (Verde et al. 2019) with the inference from early Universe

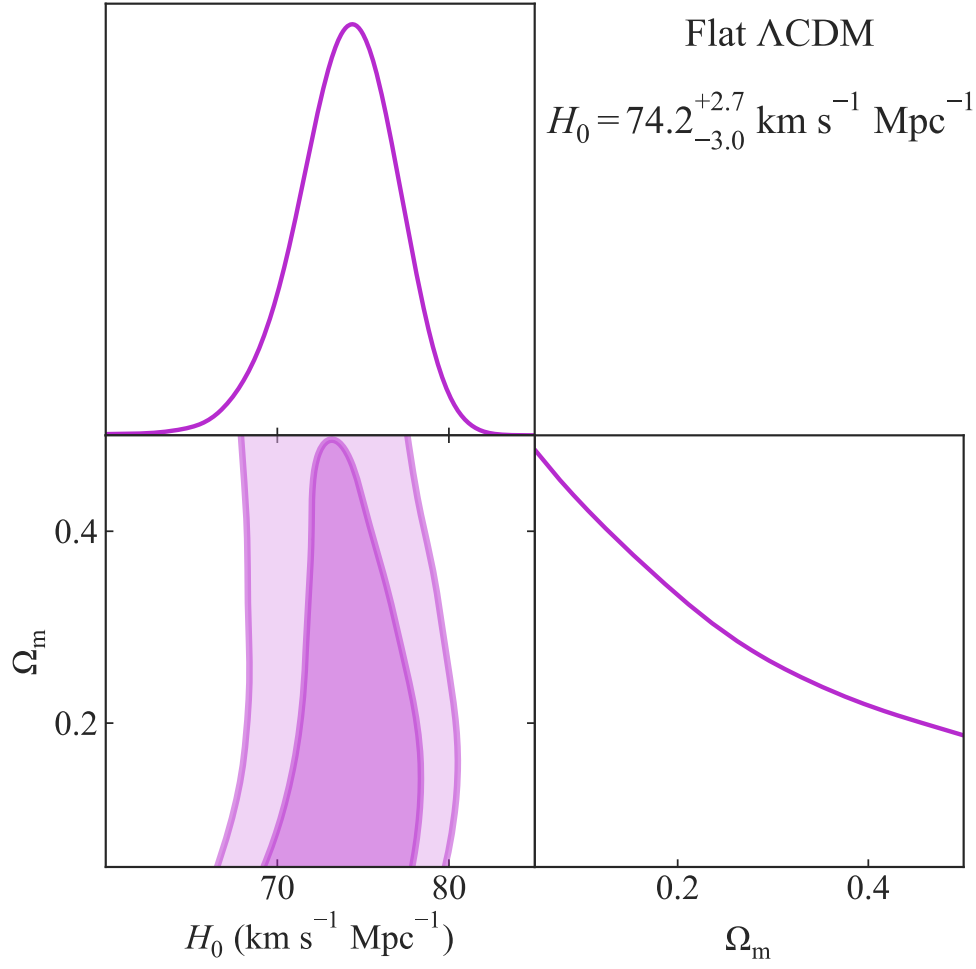


Figure 3.11: Posterior probability distribution functions of H_0 and Ω_m in the Λ CDM cosmology for the 2D distance posterior in Fig. 3.9. The inferred Hubble constant is $H_0 = 74.2^{+2.7}_{-3.0} \text{ km s}^{-1} \text{ Mpc}^{-1}$.

probes (Planck Collaboration 2018; Abbott et al. 2018b).

The one presented in this chapter is the first of two independent cosmographic analysis of the lens system DES J0408–5354, which is based on the lens-modelling software LENSTRONOMY. A second independent and blind analysis using the lens-modelling software GLEE will be presented in a future work (Yıldırım et al., in preparation). In this future paper, we will compare the results from the two modelling efforts and quantitatively evaluate the systematic uncertainty that may arise due to using different softwares and adopting different modelling choices by different investigators. The posterior probability distribution function of H_0 from DES J0408–5354 will be combined with previous measurements by the H0LiCOW team after the second analysis is complete, so as to include this modelling systematic uncertainty in the combination.

The analysis presented in this chapter can be improved in the future. Due to a multitude complexities required in the lens model of DES J0408–5354, we fix the distance ratios between the multiple lens and source planes in our analysis using a fiducial Λ CDM cosmology to make our analysis computationally feasible. We show that the choice of fiducial cosmology has negligible impact on our inference within the Λ CDM model. However, it would be ideal to treat the distance ratios as independent non-linear parameters in the model. We leave this improvement to be implemented in future works, where more general cosmological models will be considered. Furthermore, the precision on the inferred H_0 can be improved in the future with the help of spatially resolved kinematics (Shajib et al. 2018; Yıldırım et al. 2019).

In the modelling, more general mass profiles can be used in the composite model – e.g., the generalized NFW profile, or a mass-to-light ratio gradient in the stellar component (e.g., Zhao 1996; Sonnenfeld et al. 2018a). However, these types of generalized mass profile had been computationally intractable for lens modelling in the elliptical case until only recently (Shajib 2019). Given the computational cost of this study ($\sim 10^6$ CPU h) already pushing far beyond the typical case of modelling endeavours for a single lens system, we leave the explorations of more general mass models and estimation of the corresponding impact in the

inference of H_0 for future studies.

Improving the precision on H_0 measurement from each single lens system, increasing the number of systems to ~ 40 , and investigating the presence of yet unknown systematic errors are all necessary steps towards reaching 1 per cent precision from time-delay cosmography (Shajib et al. 2018). The analysis presented in this chapter took one step in each direction.

Acknowledgements

We thank the anonymous referee for helpful comments that improved this manuscript. AJS was supported by the National Aeronautics and Space Administration (NASA) through the Space Telescope Science Institute (STScI) grant HST-GO-15320. AJS was also supported by the Dissertation Year Fellowship from the University of California, Los Angeles (UCLA) graduate division.

AJS acknowledges the hospitality of the Aspen Center of Physics (ACP) and the Munich Institute for Astro- and Particle Physics (MIAPP) of the Excellence Cluster "Universe", where part of this research was completed. ACP is supported by National Science Foundation grant PHY-1607611.

Funding for the DES Projects has been provided by the U.S. Department of Energy, the U.S. National Science Foundation, the Ministry of Science and Education of Spain, the Science and Technology Facilities Council of the United Kingdom, the Higher Education Funding Council for England, the National Center for Supercomputing Applications at the University of Illinois at Urbana-Champaign, the Kavli Institute of Cosmological Physics at the University of Chicago, the Center for Cosmology and Astro-Particle Physics at the Ohio State University, the Mitchell Institute for Fundamental Physics and Astronomy at Texas A&M University, Financiadora de Estudos e Projetos, Fundação Carlos Chagas Filho de Amparo à Pesquisa do Estado do Rio de Janeiro, Conselho Nacional de Desenvolvimento Científico e Tecnológico and the Ministério da Ciência, Tecnologia e Inovação, the Deutsche

Forschungsgemeinschaft and the Collaborating Institutions in the Dark Energy Survey.

The Collaborating Institutions are Argonne National Laboratory, the University of California at Santa Cruz, the University of Cambridge, Centro de Investigaciones Energéticas, Medioambientales y Tecnológicas-Madrid, the University of Chicago, University College London, the DES-Brazil Consortium, the University of Edinburgh, the Eidgenössische Technische Hochschule (ETH) Zürich, Fermi National Accelerator Laboratory, the University of Illinois at Urbana-Champaign, the Institut de Ciències de l'Espai (IEEC/CSIC), the Institut de Física d'Altes Energies, Lawrence Berkeley National Laboratory, the Ludwig-Maximilians Universität München and the associated Excellence Cluster Universe, the University of Michigan, the National Optical Astronomy Observatory, the University of Nottingham, The Ohio State University, the University of Pennsylvania, the University of Portsmouth, SLAC National Accelerator Laboratory, Stanford University, the University of Sussex, Texas A&M University, and the OzDES Membership Consortium.

Based in part on observations at Cerro Tololo Inter-American Observatory, National Optical Astronomy Observatory, which is operated by the Association of Universities for Research in Astronomy (AURA) under a cooperative agreement with the National Science Foundation.

The DES data management system is supported by the National Science Foundation under Grant Numbers AST-1138766 and AST-1536171. The DES participants from Spanish institutions are partially supported by MINECO under grants AYA2015-71825, ESP2015-66861, FPA2015-68048, SEV-2016-0588, SEV-2016-0597, and MDM-2015-0509, some of which include ERDF funds from the European Union. IFAE is partially funded by the CERCA program of the Generalitat de Catalunya. Research leading to these results has received funding from the European Research Council under the European Union's Seventh Framework Program (FP7/2007-2013) including ERC grant agreements 240672, 291329, and 306478. We acknowledge support from the Australian Research Council Centre of Excellence for All-sky Astrophysics (CAASTRO), through project number CE110001020, and the Brazilian

Instituto Nacional de Ciência e Tecnologia (INCT) e-Universe (CNPq grant 465376/2014-2).

This manuscript has been authored by Fermi Research Alliance, LLC under Contract No. DE-AC02-07CH11359 with the U.S. Department of Energy, Office of Science, Office of High Energy Physics. The United States Government retains and the publisher, by accepting the article for publication, acknowledges that the United States Government retains a non-exclusive, paid-up, irrevocable, world-wide license to publish or reproduce the published form of this manuscript, or allow others to do so, for United States Government purposes.

This research made use of LENSTRONOMY (Birrer et al. 2015; Birrer & Amara 2018), DY-POLYCHORD (Higson et al. 2019), POLYCHORD (Handley et al. 2015), COSMOHAMMER (Akseret et al. 2013), FASTELL (Barkana 1999), NUMPY (Oliphant 2015), SCIPY (Jones et al. 2001), ASTROPY (Astropy Collaboration 2013, 2018), JUPYTER (Kluyver et al. 2016), MATPLOTLIB (Hunter 2007), SEABORN (Waskom et al. 2014), NESTCHECK (Higson 2018), SEXTRACTOR (Bertin & Arnouts 1996), EMCEE (Foreman-Mackey et al. 2013), COLOSSUS (Diemer 2018), and GETDIST (<https://github.com/cmbant/getdist>).

3.A Impact of fiducial cosmology in the lens modelling

We check the impact of fixing the distance ratios between the lens and the source planes with a fiducial Λ CDM cosmology with density parameters $\Omega_m = 0.3$ and $\Omega_\Lambda = 0.7$. For this purpose, we run two separate lens models with the same model setup for the power-law mass profile, but with the cosmological parameters ($\Omega_m = 0.1$, $\Omega_\Lambda = 0.9$) and ($\Omega_m = 0.45$, $\Omega_\Lambda = 0.55$) to fix the distance ratios. Within this wide-range of Ω_m values within the flat Λ CDM cosmology, H_0 only shifts by $\lesssim 1$ per cent (Fig. 3.12). As this shift is much smaller than the precision of the measured Hubble constant allowed by the quality of our data, we conclude that our inferred cosmological distance posterior on the $D_{\Delta t}$ - D_d plane is effectively independent of the choice of cosmological parameters within the flat Λ CDM cosmology.

However, we find that the inferred distance posteriors depend on the fiducial cosmology

within the w CDM model. If we adopt the fiducial w CDM cosmology with $w = -1.06$, $\Omega_m = 0.3$, $\Omega_{de} = 0.7$, then the inferred H_0 shifts by approximately 3 per cent from that inferred from the cosmology with $w = -1$ (Fig. 3.13). We adopt the shift $\Delta w = 0.06$ for comparison, as this range in w is the joint precision from the *Planck* with CMB lensing, SNIae, and baryon acoustic oscillation measurements (Planck Collaboration 2018). This significant shift in H_0 demonstrate that our double source plane treatment is sensitive to the dark energy equation of state parameter w (e.g. Gavazzi et al. 2008; Collett et al. 2012; Collett & Auger 2014). Therefore, our distance posteriors should not be used to constrain cosmological parameters in extended cosmologies other than the flat Λ CDM model. We leave the computation of a posterior distribution function valid in more general cosmologies for future work.

3.B Impact of likelihood computation region choice

We check if our adopted region for imaging likelihood computation can be a source of systematic bias in the lens modelling. We perform the modelling procedure for two different region sizes keeping every other settings in the model the same for a power-law model. The regular region sizes are 4.3, 3.3, and 3.3 arcsec in radius for the F160W, F814W, and F475X bands, respectively. The larger region sizes are larger by 0.2 arcsec in each band. The median of the effective time-delay distance shifts by less than 0.1 per cent and the median of the angular diameter distance shifts by less than 2 per cent between these two choices of the likelihood computation region (Fig. 3.14).

3.C Impact of the convergence from the group containing G1

We estimate the convergence at G1’s centre from the galaxy group containing G1 [group ID 5 in Buckley-Geer et al. (2020)]. We randomly sample halos from the centroid and velocity

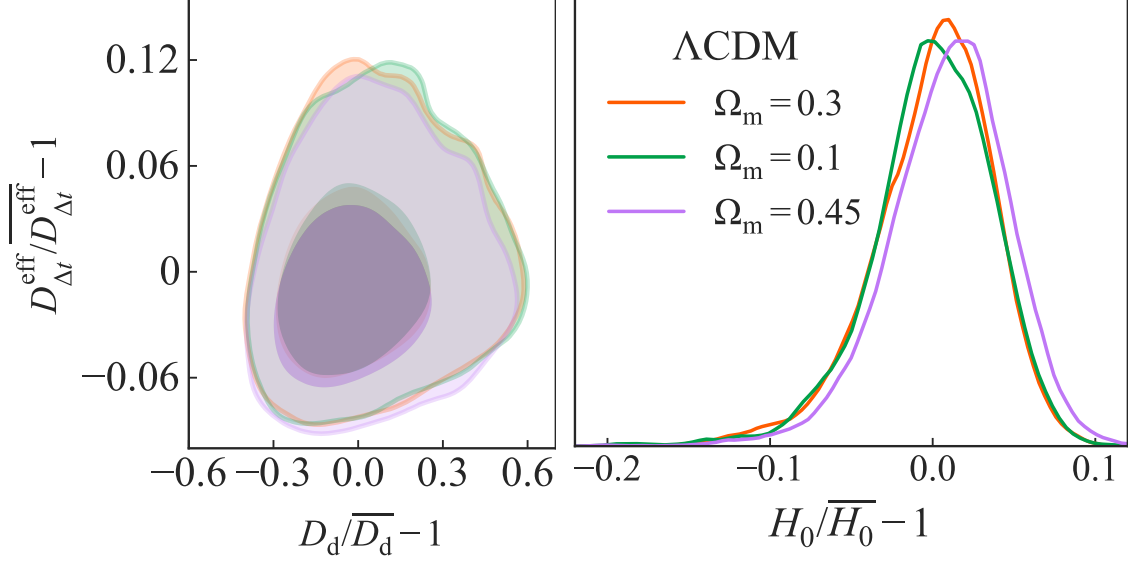


Figure 3.12: Comparison of the distance posteriors and inferred H_0 for different fiducial cosmologies within the flat ΛCDM model. We compare between three set of cosmological parameters: $\Omega_m = 0.3$, $\Omega_\Lambda = 0.7$ (orange), $\Omega_m = 0.1$, $\Omega_\Lambda = 0.9$ (green), and $\Omega_m = 0.45$, $\Omega_\Lambda = 0.55$ (purple). The distance posteriors are from identical lens model setups with the power-law mass profile except for the fiducial cosmology. H_0 shifts by less than 1 per cent within these wide range of Ω_m values. This shift is much smaller than the precision on H_0 allowed by our current data quality. As a result, we can treat the distance posteriors inferred from our analysis to be independent of cosmological assumptions within the flat ΛCDM cosmology.

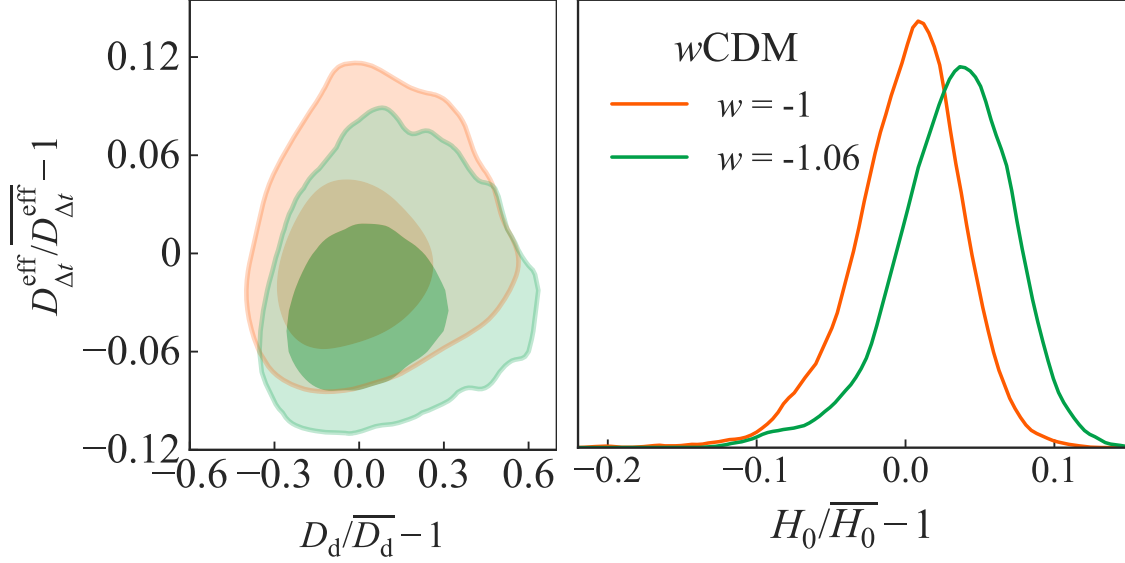


Figure 3.13: Comparison of the distance posteriors and inferred H_0 for different fiducial cosmologies within the w CDM model. We compare between three set of cosmological parameters: $w = -1$, $\Omega_m = 0.3$, $\Omega_\Lambda = 0.7$ (orange), and $w = -1.06$, $\Omega_m = 0.1$, $\Omega_\Lambda = 0.9$ (green). The distance posteriors are from identical lens model setups with the power-law mass profile except for the fiducial cosmology. H_0 shifts by ~ 3 per cent for a shift $\Delta w = 0.06$, which is approximately the joint precision on w from the *Planck* with CMB lensing, SNIae, and the baryon acoustic oscillation measurements (Planck Collaboration 2018). This shift in H_0 shows that the double source plane treatment in our analysis is sensitive to the dark energy equation of state parameter w (Gavazzi et al. 2008; Collett & Auger 2014). As a result, our distance posterior should not be used to constrain parameters in cosmologies that extend the flat Λ CDM model.

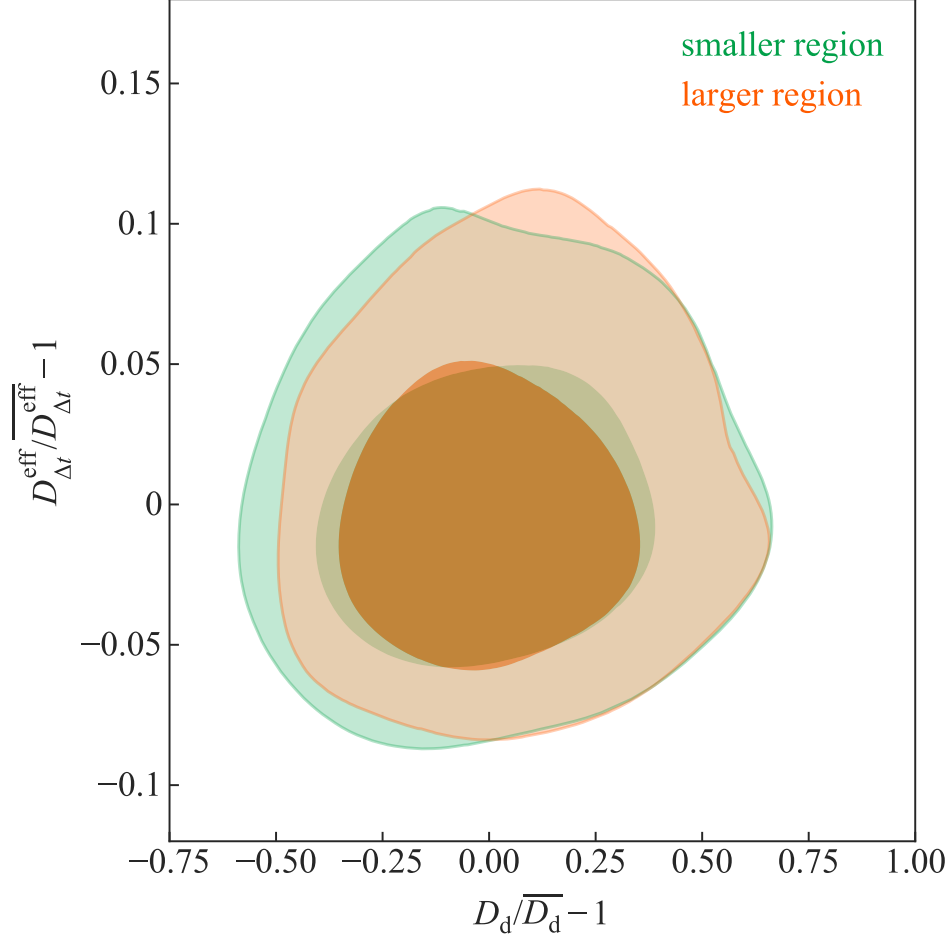


Figure 3.14: Comparison of the distance posteriors from the power-law lens model for two likelihood computation region sizes. The smaller regions have radii 4.3, 3.3, and 3.3 arcsec in the F160W, F814W, F475X bands, respectively. The larger region sizes are 4.5, 3.5, and 3.5 arcsec in the same order. All the other model setups are same between the two runs. The distance posteriors are almost identical. Therefore, the choice of likelihood computation region has negligible impact in our analysis.

dispersion distributions estimated as described in Buckley-Geer et al. (2020). However, we use a uniform prior to obtain the velocity dispersion for the halo, whereas Buckley-Geer et al. (2020) adopt the Jeffrey’s prior. We convert the group’s velocity dispersion into halo mass using the scaling relation

$$\log_{10} [h(z)M_{200}] = 13.98 + 2.75 \log_{10} \left(\frac{\sigma_{\text{group}}}{500 \text{ km s}^{-1}} \right) \quad (3.61)$$

(Munari et al. 2013). We weight this halo mass distribution using the halo mass function from Tinker et al. (2008) corresponding to our fiducial cosmology and the lens redshift. We obtain the concentration parameter distribution using the theoretical $M_{200}-c$ relation from Diemer & Joyce (2019) with 0.16 dex uncertainty. We also apply 10 per cent uncertainty on M_{200} to remove any strong dependency on H_0 through the fiducial cosmology. We compute the convergence distribution at G1’s centre due to this distribution of the halo masses and we apply a cut in the group’s shear distribution $\gamma_{\text{group}} < 0.1$ to remove halos that are inconsistent with the model predicted shear (Fig. 3.15). The median of the group’s convergence distribution is 0.004. As we are explicitly accounting for the group’s convergence here, we re-estimate κ_{ext} after removing the galaxies in this group from the number count statistic of Buckley-Geer et al. (2020). The re-estimated κ_{ext} decreases by 0.005 for the power-law mass models and by 0.008 for the composite mass models. As a result, explicitly accounting for the group’s convergence decreases H_0 by approximately 0.4 per cent. This shift is negligible compared to the 3.9 per cent uncertainty in our estimated value of H_0 .

3.D Checking for the existence and impact of a dark substructure

Agnello et al. (2017) propose a possible dark subhalo near image D toward the North–East direction. We check the impact of such a dark substructure in our analysis by including a mass profile for the substructure in our lens model. We check with both SIS and spherical NFW profile for the substructure. We take a broad uniform prior of $0.8 \text{ arcsec} \times 0.8 \text{ arcsec}$ for the centroid of the mass profile to encompass the possible position of the substructure

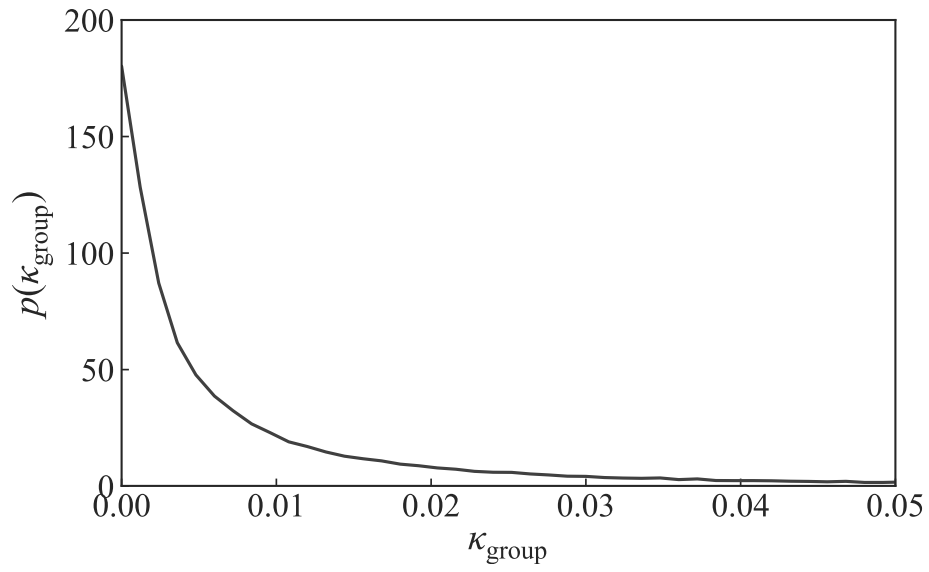


Figure 3.15: Distribution of the convergence at G1’s centre from the galaxy group’s halo containing G1. The distribution $p(\kappa_{\text{group}})$ is estimated for the estimated centroid and velocity dispersion of this group in Buckley-Geer et al. (2020).

given in fig. 9 of Agnello et al. (2017).

For both of the SIS and NFW profiles, our lens model constrains the possible position of the mass profile for the potential substructure (Fig. 3.16). Interestingly, the constrained position is consistent with the proposed position by Agnello et al. (2017), although the model had the freedom to offset the position by ~ 0.4 arcsec from the constrained position. We estimate the SIS velocity dispersion of this possible dark substructure to be $\sigma_{\text{SIS}} = 33.7^{+1.9}_{-1.3}$ km s $^{-1}$. From the model with the NFW profile for the dark substructure, we estimate the halo mass $\log_{10}(M_{200}/M_{\odot}) = 10.65^{+0.10}_{-0.06}$, halo radius $r_{200} = 45.7^{+3.5}_{-2.1}$ kpc, and concentration $c_{200} = 12.2^{+4.1}_{-2.2}$.

However, we do not add the potential substructure in our final lens model as the addition of the dark substructure shifts the estimated H_0 by less than 1 per cent. Moreover, it is not clear if the constrained parameters for the additional mass profile to account for the dark substructure indeed reflect the existence of the substructure. A similar effect can also arise if the additional source component S2 lies at a redshift between the quasar and the central deflector G1. The proximity of the constrained position of the dark substructure and the lensed position of S2 hints this scenario to be a possibility.

Agnello et al. (2017) use the dust-corrected and delay-corrected flux ratios observed in the DES data as a constraint for the lens model and propose that the existence of a dark substructure fits the data better. We check if microlensing can be a possible source for the deviation of the flux ratios from a smooth model observed by Agnello et al. (2017). We derive the amplitude of microlensing in images A, B, and D by comparing their MUSE spectra. Microlensing is stronger in the continuum than in the broad emission lines. Therefore, we can isolate the microlensed fraction of the spectra if we assume that microlensing is more important in one of the lensed images under scrutiny and derive a lower limit on the amplitude of microlensing effect in the continuum emission (e.g. Sluse et al. 2012b). This procedure reveals substantial differential microlensing between the continuum and the broad lines when we consider image pairs A–D and B–D, but not A–B. The data are compatible

with a microlensing demagnification of image D by at least a factor of 2. This demagnification translates into a microlensing corrected flux ratio $\Delta m_{AD} = 0.25$ mag. This estimate, however, may be affected by systematic errors caused by intrinsic variability. From the past light-curves of this system, we estimate that over the period corresponding to the time delay between images A and D, this systematic error could reach up to 0.2 mag. Therefore, we cannot definitively attribute the observed “flux-ratio anomaly” to microlensing. In summary, whereas we cannot find strong evidence for the existence of the potential substructure, we also cannot rule out its existence. Since the presence or the impact of the dark substructure is not significant in our analysis, we omit it in our lens models for simplicity.

3.E Nested sampling settings

In this Appendix, we provide our adopted settings for the nested sampling software DYPOLYCHORD and validate that the numerical requirements for our analysis are met.

We choose the DYPOLYCHORD settings `ninit = 100`, `nrepeats = 30`, `nconst.live = 140`, `dynamic_goal = 0.9`, `precision_criterion = 0.001` [see Higson et al. (2019) for explanation of these settings]. To check the appropriateness of these settings, we run two sampling runs with the same lens model and sampler settings (Fig. 3.17). We find that the posteriors PDFs of the parameters are consistent within 1σ between the two runs, therefore we accept the chosen settings to be appropriate for sufficient exploration of the prior space. However, we find the estimated evidence values to differ by more than the estimated statistical uncertainty. This difference indicates that there is a systematic scatter in the computed evidence value. To estimate this scatter, we run a second set of nested sampling runs for 17 different lens models with `precision_criterion = 0.01`. We choose a lower `precision_criterion` for this second set of runs to make the sampling run terminate faster. A lower `precision_criterion` does not largely impact the evidence values, although it may affect the posterior estimation (Higson et al. 2018). As we are only interested to ob-

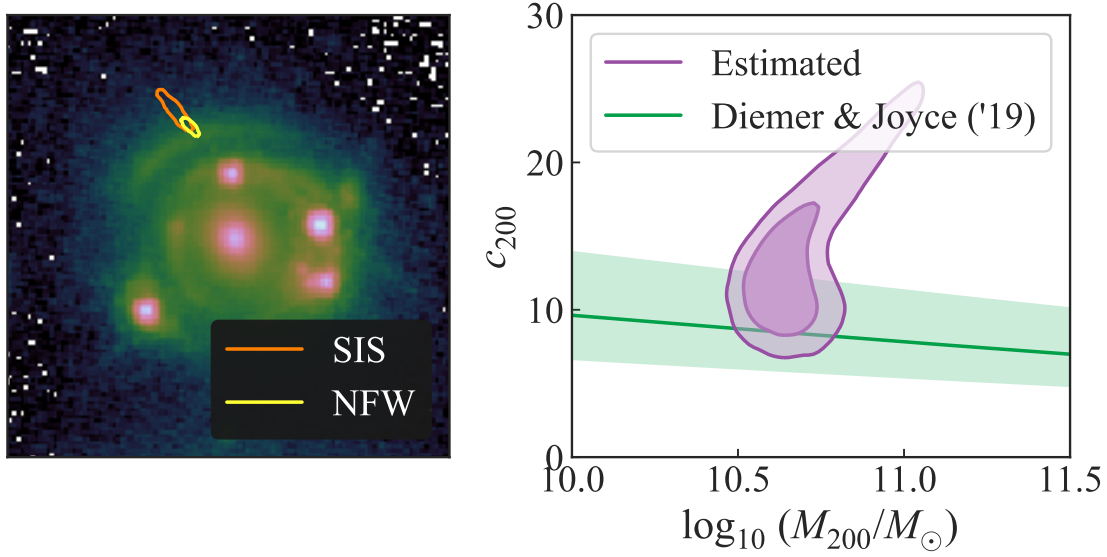


Figure 3.16: Constraints from our lens model for the position and NFW halo properties of the dark substructure proposed by Agnello et al. (2017). **Left-hand panel:** 2σ credible region for the position of the dark substructure in our lens model assuming the SIS profile (the orange contour) and the NFW profile (the yellow contour) for the substructure. **Right-hand panel:** The constraint on the M_{200} - c_{200} plane assuming the NFW profile for the dark substructure. The purple contours show the 1σ and 2σ credible regions. We show a comparison with the theoretical c_{200} - M_{200} relation for our fiducial cosmology from Diemer & Joyce (2019).

Table 3.7: Uncertainty contributions from different parts of the cosmographic analysis.

Analysis component	Uncertainty budget (per cent)
Time-delay measurement	1.8
κ_{ext} estimation	3.3
Lens modelling and other sources	1.0
Total uncertainty	3.9

tain a conservative estimate of the scatter present in the computed $\log \mathcal{Z}$ values, this lower `precision_criterion` is sufficient for this purpose. By taking the mean of the evidence difference between runs from the two sets with the same lens model, we estimate the scatter in the evidence value as 24. Therefore, we take $\sigma_{\log \mathcal{Z}}^{\text{numeric}} = 24$ as the numerical error in the computed evidence values. Albeit, if we increase `nlive_const` or `nrepeats`, we can decrease the error in the computed $\log \mathcal{Z}$ values in the exchange of a higher computational cost. However, as we down-weight the relative evidence ratios to account for sparse sampling of our models from the model space, this numerical error in $\log \mathcal{Z}$ is a subdominant factor (Section 3.6.1).

3.F Summary of uncertainty budget and systematic checks

In this appendix, we summarize the uncertainty budgets from different parts of the cosmographic analysis (Table 3.7) and the systematic checks performed in our analysis with their impacts on the inferred H_0 in Table 3.8.

3.G Model summary and parameter priors

In this appendix, we provide the priors for the parameters in our lens models (Table 3.9).

To make the nested sampler efficiently explore and integrate over the high-dimensional

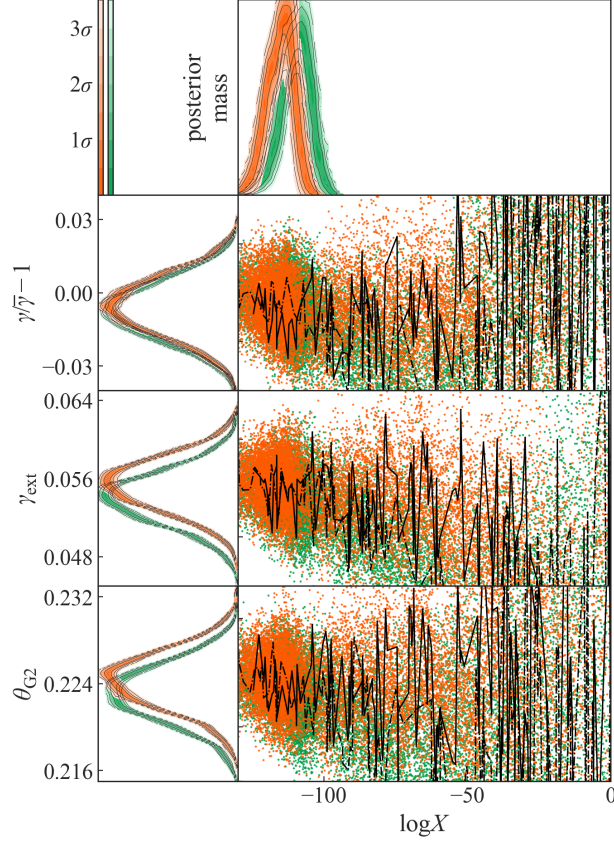


Figure 3.17: NESTCHECK diagnostic plot showing samples' distributions in two different runs with the same lens model for our chosen sampling settings. The top right-hand panel shows the relative posterior mass as a function of $\log X$, where X is the prior volume fraction. The next three panels show the progressions of sampling (right to left) for three of the main lens mass parameters. The black solid and dashed lines show the evolution of one random thread of the dynamic nested sampler. The left column shows the posterior distributions of each parameter. The coloured contours represent the iso-probability credible regions of the probability density functions. The posteriors of the parameters are consistent within 1σ , therefore we accept that the chosen settings allow for sufficient exploration of the prior volume.

Table 3.8: Summary of systematic checks and their impacts on the inferred H_0 . The relevant section in the chapter is referenced for each systematic check.

Systematic check	ΔH_0 (per cent)
Fixing $\Omega_m = 0.10$ in fiducial cosmology (App. 3.A)	−0.06
Fixing $\Omega_m = 0.45$ in fiducial cosmology (App. 3.A)	+0.94
Choosing a larger likelihood computation region (App. 3.B)	+0.10
Explicitly accounting for the galaxy group (App. 3.C)	−0.40
Accounting for a possible dark subhalo near S3 (App. 3.D)	−0.46
Not accounting for the deflection by S2’s mass (Note, we included S2’s mass in our models, thus already marginalizing in our quoted posterior; Section 3.5.6)	+0.95
Accounting for Tie & Kochanek (2018)’s microlensing time-delay (Section 3.6.2.3)	−0.10
Total systematic shift	−0.92–0.08

($\sim 60D$) prior volume in our models, we narrow down the width of the uniform priors for some of the parameters more than that would be known purely *a priori*. We choose these prior bounds by looking at the posterior PDFs for the lens models from the initial exploratory phase of this study and we further adjust these prior widths through trial and error. We check that the posterior PDFs of the parameters are fully contained within the chosen bounds for our final lens models, unless we specifically set the bound using an empirical or physical prior. Below we explain some of the parameters from Table 3.9 that were not introduced within the main body of this chapter.

The amplitude of the Chameleon convergence profile is parameterized with the deflection angle at 1 arcsec, α_1^{Chm} . The ellipticity parameters e_1 and e_2 in the relevant profiles are related to the axis ratio q and the position angle ϕ as

$$\begin{aligned} q &= \frac{1 - \sqrt{e_1^2 + e_2^2}}{1 + \sqrt{e_1^2 + e_2^2}}, \\ \tan 2\phi &= \frac{e_2}{e_1}. \end{aligned} \tag{3.62}$$

Parameterizing the ellipticity with e_1 and e_2 avoids the periodicity in the polar coordinate ϕ and makes the sampling more efficient. The centroids (θ_1^c, θ_2^c) of the relevant profiles are relative to the coordinate RA 04:08:21.71 and Dec -53:53:59.34. We take a uniform prior $\mathcal{U}(-5 \times 10^4, 5 \times 10^4)$ for the amplitudes of the shapelet components – which are linear parameters – to compute the evidence using equation (3.35).

Table 3.9: Prior for the model parameters.

Model component	Parameter	Prior
G1 mass, power law	γ	$\mathcal{U}(1.80, 2.15)$
G1 mass, composite	r_s^{NFW} (arcsec)	$\mathcal{N}(12.42, 2.94)$ with bound [5.6, 19.3] (Section 3.5.2)
G1 mass, composite	α_1^{Chm} (arcsec)	$\mathcal{U}(0.2, 1.5)$
External shear	γ_{ext}	$\mathcal{U}(0.01, 0.09)$
External shear	ψ_{ext} (rad)	$\mathcal{U}(0, \pi)$
G2 mass, SIS	θ_E (arcsec)	$\mathcal{U}(0.19, 0.27)$
G3 mass, SIS	θ_E (arcsec)	$\mathcal{N}(0.772, 0.024)$ with bound [0.3, 1.6] (Section 3.5.4.3, Fig. 3.3)
G4 mass, SIS	θ_E (arcsec)	$\mathcal{N}(0.353, 0.012)$ with bound [0.0, 1.0] (Section 3.5.4.3, Fig. 3.3)
G4 mass, NFW	$\log_{10}(M_{200}/M_\odot)$	Empirical prior with bound [11.3, 13.4] (Section 3.5.4.4, Fig. 3.3)
G4 mass, NFW	c_{200}	Empirical prior with bound [0.0, 16.0] (Section 3.5.4.4, Fig. 3.3)
G5 mass, SIS	θ_E (arcsec)	$\mathcal{N}(0.046, 0.002)$ with bound [0.0, 0.2] (Section 3.5.4.3, Fig. 3.3)
G5 mass, NFW	$\log_{10}(M_{200}/M_\odot)$	Empirical prior with bound [10.8, 12.3] (Section 3.5.4.4, Fig. 3.3)
G5 mass, NFW	c_{200}	Empirical prior with bound [0.0, 16.5] (Section 3.5.4.4, Fig. 3.3)
G6 mass, SIS	θ_E (arcsec)	$\mathcal{N}(0.070, 0.004)$ with bound [0.0, 0.3] (Section 3.5.4.3, Fig. 3.3)
G6 mass, NFW	$\log_{10}(M_{200}/M_\odot)$	Empirical prior with bound [11.4, 12.5] (Section 3.5.4.4, Fig. 3.3)
G6 mass, NFW	c_{200}	Empirical prior with bound [0.0, 20.0] (Section 3.5.4.4, Fig. 3.3)
S2 mass, SIS	θ_E (arcsec)	$\mathcal{N}(0.0022, 9.98 \times 10^{-6})$ with bound [0.000, 0.022] (Section 3.5.4.3)

Continued on next page

Table 3.9 – *Continued from previous page*

Model component	Parameter	Prior
S1 light, Sérsic	θ_{eff} (arcsec)	$\mathcal{U}(0.04, 0.15)$
S1 light, Sérsic	n_s	$\mathcal{U}(0.6, 5.0)$
S1 light, Sérsic	e_1	$\mathcal{U}(-0.05, 0.35)$
S1 light, Sérsic	e_2	$\mathcal{U}(-0.16, 0.20)$
S1 light, F814W+F475X, shapelets	ς (arcsec)	$\mathcal{U}(0.06, 0.11)$
S1 light, F160W, shapelets	ς (arcsec)	$\mathcal{U}(0.08, 0.15)$
S2 light, Sérsic	θ_{eff} (arcsec)	$\mathcal{U}(0.08, 0.40)$
S2 light, Sérsic	n_s	$\mathcal{U}(1.0, 5.0)$
S2 light, Sérsic	e_1	$\mathcal{U}(0.04, 0.37)$
S2 light, Sérsic	e_2	$\mathcal{U}(-0.20, 0.00)$
S2 light	θ_1^c (arcsec)	$\mathcal{U}(-0.47, 0.30)$
S2 light	θ_2^c (arcsec)	$\mathcal{U}(-2.48, -1.48)$
S2 light, shapelets	ς (arcsec)	$\mathcal{U}(0.06, 0.12)$
S3 light, Sérsic	θ_{eff} (arcsec)	$\mathcal{U}(0.18, 0.90)$
S3 light, Sérsic	n_s	$\mathcal{U}(0.6, 2.5)$
S3 light, Sérsic	e_1	$\mathcal{U}(0.20, 0.42)$
S3 light, Sérsic	e_2	$\mathcal{U}(0.00, 0.35)$
S3 light	θ_1^c (arcsec)	$\mathcal{U}(0.75, 1.80)$

Continued on next page

Table 3.9 – *Continued from previous page*

Model component	Parameter	Prior
S3 light	θ_2^c (arcsec)	$\mathcal{U}(1.70, 2.30)$
G1 light, F814W	θ_{eff} (arcsec)	$\mathcal{N}(0.61, 0.27)$ with bound $[0.1, 2.7)$ (Section 3.5.2)
G1 light, F814W	n_s	$\mathcal{U}(2.0, 8.0)$
G1 light, F814W+F475X	e_1	$\mathcal{U}(-0.20, 0.00)$
G1 light, F814W+F475X	e_2	$\mathcal{U}(-0.05, 0.13)$
G1 light	θ_1^c (arcsec)	$\mathcal{U}(0.023, 0.035)$
G1 light	θ_1^c (arcsec)	$\mathcal{U}(-0.010, 0.003)$
G1 light, F475X	θ_{eff} (arcsec)	$\mathcal{N}(0.61, 0.27)$ with bound $[0.1, 2.7)$ (Section 3.5.2)
G1 light, F475X	n_s	$\mathcal{U}(1.0, 5.0)$
G1 light, F160W, Sérsic 1	θ_{eff} (arcsec)	$\mathcal{N}(0.61, 0.27)$ with bound $[0.1, 2.7)$ (Section 3.5.2)
G1 light, F160W, Sérsic 1	n_s	$\mathcal{U}(1.0, 5.0)$
G1 light, F160W, Sérsic 1	e_1	$\mathcal{U}(-0.25, 0.00)$
G1 light, F160W, Sérsic 1	e_2	$\mathcal{U}(-0.10, 0.12)$
G1 light, F160W, Sérsic 2	θ_{eff} (arcsec)	$\mathcal{N}(0.61, 0.27)$ with bound $[0.1, 2.7)$ (Section 3.5.2)
G1 light, F160W, Sérsic 2	n_s	$\mathcal{U}(0.6, 6.0)$
G1 light, F160W, Sérsic 2	e_1	$\mathcal{U}(-0.05, 0.10)$
G1 light, F160W, Sérsic 2	e_2	$\mathcal{U}(0.07, 0.25)$
G1 light, double Chameleon	$I_{0,\text{Chm1}}/I_{0,\text{Chm2}}$	$\mathcal{U}(0.2, 9.5)$

Continued on next page

Table 3.9 – *Continued from previous page*

Model component	Parameter	Prior
G1 light, Chameleon 1	w_c (arcsec)	$\mathcal{U}(0.00, 0.10)$
G1 light, Chameleon 1	w_t (arcsec)	$\mathcal{U}(0.20, 1.00)$
G1 light, Chameleon 1	e_1	$\mathcal{U}(-0.25, 0.25)$
G1 light, Chameleon 1	e_2	$\mathcal{U}(-0.25, 0.25)$
G1 light, Chameleon 2	w_c (arcsec)	$\mathcal{U}(0.01, 1.50)$
G1 light, Chameleon 2	w_t (arcsec)	$\mathcal{U}(2.50, 9.00)$
G1 light, Chameleon 2	e_1	$\mathcal{U}(-0.20, 0.20)$
G1 light, Chameleon 2	e_2	$\mathcal{U}(-0.20, 0.20)$
G2 light	θ_{eff} (arcsec)	$\mathcal{U}(0.25, 1.10)$
G2 light	n_s	$\mathcal{U}(2.0, 6.0)$
G2 light	θ_1^c (arcsec)	$\mathcal{U}(-1.60, -1.56)$
G2 light	θ_2^c (arcsec)	$\mathcal{U}(-0.97, -0.93)$
Image A	$\Delta\alpha$ (arcsec)	$\mathcal{U}(1.940, 1.948)$
Image A	$\Delta\delta$ (arcsec)	$\mathcal{U}(-1.576, -1.568)$
Image B	$\Delta\alpha$ (arcsec)	$\mathcal{U}(-1.819, -1.809)$
Image B	$\Delta\delta$ (arcsec)	$\mathcal{U}(0.263, 0.290)$
Image C	$\Delta\alpha$ (arcsec)	$\mathcal{U}(-1.935, -1.926)$
Image C	$\Delta\delta$ (arcsec)	$\mathcal{U}(-0.954, -0.940)$

Continued on next page

Table 3.9 – *Continued from previous page*

Model component	Parameter	Prior
Image D	$\Delta\alpha$ (arcsec)	$\mathcal{U}(0.096, 0.110)$
Image D	$\Delta\delta$ (arcsec)	$\mathcal{U}(1.385, 1.392)$
Differential dust extinction	τ_0^{F814W}	$\mathcal{U}(0.1, 2.0)$

CHAPTER 4

Improving time-delay cosmography with spatially resolved kinematics

This chapter was published as Shajib, A. J., T. Treu, & A. Agnello. 2018, MNRAS, 473, 210, and reproduced here with minor formatting changes.

4.1 Background

Our current understanding of cosmography, i.e. the description of geometry and kinematics of the Universe, has been largely acquired from the measurements of cosmic distances as a function of redshift. For example, relative luminosity distance measurements using Type Ia supernovae led to the discovery of dark energy (Riess et al. 1998; Perlmutter et al. 1999). More recently, baryon acoustic oscillation (BAO) in galaxy clustering has been used to determine angular diameter distances as a function of redshifts (Eisenstein et al. 2005; Alam et al. 2017).

Absolute distances, and the Hubble constant H_0 in particular, play a central role in cosmography. In fact, the uncertainty on H_0 is currently one of the main limiting factors in cosmological inferences based on the cosmic microwave background (CMB; e.g. Suyu et al. 2012; Weinberg et al. 2013). The tension between the recent measurement of the local value of H_0 to 2.4 per cent precision determined from Type Ia supernovae (Riess et al. 2016; Bernal et al. 2016), and that extrapolated from the CMB assuming a flat Λ cold dark matter (Λ CDM) cosmology highlights the importance of absolute distances. If the tension cannot

be explained as residual systematic uncertainties in one (or both) measurements, it may be an indication of new physics, like additional families of relativistic particles, departures from flatness, or dark energy that is not the cosmological constant (Riess et al. 2016). In this context, independent and precise measurements of absolute distances are needed to resolve this tension, and may be required in order to disprove conclusively the standard flat Λ CDM model.

Gravitational lens systems where the source is variable in time provide a powerful direct measurement of distances, that is completely independent of the local distance ladder and the CMB (Refsdal 1964). Substantial progress in data quality, monitoring campaigns, and modelling techniques over the past decade has finally allowed this technique to deliver on its promises (see Treu & Marshall 2016, for a historical perspective and a review of current methods). It has recently been shown that just three lenses are sufficient to determine H_0 to 3.8 per cent precision (e.g. Suyu et al. 2010, 2013; Bonvin et al. 2017), in Λ CDM.

The primary distance measurement is the so-called time-delay distance $D_{\Delta t}$, a multiplicative combination of the three angular diameter distances between the observer, the deflector, and the source. By combining the time-delay measurement with the stellar velocity dispersion measurements of the deflector, it is possible to measure also the angular diameter distance D_d to the deflector (Grillo et al. 2008; Paraficz & Hjorth 2009; Jee et al. 2015), thereby improving the constraints on the cosmological parameters (Jee et al. 2016).

In order to harness the power of strong lenses to constrain cosmography one needs to break two families of degeneracy. The first one is the mass-sheet degeneracy (MSD; Falco et al. 1985) and its generalizations (Schneider & Sluse 2013, 2014; Xu et al. 2016) that affect the interpretation of lensing observables. Breaking this degeneracy requires making appropriate physical assumptions on the mass profile of the main deflector (Xu et al. 2016) or on the properties of the source (Birrer et al. 2016), measuring the lensing effects along the line of sight (Suyu et al. 2010, 2013; Greene et al. 2013; Sluse et al. 2017; Rusu et al. 2017), and including as much non-lensing information as possible, especially stellar velocity dispersion

of the deflector (Treu & Koopmans 2002b; Koopmans et al. 2003; Suyu et al. 2010, 2013, 2014; Wong et al. 2017). The interpretation of stellar velocity dispersion data introduces the second degeneracy, known as the mass-anisotropy degeneracy (see, e.g. van der Marel 1994; Courteau et al. 2014, and references therein), whereby different combinations of mass profiles and stellar orbits can reproduce the same kinematic profiles. This holds especially for elliptical galaxies, which constitute most of the deflectors in strong lens samples. Even though lens galaxies and nearby ellipticals are on average consistent with simple density profiles and modest anisotropy (Koopmans et al. 2009; Barnabè et al. 2011; Agnello et al. 2014), there are significant system-to-system variations and appreciable systematic uncertainties. Also the exploration of different anisotropy profiles can affect the inference on the mass profile, privileging regions of parameters space where the inferred masses depend weakly on the anisotropy parameters (e.g. at large anisotropy radii, Agnello et al. 2014), a problem that is exacerbated by kinematic data within the half-light radius. The mass-anisotropy degeneracy is alleviated in the *virial regime* of large apertures (e.g. Treu & Koopmans 2002a; Agnello et al. 2013), so a combination of extended radial coverage and a tight control on systematics can be used to aid cosmography with lensing and stellar dynamics (e.g. Birrer et al. 2016).

Spatially resolved kinematics of galaxy scale lensed quasars is challenging with seeing limited observations, owing to the presence of bright quasar within the typical separation of the order of arcsecond. Diffraction limited spectroscopy is needed to make progress, either from the ground with the assistance of laser guide star adaptive optics (AO), or from space. Recent advances in AO technology and the imminent launch of the *James Webb Space Telescope* (*JWST*) make this kind of measurement feasible, and calls for a detailed investigation of its potential for cosmography.

In this paper, we investigate the improvements to time-delay cosmography that can be expected in the next few years by combining spatially resolved kinematics with lensing data. Unfortunately, state of the art modelling techniques are too computationally expensive at present to carry out a full-blown pixel-based analysis of a large number of mock systems.

Thus, in order to keep the computational cost manageable, we develop a framework to simulate and model mock lenses in a simplified and effective manner, but calibrated to yield realistic uncertainties as they would be obtained with a pixel-based analysis. We then apply these techniques to study the precision and accuracy that can be achieved on D_d and $D_{\Delta t}$ per system for plausible observational data quality that can be expected for current (e.g. OSIRIS on Keck, Larkin et al. 2006), imminent (NIRSPEC on *JWST*), and future (e.g. IRIS on the Thirty Metre Telescope (TMT), Wright et al. 2016) integral field spectrographs (IFSs). Finally, we use our results on the estimated precision of D_d and $D_{\Delta t}$ to forecast the cosmological precision that can be attained with the current sample of nine lenses for which accurate time delays and deep *Hubble Space Telescope* (*HST*) imaging data are available, and for a sample of 40 lenses that is expected to be completed in the next few years by a dedicated follow-up campaign of newly discovered lenses from ongoing wide field imaging surveys [e.g. the STRong lensing Insights into the Dark Energy Survey (STRIDES)¹].

Our work builds upon and extends previous work by Jee et al. (2016) in two important ways. First, we consider spatially resolved kinematics whereas Jee et al. (2016) focused on integrated quantities. As we will show, this aspect allows us to let anisotropy be a free parameter and show that the mass-anisotropy degeneracy can be overcome. Secondly, rather than assuming a target uncertainty on the two distances $D_{\Delta t}$, D_d [Jee et al. (2016) adopted a fiducial 5 per cent uncertainty on both], we derive them from realistic assumptions about the measurements exploring different scenarios corresponding to variation in data quality, e.g. effect of including kinematics, improved instrumental precision, and observing conditions. We then use these uncertainties to infer the attainable precisions on the cosmological parameters.

The structure of this chapter is as follows. In Section 4.2 we briefly review the strong gravitational lensing formalism and describe the mass models we used to simulate the deflec-

¹STRIDES is a Dark Energy Survey Broad External Collaboration; PI: Treu. <http://strides.astro.ucla.edu>

tor galaxy mass distribution. In Section 4.3 we describe the methods to create mock lensing and kinematic data from simulated strong lens systems. We present our results on the precision of the cosmological distances in Section 4.4 and forecast the cosmological parameter uncertainties in Section 4.5. We follow that with our discussion about the study and comparison with previous works in Section 4.6 and the limitations of this work in Section 4.7. Lastly, we conclude the paper with a summary in Section 4.8.

4.2 Model ingredients

Multiply-imaged quasars are ideal candidates for time-delay cosmography as the time delay can be measured by monitoring quasar variability. The deflector in such a system is usually an elliptical galaxy. In this section, we first present a brief review of the strong gravitational lensing formalism in Section 4.2.1. Then in Section 4.2.2 we describe the models we use to simulate realistic deflector mass distributions.

4.2.1 Strong gravitational lensing

In this subsection, we set the notation by briefly reviewing the theory of strong gravitational lensing (see Schneider et al. 2006, for a detailed description). Let us consider a strong gravitational-lens system with the deflector at the origin and the background source at β . Then, the image positions θ are given by the solutions of the lensing equation

$$\beta = \theta - \alpha(\theta), \quad (4.1)$$

where $\alpha(\theta) = \nabla_{\theta}\psi(\theta)$ is the deflection angle and ψ is the deflection potential. The dimensionless quantity convergence κ is defined as $\kappa(\theta) \equiv \Sigma(\theta)/\Sigma_{\text{cr}}$, where $\Sigma(\theta)$ is the projected surface mass density of the deflector and Σ_{cr} is the critical surface density for lensing given

by

$$\Sigma_{\text{cr}} = \frac{c^2}{4\pi G} \frac{D_s}{D_d D_{\text{ds}}}, \quad (4.2)$$

where D_s , D_d , and D_{ds} are the angular diameter distances between the observer and the source, between the observer and the deflector, and between the deflector and the source, respectively. The deflection potential is related to the convergence by the Poisson equation

$$\kappa(\boldsymbol{\theta}) = \frac{1}{2} \nabla_{\boldsymbol{\theta}}^2 \psi(\boldsymbol{\theta}). \quad (4.3)$$

The Einstein radius of the lens system is given by the solution of Equation (4.1) with $\beta = 0$ which is the case where the source lies directly behind the deflector. The Einstein radius can be expressed as

$$\theta_{\text{Ein}} = \sqrt{\frac{4GM(\theta_{\text{Ein}} D_d) D_{\text{ds}}}{c^2 D_s D_d}}, \quad (4.4)$$

where $M(r)$ is the enclosed mass of the deflector within a radius r .

The time delay between two images is

$$\Delta t_{ij} = \frac{D_{\Delta t}}{c} \left[\frac{1}{2} (\boldsymbol{\theta}_i - \boldsymbol{\beta})^2 - \frac{1}{2} (\boldsymbol{\theta}_j - \boldsymbol{\beta})^2 - \psi(\boldsymbol{\theta}_i) + \psi(\boldsymbol{\theta}_j) \right]. \quad (4.5)$$

Here $D_{\Delta t}$ is the time-delay distance given by

$$D_{\Delta t} = (1 + z_d) \frac{D_s D_d}{D_{\text{ds}}}, \quad (4.6)$$

where z_d is the redshift of the deflector.

The mass-sheet transformation (MST; Falco et al. 1985)

$$\kappa(\theta) \rightarrow \kappa'(\theta) = (1 - \lambda) + \lambda \kappa(\theta), \quad (4.7)$$

$$\beta \rightarrow \beta' = \lambda \beta \quad (4.8)$$

leaves the image positions invariant. The additive term $(1 - \lambda)$ can be internal to the deflector mass distribution affecting the time delay and the velocity dispersion as

$$\Delta t' = \lambda \Delta t, \quad (4.9)$$

$$\sigma'_* = \sqrt{\lambda} \sigma_*.$$

Furthermore, this additive term can be due to the line-of-sight structures external to the deflector mass distribution, quantified as the external convergence $\kappa_{\text{ext}} = 1 - \lambda_{\text{ext}}$, which only affects the time-delay. Schneider & Sluse (2013) point out that assuming a power-law profile for the deflector mass distribution breaks the MSD as the MST of a power law is not a power law. Therefore, it is necessary to consider more flexible models for the deflector mass distribution or families of mass models connected by the source-position transformation (SPT; Schneider & Sluse 2014) to obtain unbiased measurements of the cosmological parameters.

4.2.2 Deflector mass model

We need to model the mass distribution of the deflector in order to compute spatially resolved kinematics of the deflector and lensing data of the background source. We require this model to be realistic, yet simple enough to be computationally efficient to create mock data for numerous realizations of a lens system while performing the Bayesian inference. Therefore, for simplicity we assume spherically symmetric mass profiles for the deflector instead of elliptical mass profiles. This assumption simplifies many computational tasks by reducing a number of two-dimensional problems to only one-dimensional, namely the radial, ones. Naturally, real lenses are typically not spherical, so our spherical models are not intended literally, but to be representative of non-spherical models, after marginalization over all the non-spherical parameters. As we shall see in Section 4.3 we will tune the uncertainties in our spherical models so as to effectively reproduce the uncertainty of non-spherical models.

Following standard practice (e.g. Treu & Koopmans 2002b; Suyu et al. 2014), we describe the mass distribution of the deflector using two components: dark matter and luminous matter, where the luminous matter resides within a dark matter halo. We choose the Navarro-Frenk-White (NFW) profile (Navarro et al. 1996) for the dark matter distribution and Jaffe profile (Jaffe 1983) for the luminous matter distribution. It is empirically known that the total mass distribution in a galaxy, as a combination of the dark matter and lumi-

nous matter distributions, closely follows an isothermal profile, which is a power-law profile with the power-law slope $\gamma \approx 2$ (Treu & Koopmans 2004; Koopmans 2006; Koopmans et al. 2009; Auger et al. 2010b; Dutton & Treu 2014).

4.2.2.1 NFW profile

The NFW profile describes the mass distribution in the dark matter haloes as suggested by cosmological N -body simulations (Navarro et al. 1996, 1997). The spherical NFW profile has the form

$$\rho(r) = \frac{\rho_s}{(r/r_s)(1 + r/r_s)^2}, \quad (4.10)$$

where ρ_s and r_s are the scale density and radius, respectively. The convergence κ implied by this mass profile is (Bartelmann 1996)

$$\kappa(\theta) = \frac{2\kappa_s}{(x^2 - 1)} [1 - \mathcal{F}(x)], \quad (4.11)$$

where $x = \theta D_d/r_s$, $\kappa_s = \rho_s r_s/\Sigma_{cr}$ is the scale convergence, and the function $\mathcal{F}(x)$ is given by

$$\mathcal{F}(x) = \begin{cases} \sec^{-1}(x)/\sqrt{x^2 - 1} & (x > 1), \\ 1 & (x = 1), \\ \operatorname{sech}^{-1}(x)/\sqrt{1 - x^2} & (x < 1). \end{cases} \quad (4.12)$$

The deflection angle for the NFW profile can be derived as (Meneghetti et al. 2003)

$$\alpha(\theta) = \frac{2}{\theta} \int^\theta \theta' \kappa(\theta') d\theta' = \frac{4\kappa_s \theta_s}{x} [\ln(x/2) + \mathcal{F}(x)], \quad (4.13)$$

where $\theta_s = r_s/D_d$. The deflection potential for the NFW profile is then

$$\psi(\theta) = \int \alpha(\theta) d\theta = 2\kappa_s \theta_s^2 \left[\log^2 \left(\frac{x}{2} \right) + (x^2 - 1) \mathcal{F}^2(x) \right]. \quad (4.14)$$

4.2.2.2 Jaffe profile

The Jaffe profile is given by

$$\rho(r) = \frac{\rho_s}{(r/r_s)^2 (1 + r/r_s)^2}, \quad (4.15)$$

where ρ_s and r_s are the scale density and radius, respectively. This profile reproduces well the $R^{1/4}$ surface brightness profile in projection with $r_s = R_{\text{eff}}/0.763$, where R_{eff} is the effective radius. The convergence for the Jaffe profile is given by (Jaffe 1983)

$$\kappa(\theta) = \kappa_s \left[\frac{\pi}{x} + 2 \frac{1 - (2 - x^2)\mathcal{F}(x)}{1 - x^2} \right], \quad (4.16)$$

where $x = \theta D_d / r_s$, $\kappa_s = \rho_s r_s / \Sigma_{\text{cr}}$ is the scale convergence, and $\mathcal{F}(x)$ is given in Equation (4.12). The deflection angle for the Jaffe profile can be derived as (Bartelmann & Meneghetti 2004)

$$\alpha(\theta) = 2\kappa_s \theta_s [\pi - 2x\mathcal{F}(x)], \quad (4.17)$$

where $\theta_s = r_s / D_d$. The deflection potential that reproduces the convergence in Equation (4.16) is

$$\psi(\theta) = 2\kappa_s \theta_s^2 [\pi x + \log(x^2) - 2(x^2 - 1)\mathcal{F}(x)]. \quad (4.18)$$

4.2.2.3 Power-law mass profile

The elliptical power-law model is often used to describe galaxy scale lenses (e.g. Suyu et al. 2013). In order to calibrate the uncertainty in our models we use the spherical power law mass density profile as a baseline comparison. This mass density profile is given by

$$\rho(r) = \rho_0 \left(\frac{r}{r_0} \right)^{-\gamma}. \quad (4.19)$$

The deflection angle for the power law mass profile is given by

$$\alpha(\theta) = \left(\frac{\theta_{\text{Ein}}}{\theta} \right)^{\gamma-2} \theta_{\text{Ein}}, \quad (4.20)$$

where θ_{Ein} is the Einstein radius.

4.3 Creating mock data

In order to measure D_d and $D_{\Delta t}$, three sets of data are necessary: (1) imaging data of the lensed images of the quasar and its host galaxy, (2) time delays from a monitoring campaign,

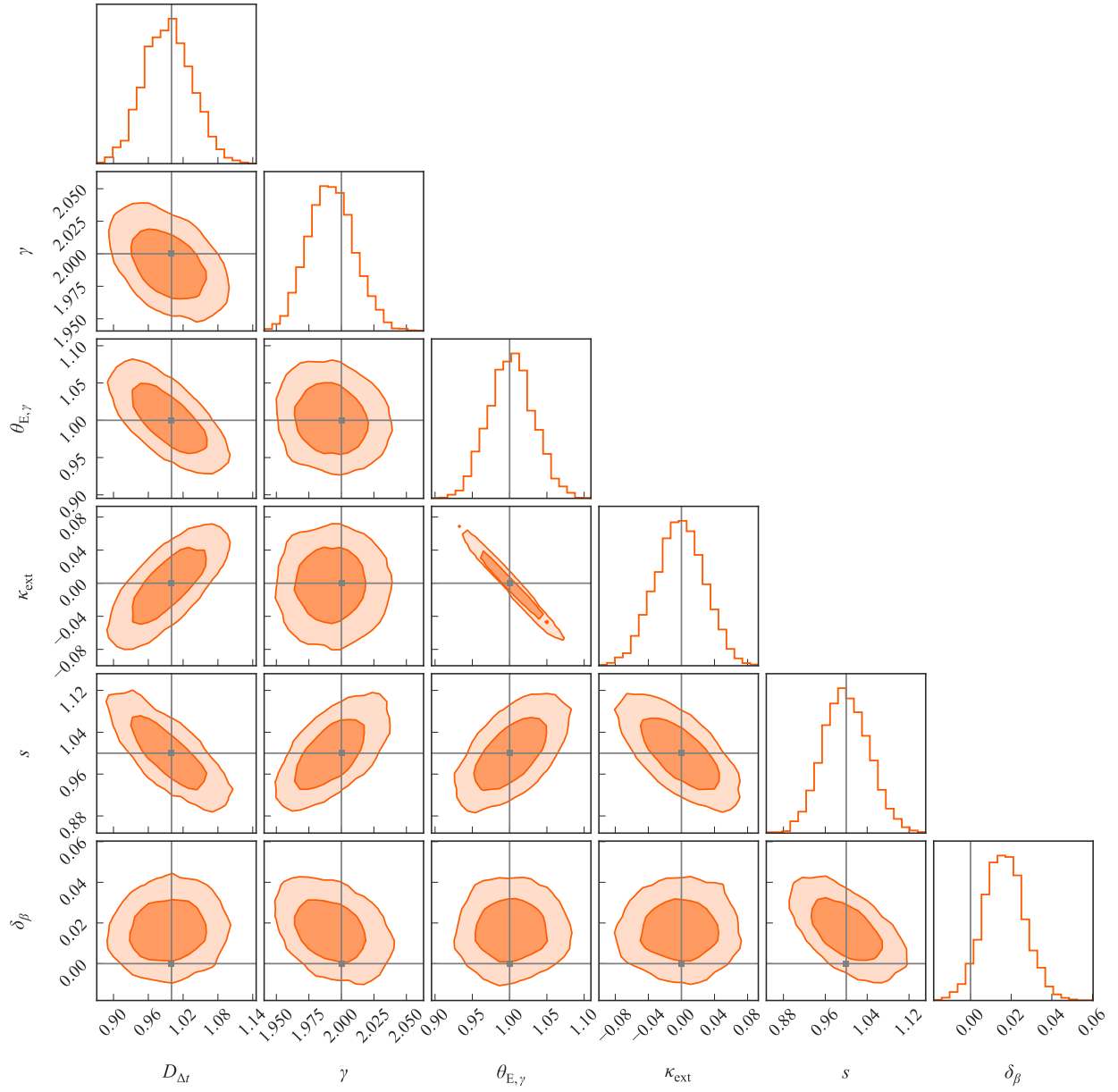


Figure 4.1: Posterior PDF of the model parameters for a power-law mass profile inferred from lensing data with 230 conjugate points. $D_{\Delta t}$, $\theta_{E,\gamma}$, and δ_β are normalized with $D_{\Delta t}^{\text{fiducial}}$, θ_E , and θ_E , respectively, where θ_E is the true Einstein radius of the lens system. Grey lines show the true values of the parameters and orange contours show the 1σ and 2σ confidence regions. The uncertainty on the power-law slope is $\delta\gamma = 0.02$ and the time-delay distance $D_{\Delta t}$ is simultaneously estimated with 4.2 per cent uncertainty for an assumed Gaussian prior with 3 per cent uncertainty on $(1 - \kappa_{\text{ext}})$.

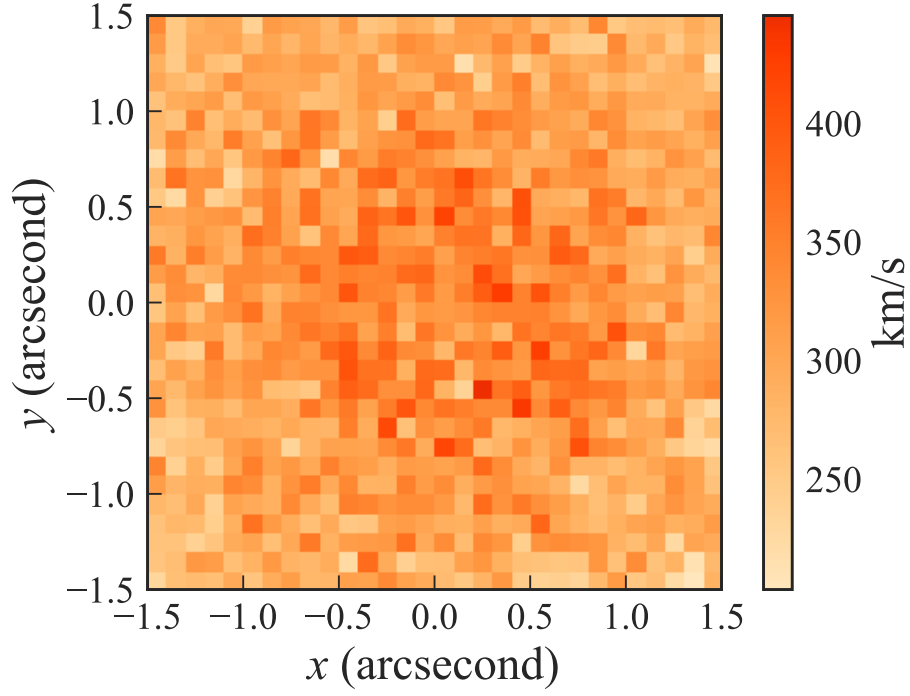


Figure 4.2: Line-of-sight velocity dispersion for a combination of NFW (dark component) and Jaffe (luminous component) profiles. 5 per cent random Gaussian noise was added to the velocity dispersion and it was smoothed with a Gaussian of FWHM=0.1 arcsec to take the effect of seeing into account.

and (3) kinematics of the deflector. In this section we describe how we create mock data of each kind for a given strong lens system. First, in Section 4.3.1 we describe how we use a set of conjugate points to mimic the detailed modelling of the lensed quasar host, which would be otherwise too computationally expensive to carry out for large number of systems. Then, in Section 4.3.2 we describe how we create the full simulated data sets.

4.3.1 Mimicking extended source reconstruction with conjugate points

For the sake of speed, instead of carrying out a full extended source reconstruction analysis, we describe each extended source as a set of points, and analyse them with the so-called conjugate point techniques (Gavazzi et al. 2008). In order to obtain realistic results, we need to determine how many points to simulate and the associated astrometric uncertainty we want to associate with each one. The amount of information depends on both quantities, so we start by setting the latter and then adjust the former to obtain a realistic precision. Computing time depends on the number of points, so we adopt the smallest number that allows us to achieve realistic precision on the model parameters while keeping the computing time short enough for our purposes. In order to calibrate our model we focus on the slope of the mass density profile of a power-law mass model, which is the main parameter controlling the velocity dispersion and time delay at a fixed *Einstein* radius (e.g. Wucknitz 2002; Suyu et al. 2012). Thus, the minimum number of necessary source point is chosen such that, for a power-law deflector mass profile given in Equation (4.19), the power-law exponent can be inferred from the set of conjugate points with an uncertainty $\delta\gamma \sim 0.02$. We set this criterion to match with the precision on power-law slope γ attainable by current (Suyu et al. 2013; Wong et al. 2017) and future technologies (Meng et al. 2015) from a full-blown computationally intensive lens modelling effort.

We used a set of uniformly spaced points within a circle with 20 mas minimum separation between neighbouring points to mimic an extended source. We assumed a power law mass profile given in Equation (4.19) for the deflector and created mock image data for the given

source points. We set the uncertainty in the image position as $\sigma_\theta = 60$ mas (corresponding to approximately half a pixel on the *HST* Wide Field Camera 3 infrared channel). The mock lens system in our analysis only produces two lensed images due to the assumed spherical symmetry. In doubly-imaged lens systems, there is a degeneracy between the power-law slope γ and the Einstein radius θ_{Ein} for asymmetric lens configurations whereas θ_{Ein} is completely independent of γ for a perfectly symmetric lens configuration (Suyu et al. 2012). Therefore, the number of conjugate points with fixed positional uncertainty needed to achieve a particular $\delta\gamma$ by breaking this degeneracy depends on the asymmetry of the lens configuration. We fix $\beta_{\text{centre}} = \theta_{\text{Ein}}/2$ for the rest of this study which is the case in the middle between the two extremes of perfect symmetry and maximal asymmetry.

We tuned this setup to give realistic errors on model parameters by analysing mock data to obtain the posterior probability distribution function (PDF) of the model parameters: the power law slope of the mass profile γ , the Einstein radius θ_{Ein} , and the source-point positions β . From Bayes' theorem, the posterior PDF follows

$$P(\gamma, \theta_{\text{Ein},\gamma}, \beta, \kappa_{\text{ext}} | \boldsymbol{\theta}) \propto P(\boldsymbol{\theta} | \gamma, \theta_{\text{Ein},\gamma}, \beta, \kappa_{\text{ext}}) P(\gamma, \theta_{\text{Ein},\gamma}, \beta, \kappa_{\text{ext}}), \quad (4.21)$$

where $\boldsymbol{\theta}$ is the mock data for image positions, $\theta_{\text{Ein},\gamma}$ is the Einstein radius for the power-law mass profile, and κ_{ext} is the external convergence. The first term on the right-hand side is the likelihood of the data given the model parameters, and the second one is the prior PDF of the model parameters.

To sample from the posterior PDF through the Markov Chain Monte Carlo (MCMC) method, we use the COSMOHAMMER package (Akeret et al. 2013), which embeds EMCEE (Foreman-Mackey et al. 2013), a PYTHON implementation of an affine-invariant ensemble sampler for MCMC proposed by Goodman & Weare (2010). We first find the maxima of the likelihood function for the given image positions treating the source-point positions uncorrelated using the particle swarm optimization routine (Kennedy & Eberhart 1995) included in COSMOHAMMER. We tuned the settings of the optimization process to find the maxima with ~ 99 per cent accuracy. We then treat the source-point positions at the the

Table 4.1: Priors for joint analysis with power-law mass profile

Parameter	Prior
$D_{\Delta t}$	Uniform in $[0, 2] \times D_{\Delta t}^{\text{fiducial}*}$
γ	Uniform in $[1, 3]$
$\theta_{\text{Ein}, \gamma}$	Uniform in $[0.5, 2]$ arcsec
κ_{ext}	Gaussian with 3 per cent uncertainty on $(1 - \kappa_{\text{ext}})$
s	Uniform in $[0, 2]$
δ_{β}	Uniform in $[-0.5, 0.5]$ arcsec

* $D_{\Delta t}^{\text{fiducial}}$ is the fiducial value of the time-delay distance.

maxima of the likelihood function as the reconstructed source. We sample from the posterior PDF of the source-point positions as

$$\boldsymbol{\beta}_{\text{sampled}} = s\boldsymbol{\beta}_{\text{reconstructed}} + \delta_{\beta}, \quad (4.22)$$

using two parameters: a rescaling factor s for the source plane, and an offset δ_{β} . Equation (4.22) is essentially a SPT (Schneider & Sluse 2014)

$$\boldsymbol{\beta} \rightarrow \boldsymbol{\beta}' = [1 + f(\boldsymbol{\beta})]\boldsymbol{\beta}, \quad (4.23)$$

which is a generalization of the MST and leaves the strong lensing properties invariant. This allows us to incorporate the degeneracies induced by the SPT into our model.

We impose a Gaussian prior with 3 per cent uncertainty for $(1 - \kappa_{\text{ext}})$ and uniform priors in appropriately large ranges for all the other parameters. The details of the chosen priors are given in Table 4.1. After performing this analysis for various numbers of source points, we find that the uncertainty of the power law exponent achieves our target $\delta\gamma \sim 0.02$ for a source with 230 points (Figure 4.1). In comparison, a conservative choice of $\delta\gamma \sim 0.04$ can be achieved by adopting a source with 130 points. We also jointly sample the posterior PDF of the time-delay distance $D_{\Delta t}$ by adding a mock time-delay measurement to the data set.

The posterior PDF of the joint analysis is

$$\begin{aligned} P(X|\boldsymbol{\theta}, \Delta t) &\propto P(\boldsymbol{\theta}, \Delta t|X)P(X) \\ &\propto P(\boldsymbol{\theta}|X)P(\Delta t|X)P(X), \end{aligned} \quad (4.24)$$

where X are the model parameters $\{D_{\Delta t}, \gamma, \theta_{\text{Ein}, \gamma}, \kappa_{\text{ext}}, s, \delta_{\beta}\}$. The second line in Equation (4.24) is implied because the image positions and the time-delay data are independent measurements. The marginalized uncertainty of $D_{\Delta t}$ from the joint analysis is 4.2 per cent which is comparable to the state of the art measurements of the time-delay distance (Suyu et al. 2013; Wong et al. 2017) after taking the difference in the uncertainty of κ_{ext} into account. We thus conclude that the analysis of 230 correlated points with positional uncertainty 60 mas with a spherical model approximates well the extended source reconstruction with a non-spherical model as far as the main parameters controlling D_{d} and $D_{\Delta t}$ are concerned. Therefore, we adopt this setup when we analyse two component mass models.

4.3.2 Mock lensing data with spatially resolved velocity dispersion

We choose a composite mass model for the deflector galaxy assuming the NFW profile for the dark matter component and the Jaffe profile for the luminous matter component.

We assumed that in projection one-third of the total mass comes from the dark matter component within half of the half-light radius (Auger et al. 2010b), to obtain the normalizations for the NFW and Jaffe profiles.

First, we created mock lensing data for 230 conjugate points for the adopted deflector mass profile. Random Gaussian noise with standard deviation $\sigma_{\theta} = 60$ mas was added to the conjugate point positions.

The velocity dispersion profile for a mass distribution can be obtained by solving the spherical Jean's equation, which is given by

$$\frac{1}{l(r)} \frac{d(l\sigma_r^2)}{dr} + 2\beta_{\text{ani}}(r) \frac{\sigma_r^2}{r} = -\frac{GM(\leq r)}{r^2}. \quad (4.25)$$

Here, $l(r)$ is the luminosity density of the galaxy, σ_r is the radial velocity dispersion and $\beta_{\text{ani}}(r)$ is the anisotropy profile given by

$$\beta_{\text{ani}} = 1 - \frac{\sigma_t^2}{\sigma_r^2}, \quad (4.26)$$

where σ_t is the tangential velocity dispersion for a spherically symmetric mass distribution. The surface-brightness-weighted, line-of-sight velocity dispersion can be obtained by solving this equation as (Mamon & Łokas 2005)

$$I(R)\sigma_{\text{los}}^2(R) = 2G \int_R^\infty k\left(\frac{r}{R}, \frac{r_{\text{ani}}}{R}\right) l(r)M(r) \frac{dr}{r}, \quad (4.27)$$

where $I(R)$ is the surface brightness. For Osipkov-Merritt anisotropy parameter $\beta_{\text{ani}}(r) = 1/(1 + r_{\text{ani}}^2/r^2)$ (Osipkov 1979; Merritt 1985a,b), the function $k(u, u_{\text{ani}})$ is given by

$$\begin{aligned} k(u, u_{\text{ani}}) = & \frac{u_{\text{ani}}^2 + 1/2}{(u_{\text{ani}}^2 + 1)^{3/2}} \left(\frac{u^2 + u_{\text{ani}}^2}{u} \right) \tan^{-1} \sqrt{\frac{u^2 - 1}{u_{\text{ani}}^2 + 1}} \\ & - \frac{1/2}{u_{\text{ani}}^2 + 1} \sqrt{1 - 1/u^2}. \end{aligned} \quad (4.28)$$

Using Equation (4.27), we computed the line-of-sight velocity dispersion weighted by surface brightness in a given bin size (e.g. 0.1 arcsec). To take seeing into account, we convolved the surface-brightness-weighted line-of-sight velocity dispersion image with a Gaussian kernel of a given full width at half-maximum (FWHM) and then normalized it to obtain the line-of-sight velocity dispersion as

$$\tilde{\sigma}_{\text{los}}^2(x, y) = \frac{I\sigma_{\text{los}}^2 * g(x, y)}{I * g(x, y)}, \quad (4.29)$$

where $g(x, y)$ is a two-dimensional Gaussian function, and the symbol ‘ $*$ ’ denotes the convolution (Figure 4.2). Finally, we added random Gaussian noise with a given standard deviation to each pixel. We also added a random Gaussian noise with 2 per cent standard deviation to the time delay, typical of the best measurements (e.g. Bonvin et al. 2017).

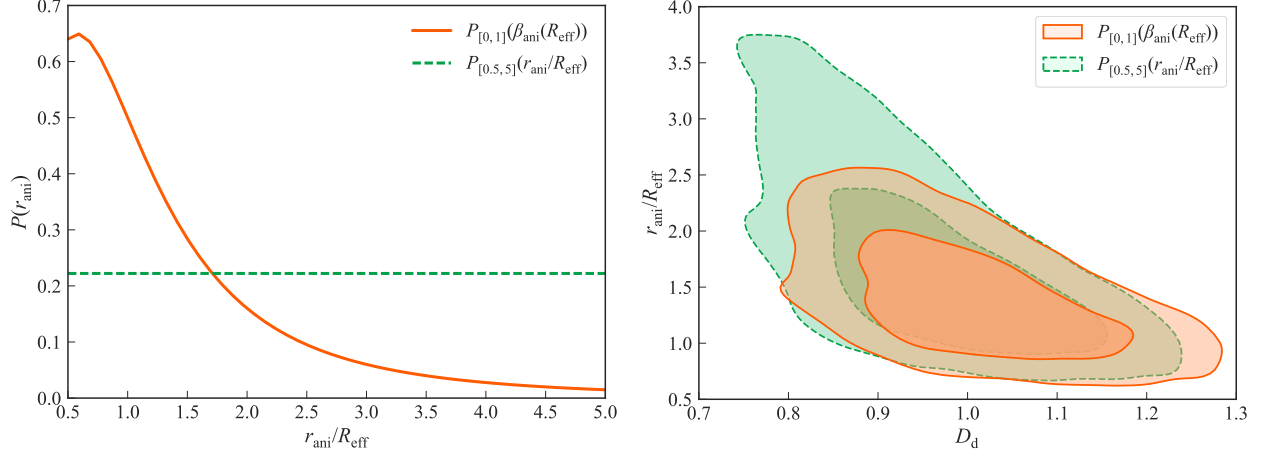


Figure 4.3: Priors for the anisotropy radius r_{ani} (left) and their effects on the mass-anisotropy degeneracy breaking (right). The two chosen priors are uniform prior for r_{ani} in $[0.5, 5] \times R_{\text{eff}}$ [labelled $P_{[0.5,5]}(r_{\text{ani}}/R_{\text{eff}})$, solid] and uniform prior for $\beta_{\text{ani}}(R_{\text{eff}})$ in $[0, 1]$ [labelled $P_{[0,1]}(\beta_{\text{ani}}(R_{\text{eff}}))$, dashed]. In the right plot, the contours represent 1σ and 2σ confidence regions and D_d is normalized with D_d^{fiducial} . $P_{[0,1]}(\beta_{\text{ani}}(R_{\text{eff}}))$ puts more weight in the region $r_{\text{ani}}/R_{\text{eff}} < 2$, where the assumed value of r_{ani} in our model lies, in comparison with $P_{[0.5,5]}(r_{\text{ani}}/R_{\text{eff}})$ and it leads to a more unbiased and constrained estimate of the angular diameter distance D_d .

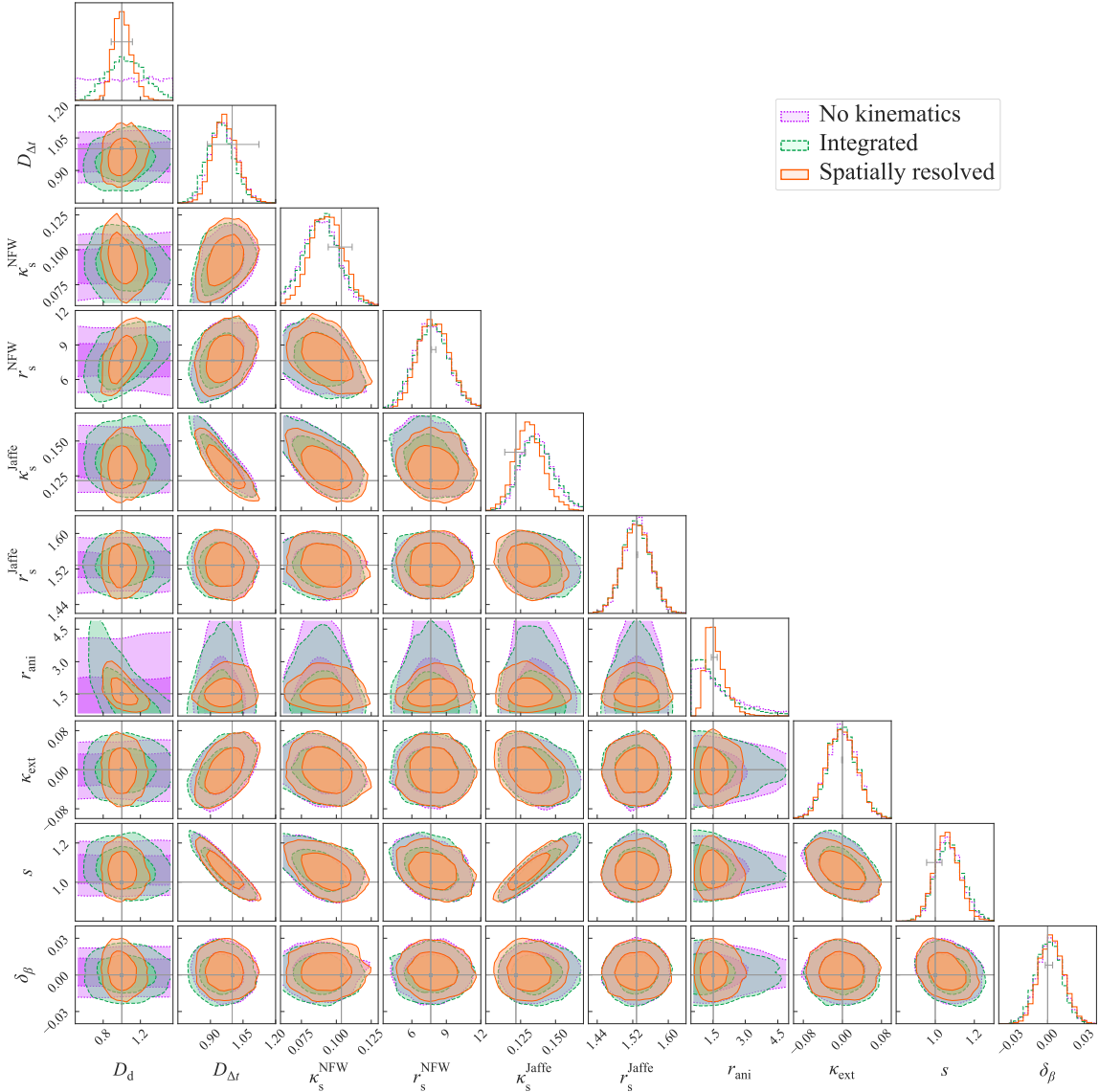


Figure 4.4: Posterior PDF of the model parameters given from joint analysis with lensing and time delay data with spatially resolved kinematics (solid), with integrated kinematics (dashed), and without any kinematics (dotted). The contours for each case represent 1σ and 2σ confidence regions. The model parameters D_d , $D_{\Delta t}$, r_s^{NFW} , r_s^{Jaffe} , r_{ani} , and δ_β are normalized with D_d^{fiducial} , $D_{\Delta t}^{\text{fiducial}}$, R_{Ein} , R_{Ein} , R_{Ein} , and θ_{Ein} , respectively, where R_{Ein} is the true Einstein radius with the dimension of length. Grey solid lines show the true values of the parameters. D_d can only be determined with kinematics. The anisotropy radius r_{ani} is also well determined with kinematics showing that the mass-anisotropy degeneracy is overcome.

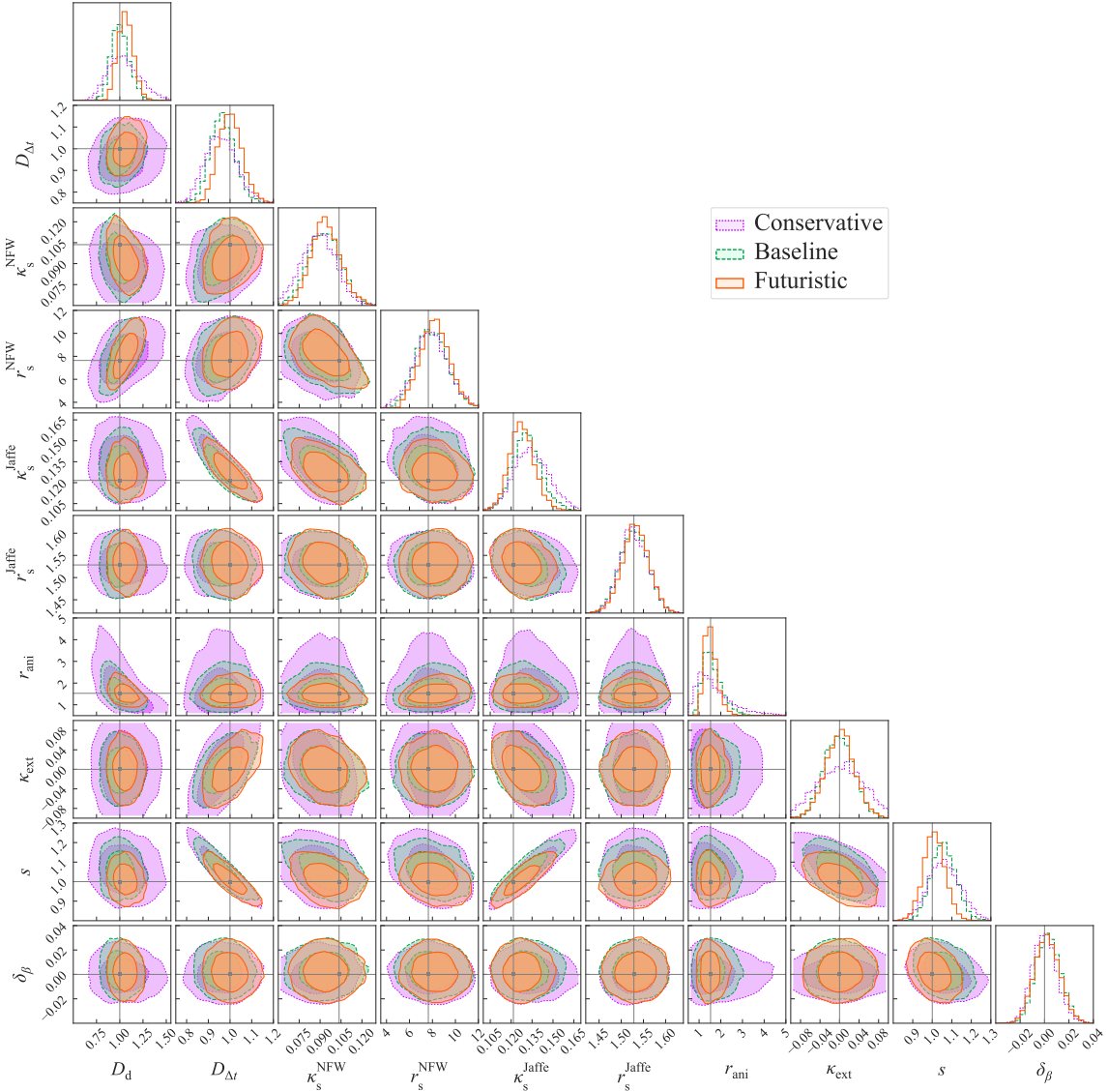


Figure 4.5: Posterior PDF of the model parameters given from joint analysis with lensing and time delay data with spatially resolved kinematics for baseline (dashed), futuristic (solid), and conservative (dotted) setups. The contours for each case represent 1σ and 2σ confidence regions. The model parameters D_d , $D_{\Delta t}$, r_s^{NFW} , r_s^{Jaffe} , r_{ani} , and δ_β are normalized with D_d^{fiducial} , $D_{\Delta t}^{\text{fiducial}}$, R_{Ein} , R_{Ein} , R_{Ein} , and θ_{Ein} , respectively, where R_{Ein} is the true Einstein radius with the dimension of length. Grey solid straight lines show the true values of the parameters. The constraints on the model parameters become tighter with higher quality of spatially resolved stellar kinematics.

4.4 Precision on Cosmological Distance Measurements

In this section we use the mock data created as described in the previous section to estimate the uncertainties of the angular diameter and time-delay distances using the MCMC method.

We performed a joint analysis to obtain the posterior PDF of the model parameters X given the mock lensing data with velocity dispersion and the time delay data. From Bayes' theorem, the posterior PDF follows

$$P(X|\boldsymbol{\theta}, \boldsymbol{\sigma}_*, \Delta t) \propto P(\boldsymbol{\theta}, \boldsymbol{\sigma}_*, \Delta t|X)P(X), \quad (4.30)$$

where $P(\boldsymbol{\theta}, \boldsymbol{\sigma}_*, \Delta t|X)$ is the likelihood of the data given the model parameters, $P(X)$ is the prior PDF of the model parameters, $\boldsymbol{\theta}$ is the image position data, $\boldsymbol{\sigma}_*$ is the velocity dispersion data, Δt is the time delay between images, and X contains all the model parameters $\{D_d, D_{\Delta t}, \kappa_s^{\text{NFW}}, r_s^{\text{NFW}}, \kappa_s^{\text{Jaffe}}, r_s^{\text{Jaffe}}, r_{\text{ani}}, \kappa_{\text{ext}}, \boldsymbol{\beta}\}$. As the image positions, the velocity dispersion, and the time delay are independent data, the likelihood of the data given the model parameters can be written as

$$P(\boldsymbol{\theta}, \boldsymbol{\sigma}_*, \Delta t|X) = P(\boldsymbol{\theta}|X)P(\boldsymbol{\sigma}_*|X)P(\Delta t|X). \quad (4.31)$$

As it is often the case in high dimensional spaces, it is important to choose the priors carefully (e.g. Brewer et al. 2014). If the priors are not carefully chosen, the marginalized one-dimensional posteriors on each parameter can be significantly skewed (e.g. Birrer et al. 2016), resulting in the median and mode of the PDF to be a biased estimator of the true value. Naturally this bias can be mitigated or eliminated by using the full PDF and not just point estimators. However, it is important to use priors that are as informative as possible. We impose Gaussian priors on r_s^{Jaffe} and κ_{ext} , as r_s^{Jaffe} can be measured directly by fitting the surface brightness profile of the lens, whereas κ_{ext} can be inferred indirectly by comparing the statistics of galaxies along the line of sight to the lens with simulated light cones (Hilbert et al. 2009; Suyu et al. 2013; Greene et al. 2013; Collett et al. 2013; Rusu et al. 2017). We set a Gaussian prior for r_s^{NFW} with 20 per cent uncertainty (Table 4.2). Note, this is a

Table 4.2: Priors for joint analysis with composite mass model

Parameter	Prior
D_d	Uniform in $[0, 2] \times D_d^{\text{fiducial}}$ *
$D_{\Delta t}$	Uniform in $[0, 2] \times D_{\Delta t}^{\text{fiducial}}$ *
κ_s^{NFW}	Jeffrey's prior
r_s^{NFW}	Gaussian with 20 per cent uncertainty
κ_s^{Jaffe}	Jeffrey's prior
r_s^{Jaffe}	Gaussian with 2 per cent uncertainty
r_{ani}	Uniform prior for β_{ani} in $[0, 1]$
κ_{ext}	Gaussian prior on $(1 - \kappa_{\text{ext}})$
s	Uniform in $[0, 2]$
δ_β	Uniform in $[-0.5, 0.5]$ arcsec

* D_d^{fiducial} and $D_{\Delta t}^{\text{fiducial}}$ are the fiducial values of the angular diameter distance to the deflector and the time-delay distance.

conservative choice comparing to the 14 per cent uncertainty adopted by Wong et al. (2017) based on the results of Gavazzi et al. (2007). We choose Jeffrey's prior $P(\xi) \propto 1/\xi$ for κ_s^{NFW} and κ_s^{Jaffe} . We tested two prior choices for r_{ani} : (a) uniform in $[0.5, 5] \times R_{\text{eff}}$ (hereafter referred to as $P_{[0.5,5]}(r_{\text{ani}}/R_{\text{eff}})$, as used in Suyu et al. 2012; Birrer et al. 2016; Wong et al. 2017), and (b) a uniform prior for $\beta_{\text{ani}}(R_{\text{eff}})$ in $[0, 1]$ (hereafter referred as $P_{[0,1]}(\beta_{\text{ani}}(R_{\text{eff}}))$). $P_{[0,1]}(\beta_{\text{ani}}(R_{\text{eff}}))$ puts more weight in the region $r_{\text{ani}}/R_{\text{eff}} < 2$, where the assumed value of r_{ani} in our model lies, in comparison with $P_{[0.5,5]}(r_{\text{ani}}/R_{\text{eff}})$ and it results in a more unbiased and constrained estimate of the angular diameter distance D_d (Figure 4.3). Adopting a more restricting uniform prior for r_{ani} in $[0.5, 2] \times R_{\text{eff}}$ produces a similar constraint on D_d as the one by adopting $P_{[0,1]}(\beta_{\text{ani}}(R_{\text{eff}}))$. We set $P_{[0,1]}(\beta_{\text{ani}}(R_{\text{eff}}))$ as the prior for r_{ani} for the rest of this study.

We have examined the effect of having spatially resolved velocity dispersion data on the uncertainties of the model parameters by studying three cases: (1) without any kinematics, (2) with integrated velocity dispersion data of the deflector within 1.2 arcsec radius, and (3) with spatially resolved velocity dispersion data. We adopted three observational settings, which reflect variation in qualities of observation instruments and conditions. These settings are (1) “baseline”: representative of the resolution and precision that can be achieved with integral field spectrographs (IFSs) on current and upcoming instruments, e.g. OSIRIS on Keck or NIRSPEC on the *JWST*, with the precision on the velocity dispersion and the external convergence that can be expected in the best cases, (2) “conservative”: same as baseline but with conservative precision on the velocity dispersion and the external convergence, and (3) “futuristic”: for IFSs on upcoming extremely large telescopes, e.g. IRIS on Thirty Meter Telescope (TMT) (Table 4.3). It is beyond the scope of this paper to estimate the amount of exposure time required to meet these goals for each one of the instrumental setups and to analyse the sources of systematic uncertainties. This exploration is left for future work.

As expected, D_d can only be measured by adding the stellar kinematic information to the lensing and time-delay data (Figure 4.4). When integrated stellar kinematics is added, the anisotropy radius r_{ani} is not constrained due to the mass-anisotropy degeneracy. Given our parametrization and assumptions, D_d absorbs most of the improvement after adding the integrated stellar kinematics, since the precision of $D_{\Delta t}$ is limited by the assumed priors on time delay and external convergence. If one were to consider more flexible models, the gain would be even more significant, highlighting the importance of kinematics. In the real world of course, having additional information is not only helpful for improving the precision but also for checking for systematics and improving the accuracy. Using spatially resolved velocity dispersion data can improve uncertainty on D_d from ~ 20 to ~ 10 per cent for the baseline setup and from ~ 27 to ~ 17 per cent for the conservative setup with respect to using integrated velocity dispersion data (Figure 4.5). Moreover, the anisotropy radius r_{ani} is well-determined only when spatially resolved kinematics is introduced (Figure 4.4), which

demonstrates that spatially resolved kinematics help break the mass-anisotropy degeneracy and allow us to use the anisotropy radius r_{ani} as a free parameter. For our adopted lensing data quality equivalent to $\delta\gamma \sim 0.02$, the lens model parameters are limited by modelling uncertainties, thus the addition of the spatially resolved kinematics improves the constraints only by ~ 1 per cent. If we adopt a conservative lensing data quality equivalent to $\delta\gamma \sim 0.04$, the addition of the spatially resolved kinematics leads to more relative improvement in the constraints on the model parameters, e.g. uncertainty on $D_{\Delta t}$ improves by ~ 3 per cent compared to the case with only integrated kinematics. In comparison to our adopted lensing data quality ($\delta\gamma \sim 0.02$), this conservative lensing data quality worsens the constraint $D_{\Delta t}$ by ~ 2 per cent (from ~ 6 to ~ 8 per cent). The constraint on D_d does not significantly change (within 1 per cent), as D_d is limited by the quality of the stellar kinematics data. The uncertainties on D_d and $D_{\Delta t}$ for different data sets and observational setups are summarized in Table 4.4.

To check for bias in point estimators of the model parameters, we performed 25 joint analyses for different noise realizations using the same lensing parameters with the “baseline” setup. The 1σ regions of the parameter estimates from these analyses are shown in with horizontal error bars in the one-dimensional histograms of Figure 4.4. All the point estimators of the model parameters are within 1σ of the true values. We note however, that it is highly preferable to not adopt point estimators of individual parameters, but rather take into account the full (asymmetric) posterior PDF.

Table 4.3: Parameters for different observational setups.

Observational setup [*]	Annulus width	$N_{\text{annuli}}^{\dagger}$	PSF FWHM	Parameter uncertainties				
				a_{Jaffe}	$1 - \kappa_{\text{ext}}$	Δt	σ_*	θ
	(arcsecond)		(arcsecond)	(per cent)	(per cent)	(per cent)	(per cent)	(mas)
Baseline	0.1	12	0.1	2	3	2	5	60
Conservative	0.2	6	0.1	2	5	2	10	60
Futuristic	0.05	24	0.03	2	3	2	5	60

^{*} The “baseline” and “conservative” setups represent what we can expect to obtain with current and upcoming diffraction limited IFSs, e.g. OSIRIS on Keck and NIRSPEC on *JWST*. The “futuristic” setup is for diffraction-limited IFSs on upcoming extremely large telescopes, e.g. TMT or E-ELT.

[†] N_{annuli} refers to the number of annuli for the spatially resolved kinematics for each observational setup.

Table 4.4: Uncertainties of D_d and $D_{\Delta t}$ for a single lens with different observational setups.

Model	Kinematics data	σ_{D_d} (per cent)	$\sigma_{D_{\Delta t}}$ (per cent)
	No	-	6.5
Baseline	Integrated	19.8	6.5
	Resolved	9.6	5.8
Conservative	Integrated	27.0	7.8
	Resolved	16.7	7.5
Futuristic	Resolved	7.7	5.3

Table 4.5: Cosmological models and parameter priors.

Model name	Description	Priors
Λ CDM	Flat Λ CDM cosmology	$h \in [0, 1.5], \Omega_{\text{m}} \in [0, 1]$
$\text{o}\Lambda$ CDM	Non-flat Λ CDM cosmology	$h \in [0, 1.5], \Omega_{\Lambda} \in [0, 1], \Omega_{\text{k}} \in [-0.5, 0.5], \Omega_{\text{m}} > 0$
w CDM	Flat w CDM cosmology	$h \in [0, 1.5], \Omega_{\Lambda} \in [0, 1], w \in [-2.5, 0.5]$
N_{eff} CDM	Flat N_{eff} CDM cosmology	$h \in [0, 1.5], \Omega_{\Lambda} \in [0, 1], N_{\text{eff}} \in [1, 5]$
ow CDM	Non-flat w CDM cosmology	$h \in [0, 1.5], \Omega_{\Lambda} \in [0, 1], \Omega_{\text{k}} \in [-0.5, 0.5], \Omega_{\text{m}} > 0, w \in [-2.5, 0.5]$
w_a CDM	Flat w_a CDM cosmology	$h \in [0, 1.5], \Omega_{\Lambda} \in [0, 1], w_0 \in [-2.5, 0.5], w_a \in [-8, 4.5]$

4.5 Cosmological inference

Having estimated the precision attainable on the two distances for a single lens, we now turn to the estimation of cosmological parameters from samples of time-delay lenses. First, in Section 4.5.1. we investigate the precisions achievable from time delay lensing data alone. Then, in Section 4.5.2, we combine the lensing information with *Planck* data to illustrate complementarity in the determination of the cosmological parameters.

4.5.1 Cosmology from strong lensing alone

We performed a Bayesian analysis to obtain the posterior PDF of the cosmological parameters C given the inferred angular diameter and time-delay distances computed in Section 4.4. The posterior PDF is given by Bayes' theorem as

$$P(C|D, Z) \propto P(D|C, Z)P(C), \quad (4.32)$$

where D is the set of measurements of D_d and $D_{\Delta t}$ for the strong lenses, and Z is the set of redshifts pairs (z_d, z_s) for the lenses. To efficiently compute the likelihood term $P(D|C, Z)$, we approximate the posterior PDF of D_d and $D_{\Delta t}$ of each lens by its best fit bivariate normal distribution function as

$$P(D_d, D_{\Delta t}) = \frac{1}{2\pi\sigma_{D_d}\sigma_{D_{\Delta t}}\sqrt{1-\rho_{\text{cor}}^2}} \exp\left[-\frac{z(D_d, D_{\Delta t})}{2(1-\rho_{\text{cor}}^2)}\right], \quad (4.33)$$

where

$$z(D_d, D_{\Delta t}) = \frac{(D_d - \mu_{D_d})^2}{\sigma_{D_d}^2} + \frac{(D_{\Delta t} - \mu_{D_{\Delta t}})^2}{\sigma_{D_{\Delta t}}^2} - \frac{2\rho_{\text{cor}}(D_d - \mu_{D_d})(D_{\Delta t} - \mu_{D_{\Delta t}})}{\sigma_{D_d}\sigma_{D_{\Delta t}}}, \quad (4.34)$$

and $\rho_{\text{cor}} = \text{cov}(D_d, D_{\Delta t})/\sigma_{D_d}\sigma_{D_{\Delta t}}$ with $\text{cov}(D_d, D_{\Delta t})$ being the covariance between the two distances. μ_{D_d} and $\mu_{D_{\Delta t}}$ are the means of D_d and $D_{\Delta t}$, respectively. Assuming the posterior PDF as a bivariate normal distribution function is accurate to the order of Fisher matrix approximation. As we are only interested in the precision of cosmological parameters, we choose μ_{D_d} and $\mu_{D_{\Delta t}}$ to be the fiducial values of the angular and time-delay distances.

Table 4.6: Uncertainties of D_d and $D_{\Delta t}$ for different lens systems.

Lens system	z_d	z_s	Velocity dispersion data	σ_{D_d} (per cent)	$\sigma_{D_{\Delta t}}$ (per cent)
HE0047	0.41	1.66	Resolved	9.6	5.9
J1206	0.75	1.79	Resolved	8.8	5.4
HE0435	0.46	1.69	Resolved	9.5	7.0
HE1104	0.73	2.32	Resolved	9.1	5.5
RXJ1131	0.29	0.65	Resolved	10.0	6.6
J0246	0.73	1.68	Resolved	8.9	5.5
HS2209	0.38 [*]	1.07	Integrated	21.7	7.0
WFI2033	0.66	1.66	Integrated	18.5	6.1
B1608	0.63	1.39	Integrated	19.8	6.1

^{*} The deflector redshift for HS2209 has not been accurately measured yet, therefore we used a fiducial redshift of $z = 0.38$. The results are not sensitive to the assumed redshift.

The quoted uncertainties on the parameters are determined from the 16- and 84-percentiles of the posterior PDF. We have considered six different cosmological models for this analysis (Table 4.5). The first one is the basic flat Λ CDM model. The next three models are one-parameter extensions of the basic Λ CDM model for Ω_K , w , and N_{eff} , labelled as $\text{o}\Lambda\text{CDM}$, $w\text{CDM}$, and $N_{\text{eff}}\text{CDM}$ models, respectively. The last two cosmological models are two-parameter extensions from the basic Λ CDM model, relaxing (Ω_K, w) and (w_0, w_a) , labelled as owCDM and $w_a\text{CDM}$ models, respectively. In the $w_a\text{CDM}$ model, the dark-energy equation-of-state parameter w is given by (Chevallier & Polarski 2001; Linder 2003)

$$w(a) = w_0 + w_a(1 - a), \quad (4.35)$$

where, a is the scale factor. We examined the parameter uncertainties primarily using the fiducial cosmology: $H_0 = 70 \text{ km/s/Mpc}$, $\Omega_m = 0.3$, $\Omega_\Lambda = 0.7$, $\Omega_K = 0$, $w = -1$.

First, we explored the uncertainties on the cosmological parameters achievable by using nine real lenses for which accurate time delay measurements and deep *HST* imaging data are readily available. The details of these nine lenses are given in Table 4.6. Out of these nine lenses, we consider six lenses to have spatially resolved kinematics and the remaining three to have integrated kinematics from the “baseline” observational setup, since three of the lenses are currently outside of the reach of OSIRIS on Keck. Spatially resolved kinematics for all nine systems could be obtained with *JWST*, so our estimate should be considered as conservative in this respect. Then, to explore the strength of using strong lenses to measure the cosmological parameters, we repeated the analysis for a simulated sample of 40 strong lenses expected to be available in the next few years through dedicated follow-up of newly discovered systems. Thus, we created a mock catalogue of 31 lenses with a redshift distribution that resembles the one for the nine lenses given in Table 4.6 in the following manner. First, we fit a Gaussian distribution to the redshift distribution of deflectors of the nine lenses and sampled from this fitted Gaussian distribution. Next, we also fit a Gaussian distribution to the distribution of the ratios of the deflector and source redshifts from the nine lenses and sampled from this distribution to determine the source redshift for each of

Table 4.7: Uncertainties on cosmological parameters.

Data sets	H_0 (km/s/Mpc)	$\sigma(H_0)$ (per cent)	Ω_m	$\sigma(\Omega_m)$	Ω_k	$\sigma(\Omega_k)$	w	$\sigma(w)$	N_{eff}	$\sigma(N_{\text{eff}})$
Λ CDM										
L9*	69.7 ± 1.4	2.0	$0.33^{+0.09}_{-0.12}$	0.11	-	-	-	-	-	-
L40*	69.91 ± 0.64	0.92	$0.307^{+0.042}_{-0.047}$	0.044	-	-	-	-	-	-
L9+ <i>Planck</i>	$68.35^{+0.82}_{-0.73}$	1.1	0.300 ± 0.010	0.010	-	-	-	-	-	-
L40+ <i>Planck</i>	$69.45^{+0.59}_{-0.43}$	0.74	$0.2866^{+0.0058}_{-0.0061}$	0.0059	-	-	-	-	-	-
o Λ CDM										
L9	69.6 ± 2.3	3.3	$0.35^{+0.19}_{-0.22}$	0.20	-0.01 ± 0.27	0.27	-	-	-	-
L40	70.0 ± 1.1	1.6	$0.308^{+0.087}_{-0.091}$	0.089	0.00 ± 0.12	0.12	-	-	-	-
L9+ <i>Planck</i> [†]	$56.3^{+1.1}_{-0.9}$	1.8	$0.443^{+0.018}_{-0.016}$	0.017	-0.0341 ± 0.0048	0.0048	-	-	-	-
L40+ <i>Planck</i> [†]	$56.47^{+0.44}_{-0.47}$	0.81	$0.441^{+0.011}_{-0.009}$	0.010	$-0.0337^{+0.0033}_{-0.0030}$	0.0031	-	-	-	-
w CDM										
L9	$70.2^{+3.5}_{-4.3}$	6.2	$0.34^{+0.12}_{-0.13}$	0.13	-	-	$-1.11^{+0.66}_{-0.48}$	0.57	-	-
L40	$70.2^{+1.8}_{-2.2}$	2.9	0.307 ± 0.050	0.050	-	-	$-1.03^{+0.24}_{-0.21}$	0.22	-	-
L9+ <i>Planck</i>	$71.9^{+2.1}_{-1.8}$	2.8	$0.276^{+0.014}_{-0.015}$	0.015	-	-	-1.157 ± 0.081	0.081	-	-
L40+ <i>Planck</i>	$71.50^{+0.96}_{-0.79}$	1.2	$0.2779^{+0.0060}_{-0.0058}$	0.0059	-	-	$-1.127^{+0.054}_{-0.067}$	0.060	-	-
N_{eff} CDM										
L9	$69.7^{+1.4}_{-1.3}$	2.0	$0.33^{+0.09}_{-0.13}$	0.11	-	-	-	-	$3.0^{+1.3}_{-1.4}$	1.4
L40	69.94 ± 0.65	0.93	$0.305^{+0.042}_{-0.047}$	0.045	-	-	-	-	3.0 ± 1.4	1.4
L9+ <i>Planck</i>	$69.7^{+1.1}_{-1.0}$	1.6	$0.290^{+0.011}_{-0.010}$	0.010	-	-	-	-	3.31 ± 0.16	0.16
L40+ <i>Planck</i>	$69.94^{+0.55}_{-0.54}$	0.77	$0.2971^{+0.0084}_{-0.0076}$	0.0080	-	-	-	-	$3.33^{+0.13}_{-0.12}$	0.13
o w CDM										
L9	$71.1^{+4.0}_{-5.2}$	6.5	$0.41^{+0.24}_{-0.20}$	0.22	$-0.10^{+0.26}_{-0.29}$	0.28	$-1.25^{+0.72}_{-0.55}$	0.63	-	-
L40	$70.7^{+2.0}_{-3.1}$	3.6	$0.36^{+0.19}_{-0.14}$	0.17	$-0.06^{+0.19}_{-0.22}$	0.21	$-1.14^{+0.46}_{-0.38}$	0.42	-	-
w_a CDM										
Data sets	H_0 (km/s/Mpc)	$\sigma(H_0)$ (per cent)	Ω_m	$\sigma(\Omega_m)$	Ω_Λ	$\sigma(\Omega_\Lambda)$	w_0	$\sigma(w_0)$	w_a	$\sigma(w_a)$
L9	$70.4^{+5.0}_{-5.8}$	7.7	$0.40^{+0.12}_{-0.13}$	0.13	$0.60^{+0.12}_{-0.13}$	0.13	$-0.98^{+0.86}_{-0.77}$	0.82	$-2.2^{+3.7}_{-3.3}$	3.5
L40	$68.7^{+3.7}_{-3.6}$	5.3	$0.359^{+0.092}_{-0.078}$	0.085	$0.641^{+0.092}_{-0.078}$	0.085	$-0.77^{+0.46}_{-0.64}$	0.55	$-1.6^{+3.5}_{-2.4}$	3.0
L9+ <i>Planck</i> +BAO	$65.5^{+2.6}_{-2.2}$	3.7	0.335 ± 0.025	0.025	0.665 ± 0.025	0.025	$-0.59^{+0.28}_{-0.29}$	0.29	$-1.46^{+0.86}_{-0.85}$	0.86
L40+ <i>Planck</i> +BAO	$67.0^{+2.2}_{-2.0}$	3.2	$0.321^{+0.022}_{-0.020}$	0.021	$0.679^{+0.020}_{-0.022}$	0.021	$-0.67^{+0.23}_{-0.26}$	0.25	$-1.39^{+0.75}_{-0.77}$	0.76

* L9 refers to the set of nine lenses and L40 refers to the set of 40 lenses.

[†] For o Λ CDM model, to combine *Planck* with the lensing information, the fiducial cosmology was chosen to be the *Planck* o Λ CDM cosmology: $H_0 = 56.5$ km/s/Mpc, $\Omega_m = 0.441$, $\Omega_\Lambda = 0.592$, and $\Omega_K = -0.033$.

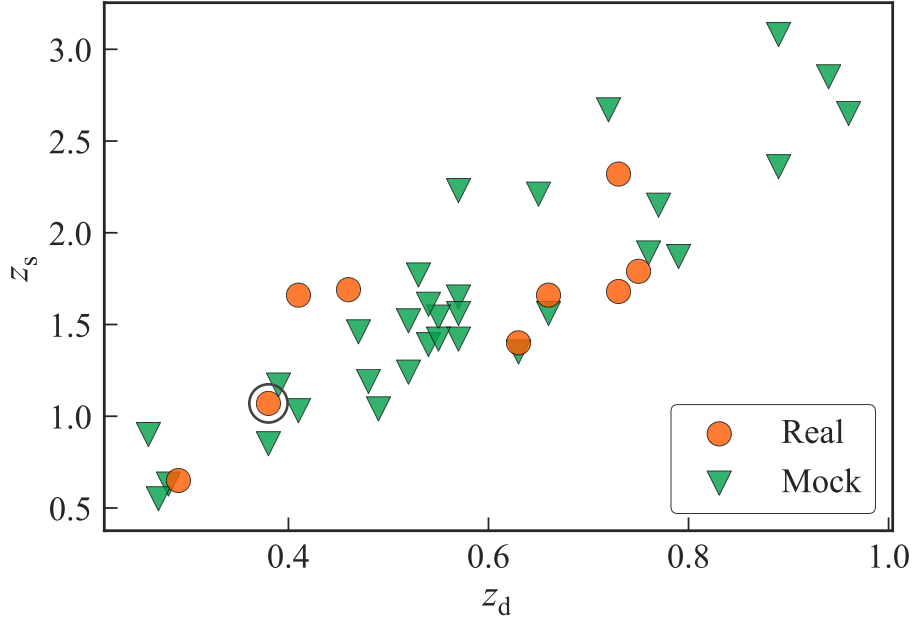


Figure 4.6: Distribution of deflector and source redshifts of the lenses. The circles show the redshifts for the nine actual lenses with measured time delays and deep *HST* imaging. The triangles show the redshifts for the 31 lenses in the mock catalogue. We assume a fiducial redshift $z_d = 0.38$ for the strong lens HS2209 as it has not been accurately measured yet and it is marked with a dark circle on the plot.

the 31 mock lensing systems. The redshift distribution of the real and mock lenses is shown in Figure 4.6.

4.5.1.1 Nine lenses

The detailed parameter uncertainties for all the cosmological models considered in this paper are tabulated in Table 4.7. For the flat Λ CDM model, H_0 is estimated with 2.0 per cent precision (69.7 ± 1.4 km/s/Mpc) and Ω_m is estimated with precision $\sigma(\Omega_m) = 0.11$.

To measure the improvement over cosmological parameter uncertainties by using spatially resolved kinematics, we did the same analysis for nine lenses without using kinematics. In

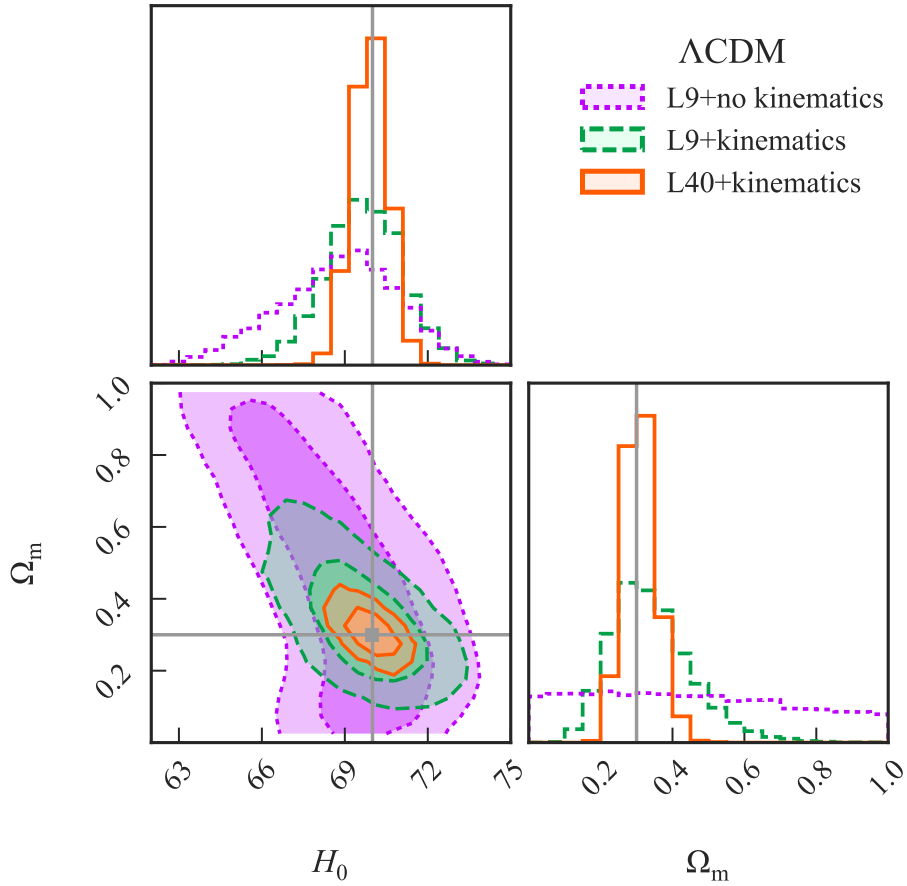


Figure 4.7: Posterior PDF of cosmological parameters for the flat Λ CDM model obtained from distance measurements for nine lenses (L9) without kinematics (dotted), for nine lenses with kinematics (dashed) and for 40 lenses (L40) with kinematics (solid). The contours represent 1σ and 2σ confidence regions. Solid straight lines show the fiducial values. Using kinematics breaks the degeneracy between parameters and improves the precision on H_0 from 3.2 to 2.0 per cent for nine lenses.

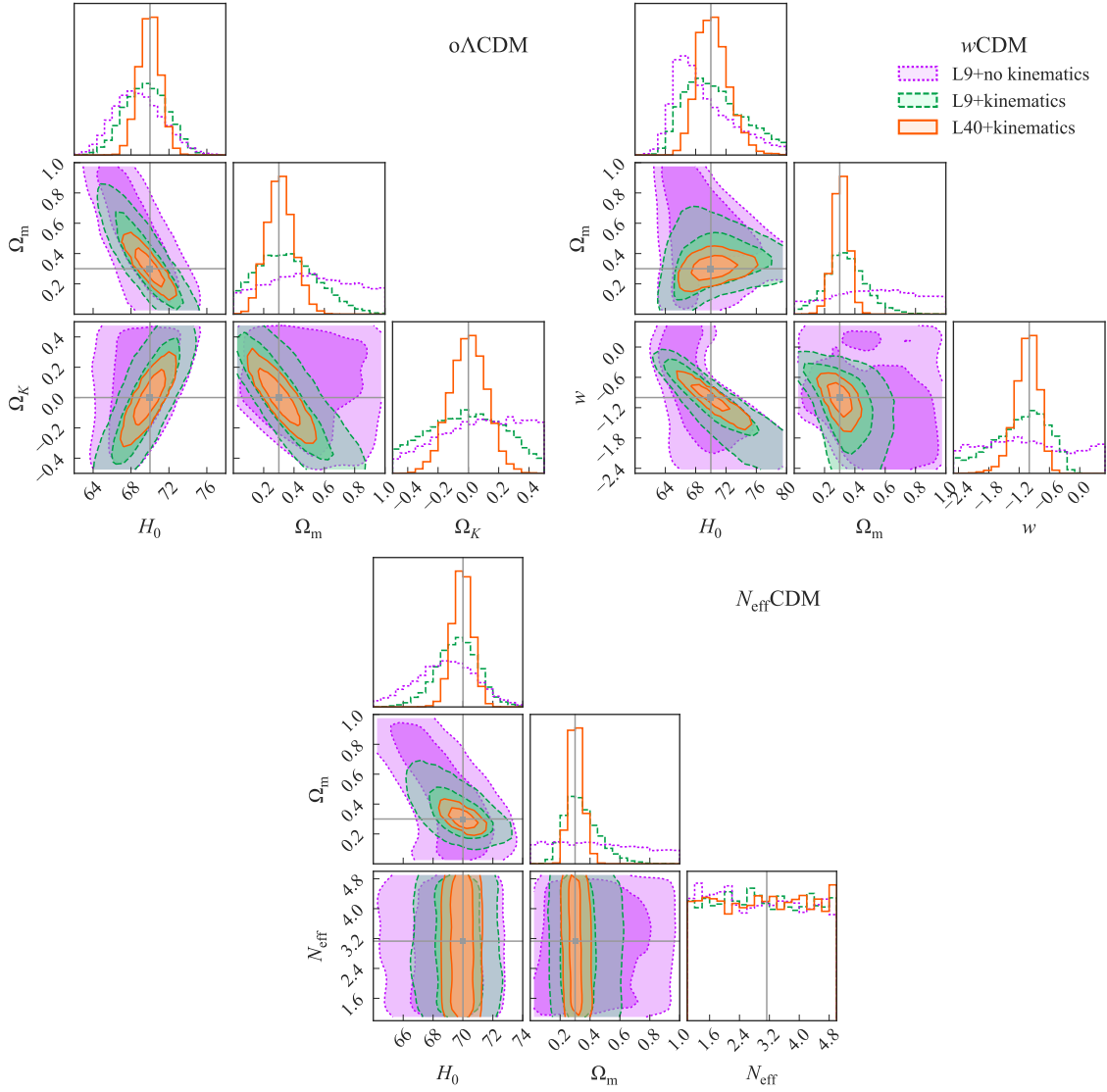


Figure 4.8: Posterior PDF of cosmological parameters obtained from distance measurements for $\text{o}\Lambda\text{CDM}$ (top left), $w\text{CDM}$ model (top right), and $N_{\text{eff}}\text{CDM}$ (bottom) models. The posterior PDF inferred from nine lenses (L9) without kinematics is shown in dotted contours, from nine lenses with kinematics is shown in dashed contours, and from 40 lenses (L40) with kinematics is shown in solid contours. The contours represent 1σ and 2σ confidence regions. Solid straight lines show the fiducial values. For all cosmological models, adding spatially resolved kinematics lifts degeneracies between the cosmological parameters and puts tighter constraints on them.

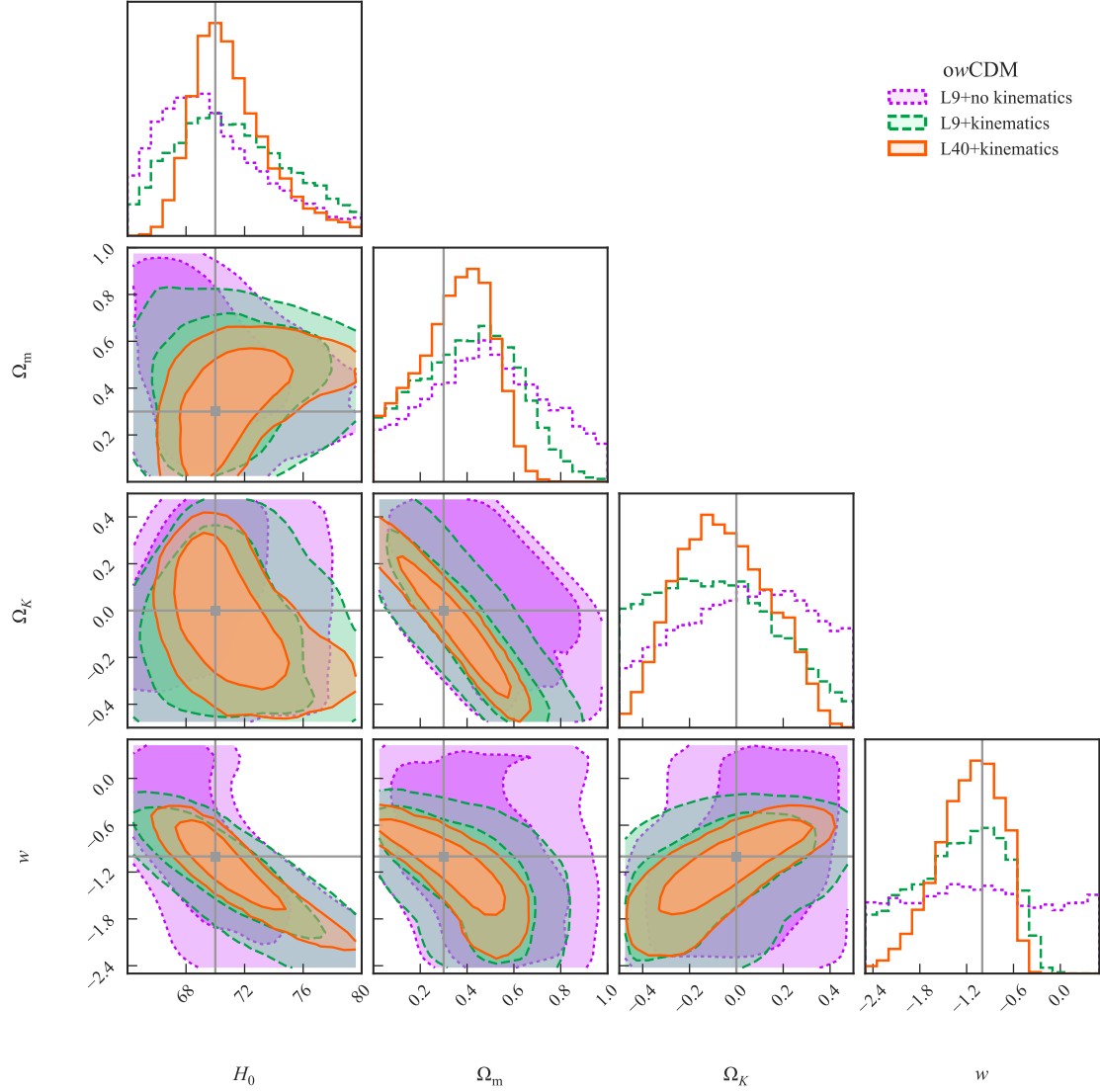


Figure 4.9: Posterior PDF of cosmological parameters obtained from the distance measurements for $owCDM$ model. The posterior PDF inferred from nine lenses (L9) without kinematics is shown in dotted contours, from nine lenses with kinematics is shown in dashed contours, and from 40 lenses (L40) with kinematics is shown in solid contours. The contours represent 1σ and 2σ confidence regions. Solid straight lines show the fiducial values. This is a further illustration of the role of spatially resolved kinematics in breaking degeneracies between the parameters for a two-parameter extension from the basic Λ CDM model.

that case, the parameter uncertainties are $\sigma(H_0) = 3.2$ per cent and $\sigma(\Omega_m) = 0.32$. Using spatially resolved kinematics for nine lenses leads to an improvement in the precision of H_0 from 3.2 to 2.0 per cent. If we adopt the conservative lensing data quality equivalent to $\delta\gamma \sim 0.04$, addition of the spatially resolved stellar kinematics for nine lenses still improves the precision of H_0 by 1 per cent from 3.9 to 2.9 per cent. Without any kinematics there is a very strong degeneracy in Ω_m , which can be broken by adding the stellar kinematics information (Figure 4.7).

For the Λ CDM model with our “primary” fiducial cosmology, the cosmological parameter uncertainties are estimated to be $\sigma(H_0) = 3.3$ per cent, $\sigma(\Omega_m) = 0.2$, $\sigma(\Omega_K) = 0.27$ (Figure 4.8). For the flat w CDM model, we estimate the cosmological parameters uncertainties to be $\sigma(H_0) = 6.2$ per cent, $\sigma(\Omega_m) = 0.13$, and $\sigma(w) = 0.57$ (Figure 4.8). For the N_{eff} CDM model, the parameter uncertainties are estimated to be $\sigma(H_0) = 2.0$ per cent, $\sigma(\Omega_m) = 0.11$ and N_{eff} is completely degenerate.

For the ow CDM model, where we relax Ω_K and w from the flat Λ CDM model, we estimate the parameters with uncertainties $\sigma(H_0) = 6.5$ per cent, $\sigma(\Omega_m) = 0.22$, $\sigma(\Omega_K) = 0.28$, $\sigma(w) = 0.63$. For the w_a CDM model, w_0 and w_a are estimated with uncertainties $\sigma(w_0) = 0.82$ and $\sigma(w_a) = 3.5$, respectively.

4.5.1.2 40 lenses

For the flat Λ CDM model, using distance measurement uncertainties from 40 lenses we estimate H_0 with 0.92 per cent precision and Ω_m with $\sigma(\Omega_m) = 0.044$. For the conservative lensing data quality equivalent to $\delta\gamma \sim 0.04$, the sample of 40 lenses constraints H_0 with 1.3 per cent uncertainty. The parameter uncertainties are estimated for Λ CDM model to be $\sigma(H_0) = 1.6$ per cent, $\sigma(\Omega_m) = 0.089$, and $\sigma(\Omega_K) = 0.12$ and for w CDM model to be $\sigma(H_0) = 2.9$ per cent, $\sigma(\Omega_m) = 0.05$, and $\sigma(w) = 0.22$. For N_{eff} CDM model, we estimate the parameter uncertainties to be $\sigma(H_0) = 0.93$ per cent, $\sigma(\Omega_m) = 0.045$. Adding more lens to the sample does not improve the degeneracy in N_{eff} showing time-delay cosmography is

insensitive to N_{eff} .

For the ow CDM model, we estimate the parameter uncertainties to be $\sigma(H_0) = 3.6$ per cent, $\sigma(\Omega_m) = 0.17$, $\sigma(\Omega_K) = 0.21$, $\sigma(w) = 0.42$ (Figure 4.9). For the w_a CDM model, w_0 and w_a are estimated with uncertainties $\sigma(w_0) = 0.55$ and $\sigma(w_a) = 3.0$, respectively.

4.5.2 Joint analysis with *Planck*

We combined the inference on cosmography from strong lensing with *Planck* 2015 data release (Planck Collaboration 2016a, hereafter *Planck*).² To combine the two data sets, we followed the importance sampling method prescribed by Lewis & Bridle (2002) and implemented by Suyu et al. (2010, 2013), and Bonvin et al. (2017). We used the bivariate normal distribution fit of the posterior PDF of D_d and $D_{\Delta t}$ given in Equation (4.33) to compute the “importance” or weight of each point in the *Planck* chain.

For many combinations of cosmological model and parameters, the confidence regions from the time-delay cosmography are orthogonal to the ones from the *Planck*. As a result, combining the inferences from the time-delay cosmography with the *Planck* leads to much tighter constraints (Figure 4.10).

For flat Λ CDM model, combining *Planck* with nine lenses leads to an 1.1 per cent measurement of H_0 . For the combination of 40 lenses and *Planck*, the precision of H_0 becomes 0.74 per cent (Table 4.7) in the flat Λ CDM model.

For $o\Lambda$ CDM model, the maximum likelihood regions of the *Planck* and the lensing data with the “primary” fiducial cosmology are too far apart to implement the importance sampling method. Therefore, we used the *Planck* values, $H_0 = 56.5$ km/s/Mpc, $\Omega_m = 0.441$, $\Omega_\Lambda = 0.592$, $\Omega_K = -0.033$ as the fiducial cosmology to generate the lensing likelihood to combine with the *Planck* likelihood. This combination gives $\sigma(H_0) = 1.8$

²We used the *Planck* chains designated by “plikHM_TT_lowTEB” which uses the baseline high-l *Planck* power spectra and low-l temperature and LFI polarization.

per cent, $\sigma(\Omega_m) = 0.017$, and $\sigma(\Omega_K) = 0.0048$ for nine lenses and $\sigma(H_0) = 0.81$ per cent, $\sigma(\Omega_m) = 0.01$, and $\sigma(\Omega_K) = 0.0031$ for 40 lenses.

For the w CDM model, the precision of w is estimated to be $\sigma(w) = 0.081$ and $\sigma(w) = 0.060$ for combination of *Planck* with nine and 40 lenses, respectively. For the N_{eff} CDM model, we constrain the number of relativistic species with $\sigma(N_{\text{eff}}) = 0.16$ and $\sigma(N_{\text{eff}}) = 0.13$ by combining *Planck* with nine and 40 lenses, respectively.

We did not combine *Planck* with the lensing likelihoods for Λ CDM model as the *Planck* collaboration did not publicly release the parameter chains for this model. For w_a CDM model, we combined the lensing information with *Planck*+BAO constraints. From the joint analysis, we estimate the parameter uncertainties to be $\sigma(w_0) = 0.29$ and $\sigma(w_a) = 0.86$ giving dark-energy figure of merit (FoM; given by the inverse of the area enclosed by the 1σ confidence contour in the $w_0 - w_a$ plane) 0.85 for nine lenses, and $\sigma(w_0) = 0.27$ and $\sigma(w_a) = 0.82$ giving an FoM = 1.11 for 40 lenses (Figure 4.11).

4.6 Discussion and Comparison with Previous Work

We explored how incorporating spatially resolved kinematics of the deflector in addition to the lensing and time-delay data improves the precision of the inferred cosmological parameters. We showed that the addition of the spatially resolved kinematics to the lensing and time-delay data helps break the mass-anisotropy degeneracy and leads to improved precision in the determination of the angular diameter distance of the deflector (from ~ 20 to ~ 10 per cent). We found that the time-delay distances can be simultaneously measured with ~ 6 per cent accuracy, which is comparable to the 6 per cent measurement of the time-delay distance for the lens RXJ1131-1231 (Suyu et al. 2013) and the 7.6 per cent measurement for the lens HE0435-1223 (Wong et al. 2017). These precision margins are achievable by current and future IFSSs, e.g. OSIRIS on Keck with laser guide star AO or space-based instruments, e.g. NIRSPEC on *JWST*. Future telescopes like TMT or E-ELT would improve these precisions

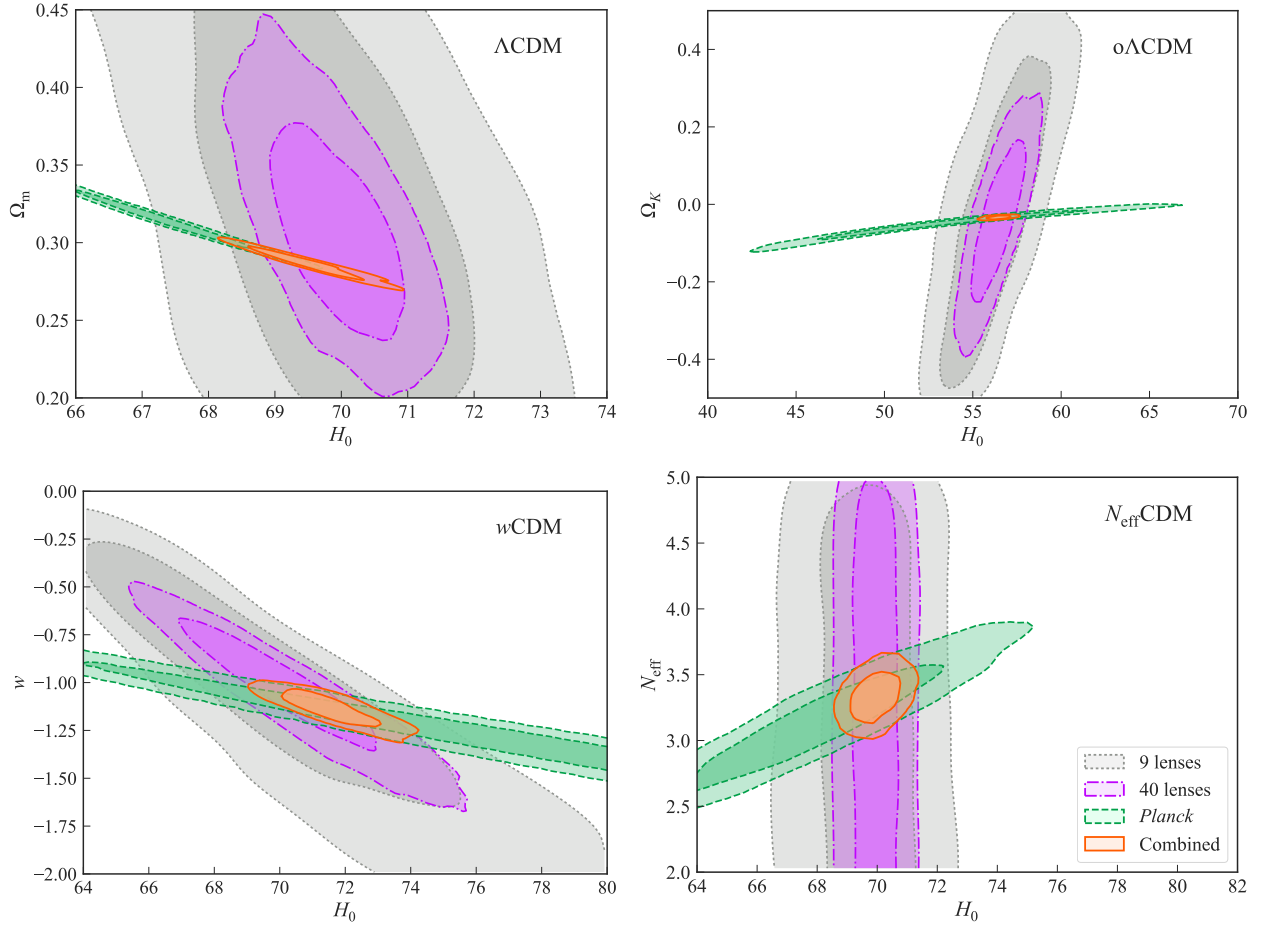


Figure 4.10: 1σ and 2σ regions of cosmological parameters obtained from lensing data alone and in combination with *Planck* for ΛCDM (top left), $o\Lambda\text{CDM}$ (top right), $w\text{CDM}$ (bottom left), and $N_{\text{eff}}\text{CDM}$ (bottom right) models. The constraints from nine lenses with spatially resolved kinematics are shown with dotted contours, from 40 lenses with spatially resolved kinematics are shown with dash-dotted contours, from *Planck* are shown in dashed contours, and from the combination of *Planck* and 40 lenses are shown in solid contours. In all cases, adding the lensing information to the *Planck* data improves the constraints on the cosmological parameters.

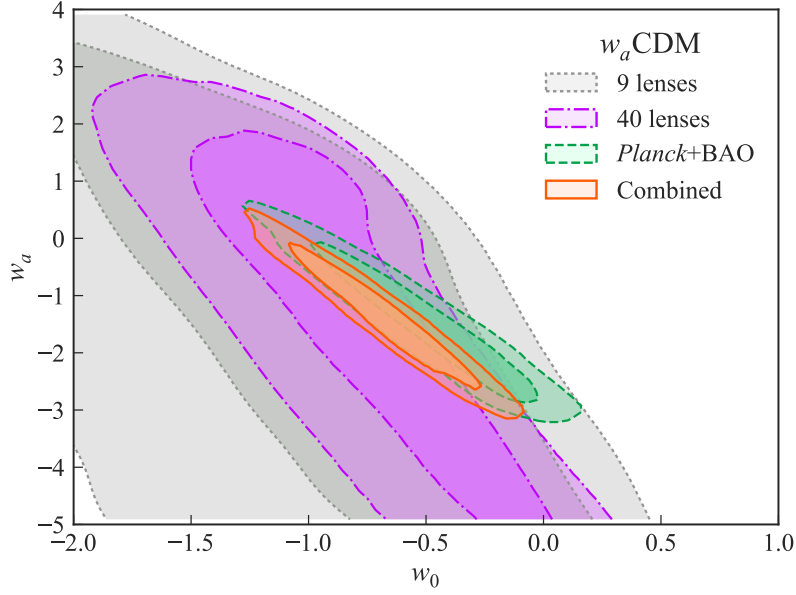


Figure 4.11: 1σ and 2σ confidence regions of the dark energy equation of state parameters obtained from lensing data alone and in combination with *Planck* for w_a CDM model. The constraints from nine lenses with spatially resolved kinematics are shown with dotted contours, from 40 lenses with spatially resolved kinematics are shown with dash-dotted contours, from *Planck* are shown in dashed contours, and from the combination of *Planck* and 40 lenses are shown in solid contours. Adding lensing measurements to the *Planck*+BAO data improves the dark energy FoM by 56 per cent.

further. Jee et al. (2016) assume 5 per cent precision on both angular diameter and time-delay distances; however we found that 5 per cent precision on angular diameter distance measurement is probably beyond reach with current or imminent technology.

We confirmed the result by Linder (2011) and Jee et al. (2016) that combining lensing information with CMB and other external data sets can greatly improve the constraints on the cosmological parameters. Linder (2011) finds that by combining time-delay distance measurements with 5 per cent uncertainty from 150 hypothetical strong lens systems with the CMB and supernova constraints, dark energy FoM can be improved by almost a factor of 5. Jee et al. (2016) find that combining angular diameter and time-delay distance measurements with 5 per cent uncertainties on both from 55 lenses with *Planck*+BAO+JLA constraints improves the precision on w_a and the dark energy figure of merit by approximately a factor of 2 for the time-varying dark energy model. In our study, combining angular diameter and time-delay distance measurements with ~ 10 per cent and ~ 6 per cent uncertainties, respectively, from 40 lenses with *Planck*+BAO data improves the *Planck*+BAO constraint on w_a by 13 per cent and the dark energy FoM by 56 per cent, consistent with previous results after taking into account the differences.

4.7 Limitation of this present work

In order to model a large number of lenses in a computationally efficient manner we adopted many simplifying assumptions. First, we used a collection of conjugate points to replace the detailed modelling of the lensed quasar host galaxy. Secondly, we assumed spherical symmetry to speed up the calculations. By requiring the uncertainty on the effective mass density profile slope to be equal to 0.02, the precision obtained by full-blown models, this procedure ensures that we get realistic uncertainties on distances. We know from full pixel-based simulations that such precision can be attained by modelling images obtained with reasonable exposure time using current and future technology (Meng et al. 2015). A similar

study is required to estimate the exposure times required to carry out the spectroscopic observations (Meng et al. 2017, in preparation).

We assumed a 3-5 per cent uncertainty for the external convergence as it can be indirectly estimated by comparing the statistics of galaxy number counts along the line of sight with simulated light cones from the Millennium Simulation. This approach has the caveat of being dependent on the assumed cosmology and thus possibly biasing the final cosmological inferences (Rusu et al. 2017). Moreover, there can be ~ 25 per cent deviation in the inferred κ_{ext} between the *Planck* cosmology and the Millennium Simulation. This would leave some residual systematics to be accounted for when analysing real-life lenses. With the most pessimistic approach of 25 per cent variation between median κ_{ext} inferred from ray-tracing, this would mean that a median value of $\kappa_{\text{ext}} = 0.04$ would impart a 1 per cent systematic uncertainty on H_0 . However, κ_{ext} can be shown to depend primarily on $\Omega_m \sigma_8$ where σ_8 is the root-mean-square fluctuation of the mass density, while other contributions are sub-dominant (Equation C4 in Rusu et al. 2017). This means that one can perform a complete cosmographic inference, where also Ω_m and σ_8 are varied when importance-sampling from the CMB chains. Whereas the product $\Omega_m \sigma_8$ (hence the reconstructed median κ_{ext}) can vary appreciably between “different” CMB experiments (with different setups, or different multipole coverage, or beam characterization), its possible variation is smaller within the same CMB experiment, which means that the median κ_{ext} inferred will vary by less than the most pessimistic estimate (25 to 1 per cent on H_0). Hence, regardless of whether $\Omega_m \sigma_8$ are varied or kept at a fiducial value when considering κ_{ext} , time-delays are still a robust way of probing departures from flat- Λ CDM as inferred from within a particular CMB probe, without particular worries from the κ_{ext} reconstruction, with sub-percent accuracy. There are, in fact, other factors affecting the accuracy of κ_{ext} reconstruction, such as the choice of weighting scheme in terms of distances and masses, or the importance of a multi-plane approach. However, when dealing with real-life lenses, these have been (and are being) discussed at length for each individual system while still at blinded-inference stage. Different

lenses have required different evaluations of κ_{ext} , but after unblinding they have all given consistent H_0 results, which suggests that this side of reconstruction systematics is currently under control. Part of the reason may be that the width of the κ_{ext} PDF is not negligible with respect to the median, so any systematics affecting the shift in κ_{ext} are still comprised within 1σ from the “true” value.

Finally, we emphasize that our study takes into account systematic uncertainties only in an indirect manner. Possible sources of known systematics can be contamination from the bright quasar images to the the host galaxy flux or the deflector spectra, unaccounted line-of-sight contribution to the projected mass etc. We assumed that these sources of known systematics can be accounted by our chosen error budget for different mock data and model parameters, e.g. 5-10 per cent uncertainty on the velocity dispersion and 3-5 per cent uncertainty on the external convergence, which are realistic error budgets for these quantities from the state of the art measurements. It would be useful to carry out a systematic investigation of strategies that may be required to limit any potential bias arising from these systematic uncertainties to be well below the statistical errors.

4.8 Summary

Strong lenses with measured time delays can be used as probes to constrain cosmological parameters through the measurement of the angular diameter distance to the deflector and the time-delay distance. However, spatially resolved kinematics is essential to measure the angular diameter distance to the deflector and it also helps break the mass-anisotropy degeneracy. In this paper, we used a realistic model of a deflector galaxy to create mock lensing and kinematic data and estimated the achievable precisions of the cosmological parameters. The main conclusions of this study are as follows

1. The angular diameter distance to the deflector can be measured to approximately 10 per cent uncertainty by including spatially resolved kinematics from current ground-

based IFS with laser guide star AO, e.g. OSIRIS on Keck, or with space-based instruments, e.g. NIRSPEC on *JWST*, to the imaging data of the lensed quasar and the time-delay measurement. The time-delay distance can be simultaneously measured to ~ 6 per cent uncertainty.

2. Using spatially resolved kinematics improves the precision on angular diameter distance per system from ~ 20 to ~ 10 per cent over using integrated kinematic data.
3. H_0 can be measured to 2.0 per cent precision using lensing and spatially resolved kinematics from nine lenses and to sub-percent precision (0.9 per cent) from 40 lenses.
4. The uncertainty on H_0 improves from 3.2 to 2.0 per cent by adding the spatially resolved kinematics to the lensing and time-delay data for nine strong lens systems.
5. Combining *Planck* with lensing and spatially resolved kinematics data can break degeneracies between the cosmological parameters and greatly improve the constraints on them. Especially, for the time-dependent dark energy parameter model, the dark energy FoM is improved by 56 per cent by combining a sample of 40 lenses with measured time delays and kinematics with *Planck*+BAO constraints.

This is a very interesting time for time-delay cosmography as several wide-field and deep-sky surveys such as the Dark Energy Survey, *Euclid*, the Wide Field Infrared Survey Telescope (WFIRST), the Large Synoptic Survey Telescope (LSST), should allow for the discovery and follow-up of tens to hundreds of multiply imaged quasars (Oguri & Marshall 2010). The launch of NIRSPEC on *JWST*, scheduled for 2018, and the constantly improving ground-based instruments with laser guide star AO (e.g. OSIRIS on Keck) make it possible to have high-quality spatially resolved kinematics for these lens systems. In turn, this can lead to the measurement of the Hubble parameter to sub-per-cent precision. Combining the distance measurements from strong lens systems to other cosmological probes, i.e. CMB, BAO, and Type Ia supernova, would help tightly constraint the cosmological parameters

leading to a deeper understanding of dark energy, dark matter, and other fundamental properties of our Universe.

Acknowledgment

We thank Simon Birrer, Inh Jee, Eiichiro Komatsu, Philip J. Marshall, Sherry H. Suyu, and Xin Wang for many insightful conversations. We also thank the anonymous referee whose comments helped us to improve this work. AS acknowledges support by the National Science Foundation through grant AST-1450141. This work used computational and storage services associated with the Hoffman2 Shared Cluster provided by UCLA Institute for Digital Research and Education's Research Technology Group. This research made use of Astropy, a community-developed core PYTHON package for Astronomy (Astropy Collaboration 2013), and the CORNER.PY code at <https://github.com/dfm/corner.py> (Foreman-Mackey 2016).

CHAPTER 5

Automated and uniform modelling of lensed quasars

This chapter was published as Shajib, A. J., S. Birrer, T. Treu, M. W. Auger, A. Agnello, T. Anguita, E. J. Buckley-Geer, J. H. H. Chan, T. E. Collett, F. Courbin, C. D. Fassnacht, J. Frieman, I. Kayo, C. Lemon, H. Lin, P. J. Marshall, R. McMahon, A. More, N. D. Morgan, V. Motta, M. Oguri, F. Ostrowski, C. E. Rusu, P. L. Schechter, T. Shanks, S. H. Suyu, G. Meylan, T. M. C. Abbott, S. Allam, J. Annis, S. Avila, E. Bertin, D. Brooks, A. Carnero Rosell, M. Carrasco Kind, J. Carretero, C. E. Cunha, L. N. da Costa, J. De Vicente, S. Desai, P. Doel, B. Flaugher, P. Fosalba, J. García-Bellido, D. W. Gerdes, D. Gruen, R. A. Gruendl, G. Gutierrez, W. G. Hartley, D. L. Hollowood, B. Hoyle, D. J. James, K. Kuehn, N. Kuropatkin, O. Lahav, M. Lima, M. A. G. Maia, M. March, J. L. Marshall, P. Melchior, F. Menanteau, R. Miquel, A. A. Plazas, E. Sanchez, V. Scarpine, I. Sevilla-Noarbe, M. Smith, M. Soares-Santos, F. Sobreira, E. Suchyta, M. E. C. Swanson, G. Tarle, & A. R. Walker. 2019, MNRAS, 483, 5649, and reproduced here with minor formatting changes.

5.1 Background

Strong gravitational lensing is the effect where light from a background object is deflected by a foreground mass distribution (e.g. galaxy or galaxy cluster) and multiple images of the background object form. Strong gravitational lenses are powerful probes to answer a variety of astrophysical and cosmological questions (see, e.g., Treu 2010), as we discuss briefly below.

According to the concordance model in cosmology, our Universe consists of 5 per cent

baryonic matter, 26 per cent dark matter, and 69 per cent dark energy accounting for a cosmological constant Λ (Planck Collaboration 2018). This model is known as the Λ cold dark matter (Λ CDM) model. The predictions of the Λ CDM model have been extensively tested with good agreement to observations spanning from the largest scale up to the horizon down to ~ 1 Mpc (e.g. Dawson et al. 2013; Shajib & Wright 2016; Planck Collaboration 2018). However, there also have been observations that are in tension with the flat Λ CDM paradigm. For instance, there is a tension at the $\gtrsim 3\sigma$ level between the local measurement of H_0 from Type Ia supernovae (Riess et al. 2016; Riess et al. 2018; Riess et al. 2018; Bernal et al. 2016) and that extrapolated from the *Planck* cosmic microwave background measurement for a flat Λ CDM cosmology. This tension may arise from unknown systematic uncertainties in one or both of the measurements, or might point to new physics, e.g. additional species of relativistic particles, a non-flat cosmology, or dynamic dark energy. Therefore, it is crucial to have precise and independent measurements of H_0 to settle this discrepancy.

In a gravitational lens, if the background source is time-variable (typically a quasar, but also a supernova as originally proposed), the delay between the arrival time of photons for the different images can be used to measure the so-called ‘time-delay distance’ (Refsdal 1964; Suyu et al. 2010). This distance is inversely proportional to H_0 , thus it can be used to constrain H_0 and other cosmological parameters (for a detailed review, see Treu & Marshall 2016). H_0 has been determined to 3.8 per cent precision using three lens systems in the flat Λ CDM cosmology (Suyu et al. 2010, 2013, 2017; Sluse et al. 2017; Rusu et al. 2017; Wong et al. 2017; Bonvin et al. 2017; Tihhonova et al. 2018). With a large sample size of about 40 lenses, it is possible to measure H_0 with the per cent precision (Jee et al. 2016; Shajib et al. 2018) necessary to resolve the H_0 tension and make the most of other dark energy probes (Linder 2011; Suyu et al. 2012; Weinberg et al. 2013).

One of the baryonic components in dark matter is low-mass star. Surprisingly, recent studies have shown that the low-mass star contribution in massive elliptical galaxies is significantly underestimated if the stellar initial mass function (IMF) of the Milky Way is assumed

(Treu et al. 2010; van Dokkum & Conroy 2010; Auger et al. 2010b; Cappellari et al. 2012; Schechter et al. 2014). Precise knowledge about the IMF is key in measuring almost any extragalactic quantity involving star and metal formation. Measuring the stellar mass-to-light ratio in the deflectors of quadruply imaged lensed quasars (henceforth quads) from microlensing statistics provides one of the most robust methods to constrain the IMF (e.g. Oguri et al. 2014; Schechter et al. 2014).

Quads also provide a unique test of small-scale structure formation (Kauffmann et al. 1993; Witt et al. 1995; Klypin et al. 1999; Moore et al. 1999; Boylan-Kolchin et al. 2011; Metcalf & Madau 2001; Dalal & Kochanek 2002; Yoo et al. 2006; Keeton & Moustakas 2009; Moustakas et al. 2009) by measuring the subhalo mass function (Metcalf & Zhao 2002; Kochanek & Dalal 2004; Amara et al. 2006; Metcalf & Amara 2012; Nierenberg et al. 2014, 2017; Xu et al. 2015; Birrer et al. 2017, see also for studies involving extended source only, Koopmans 2005; Vegetti & Koopmans 2009; Vegetti et al. 2010, 2012, 2018; Hezaveh et al. 2016), independent of their luminosity function. With a large sample of quads, Gilman et al. (2018) demonstrate the possibility of constraining the free-streaming length of dark matter particles more precisely than current limits based on the Lyman- α forest (Viel et al. 2013).

Until recently, all of these methods could only be applied to a small sample of known quads. However, such systems are currently being discovered at a rapidly increasing rate due to multiple strong-lens search efforts involving various large-area sky surveys (e.g. Agnello et al. 2015a, 2018d,c; Williams et al. 2017, 2018; Schechter et al. 2017; Sonnenfeld et al. 2018b; Lemon et al. 2018; Anguita et al. 2018, Treu et al. 2018, submitted). With more deep wide-field surveys, e.g. *Wide-Field Infrared Survey Telescope*, *Large Synoptic Survey Telescope*, *Euclid*, etc., coming online within the next decade, the sample size of quads is expected to increase by two orders of magnitude or more (Oguri & Marshall 2010; Collett 2015).

Modelling such lens systems has so far been carried out for individual systems while fine-tuning the modelling approach on a case-by-case basis. However, with the rapidly increasing

rate of discovery, it is essential to develop a modelling technique that is applicable to a wide variety of quads to efficiently reduce the time and human labour necessary in this endeavour. Given the large diversity in the morphology and complexity of quads, this is an interesting problem to pose: is every quad different or ‘unhappy in its own way’ that requires careful decision-making by a human in the modelling procedure, or are the quads similar or ‘happy’ to some extent so that a uniform modelling technique can be applied to generate acceptable models without much human intervention?

Recently, some initial strides have been undertaken along the lines of solving this problem for strong lenses with extended sources. Nightingale et al. (2018) devised an automated lens modelling procedure using Bayesian model comparison. Hezaveh et al. (2017) and Perreault Levasseur et al. (2017) applied machine learning techniques to automatically model strong gravitational lenses and constrain the model parameters. In this chapter, we devise a general framework or decision-tree that can be applied to model-fitting of quads both in a single band and simultaneously in multiple bands. We implement this uniform modelling approach using the publicly available lens-modelling software *LENSTRONOMY* (Birrer & Amara 2018, based on Birrer et al. 2015) to a sample of 13 quads from the *Hubble Space Telescope (HST)* data in three bands. *LENSTRONOMY* comes with sufficient modelling tools and the architecture allows a build-up in complexity as presented in this work. We report the model parameters and other derived quantities for these lens systems.

To demonstrate the scientific capabilities of such a sample of strong-lens systems, we study the properties of the deflector galaxy mass distribution, specifically the alignment of the mass and light distributions in them. The distribution of dark matter and baryons in galaxies can test predictions of Λ CDM and galaxy formation theories (e.g. Dubinski 1994; Ibata et al. 2001; Kazantzidis et al. 2004; Macciò et al. 2007; Debattista et al. 2008; Lux et al. 2012; Read 2014). N-body simulations with only dark matter particles predict nearly triaxial, prolate haloes (Dubinski & Carlberg 1991; Warren et al. 1992; Navarro et al. 1996; Jing & Suto 2002; Macciò et al. 2007). In the presence of baryons, the halos become rounder

(Dubinski & Carlberg 1991; Dubinski 1994; Warren et al. 1992). With a modestly-triaxial luminous galaxy embedded in the dark matter halo, large misalignments ($\sim 16 \pm 19\text{deg}$) between the projected light and mass major axes can be produced (Romanowsky & Kochanek 1998). For disk galaxies, the dark matter distribution is shown to be well-aligned with the light distribution (Katz & Gunn 1991; Dubinski & Carlberg 1991; Debattista et al. 2008).

As the lensing effect is generated by mass, strong gravitational lenses give independent estimates of the mass distribution that can be compared with the observed light distribution. The deflectors in quads are typically massive ellipticals (with Einstein mass $M_E \gtrsim 10^{11.5} M_\odot$). Most of the massive ellipticals are observed to be slow rotators with uniformly-distributed misalignments between the kinematic and photometric axes (Ene et al. 2018). The uniform distribution of misalignments suggests these massive ellipticals to be intrinsically triaxial. Massive ellipticals can also have of stellar populations and dust distribution with different geometries producing isophotal twist which can create a misalignment between the mass and light distributions (Goullaud et al. 2018). For lens systems, a tight alignment within $\pm 10\text{deg}$ between the major axes of the mass and light distribution has been observed for deflector galaxies with weak external shear, whereas galaxies with strong external shear can be highly misaligned (Keeton et al. 1998; Kochanek 2002; Treu et al. 2009; Sluse et al. 2012a; Gavazzi et al. 2012; Bruderer et al. 2016). However, there has been some conflict about the correlation between the ellipticity of the mass and light distributions with reports of both strong correlation (Sluse et al. 2012a; Gavazzi et al. 2012) and no correlation (Keeton et al. 1998; Ferreras et al. 2008; Rusu et al. 2016).

this chapter is organized as follows. In Section 5.2, we describe the data used in this study. We describe our methodology in Section 5.3 and the results in Section 5.4. Finally, we summarize the paper followed by a discussion in Section 5.5. When necessary, we adopt a fiducial cosmology with $H_0 = 70 \text{ km s}^{-1} \text{ Mpc}^{-1}$, $\Omega_m = 0.3$, $\Omega_\Lambda = 0.7$, and $\Omega_r = 0$. All magnitudes are given in the AB system.

Table 5.1: Observation information and references for the lens systems.

System name	Observation date	Total exposure time			Reference
		(seconds)			
		F160W	F814W	F475X	
PS J0147+4630	2017 Sept 13	2196.9	1348.0	1332.0	Berghea et al. (2017)
SDSS J0248+1913	2017 Sept 5	2196.9	1428.0	994.0	Ostrovski et al. (in preparation), Delchambre et al. (2018)
ATLAS J0259-1635	2017 Sept 7	2196.9	1428.0	994.0	Schechter et al. (2018)
DES J0405-3308	2017 Sept 6	2196.9	1428.0	1042.0	Anguita et al. (2018)
DES J0408-5354	2018 Jan 17	2196.9	1428.0	1348.0	Lin et al. (2017); Diehl et al. (2017); Agnello et al. (2017)
DES J0420-4037	2017 Nov 23	2196.9	1428.0	1158.0	Ostrovski et al. (in preparation)
PS J0630-1201	2017 Oct 5	2196.9	1428.0	980.0	Ostrovski et al. (2018); Lemon et al. (2018)
SDSS J1251+2935	2018 Apr 26	2196.9	1428.0	1010.0	Kayo et al. (2007)
SDSS J1330+1810	2018 Aug 15	2196.9	1428.0	994.0	Oguri et al. (2008)
SDSS J1433+6007	2018 May 4	2196.9	1428.0	1504.0	Agnello et al. (2018a)
PS J1606-2333	2017 Sept 1	2196.9	1428.0	994.0	Lemon et al. (2018)
DES J2038-4008	2017 Aug 29	2196.9	1428.0	1158.0	Agnello et al. (2018c)
WISE J2344-3056	2017 Sept 9	2196.9	1428.0	1042.0	Schechter et al. (2017)

5.2 *HST* sample

Our sample consists of twelve quads and one five-image system. Some of these systems were discovered by the STRong-lensing Insights into the Dark Energy Survey (STRIDES)¹ collaboration [STRIDES paper I Treu et al. (2018), paper II Anguita et al. (2018), and paper III Ostrovski et al. (in preparation)], some are recent discoveries by independent searches outside of the Dark Energy Survey (DES), and some are selected from the literature. In this section, we first describe the high-resolution imaging data obtained through *HST*. We then briefly describe the lens systems in the sample.

¹STRIDES is a Dark Energy Survey Broad External Collaboration; PI: Treu. <http://strides.astro.ucla.edu>.

5.2.1 Data

Images of the lenses were obtained using the *HST* Wide Field Camera 3 (WFC3) in three filters: F160W in the infrared (IR) channel, and F814W and F475X in the ultraviolet-visual (UVIS) channel (ID 15320, PI Treu). In the IR channel filter, we used a 4-point dither pattern and STEP100 readout sequence for the MULTIACCUM mode. This approach guarantees a sufficient dynamic range to expose both the bright lensed quasar images and the extended host galaxy. For the UVIS channel filters, we used a 2-point dither pattern. Two exposures at each position, one short and one long, were taken. Total exposure times for all the quads and the corresponding dates of observation are tabulated in Table 5.1.

The data were reduced using ASTRODRIZZLE. The pixel size after drizzling is $0''.08$ in the F160W band, and $0''.04$ in the F814W and F475X bands.

5.2.2 Quads in the sample

In this subsection, we give a brief description of each quad in our sample (Fig. 5.1).

5.2.2.1 PS J0147+4630

This quad was serendipitously discovered from the Panoramic Survey Telescope and Rapid Response System (Pan-STARRS) survey (Berghea et al. 2017). The source redshift is $z_s = 2.341 \pm 0.001$ (Lee 2017) and the deflector redshift is $z_d = 0.5716 \pm 0.0004$ (Lee 2018). Initial models from the Pan-STARRS data suggests a relatively large external shear $\gamma_{\text{ext}} \sim 0.13$.

5.2.2.2 SDSS J0248+1913

This lens system was discovered in Sloan Digital Sky Survey (SDSS) imaging data using the morphology-independent Gaussian-mixture-model supervised-machine-learning technique described in Ostrovski et al. (2017) applied to SDSS u, g and i, and *Wide-field In-*

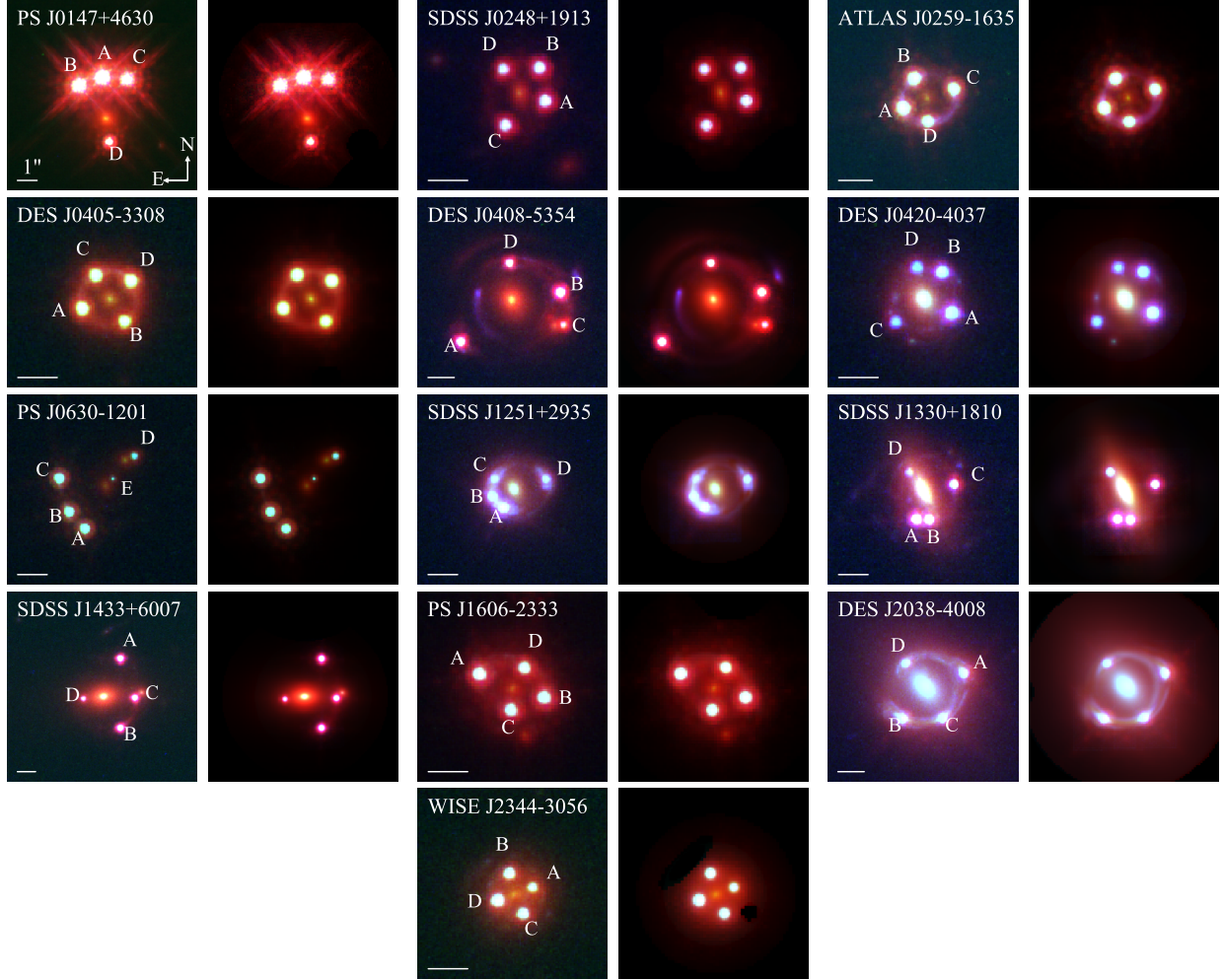


Figure 5.1: Comparison between the observed (first, third and fifth columns) and reconstructed (second, fourth and sixth columns) strong-lens systems. The three *HST* bands: F160W, F814W, and F475X are used in the red, green, and blue channels, respectively, to create the red-green-blue (RGB) images. Horizontal white lines for each system are rulers showing 1 arcsec. The relative intensities of the bands have been adjusted for each lens system for clear visualisation of the features in the system.

frared Survey Explorer (WISE) W1 and W2 catalogue level photometry (Ostrovski et al., in preparation). The lensing nature was confirmed via optical spectroscopy with the Echelle Spectrograph and Imager (ESI) on the Keck telescope in 2016 December prior to the *HST* observations presented here and will be described in Ostrovski et al. (in preparation). Delchambre et al. (2018) report the independent discovery of this spectroscopically confirmed lensed system as a lensed quasar candidate using *Gaia* observations. The lens system resides in a dense environment with several other galaxies within close proximity. Part of the lensed arc from the extended source is noticeable in the F160W band in IR.

5.2.2.3 ATLAS J0259-1635

This lens system was discovered in VLT Survey Telescope (VST)-ATLAS survey from candidates selected with quasar-like *WISE* colours (Schechter et al. 2018). The source for this system is at redshift $z_s = 2.16$ (Schechter et al. 2018).

5.2.2.4 DES J0405-3308

The discovery of this system is reported by Anguita et al. (2018). A complete or partial Einstein ring is noticeable in all the *HST* bands. The source redshift is $z_s = 1.713 \pm 0.001$ (Anguita et al. 2018).

5.2.2.5 DES J0408-5354

This system was discovered in the DES Year 1 data (Lin et al. 2017; Diehl et al. 2017; Agnello et al. 2017). The deflector redshift is $z_d = 0.597$ and the quasar redshift is $z_s = 2.375$ (Lin et al. 2017). This is a very complex lens system with multiple lensed arcs noticeable in addition to the quasar images. The sources of the lensed arcs can be components in the same source plane as the lensed quasar or they can be at different redshifts. This system has measured time-delays between the quasar images: $\Delta t_{AB} = -112 \pm 2.1$ days,

$\Delta t_{\text{AD}} = -155.5 \pm 12.8$ days, and $\Delta t_{\text{BD}} = -42.4 \pm 17.6$ days (Courbin et al. 2018).

5.2.2.6 DES J0420-4037

This lens system was discovered in DES imaging data using the morphology-independent Gaussian-mixture-model supervised-machine-learning technique described in Ostrovski et al. (2017) applied to DES g, r and i, Visible and Infrared Survey Telescope for Astronomy (VISTA) J and K, and *WISE* W1 and W2 catalogue level photometry (Ostrovski et al., in preparation). Several small knots are noticeable near the quasar images that are possibly multiple images of extra components in the source plane.

5.2.2.7 PS J0630-1201

This system is a five-image lensed quasar system (Ostrovski et al. 2018). The discovery was the result of a lens search from *Gaia* data from a selection of lens candidates from Pan-STARRS and *WISE*. The source redshift is $z_s = 3.34$ (Ostrovski et al. 2018).

5.2.2.8 SDSS J1251+2935

This quad was discovered from the SDSS Quasar Lens Search (SQLS; Oguri et al. 2006; Inada et al. 2012) (Kayo et al. 2007). The source redshift is $z_s = 0.802$ and the deflector redshift is $z_d = 0.410$ measured from the SDSS spectra (Kayo et al. 2007).

5.2.2.9 SDSS J1330+1810

This lens system was also discovered from the SQLS (Oguri et al. 2008). The redshifts of the deflector and the source are $z_d = 0.373$ and $z_s = 1.393$, respectively (Oguri et al. 2008).

5.2.2.10 SDSS J1433+6007

This lens system was discovered in the SDSS data release 12 photometric catalogue (Agnello et al. 2018a). The redshifts of the source and deflector are $z_s = 2.737 \pm 0.003$ and $z_d = 0.407 \pm 0.002$, respectively (Agnello et al. 2018a).

5.2.2.11 PS J1606-2333

This quad was discovered from *Gaia* observations through a candidate search with quasar-like *WISE* colours over the Pan-STARRS footprint (Lemon et al. 2018). The main deflector has a noticeable companion near the South-most image.

5.2.2.12 DES J2038-4008

This lens system was discovered from a combined search in *WISE* and *Gaia* over the DES footprint (Agnello et al. 2018c). The deflector and the source redshifts are $z_d = 0.230 \pm 0.002$ and $z_s = 0.777 \pm 0.001$, respectively (Agnello et al. 2018c). This system has an intricate Einstein ring with complex features from the extended quasar host galaxy.

5.2.2.13 WISE J2344-3056

This lens system was discovered in the VST-ATLAS survey (Schechter et al. 2017). This is a small-size quad with reported maximum image separation $\sim 1''.1$. Several small and faint blobs are in close proximity, two of which are particularly noticeable near the North and East images.

5.3 Lens modelling

To devise a uniform approach that will suit a wide range of quads that vary in size, configuration, light profiles, etc., we need to choose from the most general models for the lens

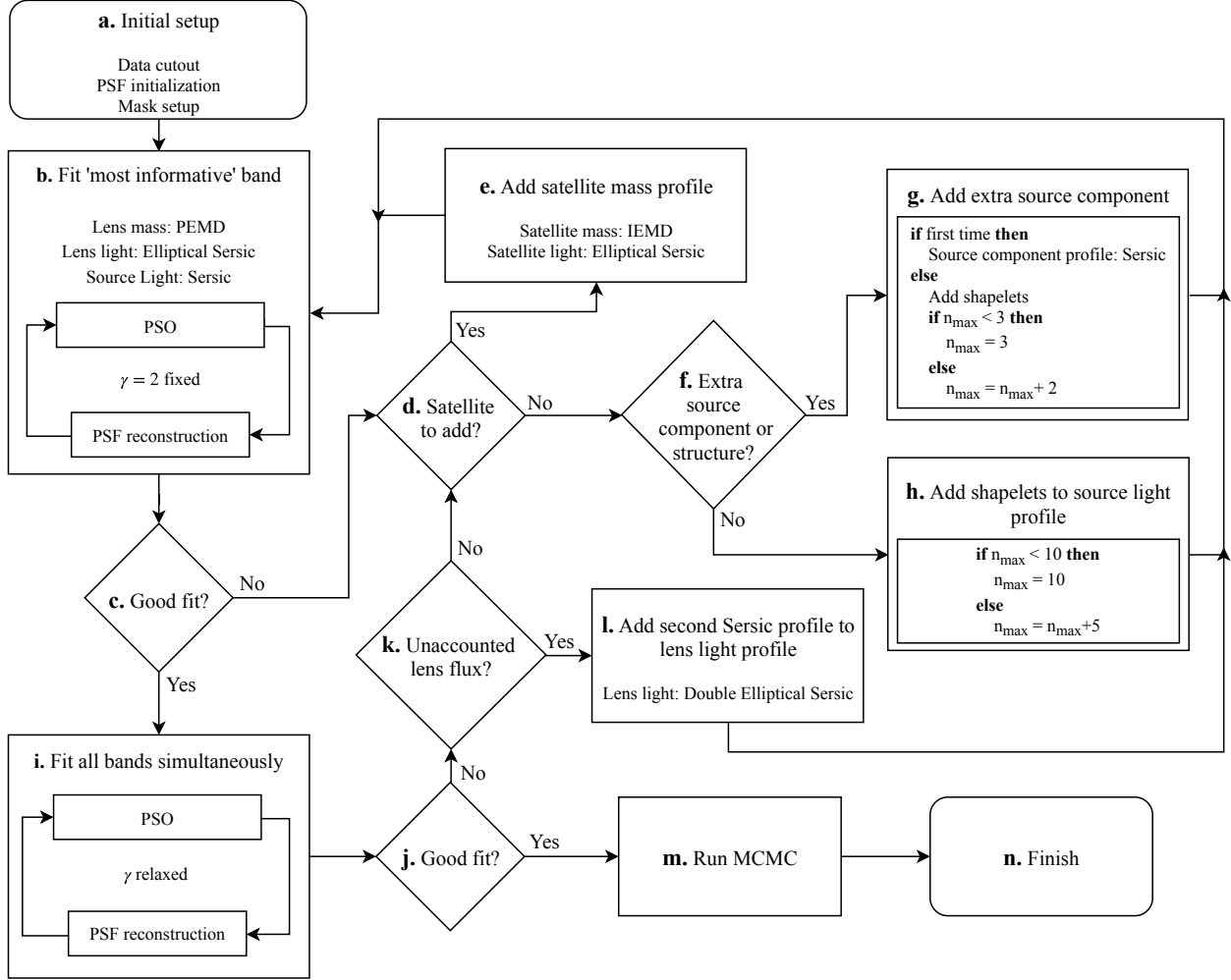


Figure 5.2: Flowchart showing the decision-tree for uniform modelling of quads to simultaneously fit multi-band data. After the initial setup (node a), the fitting is first done only with one band (node b) to iteratively choose the necessary level of complexity in the mass and light profiles (nodes d, e, f, g, h, k, l). A proposed model is accepted, if the power-law slope γ does not diverge to a bound of the allowed range (nodes j) and the p-value $\gtrsim 10^{-8}$ for the fit (nodes c, j). After deciding upon a set of profiles to simultaneously model the multi-band data (node i), the uncertainties on the model parameters are obtained by running a MCMC routine (node m).

mass profile and the light distributions. It is often required to fine-tune the choice of models by adding complexities to the lens model in a case-by-case basis to suit the purpose of the specific science driver of an investigator. However, such detailed lens-modelling is outside of the scope of this analysis. We only require our models to satisfactorily ($\chi^2_{\text{red}} \sim 1$) fit the data while being general enough to be applicable to a wide variety of lens systems.

We use the publicly available software package LENSTRONOMY² (Birrer & Amara 2018, based on Birrer et al. 2015) to model the quads in our sample. Prior to this work, LENSTRONOMY was used to measure the Hubble constant (Birrer et al. 2016) and to quantify lensing substructure (Birrer et al. 2017). We first adopt the simplest yet general set of profiles to model the deflector mass and light, and the source-light distributions (e.g. Section 5.3.1, 5.3.2). Then, we run a particle swarm optimization (PSO) routine through LENSTRONOMY to find the maximum of the likelihood function. After the PSO routine, we check for the goodness-of-fit of the best fit model. If the adopted profiles can not produce an acceptable fit to the data, we gradually add more mass or light profiles to account for extra complexities in the lens system, e.g, presence of satellites, complex structure near the Einstein ring, or extra lensed source components. We run the PSO routine after each addition of complexity until a set of adopted mass and light profiles can produce an acceptable model. Next, we obtain the posterior probability distribution functions (PDFs) of the model parameters using a Markov chain Monte Carlo (MCMC) routine. The PSO and MCMC routines in LENSTRONOMY utilize the COSMOHAMMER package (Akeret et al. 2013). COSMOHAMMER itself embeds EMCEE (Foreman-Mackey et al. 2013), which is an affine-invariant ensemble sampler for MCMC (Goodman & Weare 2010) written in PYTHON.

In this section, we first describe the profiles used to parameterize the mass and light distributions. Then, we explain the decision-tree of the modelling procedure.

²<https://github.com/sibirrer/lenstronomy>

5.3.1 Mass profile parameterization

We adopt a power-law elliptical mass distribution (PEMD) for the lens mass profile. This profile is parameterized as

$$\kappa = \frac{3 - \gamma}{2} \left(\frac{\theta_E}{\sqrt{q\theta_1^2 + \theta_2^2/q}} \right)^{\gamma-1}, \quad (5.1)$$

where γ is the power-law slope, θ_E is the Einstein radius, q is the axis ratio. The coordinates (θ_1, θ_2) depend on position angle ϕ through a rotational transformation of the on-sky coordinates that aligns the coordinate axes along the major and minor axes.

We also add an external shear profile parameterized by two parameters, γ_1 and γ_2 . The external-shear magnitude γ_{ext} and angle ϕ_{ext} are related to these parameters by

$$\gamma_{\text{ext}} = \sqrt{\gamma_1^2 + \gamma_2^2}, \quad \tan 2\phi_{\text{ext}} = \frac{\gamma_2}{\gamma_1}. \quad (5.2)$$

If there is a secondary deflector or a satellite of the main deflector, we choose an isothermal elliptical mass distribution (IEMD), which is a PEMD with the power-law slope γ fixed to 2.

5.3.2 Light profile parameterization

We choose the elliptical Sérsic function (Sérsic 1968) to model the deflector light profile. The Sérsic function is parameterized as

$$I(\theta_1, \theta_2) = I_e \exp \left[-k \left\{ \left(\frac{\sqrt{\theta_1^2 + \theta_2^2/q_L^2}}{\theta_{\text{eff}}} \right)^{1/n_{\text{Sérsic}}} - 1 \right\} \right]. \quad (5.3)$$

Here I_e is the amplitude, k is a constant that normalizes θ_{eff} so that it is the half-light radius, q_L is the axis ratio, and $n_{\text{Sérsic}}$ is the Sérsic index. The coordinates (θ_1, θ_2) also depend on the position angle ϕ_L that rotationally transforms the on-sky coordinates to align the coordinate axes with the major and minor axes. We add a ‘uniform’ light profile parameterized by only

one parameter, the amplitude, that can capture unaccounted flux from the lens by a single Sérsic profile.

The circular Sérsic function (with $q_L = 1$, $\phi_L = 0$) is adopted to model the host-galaxy-light distribution. We limit $\theta_{\text{eff}} > 0''.04$ (which is the pixel size in the UVIS bands) on the source plane to prevent the Sérsic profile to be too pointy effectively mimicking a point source. For a typical source redshift $z_s = 2$, $0''.04$ corresponds to ~ 0.33 kpc. This is a reasonable lower limit for the size of a lensed source hosting a supermassive black hole. If there are complex structures in the lensed arcs that can not be fully captured by a simple Sérsic profile, we add a basis set of shapelets (Refregier 2003; Birrer et al. 2015) on top of the Sérsic profile to reconstruct the source-light distribution. The basis set is parameterized by maximum order n_{max} , and a characteristic scale β . The number of shapelets is given by $(n_{\text{max}} + 1)(n_{\text{max}} + 2)/2$.

The quasar images are modelled with point sources with a point spread function (PSF) on the image plane.

5.3.3 Modelling procedure

We model the quads in a general framework to simultaneously fit the data from all three *HST* bands. Fig. 5.2 illustrates the flow of the modelling procedure. We describe the nodes of this flow-chart below. Each node is marked with a lowercase letter. Some of the decision nodes in Fig. 5.2 are self-explanatory and need no further elaboration.

a. Initial setup: We first pre-process the data in each band. A cutout with an appropriate field-of-view covering the lens and nearby environment from the whole image is chosen. The background flux estimated by SEXTRACTOR (Bertin & Arnouts 1996) from the whole image is subtracted from the cutout. We also select four or more stars from the *HST* images to estimate the initial PSF in each band. A circular mask with a suitable radius

is chosen to only include the deflector-light distribution, and the lensed quasar-images and arcs. If there is a nearby galaxy or a star, we mask it out unless we specifically choose to model the light profile of a satellite or companion galaxy, e.g., for DES J0408-5354, PS J0630-1201, SDSS J1433+6007 and PS J1606-2333. As PS J0630-1201 is a five-image lens, we allow the model the flexibility to produce more than four images.

b. Fit the ‘most informative’ band: It is important to judiciously initiate any optimization routine, such as the PSO, to efficiently find the global extremum. Finding the global maximum of the joint likelihood from all the bands together from a random initial point is often very expensive in terms of time and computational resource. Therefore, we first only fit the ‘most informative’ band to iteratively select the light and mass profiles necessary to account for the lens complexity. In this study, we choose F814W as the ‘most informative’ band. It is easier to decompose the deflector and the source-light distributions in the F814W band than in the F160W band as the deflector does not have a large flux near or beyond the Einstein ring. The resolution in the F814W band is also twice as high as in the F160W band. Furthermore, the deflector flux in the F475X band is often too small to reliably model the deflector-light distribution without a good prior. At first, we fix the power-law slope for the lens mass model at $\gamma = 2$ (i.e. the isothermal case). With each consecutive PSO routine, we narrow down the search region in the parameter space around the maximum of the likelihood. After each PSO routine, we iteratively reconstruct the PSF with the modelled-extended-light subtracted quasar images themselves. This is performed iteratively such that the extended light model updates its model with the new PSF to avoid biases and over-constraints on the PSF model. Similar procedures have been used in Chen et al. (2016); Birrer et al. (2017); Wong et al. (2017). The details are described in Birrer et al. (2019) and the reconstruction routines are part of LENSTRONOMY.

c. Good fit? We check for the goodness of fit by calculating the p-value for the total

χ^2 and degrees of freedom. We set p-value $\gtrsim 10^{-8}$ as a criterion to accept a model. This low p-value is enough to point out substantial inadequacies in the model while applicable to the wide variety of the lens systems in our sample. Implementing a higher p-value would require noise-level modelling which is hard to achieve in a uniform framework. The total χ^2 in this node is computed from the residuals in the F814W band only.

e. Add satellite mass profile: We add an IEMD for the satellite or companion mass profile. The light distribution of the satellite is modelled with an elliptical Sérsic profile. The initial centroid of the satellite is chosen approximately at the center of the brightest pixel in the satellite.

g. Add extra source component: If there are extra lensed source components, e.g., blobs or arcs, that are not part of the primary source structure near the Einstein ring, we add extra light profiles in the same source plane of the lensed quasar. We only add one light profile for each set of conjugate components. It is easier to identify and constrain the positions of additional source components on the image plane. Among the identifiable conjugate components from visual inspection, if one component is a smaller blob, and the others form arcs, we choose the blob's position in the image plane as the initial guess. First, we only add one circular Sérsic profile for each additional source component. For the second visit to this node, i.e. there is unaccounted structure or extra light near the additional lensed source components, we add shapelets with $n_{\max} = 3$ on top of the Sérsic profile. For each subsequent visit, we increase n_{\max} by 2.

h. Add shapelets to source-light profile: If there are structures near the Einstein ring, we add a basis set of shapelets on top of the Sérsic function to the primary source-light profile. We first add shapelets with $n_{\max} = 10$ and increase n_{\max} by 5 for each future visit to this node. The characteristic scale β of the shapelets is initiated with the best fit θ_{eff} of

the Sérsic profile for the source.

i. Fit all bands simultaneously: Before fitting all the bands simultaneously it is important to check astrometric alignment between the bands and correct accordingly if there is a misalignment. We align the data from the IR channel (F160W) with those from the UVIS band (F814W and F475X) by matching the positions of the four lensed quasar images. After that, we run PSO routines to fit all the bands simultaneously. Each PSO routine is followed by one iterative PSF reconstruction routine. During simultaneous fitting, only the intensities of the light profiles and shapelets are varied independently for different bands. All the other parameters, such as scalelength, ellipticity, position angle and Sérsic index, are set to be common across wavelengths, which is a common practice for simultaneous fitting of multi-band data (e.g. Stoughton et al. 2002; Lackner & Gunn 2012). As a result, for the case of a single Sérsic profile the best fit parameters are effectively an average over the wavelengths. However, we find the resultant best-fit parameters from the simultaneous fitting to be within 1σ systematic+statistical uncertainty of the ones from the individual fits of different bands for one representative system (DES J0405-3308) from our sample. Therefore, we assume that setting these parameters to be common across wavelengths is sufficient for the purpose of this study. For the case of shapelets or double Sérsic profile, the relative intensities of the shapelets or Sérsic components can freely vary across bands. This allows for more complex morphological variation across wavelengths and makes our assumption even more reasonable.

j. Good fit? We check for the goodness of fit with the same criteria described in node c. In this node, the total χ^2 is computed from the residuals in all the three bands. Moreover, we check that the power-law slope γ has not diverged to the bound of the allowed values when γ is relaxed in node i. This might happen if there is not enough complexity in the adopted model to reconstruct the observed fluxes. We also check if there is lens flux unaccounted by the single Sérsic profile. If the total flux in the ‘uniform’ light profile within

the effective radius is more than one per cent of that for the elliptical Sérsic profile, we decide that there is unaccounted lens flux. This can particularly happen in the F160W band as the lens light is more extended in the IR than in the UVIS channels and two concentric Sérsic functions provide a better fit to the lens light (Claeskens et al. 2006; Suyu et al. 2013). If there is no unaccounted lens light, we discard the ‘uniform’ profile from the set of lens-light profiles before moving to node m.

l. Add second Sérsic function to lens-light profile: If there is unaccounted lens flux, we discard the ‘uniform’ light profile and add a second Sérsic function on top of the first one with the same centroid. We fix the Sérsic indices for the two Sérsic profiles to $n_{\text{Sersic}} = 4$ (de Vaucouleurs profile) and $n_{\text{Sersic}} = 1$ (exponential). We fix these Sérsic indices for numerical stability. These profile fits should not be interpreted as bulge-disk decompositions. For a proper bulge-disk decomposition, more robust methods should be adopted to detect the presence of multiple components, e.g., Bayesian model comparison (D’Souza et al. 2014) and axis-ratio variation technique (Oh et al. 2017).

m. Run MCMC: If the PSO fitting sequence finds an acceptable model for the quad, we run a MCMC routine. The initial positions of the walkers are centered around the best fit found by the PSO fitting sequence.

n. Finish: After the MCMC routine, we check for the convergence of the chain. We accept the chain as converged, if the total number of steps is ~ 10 times the autocorrelation length, and the median and variance of the walker positions at each step are stable for 1 autocorrelation length at the end of the chain. We then calculate the best-fit value for each model parameter from the median of the walker positions at the last step. Similarly, 1σ confidence levels are computed from the 16- and 84-th percentiles in the last step.

5.3.4 Systematics

We estimate the systematic uncertainties of the lens model parameters by marginalizing over several numerical settings. We performed the modelling technique described in Section 5.3.3 with eleven different numerical settings: varying the lens-mask size, varying the mask size for extra quasar-images for PSF reconstruction, varying the sampling resolution of the reconstructed *HST* image, without PSF reconstruction, and with different realisations of the reconstructed PSF. We checked for systematics for the lens system SDSS J0248+1913. This system was chosen for two reasons: (i) this system has relatively fainter arc compared to the point source and deflector brightness, thus providing a conservative estimate of the systematics, and (ii) the modelling procedure is one of the simplest ones that enables running the modelling procedure numerous times with different settings in relatively less time. We assume the systematics are the same order of magnitude for the other lens systems in the sample.

5.4 Results

In this section, we first describe the lens models and report the model parameters along with some derived parameters for all the quads. Then, we investigate the alignment between the mass and light profiles and report our findings. In Appendix 5.A, 5.B and 5.C we report additional inferred lens model parameters that are not directly relevant for the scientific investigation carried out here but may be of interest to some readers, especially in planning future follow-up and observations.

5.4.1 Efficiency of the uniform framework

All the 13 quads are reliably (p-value ~ 1 , Table 5.2) modelled following the uniform approach described in Section 5.3. The framework was designed and tuned from the experience

gained from uniformly modelling the first ten observed quads in the sample. The three quads, SDSS J1251+2935, SDSS J1330+1810 and SDSS J1433+6007, were observed after the design phase. We effectively modelled these three lenses implementing the general framework, which validates its effectiveness. The total investigator time spent for these two lenses is ~ 3 hours per lens including data reduction, initial setup and quality control of the model outputs. The number of CPU hours (on state-of-the-art machines³) per system ranges between 50 to 500 depending on the complexity of the model.

5.4.2 Lens models

The set of profiles chosen through the decision-tree for modelling the quads along with the corresponding p-values are listed in Table 5.2. We show a breakdown of the best-fit models in each band for the quads, SDSS J0248+1913, DES J0408-5354, SDSS J1251+2935, SDSS J1433+6007, as examples, in Fig. 5.3. Model breakdowns for the rest of lenses are provided in Appendix 5.D. We show the red-green-blue (RGB) images produced from the *HST* data alongside the reconstructed RGB images for all the quads in Fig. 5.1.

We checked the robustness of the estimated lens model parameters with and without PSF reconstructions. We find the Einstein radius θ_E , axis ratio q , mass position angle ϕ , external shear γ_{ext} and shear angle ϕ_{ext} to be robustly (within 1σ systematic+statistical uncertainty) estimated. However, the power-law slope γ is affected by $\geq 1\sigma$ systematic+statistical uncertainty due to deviations of the reconstructed PSF. This is expected as γ depends on the thickness of the Einstein ring and this thickness in the reconstructed model in turn depends on the PSF.

We investigated if setting the Sérsic radius and index of the source light profile common across wavelength bands biases the measurement of the power-law slope. For one represen-

³We utilized the Hoffman2 Shared Cluster provided by UCLA Institute for Digital Research and Education’s Research Technology Group. <https://idre.ucla.edu/hoffman2>.

tative system (DES J0405+3308) from our sample, we find the power-law slope from the individual fits of different bands to agree within 1σ systematic+statistical uncertainty of the one from the simultaneous fit. Therefore, we conclude that setting the scaling parameters of the source light profile except the intensity to be common across wavelengths does not significantly ($> 1\sigma$) bias the power-law slope.

We checked if the lens model parameters are stable with increasing complexity in the model (Fig. 5.4). The stability of the Einstein radius θ_E and the external shear γ_{ext} improves if the mass profile of a satellite is explicitly modelled. For increasing complexity in modelling the source-light distribution, the power-law slope γ , the Einstein radius θ_E and the external convergence γ_{ext} are stable.

We report the lens model parameters: Einstein radius θ_E , power-law slope γ , axis ratio q , position angle ϕ , external shear γ_{ext} , and shear angle ϕ_{ext} and deflector light parameters: effective radius θ_{eff} , axis ratio q_L , and position angle ϕ_L in Table 5.3. For the deflectors fitted with double Sérsic profiles, the ellipticity and position angles are computed by fitting isophotes to the double Sérsic light distribution. We use the PHOTUTILS⁴ package in PYTHON for measuring the isophotes which implements an iterative method described by Jedrzejewski (1987). We tabulate the astrometric positions of the deflector galaxy and the quasar images in Table 5.4. The apparent magnitudes of the deflector galaxy and the quasar images in each of the three *HST* bands are given in Table 5.5.

⁴<http://photutils.readthedocs.io>

Table 5.2: Lens model profiles.

System name	Mass profiles	Lens-light profiles	Source-light profiles	p-value*	Decision flow**
PS J0147+4630	PEMD	Double elliptical Sérsic	Sérsic Point source (image plane)	1.0	abcijklbcijmn
SDSS J0248+1913	PEMD	Elliptical Sérsic	Sérsic Point source (image plane)	1.0	abcijmn
ATLAS J0259-1635	PEMD	Elliptical Sérsic	Sérsic Shapelets ($n_{\max} = 10$) Point source (image plane)	1.0	abcdfhbcijmn
DES J0405-3308	PEMD	Elliptical Sérsic	Sérsic Point source (image plane)	1.0	abcijmn
DES J0408-5354	PEMD IEMD [†]	Elliptical Sérsic Elliptical Sérsic [†]	Sérsic Shapelets ($n_{\max} = 10$) Sérsic [†] Shapelets [†] ($n_{\max} = 3$) Sérsic [†] Point source (image plane)	1.0	abcdebcdfgbcdfgbcijkdf gbcijkdfhbcijmn
DES J0420-4037	PEMD	Elliptical Sérsic	Sérsic Sérsic [†] Sérsic [†] Point source (image plane)	1.0	abcijkdfgbcijmn
PS J0630-1201	PEMD IEMD [†]	Elliptical Sérsic Elliptical Sérsic [†]	Sérsic Point source (image plane)	1.0	abcdebcijmn
SDSS J1251+2935	PEMD	Double elliptical Sérsic	Sérsic Shapelets ($n_{\max} = 10$) Point source (image plane)	1.0	abcijklbcijkdfhbcijmn
SDSS J1330+1810	PEMD	Double elliptical Sérsic	Sérsic Shapelets ($n_{\max} = 10$) Point source (image plane)	0.005	abcijklbcijkdfhbcijmn
SDSS J1433+6007	PEMD IEMD [†]	Double elliptical Sérsic Elliptical Sérsic [†]	Sérsic Point source (image plane)	1.0	abcdebcijklbcijmn
PS J1606-2333	PEMD IEMD [†]	Double elliptical Sérsic Elliptical Sérsic [†]	Sérsic Shapelets ($n_{\max} = 10$) Point source (image plane)	1.0	abcdebcdfhbcijklbcijmn
DES J2038-4008	PEMD	Double elliptical Sérsic	Sérsic Shapelets ($n_{\max} = 10$) Point source (image plane)	1.0	abcdfhbcijklbcijmn
WISE J2344-3056	PEMD	Double elliptical Sérsic	Sérsic Point source (image plane)	1.0	abcijklbcijmn

* The p-value is for the combined χ^2 from all three bands.

** Labels of nodes visited during the modelling procedure in the flow-chart shown in Fig. 5.2.

[†] Satellite or extra source component separate from the central source.

Table 5.3: Lens model parameters. The reported uncertainties are systematic and statistical uncertainties added in quadrature.

System name	θ_E (arcsec)	γ	q	ϕ (E of N) (degree)	γ_{ext}	ϕ_{ext} (E of N) (degree)	$\theta_{\text{eff}}^\dagger$ (arcsec)	q_L^\dagger	ϕ_L (E of N) † (degree)
PS J0147+4630	1.90 ± 0.01	2.00 ± 0.05	0.81 ± 0.04	-55 ± 6	0.16 ± 0.02	-72 ± 3	3.45 ± 0.10	0.93 ± 0.06	49 ± 16
SDSS J0248+1913	0.804 ± 0.004	2.19 ± 0.04	0.40 ± 0.06	46 ± 6	0.09 ± 0.02	6 ± 3	0.16 ± 0.03	0.40 ± 0.02	13 ± 1
ATLAS J0259-1635	0.75 ± 0.01	2.01 ± 0.04	0.66 ± 0.04	18 ± 6	0.00 ± 0.02	-30 ± 3	1.00 ± 0.09	0.38 ± 0.04	20 ± 4
DES J0405-3308	0.70 ± 0.01	1.99 ± 0.04	0.95 ± 0.05	41 ± 12	0.01 ± 0.02	-79 ± 5	0.44 ± 0.09	0.55 ± 0.05	37 ± 4
DES J0408-5354	1.80 ± 0.01	1.98 ± 0.04	0.62 ± 0.04	18 ± 6	0.05 ± 0.02	-15 ± 3	2.15 ± 0.09	0.82 ± 0.04	28 ± 4
DES J0420-4037	0.83 ± 0.01	1.97 ± 0.04	0.87 ± 0.04	24 ± 6	0.03 ± 0.02	-20 ± 4	0.44 ± 0.09	0.61 ± 0.04	27 ± 4
PS J0630-1201	1.02 ± 0.01	2.00 ± 0.04	0.53 ± 0.04	-27 ± 6	0.14 ± 0.02	-2 ± 3	1.64 ± 0.09	0.79 ± 0.04	12 ± 4
SDSS J1251+2935	0.84 ± 0.01	1.97 ± 0.04	0.71 ± 0.04	28 ± 6	0.07 ± 0.02	-88 ± 3	1.02 ± 0.09	0.67 ± 0.04	23 ± 4
SDSS J1330+1810	0.954 ± 0.005	2.00 ± 0.04	0.59 ± 0.06	24 ± 6	0.07 ± 0.02	8 ± 3	0.40 ± 0.03	0.28 ± 0.02	24 ± 1
SDSS J1433+6007	1.71 ± 0.01	1.96 ± 0.04	0.51 ± 0.04	-81 ± 6	0.09 ± 0.02	-30 ± 3	1.10 ± 0.09	0.56 ± 0.04	-88 ± 4
PS J1606-2333	0.63 ± 0.01	1.97 ± 0.04	0.88 ± 0.05	41 ± 10	0.16 ± 0.02	53 ± 3	1.36 ± 0.09	0.60 ± 0.07	-24 ± 5
DES J2038-4008	1.38 ± 0.01	2.35 ± 0.04	0.61 ± 0.04	38 ± 6	0.09 ± 0.02	-58 ± 3	2.85 ± 0.09	0.67 ± 0.04	38 ± 4
WISE J2344-3056	0.52 ± 0.01	1.95 ± 0.05	0.51 ± 0.06	-70 ± 6	0.06 ± 0.02	-68 ± 8	2.61 ± 0.19	0.76 ± 0.03	-69 ± 4

† Calculated from the F160W band for the lenses with double Sérsic fit for the lens light.

Table 5.4: Astrometric positions of the deflector and quasar images. The reported uncertainties are on relative astrometry and they are systematic and statistical uncertainties added in quadrature.

System name	Deflector		Image A		Image B		Image C		Image D	
	α	δ	$\Delta\alpha$	$\Delta\delta$	$\Delta\alpha$	$\Delta\delta$	$\Delta\alpha$	$\Delta\delta$	$\Delta\alpha$	$\Delta\delta$
	(degree)	(degree)	(arcsec)	(arcsec)	(arcsec)	(arcsec)	(arcsec)	(arcsec)	(arcsec)	(arcsec)
PS J0147+4630	26.792331	46.511559	-0.0046 ± 0.0002	2.0649 ± 0.0001	1.1671 ± 0.0002	1.6555 ± 0.0001	-1.2439 ± 0.0002	1.9716 ± 0.0002	-0.3462 ± 0.0005	-1.1560 ± 0.0003
SDSS J0248+1913	42.203099	19.225246	-0.787 ± 0.001	-0.175 ± 0.001	-0.645 ± 0.001	0.658 ± 0.001	0.211 ± 0.001	-0.791 ± 0.001	0.261 ± 0.001	0.620 ± 0.001
ATLAS J0259-1635	44.928561	-16.595376	0.602 ± 0.003	-0.216 ± 0.001	0.275 ± 0.001	0.658 ± 0.001	-0.883 ± 0.001	0.340 ± 0.001	-0.124 ± 0.001	-0.614 ± 0.001
DES J0405-3308	61.498964	-33.147417	0.536 ± 0.001	-0.155 ± 0.001	-0.533 ± 0.001	-0.478 ± 0.002	0.186 ± 0.002	0.686 ± 0.002	-0.684 ± 0.001	0.538 ± 0.004
DES J0408-5354	62.090451	-53.899816	1.981 ± 0.002	-1.495 ± 0.001	-1.775 ± 0.001	0.369 ± 0.001	-1.895 ± 0.002	-0.854 ± 0.002	0.141 ± 0.001	1.466 ± 0.002
DES J0420-4037	65.194858	-40.624081	-0.698 ± 0.001	-0.231 ± 0.001	-0.457 ± 0.001	0.802 ± 0.001	0.711 ± 0.001	-0.448 ± 0.001	0.172 ± 0.002	0.908 ± 0.002
PS J0630-1201	97.537601	-12.022037	0.613 ± 0.001	-1.349 ± 0.001	1.131 ± 0.001	-0.783 ± 0.001	1.470 ± 0.001	0.337 ± 0.001	-1.050 ± 0.002	1.082 ± 0.001
SDSS J1251+2935	192.781427	29.594652	0.3370 ± 0.0005	-0.6245 ± 0.0005	0.698 ± 0.001	-0.265 ± 0.001	0.628 ± 0.001	0.327 ± 0.001	-1.089 ± 0.001	0.310 ± 0.002
SDSS J1330+1810	202.577755	18.175788	0.247 ± 0.001	-1.025 ± 0.001	-0.179 ± 0.001	-1.049 ± 0.001	-1.013 ± 0.001	0.133 ± 0.002	0.4938 ± 0.0004	0.550 ± 0.002
SDSS J1433+6007	218.345420	60.120777	-0.960 ± 0.002	2.070 ± 0.003	-0.962 ± 0.003	-1.679 ± 0.003	-1.740 ± 0.002	-0.072 ± 0.002	1.056 ± 0.003	-0.127 ± 0.003
PS J1606-2333	241.500982	-23.556114	0.856 ± 0.001	0.298 ± 0.001	-0.769 ± 0.001	-0.298 ± 0.001	0.064 ± 0.001	-0.616 ± 0.001	-0.272 ± 0.001	0.449 ± 0.001
DES J2038-4008	309.511379	-40.137024	-1.529 ± 0.001	0.495 ± 0.001	0.7867 ± 0.0005	-1.216 ± 0.001	-0.735 ± 0.001	-1.186 ± 0.001	0.656 ± 0.001	0.860 ± 0.001
WISE J2344-3056	356.070739	-30.940633	-0.475 ± 0.001	0.281 ± 0.001	0.110 ± 0.001	0.632 ± 0.001	-0.235 ± 0.001	-0.376 ± 0.001	0.398 ± 0.001	-0.038 ± 0.001

[†] The relative positions of the image E are $\Delta\alpha = -0''.330 \pm 0''.003$ and $\Delta\delta = 0''.326 \pm 0''.002$.

5.4.3 Alignment between mass and light distributions

In this subsection, we report our results on the alignment between the mass and light distributions in our sample of quads (Fig. 5.5).

5.4.3.1 Centroid

The centers of the mass and light distributions match very well for most of the quads with a root-mean-square (RMS) of $0''.04$ excluding three outliers (Fig. 5.5a). The three outliers are PS J0147+4630, DES J0408-5354 and PS J0630-1201. In PS J0630-1201, there are two deflectors with comparable mass creating a total of five images. If the two deflectors are embedded in the same dark matter halo, the center of the luminous part of the deflector can have an offset from the center of the halo mass. The other two outliers also have nearby companions possibly biasing the centroid estimation.

5.4.3.2 Ellipticity

We find a weak correlation between the ellipticity parameters of the mass and light distribution for the whole sample (Fig. 5.5b). We calculate the Pearson correlation coefficient between the axis ratios q and q_L of the mass and light distributions, respectively, in the following way. We sample 1000 points from a two-dimensional Gaussian distribution that is centered on the axis ratio pair (q, q_L) for each quad. We take the standard deviation for this Gaussian distribution along each axis equal to the 1σ systematic+statistical uncertainty. We take the covariance between the sampled points for each lens as zero as we observe no degeneracy in the posterior PDF of the axis ratios for individual lenses. The Pearson correlation coefficient for the distribution of the sampled points from all the quads is $r = 0.2$ (weak correlation).

Table 5.5: Photometry of the deflector and quasar images. The deflector magnitudes are calculated from the total flux within a $5'' \times 5''$ square aperture. Magnitudes are given in the AB system. The reported uncertainties are systematic and statistical uncertainties added in quadrature.

System name	Filter	Deflector	A	B	C	D
PS J0147+4630	F160W	18.3 ± 0.1	15.46 ± 0.03	15.78 ± 0.03	16.18 ± 0.03	18.05 ± 0.03
	F814W	19.4 ± 0.1	15.79 ± 0.03	16.09 ± 0.03	16.45 ± 0.03	18.21 ± 0.03
	F475X	21.8 ± 0.3	16.39 ± 0.03	16.67 ± 0.03	17.13 ± 0.03	18.74 ± 0.03
SDSS J0248+1913	F160W	20.8 ± 0.1	19.88 ± 0.04	20.41 ± 0.04	19.91 ± 0.03	20.13 ± 0.04
	F814W	22.7 ± 0.1	20.20 ± 0.03	20.23 ± 0.03	20.43 ± 0.03	20.66 ± 0.03
	F475X	26.4 ± 0.3	21.14 ± 0.03	21.18 ± 0.03	21.35 ± 0.03	21.80 ± 0.03
ATLAS J0259-1635	F160W	20.7 ± 0.1	18.48 ± 0.03	18.57 ± 0.04	19.06 ± 0.03	19.30 ± 0.04
	F814W	22.7 ± 0.1	19.00 ± 0.03	19.16 ± 0.03	19.62 ± 0.03	19.70 ± 0.03
	F475X	–	21.08 ± 0.03	20.81 ± 0.03	21.50 ± 0.04	21.33 ± 0.03
DES J0405-3308	F160W	20.2 ± 0.1	19.43 ± 0.07	19.58 ± 0.04	19.60 ± 0.04	19.33 ± 0.03
	F814W	22.0 ± 0.1	20.22 ± 0.04	20.60 ± 0.04	20.33 ± 0.03	20.09 ± 0.03
	F475X	25.0 ± 0.3	22.16 ± 0.04	22.81 ± 0.04	22.04 ± 0.03	21.91 ± 0.03
DES J0408-5354	F160W	18.6 ± 0.1	20.18 ± 0.03	19.79 ± 0.04	20.33 ± 0.04	20.82 ± 0.04
	F814W	19.9 ± 0.1	20.38 ± 0.03	20.00 ± 0.03	21.66 ± 0.03	20.87 ± 0.03
	F475X	22.6 ± 0.3	21.20 ± 0.03	21.34 ± 0.03	23.16 ± 0.03	21.86 ± 0.04
DES J0420-4037	F160W	18.6 ± 0.1	20.18 ± 0.03	21.03 ± 0.04	21.85 ± 0.04	21.96 ± 0.05
	F814W	19.5 ± 0.1	20.44 ± 0.03	20.96 ± 0.03	21.71 ± 0.03	21.98 ± 0.04
	F475X	21.5 ± 0.3	20.66 ± 0.03	21.25 ± 0.03	22.09 ± 0.03	22.09 ± 0.03
PS J0630-1201 [†]	F160W	20.4 ± 0.1	18.71 ± 0.03	18.82 ± 0.03	18.74 ± 0.03	21.01 ± 0.04
	F814W	22.5 ± 0.1	19.70 ± 0.03	19.67 ± 0.03	19.71 ± 0.03	21.67 ± 0.03
	F475X	26.7 ± 0.3	21.06 ± 0.03	20.92 ± 0.03	21.10 ± 0.03	23.03 ± 0.03

[†] The magnitudes of image E are 22.51 ± 0.10 , $23.40 \pm .04$, and 24.77 ± 0.04 in the F160W, F814W, and F475X bands, respectively.

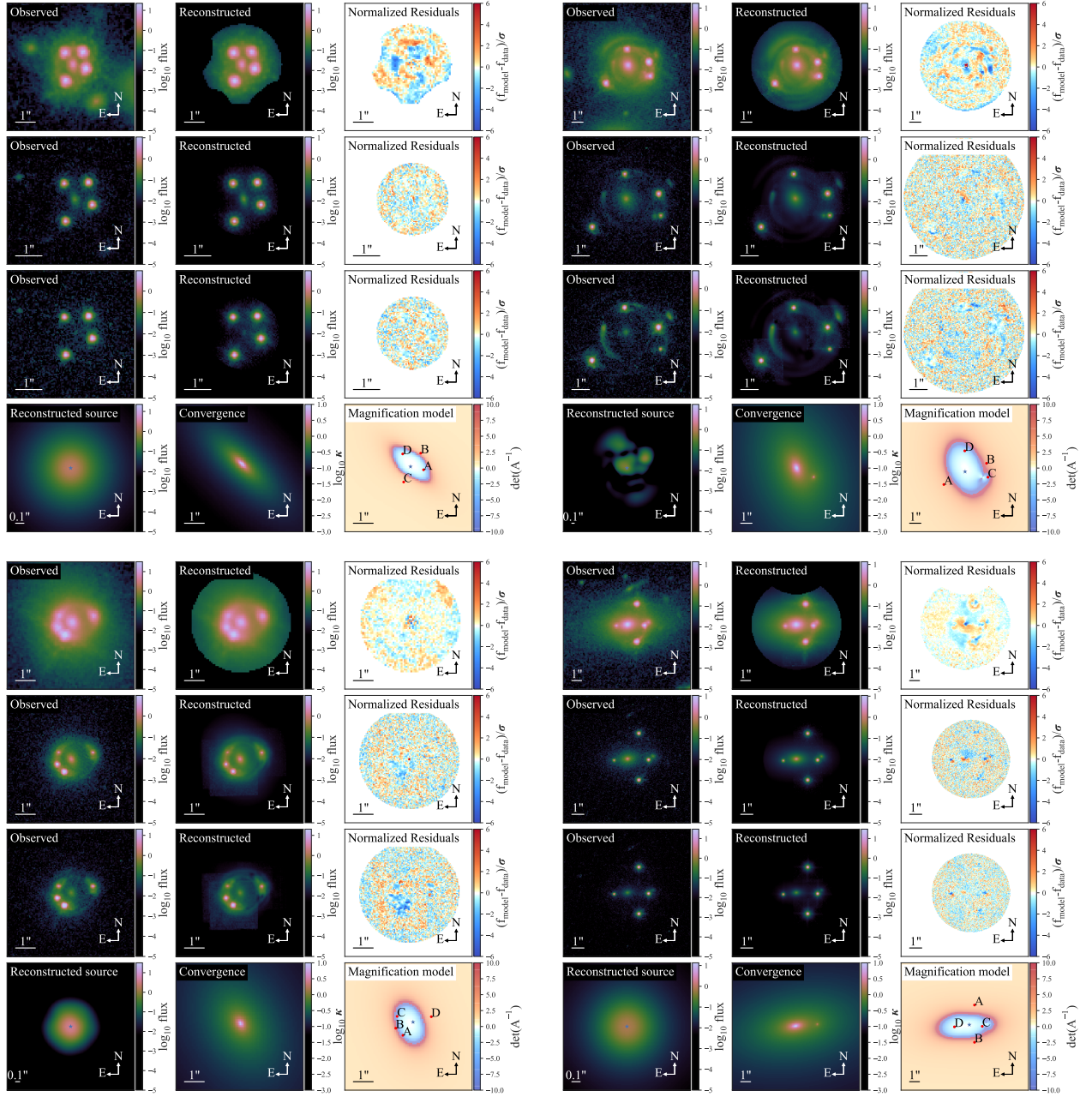


Figure 5.3: Best fit models for SDSS J0248+1913 (top left), DES J0408-5354 (top right), SDSS J1251+2935 (bottom left), and SDSS J1433+6007 (bottom right). The first three rows for each lens system show the observed image, reconstructed lens image, and the normalized residuals in three *HST* bands: F160W, F814W, and F475X, respectively. The fourth row shows the reconstructed source in the F160W band, the convergence, and the magnification model. The models for the rest of the sample are shown in Appendix 5.D (Figure 5.7, 5.8).

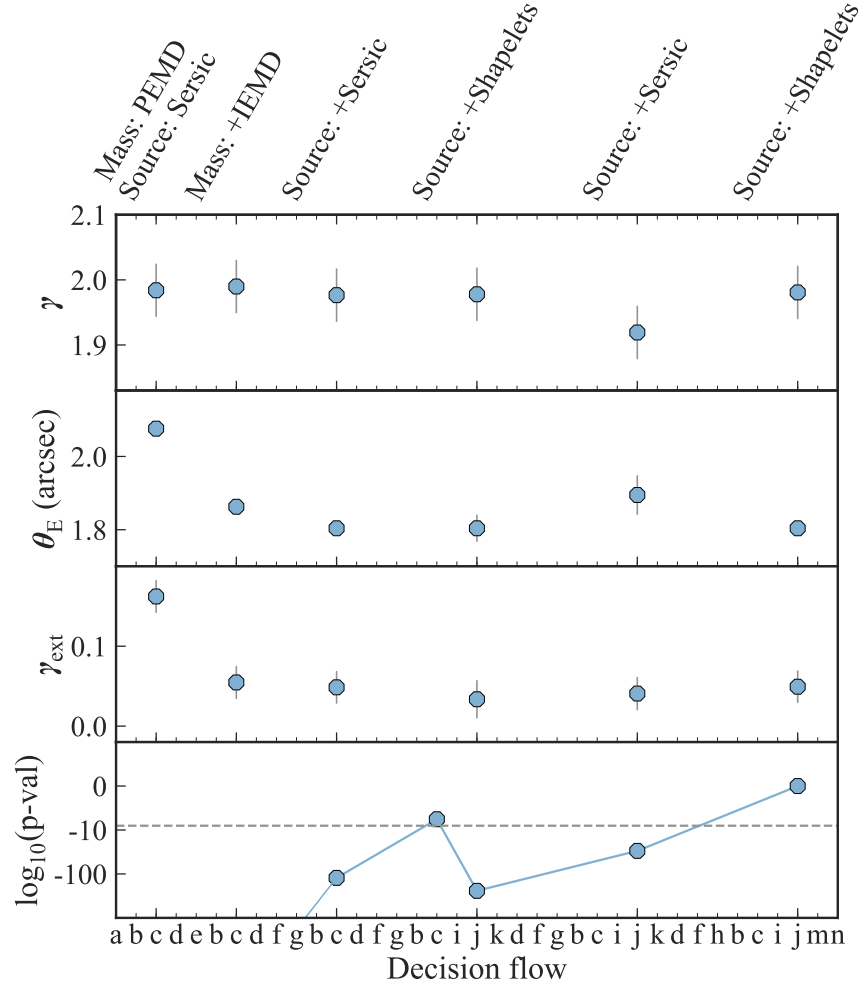


Figure 5.4: Stability of lens model parameters with increasing model complexity. The four panels show the power-law slope γ , Einstein radius θ_E , external shear γ_{ext} , and logarithm of p-value of the reduced- χ^2 of the model fit, top to bottom, along the decision-flow for the quad DES J0408-5354. The bottom-horizontal axis denotes the node identifiers along the decision flow as in Fig. 5.2. Short descriptions for added profiles at corresponding points along the decision flow are shown along the top-horizontal axis. Solid-grey lines attached to the blue circles show 1σ systematic+statistical uncertainty. The dashed-grey line at the bottom panel marks the threshold $\text{p-value}=10^{-8}$ for accepting a model. The p-value decreases after crossing the threshold the first time due to addition of the other two bands for simultaneous fitting, which requires more complexity in the model.

Table 5.6: Continued from Table 5.5.

System name	Filter	Deflector	A	B	C	D
SDSS J1251+2935	F160W	18.3 ± 0.1	19.35 ± 0.03	20.25 ± 0.05	21.30 ± 0.06	21.02 ± 0.05
	F814W	19.4 ± 0.1	20.01 ± 0.03	20.80 ± 0.04	22.80 ± 0.06	21.66 ± 0.04
	F475X	21.4 ± 0.3	20.01 ± 0.03	20.73 ± 0.04	22.73 ± 0.04	21.95 ± 0.04
SDSS J1330+1810	F160W	17.9 ± 0.1	19.17 ± 0.03	19.36 ± 0.03	20.00 ± 0.03	21.24 ± 0.05
	F814W	19.1 ± 0.1	20.11 ± 0.03	20.03 ± 0.03	20.48 ± 0.03	20.56 ± 0.03
	F475X	21.4 ± 0.3	20.31 ± 0.03	20.82 ± 0.04	21.24 ± 0.03	21.58 ± 0.04
SDSS J1433+6007	F160W	18.1 ± 0.1	20.43 ± 0.03	20.47 ± 0.04	20.55 ± 0.04	21.56 ± 0.04
	F814W	19.2 ± 0.1	20.25 ± 0.03	20.17 ± 0.03	20.45 ± 0.03	21.74 ± 0.03
	F475X	21.2 ± 0.3	20.31 ± 0.03	20.16 ± 0.03	20.49 ± 0.03	21.93 ± 0.04
PS J1606-2333	F160W	19.5 ± 0.1	19.59 ± 0.03	19.65 ± 0.04	19.99 ± 0.03	19.47 ± 0.03
	F814W	20.6 ± 0.1	19.06 ± 0.03	19.22 ± 0.03	19.38 ± 0.03	19.52 ± 0.03
	F475X	21.8 ± 0.3	19.52 ± 0.04	19.76 ± 0.04	19.97 ± 0.03	20.48 ± 0.04
DES J2038-4008	F160W	16.4 ± 0.1	18.48 ± 0.03	18.27 ± 0.03	18.60 ± 0.03	19.49 ± 0.04
	F814W	17.4 ± 0.1	20.25 ± 0.03	19.99 ± 0.03	20.05 ± 0.03	20.88 ± 0.03
	F475X	19.1 ± 0.3	21.02 ± 0.03	20.89 ± 0.03	20.71 ± 0.03	21.43 ± 0.03
WISE J2344-3056	F160W	19.0 ± 0.1	21.36 ± 0.05	20.94 ± 0.04	21.16 ± 0.06	20.78 ± 0.04
	F814W	20.0 ± 0.1	21.76 ± 0.03	21.20 ± 0.03	21.27 ± 0.03	20.76 ± 0.03
	F475X	21.6 ± 0.3	22.79 ± 0.03	21.68 ± 0.03	21.66 ± 0.03	21.13 ± 0.03

5.4.3.3 Position angle

The position angles of the elliptical mass and light distributions are well aligned for nine out of 13 quads. The standard deviation of the misalignment in position angles for these eight lenses is 11deg. (Fig. 5.5c). The systems with large misalignment also have large external shear. We find a strong correlation between the misalignment angle and the external shear magnitude ($r = 0.74$, Fig. 5.5d). We find weak correlation between the misalignment angle and the mass axis ratio q ($r = 0.21$, Fig. 5.5e).

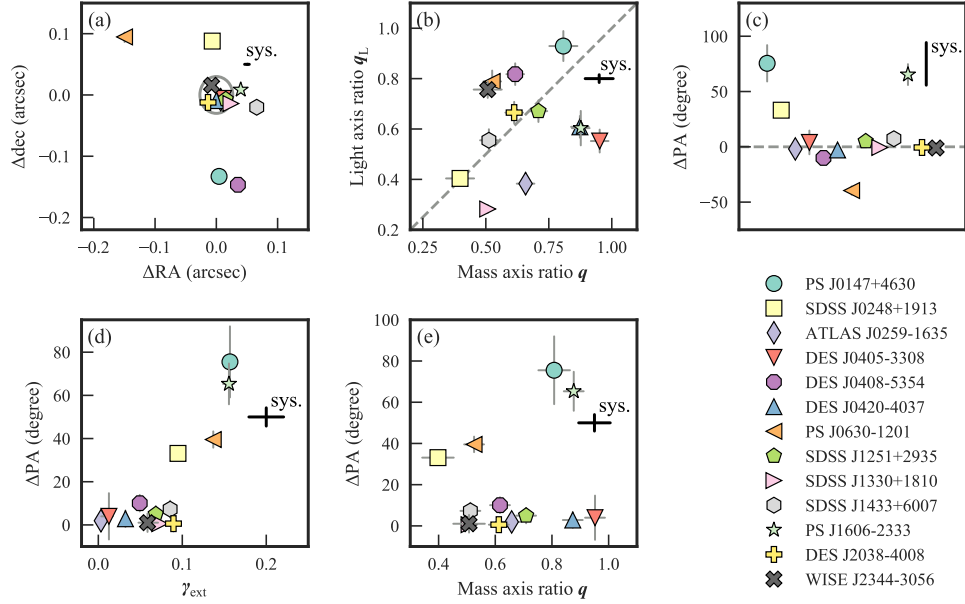


Figure 5.5: Mass and light alignments in the deflector galaxies: comparison between (a) the mass and light centroids, (b) the axis ratios of the light and mass profiles, (c) the misalignment angle (between the mass and light profiles’ position angles), (d) the misalignment angle and the external shear, and (e) the misalignment angle and the mass profile axis ratio. The thin-solid-grey lines attached to the data points show 1σ statistical uncertainty and the thick-solid-black bars annotated with ‘sys.’ in each figure show the 1σ systematic uncertainty. The systematic uncertainty is estimated by marginalizing over various numerical settings for the system SDSS J0248+1913 as described in Section 5.3.4. In (a) the solid-grey ellipse centered at (0, 0) shows the root-mean-square (RMS) spread of ΔRA and Δdec for nine lens systems excluding the systems with large deviations: PS J0147+4630, DES J0408-5354 and PS J0630-1201. This RMS spread can be taken as the upper limit of the systematics. The dashed grey line traces the perfect 1-to-1 correlation in (b) and the zero misalignment in (c) to aid visualisation. The centers of the mass and light distributions match very well (a). The systems with large offsets between the mass and light centroids have satellites or comparable-mass companions possibly biasing the centroid estimate. The axis ratios of the light and mass distributions are only weakly correlated (b). The position angles align very well within $\pm 12\text{deg}$ for eight out of the 12 systems (c). Systems with large misalignment have larger values of external shear (d). However, there is very weak to no correlation between the position angle misalignment and mass ellipticity (e).

5.4.4 Deviation of flux ratios from macro-model

Stars or dark subhalos in the deflector can produce additional magnification or de-magnification of the quasar images through microlensing and millilensing, respectively (for detailed description, see Schneider et al. 2006). In that case, the flux ratios of the quasar images will be different than those predicted by the smooth macro-model. Deviation of the flux ratios can also be produced by baryonic structures (Gilman et al. 2017) or disks (Hsueh et al. 2016, 2017), quasar variability with a time delay, and dust extinction (Yonehara et al. 2008; Anguita et al. 2008). We quantify this deviation of the flux ratios in the quasar images as a χ^2 -value by

$$\chi_f^2 = \sum_{I, J \in \{A, B, C, D\}}^{I \neq J} \frac{(f_{IJ, \text{observed}} - f_{IJ, \text{model}})^2}{\sigma_{f_{IJ}}^2}, \quad (5.4)$$

where $f_{IJ} = F_I/F_J$ is the flux ratio between the images I and J. We assume 20 per cent flux error giving $\sigma_{f_{IJ}} = 0.28f_{IJ}$. We set this error level considering the typical order of magnitude for intrinsic variability of quasars (e.g. Bonvin et al. 2017; Courbin et al. 2018). Although, many of the quads in our sample have short predicted time-delays (Table 5.10), where intrinsic variability is not a major source of deviation in flux-ratios, we take 20 per cent as a conservative error estimate for these lenses.

If the flux ratios are consistent with the macro-model, χ_f^2 is expected to follow the $\chi^2(3)$ distribution, i.e. $\chi_f^2 \sim \chi^2(3)$, as only three out of the six flux ratios are independent producing three degrees of freedom. However, the χ_f^2 -distribution is shifted toward a higher value than $\chi^2(3)$ (Fig. 5.6). The mean of the combined distribution of $\log_{10} \chi_f^2$ from all the three *HST* bands is 2.04. A Kolmogorov-Smirnov test of whether the observed χ_f^2 -distribution matches with the $\chi^2(3)$ -distribution yields a p-value of ~ 0 . The shift is higher in shorter wavelengths. The mean of the $\log_{10} \chi_f^2$'s in the F160W, F814W, and F475X bands are 1.85, 2.09, and 2.17, respectively. This is expected, as the quasar size is smaller in shorter wavelengths making it more affected by microlensing, and as shorter wavelengths are also more affected by dust extinction.

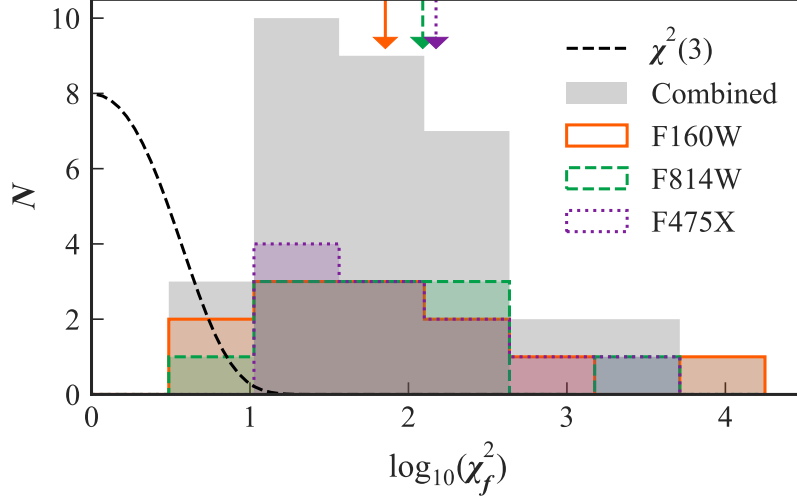


Figure 5.6: Distribution of χ_f^2 for flux-ratio anomalies from Equation (5.4) assuming 20 per cent error in flux. The distribution is for twelve quads in our sample excluding PS J0630-1201. The χ_f^2 -distributions in bands F160W, F814W, and F475X are shown in orange, green, and purple shaded regions, respectively. The χ_f^2 -distribution from all the bands combined is shown as the grey shaded region. The black dashed line shows the expected $\chi_f^2 \sim \chi^2(3)$ distribution in the absence of microlensing. The arrows on the top show the mean of the χ_f^2 -values in bands F160W (solid orange), F814W (dashed green), and F475X (dotted purple). The combined χ_f^2 -distribution is shifted to higher values. The shift is higher for shorter wavelengths, as the quasar size gets smaller with decreasing wavelength making it more susceptible to microlensing.

5.5 Summary and Discussion

We presented a general framework to uniformly model large samples of quads while attempting to minimize investigator time. We apply this framework to model a sample of 13 quads and simultaneously fit imaging data from three *HST* WFC3 bands. All the quads are satisfactorily (p-value $\gtrsim 10^{-8}$) modelled in our uniform framework. We choose the p-value threshold to be suitably low to be applicable to our quad sample with large morphological variation while being able to point out deficiencies in the modelling choice of profiles along the decision tree. In the end, most of the lens systems in our sample are modelled with p-value ~ 1 (Table 5.2). Thus, we showed that a large variety of quads can be modelled with a basic set of mass and light profiles under our framework, i.e. all the quads in our sample are ‘happy’ (or, at least ‘content’).

Only one of the quads in our sample, DES J0408-5354, has measured time delays: $\Delta t_{AB}^{\text{observed}} = -112 \pm 2.1$ days, $\Delta t_{AD}^{\text{observed}} = -155.5 \pm 12.8$ days (Courbin et al. 2018). The predicted time delays: $\Delta t_{AB}^{\text{predicted}} = -100 \pm 9$ and $\Delta t_{AD}^{\text{predicted}} = -140 \pm 13$ days (Appendix 5.C) are in good agreement with the measured values, although the measured values were not used as constraints in the modelling procedure.

In order to make the problem computationally tractable for much larger samples we made some simplifying assumptions. Thus, whereas some of the lensing quantities, such as Einstein radius, deflector center of mass, position angle and ellipticity, and image flux ratios, are robustly determined, our models are not appropriate for all applications. In particular, science cases requiring high precision might require more sophisticated modelling for each individual lens system.

The main simplifying assumptions in our work are: 1) we restricted our models to simple yet general profiles to describe the mass and light distributions. 2) we assume no colour gradient in the deflector and source fluxes. Thus, we use the same scalelengths and ellipticity in the deflector- and source-light profiles in different bands while fitting simultaneously. Some

straightforward ways to further improve the lens modelling are to allow for colour dependency of the light distribution of the source and deflector, explicitly including mass distribution of more nearby companions or satellites, increasing the number of shapelets (n_{max}), and consider composite mass models consisting of both stellar and dark matter components.

We illustrate the information content of this large sample of quads by investigating the alignment between the light and mass distributions in the deflector galaxies, and the distribution of so-called flux ratio anomalies. Our key results are as follows:

1. The centers of the mass and light distributions match very well (the RMS of the offsets is $0''.04$).
2. We find the correlation between the ellipticity of the mass and light distributions to be weak (Pearson correlation coefficient, $r = 0.2$).
3. The position angles of the major axes of the mass and light distributions are well-aligned within $\pm 11\text{deg}$ for nine out of 13 lenses.
4. Systems with high ($> 30\text{deg}$) misalignment angle between the light and mass also have large external shear ($\gamma_{\text{ext}} \gtrsim 0.1$). The Pearson correlation coefficient between the misalignment angle and the external shear is $r = 0.74$.
5. The measured flux ratios between the images depart significantly from those predicted by our simple mass models. These flux ratio anomalies are strongest in the bluest band, consistent with microlensing being the main physical driver, in addition to millilensing associated with unseen satellites.

Our finding of weak correlation between the light and mass ellipticity slightly agrees with Keeton (2001), Ferreras et al. (2008) and Rusu et al. (2016) who find no correlation. However, we do not find a strong correlation as Sluse et al. (2012a) and Gavazzi et al. (2012) report. The weak correlation between the mass and light ellipticity in our study is

consistent with the hierarchical formation scenario of elliptical galaxies where the remnants in the simulation of multiple mergers are shown to have no correlation between the halo and light ellipticity (Weil & Hernquist 1996). Moreover, some of the deflectors in our sample are disk galaxies. The projected ellipticity of disk galaxies will not be correlated with the halo ellipticity if viewed from arbitrary orientations.

Moreover, dark matter halos are expected to be rounder than the stellar distribution from simulation (Dubinski & Carlberg 1991; Warren et al. 1992; Dubinski 1994) with reported agreements to observations (Bruderer et al. 2016; Rusu et al. 2016). In our sample, the majority of the systems follow this prediction. Only three systems have significantly flatter mass distribution than the light distribution (DES J0408-5354, PS J0630-1201 and WISE J2344-3056). All these systems have satellites or comparable-mass companions and thus are not the typically relaxed systems where we expect this to hold. In contrast, four systems in our sample are significantly rounder in mass than in light: ATLAS J0259-1635, DES J0405-3308, DES J0420-4037 and PS J1606-2333. These are likely to be disk galaxies from visual inspection of their shapes. This explains the large difference in ellipticity between the mass and light.

To reliably compare the ellipticity of the light and mass distribution, the ellipticity needs to be estimated within the same aperture, or within an aperture large enough beyond which the ellipticity does not significantly evolve. From a strong-lens system, only the total (projected) mass within the Einstein radius can be estimated. If the Einstein radius is much smaller than the effective radius of the deflector galaxy, the comparison of ellipticity between light and mass may not be representative of the entire galaxy.

We find a strong alignment between the mass and light position angles, which agree very well with previous reports (Kochanek 2002; Ferreras et al. 2008; Treu et al. 2009; Gavazzi et al. 2012; Sluse et al. 2012a; Bruderer et al. 2016). Our result is also in agreement with Bruderer et al. (2016) that the systems with high misalignment ($> 30^\circ$) also have strong external shear ($\gamma_{\text{ext}} \gtrsim 0.1$). The absence of systems with high misalignment but low external

shear is in agreement with the prediction of galaxy formation models. Orbits that are highly misaligned in isolated galaxies (thus with low external shear) are shown to be rare and unstable (Heiligman & Schwarzschild 1979; Martinet & de Zeeuw 1988; Adams et al. 2007; Debattista et al. 2015). The misalignment in isolated galaxies can only be sustained by a constant gas-inflow in blue starburst galaxies (Debattista et al. 2015).

Furthermore, for systems with $\theta_E/\theta_{\text{eff}} < 1$, the lensing mass is likely to be dominated by the stellar mass. In that case, relatively stronger correlation between the mass and the light distributions is naturally expected. A comparison between the dark matter and luminous matter distribution would be more interesting in regard to directly testing Λ CDM and galaxy formation theories. However, broadly speaking, large deviations in ellipticity and alignment in our sample have to be explained by the presence of dark matter. However, direct comparison between the dark and luminous mass distributions requires composite mass models with dark and luminous components as adopted by Bruderer et al. (2016). Gomer & Williams (2018) find that two elliptical mass distributions corresponding to the dark matter and baryon with an offset can better reproduce the image positions in quads than just one smooth elliptical mass distribution with external shear. Those kinds of mass models are beyond the scope of this analysis and left for future studies.

The departures of flux-ratios from the smooth model in the disk galaxies in our sample are not at the extreme of the χ^2_f -distribution. This further supports microlensing by foreground stars being the dominant source of the flux-ratio anomaly.

Detailed follow-up of this sample is under way, to measure redshift and velocity dispersion of the deflectors as well as the time delays between the quasars and the properties of the environment. Once follow-up is completed, we will use this sample to address fundamental questions such as the determination of the Hubble Constant (e.g. Bonvin et al. 2017), the nature of dark matter (e.g. Gilman et al. 2018), and the normalization of the stellar initial mass function in massive galaxies (e.g. Schechter et al. 2014).

Acknowledgements

AJS acknowledges support by NASA through STSCI grant HST-GO-15320. Support for Program HST-GO-15320 was provided by NASA through a grant from the Space Telescope Science Institute, which is operated by the Association of Universities for Research in Astronomy, Incorporated, under NASA contract NAS5-26555.

This work is partly based on data from the ESO VLT Survey Telescope at Paranal Observatory under program ID 177.A-3011. This work used computational and storage services associated with the Hoffman2 Shared Cluster provided by UCLA Institute for Digital Research and Education's Research Technology Group.

Funding for the DES Projects has been provided by the U.S. Department of Energy, the U.S. National Science Foundation, the Ministry of Science and Education of Spain, the Science and Technology Facilities Council of the United Kingdom, the Higher Education Funding Council for England, the National Center for Supercomputing Applications at the University of Illinois at Urbana-Champaign, the Kavli Institute of Cosmological Physics at the University of Chicago, the Center for Cosmology and Astro-Particle Physics at the Ohio State University, the Mitchell Institute for Fundamental Physics and Astronomy at Texas A&M University, Financiadora de Estudos e Projetos, Fundação Carlos Chagas Filho de Amparo à Pesquisa do Estado do Rio de Janeiro, Conselho Nacional de Desenvolvimento Científico e Tecnológico and the Ministério da Ciência, Tecnologia e Inovação, the Deutsche Forschungsgemeinschaft and the Collaborating Institutions in the Dark Energy Survey.

The Collaborating Institutions are Argonne National Laboratory, the University of California at Santa Cruz, the University of Cambridge, Centro de Investigaciones Energéticas, Medioambientales y Tecnológicas-Madrid, the University of Chicago, University College London, the DES-Brazil Consortium, the University of Edinburgh, the Eidgenössische Technische Hochschule (ETH) Zürich, Fermi National Accelerator Laboratory, the University of Illinois at Urbana-Champaign, the Institut de Ciències de l'Espai (IEEC/CSIC), the Institut de

Física d'Altes Energies, Lawrence Berkeley National Laboratory, the Ludwig-Maximilians Universität München and the associated Excellence Cluster Universe, the University of Michigan, the National Optical Astronomy Observatory, the University of Nottingham, The Ohio State University, the University of Pennsylvania, the University of Portsmouth, SLAC National Accelerator Laboratory, Stanford University, the University of Sussex, Texas A&M University, and the OzDES Membership Consortium.

Based in part on observations at Cerro Tololo Inter-American Observatory, National Optical Astronomy Observatory, which is operated by the Association of Universities for Research in Astronomy (AURA) under a cooperative agreement with the National Science Foundation.

The DES data management system is supported by the National Science Foundation under Grant Numbers AST-1138766 and AST-1536171. The DES participants from Spanish institutions are partially supported by MINECO under grants AYA2015-71825, ESP2015-66861, FPA2015-68048, SEV-2016-0588, SEV-2016-0597, and MDM-2015-0509, some of which include ERDF funds from the European Union. IFAE is partially funded by the CERCA program of the Generalitat de Catalunya. Research leading to these results has received funding from the European Research Council under the European Union's Seventh Framework Program (FP7/2007-2013) including ERC grant agreements 240672, 291329, and 306478. We acknowledge support from the Australian Research Council Centre of Excellence for All-sky Astrophysics (CAASTRO), through project number CE110001020, and the Brazilian Instituto Nacional de Ciência e Tecnologia (INCT) e-Universe (CNPq grant 465376/2014-2).

This manuscript has been authored by Fermi Research Alliance, LLC under Contract No. DE-AC02-07CH11359 with the U.S. Department of Energy, Office of Science, Office of High Energy Physics. The United States Government retains and the publisher, by accepting the article for publication, acknowledges that the United States Government retains a non-exclusive, paid-up, irrevocable, world-wide license to publish or reproduce the published form of this manuscript, or allow others to do so, for United States Government purposes.

Table 5.7: Lens light parameters. The reported uncertainties are systematic and statistical uncertainties added in quadrature. The magnitudes are given in AB system.

System name	n_{Sersic}	θ_{eff} (arcsec)	I_e (F160W) (mag arcsec $^{-2}$)	I_e (F814W) (mag arcsec $^{-2}$)	I_e (F475X) (mag arcsec $^{-2}$)	q_L	ϕ_L (E of N) (degree)
PS J0147+4630	4	4.97 ± 0.03	29.7 ± 1.0	32.2 ± 1.0	34.4 ± 1.5	0.81 ± 0.01	18 ± 1
	1	0.14 ± 0.03	23.4 ± 0.9	26.7 ± 0.9	30.0 ± 1.3	0.87 ± 0.01	62 ± 1
SDSS J0248+1913	2.4 ± 1.4	0.16 ± 0.03	24.5 ± 0.4	27.8 ± 0.4	31.6 ± 0.6	0.40 ± 0.02	13 ± 1
ATLAS J0259-1635	11.8 ± 1.4	1.00 ± 0.03	28.7 ± 1.0	32.2 ± 1.0	–	0.38 ± 0.02	20 ± 1
DES J0405-3308	7.6 ± 1.4	0.44 ± 0.03	26.8 ± 1.0	30.1 ± 1.0	33.1 ± 1.5	0.55 ± 0.02	37 ± 1
DES J0408-5354	5.5 ± 1.4	2.15 ± 0.03	28.5 ± 1.0	31.3 ± 1.0	34.0 ± 1.5	0.82 ± 0.01	28 ± 2
DES J0420-4037	4.0 ± 1.4	0.44 ± 0.03	25.1 ± 1.0	27.5 ± 1.0	29.5 ± 1.5	0.61 ± 0.01	27 ± 1
PS J0630-1201	6.8 ± 1.4	1.64 ± 0.03	29.9 ± 1.0	33.5 ± 1.0	37.7 ± 1.5	0.79 ± 0.01	12 ± 1
SDSS J1251+2935	4	0.53 ± 0.03	25.5 ± 1.0	28.1 ± 1.0	30.4 ± 1.5	0.67 ± 0.01	23 ± 1
	1	5.00 ± 0.03	30.4 ± 0.9	32.6 ± 0.9	34.0 ± 1.3	0.67 ± 0.03	16 ± 3
SDSS J1330+1810	4	0.75 ± 0.03	24.8 ± 0.4	27.7 ± 0.4	31.9 ± 0.6	0.26 ± 0.01	24 ± 1
	1	0.37 ± 0.03	24.5 ± 0.4	26.7 ± 0.4	27.9 ± 0.6	0.37 ± 0.01	25 ± 1
SDSS J1433+6007	4	0.56 ± 0.03	25.4 ± 1.0	28.2 ± 1.0	30.4 ± 1.5	0.56 ± 0.02	-88 ± 2
	1	3.35 ± 0.03	28.9 ± 0.9	31.1 ± 0.9	32.8 ± 1.3	0.54 ± 0.02	-88 ± 1
PS J1606-2333	4	0.11 ± 0.03	25.2 ± 1.0	27.7 ± 1.0	–	0.56 ± 0.06	-26 ± 4
	1	1.66 ± 0.04	28.5 ± 0.9	31.0 ± 0.9	32.1 ± 1.3	0.77 ± 0.02	-11 ± 2
DES J2038-4008	4	3.36 ± 0.03	26.7 ± 1.0	29.3 ± 1.0	31.1 ± 1.5	0.64 ± 0.01	38 ± 1
	1	4.99 ± 0.03	29.2 ± 0.9	31.3 ± 0.9	32.6 ± 1.3	0.47 ± 0.01	-62 ± 1
WISE J2344-3056	4	0.61 ± 0.04	26.9 ± 1.0	30.9 ± 1.0	–	0.75 ± 0.03	-68 ± 4
	1	4.67 ± 0.05	30.1 ± 0.9	31.7 ± 0.9	33.1 ± 1.3	0.80 ± 0.07	65 ± 10

This research made use of NUMPY (Oliphant 2015), SCIPY (Jones et al. 2001), ASTROPY, a community-developed core PYTHON package for Astronomy (Astropy Collaboration 2013), JUPYTER (Kluyver et al. 2016), MATPLOTLIB (Hunter 2007), and DRAW.IO at <https://www.draw.io>.

5.A Lens light parameters

We report the parameters of the best fit Sérsic functions for the deflectors in Table 5.7.

5.B Convergence, shear and stellar convergence

The convergence κ , shear γ , and the stellar convergence κ_* at the image positions for each lens are given in Table 5.8. The convergence at the image position is given by the lens mass distribution. We assume a constant mass-to-light ratio to convert the surface brightness distribution into a stellar surface mass-density distribution. We choose the maximum normalization factor for the stellar convergence that meets these two criteria: (i) the stellar convergence is smaller than the convergence, and (ii) the integrated stellar convergence is smaller than two-thirds of the integrated convergence within half of the effective radius (Auger et al. 2010a).

5.C Time delays

The time delay between two images I and J is given by

$$\Delta t_{IJ} = \frac{D_{\Delta t}}{c} \left[\frac{1}{2}(\boldsymbol{\theta}_I - \boldsymbol{\beta})^2 - \frac{1}{2}(\boldsymbol{\theta}_J - \boldsymbol{\beta})^2 - \psi(\boldsymbol{\theta}_I) + \psi(\boldsymbol{\theta}_J) \right], \quad (5.5)$$

where $\boldsymbol{\theta}$ is the image position, $\boldsymbol{\beta}$ is the source position, ψ is the lensing potential, c is the speed of light, and $D_{\Delta t}$ is the time-delay distance given by

$$D_{\Delta t} = (1 + z_d) \frac{D_d D_s}{D_{ds}}. \quad (5.6)$$

Here z_d is the deflector redshift, D_d , D_s , and D_{ds} are the angular diameter distances between the observer and the deflector, between the observer and the source, and between the deflector and the source, respectively. The predicted time delays between the images for the quads are given in Table 5.10.

5.D Lens models

In this section, we provide rest of the lens models in Figure 5.7, 5.8 and 5.9 that were not included in Figure 5.3.

Table 5.8: Convergence, shear, and stellar convergence at the image positions. The reported uncertainties are systematic and statistical uncertainties added in quadrature. The stellar convergence, κ_* , is estimated from the F160W band for the lenses with double Sérsic fit for the lens light.

System name	Image	κ	γ	κ_*/κ
PS J0147+4630	A	0.41 ± 0.03	0.55 ± 0.04	0.37 ± 0.17
	B	0.39 ± 0.03	0.52 ± 0.04	0.37 ± 0.17
	C	0.43 ± 0.03	0.45 ± 0.03	0.27 ± 0.12
	D	0.84 ± 0.06	0.99 ± 0.08	0.41 ± 0.18
SDSS J0248+1913	A	0.63 ± 0.05	0.87 ± 0.06	0.002 ± 0.001
	B	0.26 ± 0.03	0.50 ± 0.02	0.003 ± 0.002
	C	0.20 ± 0.03	0.31 ± 0.02	0.006 ± 0.003
	D	0.87 ± 0.07	1.04 ± 0.09	0.011 ± 0.003
ATLAS J0259-1635	A	0.41 ± 0.03	0.42 ± 0.03	0.06 ± 0.03
	B	0.66 ± 0.05	0.67 ± 0.05	0.25 ± 0.15
	C	0.36 ± 0.03	0.36 ± 0.02	0.05 ± 0.03
	D	0.64 ± 0.04	0.65 ± 0.04	0.21 ± 0.11
DES J0405-3308	A	0.48 ± 0.04	0.46 ± 0.03	0.06 ± 0.02
	B	0.53 ± 0.04	0.53 ± 0.04	0.20 ± 0.08
	C	0.52 ± 0.04	0.51 ± 0.04	0.19 ± 0.08
	D	0.49 ± 0.03	0.47 ± 0.03	0.06 ± 0.02
DES J0408-5354	A	0.34 ± 0.02	0.31 ± 0.02	0.17 ± 0.06
	B	0.45 ± 0.03	0.35 ± 0.02	0.24 ± 0.09
	C	0.57 ± 0.04	0.57 ± 0.04	0.17 ± 0.07
	D	0.75 ± 0.05	0.68 ± 0.05	0.32 ± 0.13
DES J0420-4037	A	0.56 ± 0.04	0.56 ± 0.04	0.12 ± 0.05
	B	0.50 ± 0.04	0.44 ± 0.03	0.07 ± 0.03
	C	0.45 ± 0.03	0.41 ± 0.03	0.05 ± 0.02
	D	0.56 ± 0.04	0.51 ± 0.04	0.16 ± 0.06

Table 5.9: Continued from Table 5.8.

System name	Image	κ	γ	κ_{\star}/κ
PS J0630-1201	A	0.52 ± 0.04	0.45 ± 0.03	0.07 ± 0.05
	B	0.49 ± 0.03	0.52 ± 0.04	0.07 ± 0.05
	C	0.45 ± 0.03	0.55 ± 0.04	0.07 ± 0.04
	D	1.39 ± 0.10	1.23 ± 0.08	0.03 ± 0.02
SDSS J1251+2935	A	0.57 ± 0.04	0.57 ± 0.04	0.21 ± 0.08
	B	0.50 ± 0.04	0.41 ± 0.03	0.17 ± 0.07
	C	0.63 ± 0.04	0.57 ± 0.04	0.21 ± 0.09
	D	0.33 ± 0.02	0.25 ± 0.02	0.12 ± 0.05
SDSS J1330+1810	A	0.48 ± 0.08	0.43 ± 0.04	0.04 ± 0.02
	B	0.59 ± 0.09	0.52 ± 0.05	0.16 ± 0.08
	C	0.36 ± 0.06	0.43 ± 0.04	0.02 ± 0.01
	D	0.74 ± 0.12	0.71 ± 0.06	0.23 ± 0.12
SDSS J1433+6007	A	0.35 ± 0.02	0.20 ± 0.01	0.08 ± 0.03
	B	0.38 ± 0.03	0.35 ± 0.02	0.10 ± 0.04
	C	0.78 ± 0.06	0.72 ± 0.05	0.16 ± 0.06
	D	1.20 ± 0.09	1.16 ± 0.08	0.22 ± 0.09
PS J1606-2333	A	0.46 ± 0.03	0.25 ± 0.02	0.50 ± 0.20
	B	0.49 ± 0.03	0.22 ± 0.02	0.53 ± 0.22
	C	0.77 ± 0.06	0.75 ± 0.05	0.61 ± 0.25
	D	0.57 ± 0.04	0.66 ± 0.05	0.77 ± 0.31
DES J2038-4008	A	0.21 ± 0.02	0.43 ± 0.03	0.73 ± 0.27
	B	0.22 ± 0.02	0.49 ± 0.03	0.73 ± 0.27
	C	0.45 ± 0.03	0.89 ± 0.06	0.72 ± 0.28
	D	0.59 ± 0.04	1.11 ± 0.08	0.74 ± 0.26
WISE J2344-3056	A	0.79 ± 0.06	0.69 ± 0.06	0.54 ± 0.22
	B	0.37 ± 0.03	0.38 ± 0.03	0.62 ± 0.25
	C	0.37 ± 0.03	0.38 ± 0.03	0.66 ± 0.26
	D	0.82 ± 0.07	0.72 ± 0.06	0.60 ± 0.24

Table 5.10: Predicted time-delays between the quasar images. The reported uncertainties are systematic and statistical uncertainties added in quadrature. We adopt fiducial redshifts $z_d = 0.5$ and $z_s = 2$ where the redshifts are not measured yet.

System name	z_d	z_s	Δt_{AB} (days)	Δt_{AC} (days)	Δt_{AD} (days)
PS J0147+4630	0.572	2.341	-2.1 ± 0.3	-7 ± 1	-193 ± 18
SDSS J0248+1913	0.5	2.0	2.7 ± 0.2	20 ± 2	-5.9 ± 0.4
ATLAS J0259-1635	0.5	2.16	-3.6 ± 0.3	7 ± 1	-2.7 ± 0.2
DES J0405-3308	0.5	1.713	-1.7 ± 0.2	-0.9 ± 0.2	-0.3 ± 0.2
DES J0408-5354	0.597	2.375	-100 ± 9	-105 ± 9	-140 ± 13
DES J0420-4037	0.5	2.0	1.8 ± 0.2	7 ± 1	1.4 ± 0.1
PS J0630-1201	0.5	3.34	-0.12 ± 0.02	-0.09 ± 0.02	-108 ± 10
SDSS J1251+2935	0.41	0.802	0.6 ± 0.1	-0.43 ± 0.04	36 ± 3
SDSS J1330+1810	0.373	1.393	-0.20 ± 0.02	6 ± 1	-11 ± 1
SDSS J1433+6007	0.407	2.737	-24 ± 2	-36 ± 3	-100 ± 9
PS J1606-2333	0.5	2.0	-3.8 ± 0.4	-11 ± 1	-7 ± 1
DES J2038-4008	0.23	0.777	-6 ± 1	-11 ± 1	-27 ± 2
WISE J2344-3056	0.5	2.0	3.3 ± 0.4	3.4 ± 0.4	-0.6 ± 0.2

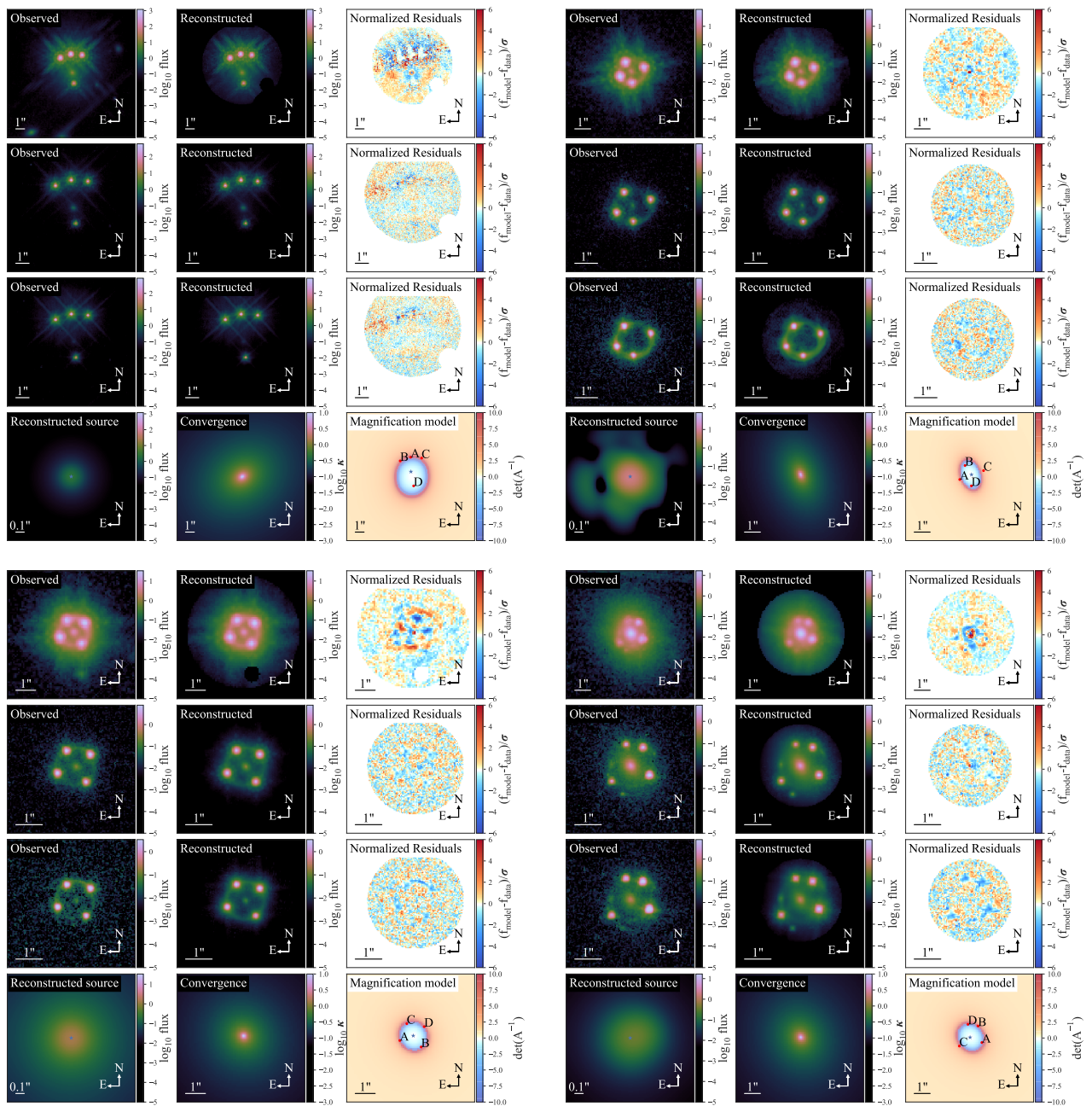


Figure 5.7: Best fit models for PS J0147+4630 (top left), ATLAS J0259-1635 (top right), DES J0405-3308 (bottom left), and DES J0420-4037 (bottom right). The first three rows for each lens system show the observed image, reconstructed lens image, and the normalized residuals in three *HST* bands: F160W, F814W, and F475X, respectively. The fourth row shows the reconstructed source in the F160W band, the convergence, and the magnification model.

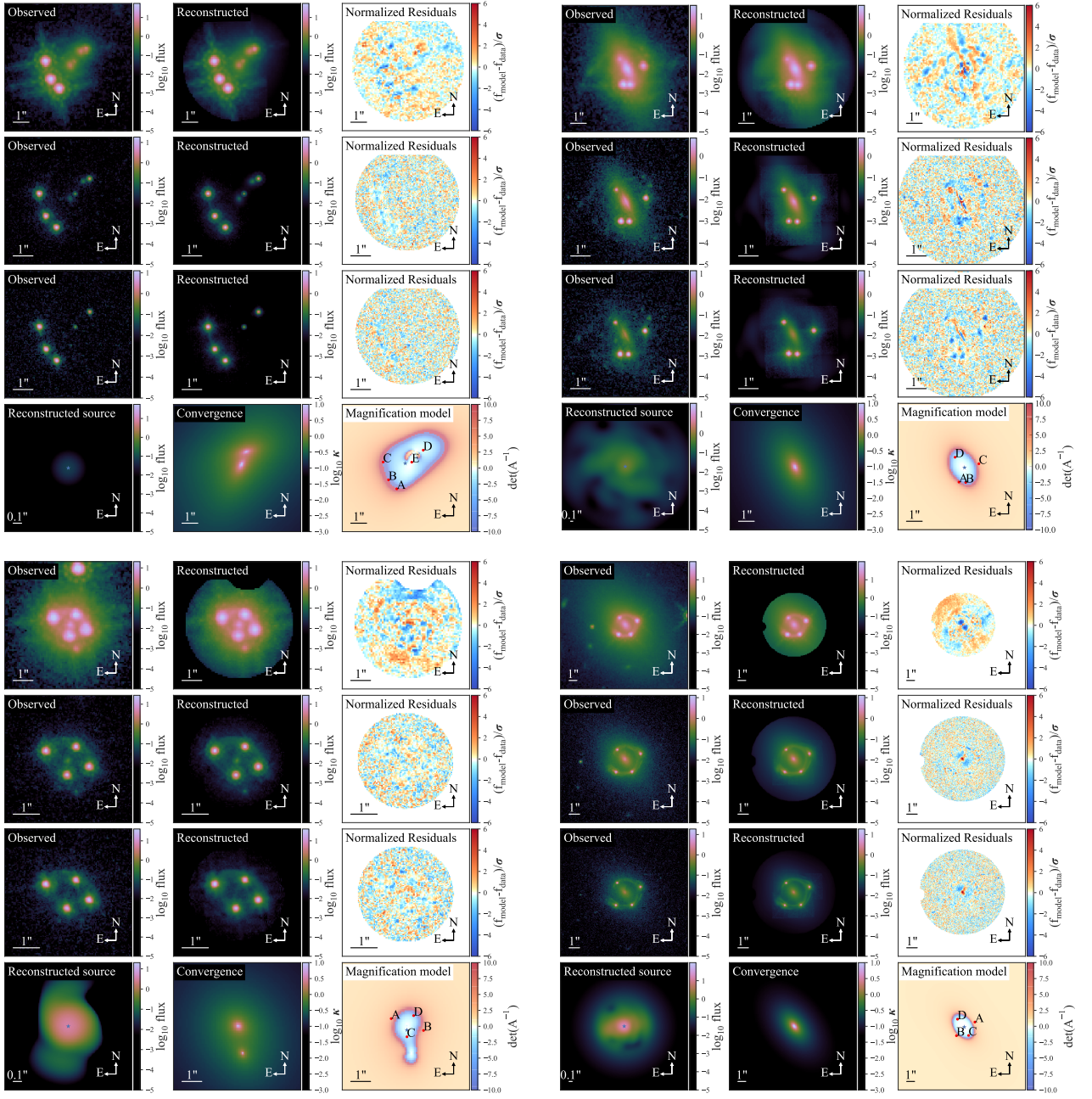


Figure 5.8: Best fit models for PS J0630-1201 (top left), SDSS J1330+1810 (top right), PS J1606-2333 (bottom left), and DES J2038-4008 (bottom right). The first three rows for each lens system show the observed image, reconstructed lens image, and the normalized residuals in three *HST* bands: F160W, F814W, and F475X, respectively. The fourth row shows the reconstructed source in the F160W band, the convergence, and the magnification model.

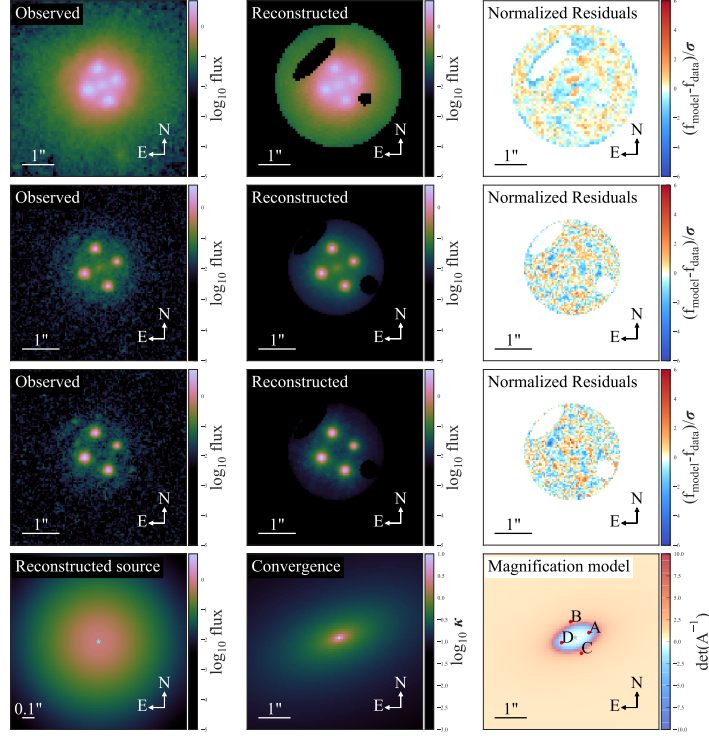


Figure 5.9: Best fit model for WISE J2344-3056. The first three rows show the observed image, reconstructed lens image, and the normalized residuals in three *HST* bands: F160W, F814W, and F475X, respectively. The fourth row shows the reconstructed source in the F160W band, the convergence, and the magnification model.

CHAPTER 6

Unified lensing and kinematic analysis of elliptical mass profiles

This chapter was published as Shajib, A. J. 2019, MNRAS, 488, 1387, and reproduced here with minor formatting changes.

6.1 Background

Gravitational lensing (hereafter, lensing) has versatile applications in astrophysics and cosmology. Lensing is the effect when light bends while passing by a massive object. If two galaxies sit along the same line-of-sight of an observer, the background galaxy appears multiple times due to lensing. This system is called a galaxy-scale strong-lensing system (hereafter, lens). Lenses are useful to measure the Hubble constant H_0 , dark matter subhalo mass function, dust characteristics in galaxies, mass of super-massive black holes, stellar initial mass function, etc. (e.g., Falco et al. 1999; Peng et al. 2006; Suyu et al. 2013; Vegetti et al. 2014; Schechter et al. 2014).

In several applications, stellar kinematics play a complementary role to lensing. Lensing-only observables suffer from mass-sheet degeneracy (MSD) – if we appropriately rescale a mass profile after adding an infinite mass-sheet on top of it, then all the lensing observables stay invariant except the time delay (Falco et al. 1985; Schneider & Sluse 2014). When a measured quantity depends on the mass profile, the MSD adds uncertainty to the measurement. Kinematics help break this degeneracy. Lensing observables probe the projected mass;

kinematic observables probe the three-dimensional potential. Thus, the lensing–kinematics combination tightly constrains the mass profile, and enables us to robustly measure astrophysical and cosmological quantities (e.g., Treu & Koopmans 2004; Barnabè et al. 2011).

In practice, it is difficult to compute lensing and kinematic quantities for elliptical mass profiles, which are required to describe the most common kind of lenses, i.e., elliptical galaxies. We need to integrate over density profiles while fitting a model to either the lensing or the kinematic data. For example, in lensing, the deflection angle is an integral over the surface density profile; in kinematics, the line-of-sight velocity dispersion is a double integral over three-dimensional mass and light profiles. For most elliptical density profiles, we are unable to express these integrals with elementary or special functions. Special functions are numerically well-studied, hence fast algorithms to compute them are usually available. Thus, these functions can be numerically convenient for evaluating model-predicted observables in large numbers (e.g., $\sim 10^6$) when sampling the lens model posterior with Markov chain Monte Carlo (MCMC) methods, or even when only searching for the best-fit model. Otherwise, it would be inefficient to numerically compute lensing and kinematic integrals for general elliptical profiles.

Usually, the numerical difficulties are circumvented through simplifying assumptions or approximations. We now outline common assumptions and approximations in kinematic and lensing analyses, noting that these can limit the accuracy and precision of the inferences.

Either axisymmetry or spherical symmetry is usually assumed for kinematic analysis. If we start with a surface density profile for lensing analysis, we need to deproject this profile along the line of sight to compute the kinematics. This deprojection has an infinite degeneracy (Contopoulos 1956). Therefore, it is necessary to choose a line-of-sight symmetry when deprojecting, for which either axisymmetry or spherical symmetry is often a convenient choice.

In lensing analysis, spherical symmetry is rarely sufficient and we need to consider ellipticity to achieve the required precision. All the lensing quantities are related to the

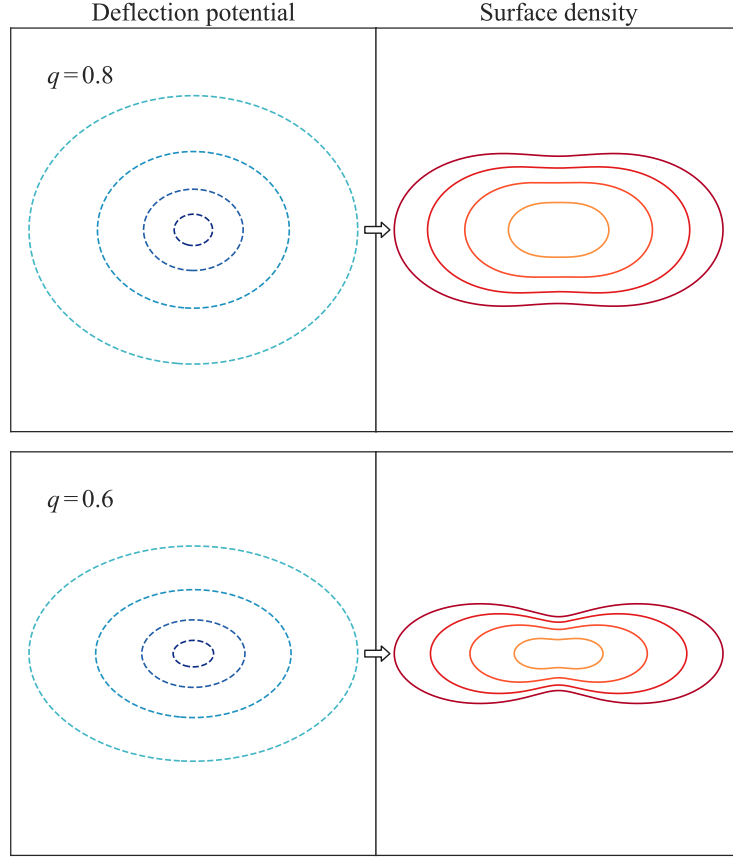


Figure 6.1: Elliptical deflection potential (left column) producing dumbbell-shaped surface-density (right column). The dashed contours in the left column are isopotential curves for Sérsic profile with $n_{\text{Sérsic}} = 4$, and the solid contours in the right column are corresponding isodensity curves. The axis ratios are $q = 0.8$ in the top row, and $q = 0.6$ in the bottom row. The dumbbell shape in surface density is unphysical and it gets more pronounced for higher ellipticity in the deflection potential. Hence, we can not use elliptical deflection potential to simplify lensing analysis of moderately elliptical galaxies. We need to treat ellipticity in the surface density, not deflection potential, to make our lensing analysis generally consistent with our physical priors.

deflection potential or its derivatives. The time delay depends on the deflection potential difference. The gradient of the deflection potential gives the deflection angle. The Hessian of the deflection potential relates to the surface density, the shear, and the magnification. To efficiently compute these quantities for the elliptical case, we can find the following three approximations in the literature:

1. *Ellipticity in deflection potential:* The gradient and the Hessian of an elliptical deflection potential can be easily computed through numerical differentiation (e.g., Kovner 1987; Golse & Kneib 2002). However, this solution is not general, as the surface density becomes dumbbell-shaped for an elliptical deflection potential with axis ratio $q \lesssim 0.6$ (Fig. 6.1, Kassiola & Kovner 1993). This oddly shaped surface-density is unphysical.
2. *Elliptical power-law profile:* We can efficiently compute the lensing quantities for the elliptical power-law profile using numerical approximation or analytical expressions (for the isothermal case, Kormann et al. 1994; and for the general case, Barkana 1998; Tessore & Metcalf 2015). This profile can be sufficient to use in statistical studies that do not require detailed modelling of individual lenses (e.g., Koopmans et al. 2009; Sonnenfeld et al. 2013). However, adopting a power-law profile artificially breaks the MSD and it could potentially bias the H_0 measurement (e.g., Schneider & Sluse 2013; Sonnenfeld 2018). Therefore, we need to explore different, physically-motivated mass models, such as a *composite model* that explicitly accounts for the luminous and the dark components (Suyu et al. 2014; Yıldırım et al. 2019).
3. *Chameleon profile:* The Sérsic profile well describes the surface brightness of a galaxy (Sérsic 1968). The Chameleon profile approximates the Sérsic profile within a few per cent (Dutton et al. 2011). We can efficiently compute lensing quantities for the Chameleon profile using analytic expressions. However, this profile only describes the baryonic component. The precise lensing analysis of elliptical Navarro–Frenk–White (NFW) profile for the dark component still lacks a general solution (Navarro et al. 1997).

In a nutshell, these approximations for elliptical lensing analysis are only applicable in restricted regimes as described above.

In this paper, we present a general method to precisely compute the gradient and the Hessian of the deflection potential for any elliptical surface-density profile. The method follows a “divide and conquer” strategy. We can approximately divide, or decompose, an elliptical profile into concentric Gaussian components (e.g., Bendinelli 1991). For this Gaussian decomposition, we devise a fast and accurate algorithm by introducing an integral transform. For each Gaussian component, we derive analytic expressions of the gradient and the Hessian of the deflection potential. For the deprojected Gaussian component, Cappellari (2008) derives the line-of-sight velocity dispersion. We can combine the computed quantities from each Gaussian component back together to obtain these quantities for the total density profile. In this way, the lensing and kinematic descriptions are self-consistently unified. At the same time, this method is general, as we can apply it to lensing with any elliptical surface-density and to kinematics with either axisymmetry or spherical symmetry. Our method is more efficient than numerical integration to compute lensing quantities for an elliptical surface-density profile.

We organize this paper as follows. In Section 6.2, we motivate the “divide and conquer” strategy behind our method and introduce an integral transform that provides a fast algorithm to decompose any elliptical surface-density profile into concentric Gaussian components. In Section 6.3, we summarize the kinematic description of the Gaussian components from Cappellari (2008). In Section 6.4, we derive the gradient and the Hessian of the deflection potential for elliptical Gaussian surface-density. Next in Section 6.5, we demonstrate a proof-of-concept for our method using simulated data. Then, we summarize the paper in Section 6.6. Additionally in Appendix 6.A, we prove some fundamental theorems for the integral transform introduced in Section 6.2. This integral transform with a Gaussian kernel is the continuous case of concentric Gaussian decomposition. The theorems in Appendix 6.A establish the existence, uniqueness, and invertibility of this transform.

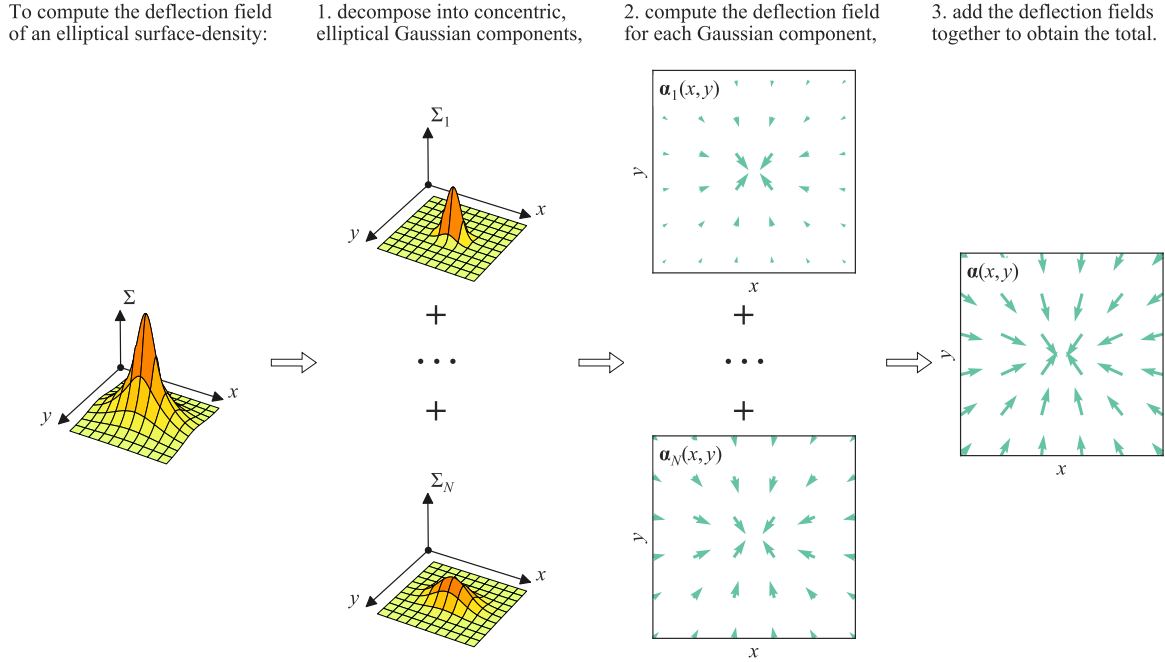


Figure 6.2: “Divide and conquer” strategy to compute lensing quantities for elliptical surface-density profile. In this figure, we choose the deflection field as the quantity of interest to illustrate the method. However, this method works equally well for other quantities such as the lensing shear and the line-of-sight velocity dispersion. Each column demonstrates one step in the strategy and the arrows show the progression of these steps. We explain each step in the text at the top of the corresponding column.

6.2 Decomposing an elliptical profile into concentric Gaussian components

We aim to decompose an elliptical surface-density profile into simpler functions to make the computation tractable. This function should be simple enough so that we can both

1. express the deflection angle in terms of elementary or special functions, and
2. easily deproject it into three-dimension and compute the enclosed mass for kinematic

analysis.

The Gaussian function meets both of these criteria. We validate criterion (i) in Section 6.4.2, where we express the deflection angle for an elliptical Gaussian surface-density profile with the complex error function. For criterion (ii), deprojecting a two-dimensional Gaussian into three-dimension is straightforward, as the Abel inversion of a two-dimensional Gaussian is a three-dimensional Gaussian. The enclosed mass for a three-dimensional Gaussian has the form of the error function, which we can efficiently compute without integrating numerically. Given these points, we approximately decompose an elliptical surface-density profile as

$$\Sigma(x, y) \approx \sum_{j=0}^J \Sigma_{0j} \exp\left(-\frac{q^2 x^2 + y^2}{2\sigma_j^2}\right), \quad (6.1)$$

where Σ_{0j} is the amplitude of the j -th Gaussian, and all the components have a common axis ratio q . Similar decomposition into concentric Gaussian components has been used in the literature to fit the surface brightness profile of galaxies [called as the multi-Gaussian expansion (MGE) by Emsellem et al. (1994), and the mixture-of-Gaussians by Hogg & Lang (2013)]. The lensing and kinematic quantities of our interest – namely the gradient and the Hessian of the deflection potential, and the line-of-sight velocity dispersion – follow the principle of superposition. As a result, we can compute these quantities separately for each Gaussian component and then add them together to recover these quantities for the total surface-density profile (see Fig. 6.2).

We describe the kinematics and lensing analyses for the Gaussian components in Sections 6.3 and 6.4, but first, we need a fast method to decompose an elliptical profile into concentric Gaussian components. Cappellari (2002) presents a method that uses non-linear optimization. However, this non-linear optimization method is computationally too expensive to implement within MCMC. Although, this method has been implemented to compute the kinematic observable while sampling from the lens model posterior (e.g., Birrer et al. 2019). Computing the kinematic observable can involve at least one numerical integration, which is the main bottleneck in efficiency, not the non-linear optimization method for

Gaussian decomposition. To make our lens-modelling method efficient, we require a **(i)** general, **(ii)** precise, and **(iii)** fast technique to decompose a function into concentric Gaussian components. In Sections 6.2.1 and 6.2.2, we provide a technique that satisfies these three requirements.

6.2.1 An integral transform for fast Gaussian decomposition

Now, we introduce an integral transform with a Gaussian kernel. Using this transform, we obtain an algorithm to efficiently decompose an elliptical surface-density profile into concentric Gaussian components.

We start with the simple one-dimensional case of the integral transform. We aim to approximate a function $F(x)$ as a sum of concentric Gaussian components as

$$F(x) \approx \sum_{n=0}^N A_n \exp\left(-\frac{x^2}{2\sigma_n^2}\right), \quad (6.2)$$

where A_n and σ_n are respectively the amplitude and the standard deviation of the n -th Gaussian component. We can convert this discrete summation into a continuous integral by taking $N \rightarrow \infty$. Accordingly, we define the following integral transform:

$$F(x) \equiv \int_0^\infty \frac{f(\sigma)}{\sqrt{2\pi}\sigma} \exp\left(-\frac{x^2}{2\sigma^2}\right) d\sigma. \quad (6.3)$$

Here, the amplitude A_n is converted into a function $f(\sigma)/\sqrt{2\pi}\sigma$. We call $F(x)$ as the *transform* of $f(\sigma)$. We prove three fundamental properties of this integral transform in Appendix 6.A. These three properties tell us that

1. this integral transform exists for most mass and light profiles of practical use,
2. the transform is unique for these functions, and
3. the integral transform is invertible.

We call $f(\sigma)$ as the *inverse transform* of $F(x)$. The inverse transform is given by

$$f(\sigma) = \frac{1}{i\sigma^2} \sqrt{\frac{2}{\pi}} \int_C z F(z) \exp\left(\frac{z^2}{2\sigma^2}\right) dz. \quad (6.4)$$

Here, i is the imaginary unit as $i = \sqrt{-1}$. Also, we have extended $F(x)$ to some region on the complex plane and wrote it as $F(z)$, where z is a complex variable. The contour C for the integral lies within the region where $F(z)$ is defined (for details, see Appendix 6.A and Fig. 6.7). In Section 6.2.1.1, we provide an algorithm that does not require C to be explicitly specified for computing the inverse transform $f(\sigma)$.

We can use the inverse transform to decompose a function into concentric Gaussian components and the forward transform to recover the original function by combining the Gaussian components. First in Section 6.2.1.1, we provide an efficient algorithm to compute the inverse transform from equation (6.4); then in Section 6.2.1.2, we discuss a method for computing the forward transform from equation (6.3).

6.2.1.1 Computing the inverse transform

The integral transform in equation (6.3) can be converted into a Laplace transform by suitable change of variables (Remark 6.A.9). Therefore, we can use any of the several algorithms available for inverse Laplace transform by appropriately changing the variables (for a simple overview of the algorithms, see Abate & Whitt 2006). In this paper, we modify the Euler algorithm to approximate equation (6.4) as

$$f(\sigma) \approx \sum_{n=0}^{2P} \eta_n \operatorname{Re} [F(\sigma \chi_n)]. \quad (6.5)$$

(Abate et al. 2000). Here, the weights η_n and nodes χ_n can be complex-valued and they are independent of $f(\sigma)$. The weights and the nodes are given by

$$\begin{aligned} \chi_n &= \left[\frac{2P \log(10)}{3} + 2\pi i n \right]^{1/2}, \\ \eta_n &= (-1)^n 2\sqrt{2\pi} 10^{P/3} \xi_p, \\ \xi_0 &= \frac{1}{2}, \quad \xi_n = 1, \quad 1 \leq n \leq P, \quad \xi_{2P} = \frac{1}{2^P}, \\ \xi_{2P-n} &= \xi_{2P-n+1} + 2^{-P} \binom{P}{n}, \quad 0 < n < P. \end{aligned} \quad (6.6)$$

We can precompute the weights and the nodes just once before the MCMC sampling. In that way, computing them does not add any extra burden in computing the likelihood. The precision of the inverse transform is $\sim \mathcal{O}(10^{-0.6P})$ (Abate & Whitt 2006). Therefore, the value of P can be appropriately chosen to achieve a required precision. Note that the decimal precision of the machine sets an effective upper limit for P . For example, the precision will not improve with increasing P when $P \gtrsim 12$ for 32-bit floating point number, and when $P \gtrsim 27$ for 64-bit floating point number. Thus, equation (6.5) gives a straightforward, fast, and precise algorithm to compute the inverse transform.

6.2.1.2 Computing the forward transform

Let us approximate the forward transform integral such that we can recover $F(x)$ from only a finite number of $f(\sigma)$ values computed at fixed σ 's. This finite number should be on the order of tens to keep the lensing analysis computationally feasible, as we have to compute lensing quantities for each Gaussian component individually. We write equation (6.3) as

$$\begin{aligned} F(x) &= \frac{1}{\sqrt{2\pi}} \int_0^\infty f(\sigma) \exp\left(-\frac{x^2}{2\sigma^2}\right) d(\log \sigma) \\ \Rightarrow F(x) &= \lim_{N \rightarrow \infty} \sum_{n=1}^N \frac{f(\sigma_n)}{\sqrt{2\pi}} \exp\left(-\frac{x^2}{2\sigma_n^2}\right) \Delta(\log \sigma)_n \\ \Rightarrow F(x) &\approx \sum_{n=1}^N A_n \exp\left(-\frac{x^2}{2\sigma_n^2}\right). \end{aligned} \tag{6.7}$$

We have recovered the form of equation (6.2) by taking logarithmically spaced σ_n . Here, the amplitudes are $A_n = w_n f(\sigma_n) \Delta(\log \sigma)_n / \sqrt{2\pi}$. The weights w_n depend on the choice of the numerical integration method. We use the trapezoidal method with weights $w_1 = 0.5$, $w_n = 1$ for $1 < n < N$, $w_N = 0.5$, as the trapezoidal method is highly efficient to numerically compute integrals of this form (Goodwin 1949). As a result, equation (6.7) efficiently recovers $F(x)$ from only a finite number of $f(\sigma)$ values.

As an example, we demonstrate the integral transform method to decompose the NFW profile and the Sérsic profile into concentric Gaussian components (Fig. 6.3). The two-

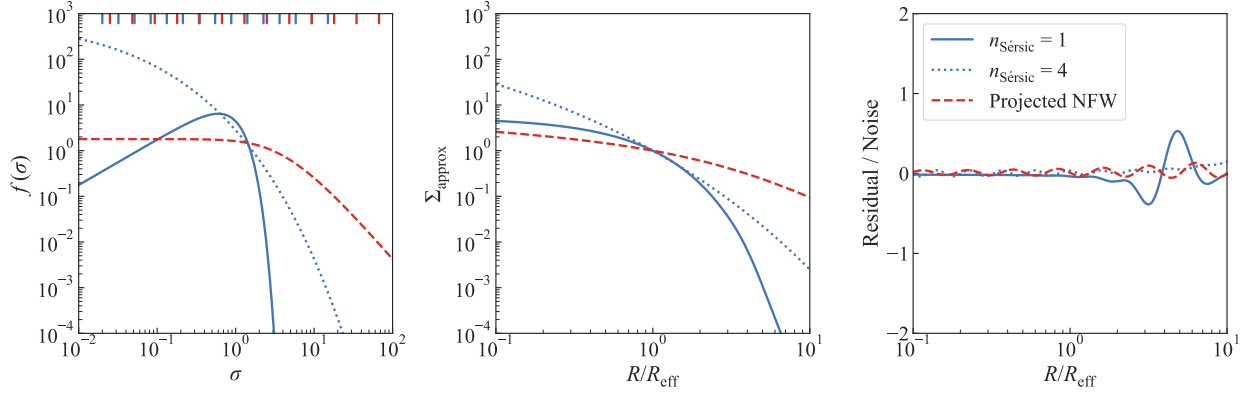


Figure 6.3: Decomposing the Sérsic profile and the projected NFW profile into concentric Gaussian components using the integral transform with a Gaussian kernel. The blue lines correspond to the Sérsic profiles with: solid for Sérsic index $n_{\text{Sérsic}} = 1$ and dotted for $n_{\text{Sérsic}} = 4$. The red, dashed lines correspond to the two-dimensional projected NFW profile. Both profiles are normalized to have $\Sigma(R_{\text{eff}}) = 1$. **Left:** the inverse transform $f(\sigma)$ of the Sérsic profiles and the projected NFW profile. Here, we choose the NFW scale radius $r_s = 5R_{\text{eff}}$. To decompose a function into 15 Gaussian components, we only need to compute $f(\sigma)$ at 15 points. These points are marked along the top border as blue ticks for the Sérsic profiles and as red ticks for the NFW profile. **Center:** recovering the original profile as $\Sigma_{\text{approx}}(R)$ using the forward transform by combining the 15 Gaussian components. We do not plot the true form of $\Sigma_{\text{Sérsic}}(R)$ or $\Sigma_{\text{NFW}}(R)$, because they are visually almost indistinguishable from $\Sigma_{\text{approx}}(R)$. **Right:** noise-normalized difference between the recovered profile $\Sigma_{\text{approx}}(R)$ and the true form of $\Sigma_{\text{Sérsic}}(R)$ or $\Sigma_{\text{NFW}}(R)$. We assume 1 per cent Poisson noise at $R = R_{\text{eff}}$ to obtain the noise level for normalizing the residual. Our method approximates the NFW profile and the Sérsic profile as a sum of 15 Gaussians within the noise level for $0.1R_{\text{eff}} \leq R \leq 10R_{\text{eff}}$.

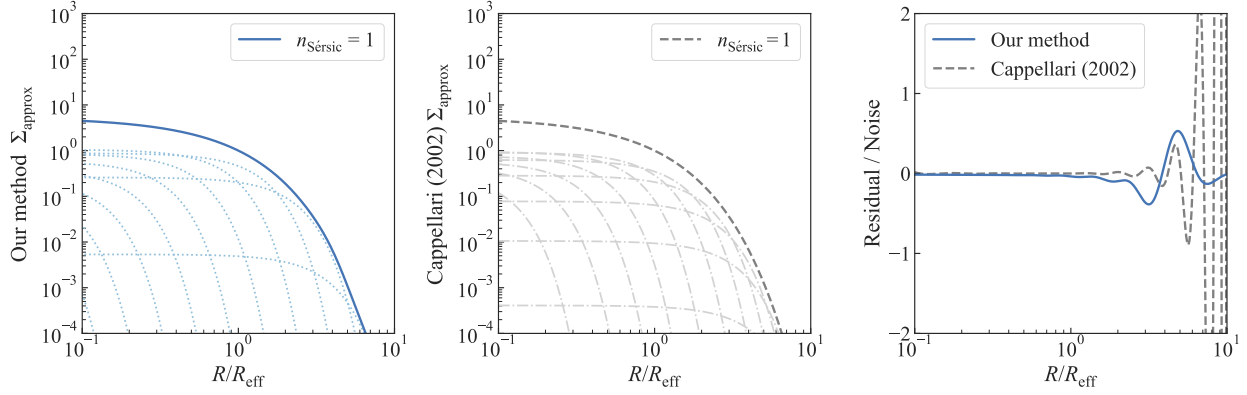


Figure 6.4: Comparison between our method and the multi-Gaussian expansion (MGE) method from Cappellari (2002) to decompose a one-dimensional function into concentric Gaussian components. Here, we only show the case for a Sérsic function with $n_{\text{Sérsic}} = 1$, however the cases for higher Sérsic indices or for the projected NFW profile are qualitatively similar or better. **Left:** the Sérsic function (solid, blue line) approximated with 15 Gaussian components using our Gaussian decomposition method. The dotted, lighter-blue lines show the individual Gaussian components. Some of the Gaussian components are out of the figure range. **Center:** same as the left figure but using the MGE method with 15 Gaussian components. The dashed, grey line shows the Sérsic function approximated by MGE and the dot-dashed, lighter-grey lines show individual Gaussian components. **Right:** comparison of the noise-normalized residual for the two methods. We assume 1 per cent Poisson noise at effective radius R_{eff} to obtain the noise level for normalizing the residual. The MGE method approximates the Sérsic function within the noise level up to $\sim 6R_{\text{eff}}$, whereas our method approximates the Sérsic function within the noise level up to $10R_{\text{eff}}$. More importantly, our method is $\sim 10^3$ times faster than the MGE method to decompose a one-dimensional function into concentric Gaussian components.

dimensional projected NFW profile is given by

$$\Sigma_{\text{NFW}}(R) = \begin{cases} \frac{2\rho_s r_s}{(R/r_s)^2 - 1} \left[1 - \frac{\sec^{-1}(R/r_s)}{\sqrt{(R/r_s)^2 - 1}} \right] & (R > r_s), \\ \frac{2}{3}\rho_s r_s & (R = r_s), \\ \frac{2\rho_s r_s}{(R/r_s)^2 - 1} \left[1 - \frac{\text{sech}^{-1}(R/r_s)}{\sqrt{1 - (R/r_s)^2}} \right] & (R < r_s) \end{cases} \quad (6.8)$$

(Bartelmann 1996). Here, ρ_s is the three-dimensional density normalization, and r_s is the scale radius. The Sérsic profile is given by

$$\Sigma_{\text{Sérsic}}(R) = \Sigma_{\text{eff}} \exp \left[-b_n \left\{ (R/R_{\text{eff}})^{1/n_{\text{Sérsic}}} - 1 \right\} \right] \quad (6.9)$$

(Sérsic 1968). Here, the normalizing factor b_n ensures that half of the total projected mass is contained within the effective radius R_{eff} . We only need to compute as many $f(\sigma)$ values as the number of Gaussian components. We can appropriately choose this number to achieve the required precision for approximating the original function within a given range of R . In this example, we set $r_s = 5R_{\text{eff}}$ and assume 1 per cent Poisson noise at $R = R_{\text{eff}}$. Then, we can approximate both the projected NFW profile and the Sérsic function within the noise level with only 15 Gaussian components in the range $0.1R_{\text{eff}} \leq R \leq 10R_{\text{eff}}$. The standard deviations σ_n of the 15 Gaussians are logarithmically spaced between $0.005r_s$ and $50r_s$ for the NFW profile, and between $0.02R_{\text{eff}}$ and $15R_{\text{eff}}$ for the Sérsic profile. Thus using the integral transform method, we can decompose a function into concentric Gaussian components within any required precision by appropriately choosing the component number N .

6.2.1.3 The integral transform method is more efficient than the MGE method.

We compare our method to decompose a one-dimensional function into concentric Gaussian components with the MGE method (Fig. 6.4). We use both methods to decompose the Sérsic function into 15 Gaussian components. The MGE method approximates the Sérsic function within the noise level up to $\sim 6R_{\text{eff}}$, whereas our method approximates the Sérsic

function within the noise level up to $10R_{\text{eff}}$ with the same number of components. Albeit, we can increase the number of Gaussian components in the MGE method to reach the desired precision. In our method, the precision of the decomposition can be affected by both P in equation (6.5) and the number of Gaussians N in equation (6.7). However, if P is appropriately chosen so that $10^{-0.6P}$ is sufficiently (e.g., by a factor of $\sim 10^{-2}$ – 10^{-4}) smaller than the required precision, then the precision predominantly depends on N . For lensing and kinematic analyses, increasing the number of Gaussian components N introduces more computational burden than increasing P . Therefore, it is advisable to first choose a sufficiently large P and then adjust the number of Gaussians to achieve the required precision. Note that the real power of our method is in its efficiency. A PYTHON implementation of our method is $\sim 10^3$ times faster than the MGE method to decompose a one-dimensional function into concentric Gaussian components with similar or better precision.

6.2.2 Decomposing a two-dimensional elliptical profile with the one-dimensional transform

So far, we have discussed the one-dimensional case of the integral transform; now we show that the one-dimensional transform is sufficient to decompose a two-dimensional elliptical profile. We can extend the one-dimensional integral transform from equation (6.3) into a two-dimensional integral transform for a function $f(\sigma_1, \sigma_2)$ as

$$F(x, y) = \int_0^\infty d\sigma_1 \int_0^\infty d\sigma_2 \frac{f(\sigma_1, \sigma_2)}{2\pi\sigma_1\sigma_2} \exp\left(-\frac{x^2}{2\sigma_1^2} - \frac{y^2}{2\sigma_2^2}\right). \quad (6.10)$$

If $F(x, y)$ is elliptically symmetric, then we can express it as $F(R)$ in terms of the *elliptical radius* $R = \sqrt{q^2x^2 + y^2}$ and axis ratio q . Then, we can write

$$\begin{aligned} F(x, y) &= F(R(q)) = \int_0^\infty F(R(\varrho)) \delta(\varrho - q) d\varrho \\ &= \int_0^\infty d\varrho \delta(\varrho - q) \int_0^\infty d\sigma \frac{f_y(\sigma)}{\sqrt{2\pi}\sigma} \exp\left(-\frac{R(\varrho)^2}{2\sigma^2}\right), \end{aligned} \quad (6.11)$$

where $f_y(\sigma)$ is the inverse transform of $F(0, y)$. If we make the change of variables $\sigma_1 = \sigma/\varrho$, $\sigma_2 = \sigma$, this integral becomes

$$F(x, y) = \frac{1}{2\pi} \int_0^\infty d\sigma_1 \int_0^\infty d\sigma_2 \frac{\sqrt{2\pi}q \delta(\sigma_2/\sigma_1 - q) f_y(\sigma_2)}{\sigma_1 \sigma_2} \times \exp\left(-\frac{x^2}{2\sigma_1^2} - \frac{y^2}{2\sigma_2^2}\right). \quad (6.12)$$

Because of the uniqueness property (Theorem 6.A.7), comparing equations (6.10) and (6.12) we can write

$$f(\sigma_1, \sigma_2) = \sqrt{2\pi}q \delta\left(\frac{\sigma_2}{\sigma_1} - q\right) f_y(\sigma_2). \quad (6.13)$$

Therefore, for an elliptically symmetric function, it is sufficient to numerically compute the one-dimensional inverse transform $f_y(\sigma_2)$ along the y -axis. As a result, we can express a two-dimensional elliptical function as a sum of concentric, elliptical Gaussian components as

$$F(x, y) \approx \sum_{n=1}^N A_n \exp\left(-\frac{q^2 x^2 + y^2}{2\sigma_n^2}\right). \quad (6.14)$$

By now, we have shown that the integral transform method meets all of our three requirements for decomposing a function into concentric Gaussian components:

1. *generality*: the method applies to most mass and light profiles of practical use,
2. *precision*: the method achieves any required precision over a given range by appropriately choosing the number of Gaussian components, and
3. *efficiency*: the method runs approximately $\sim 10^3$ times faster than the previously available method.

With these three requirements met, our lensing analysis method has cleared the first hurdle to be feasible in practice. In Section 6.4.2, we show that we can efficiently compute the gradient and the Hessian of the deflection potential for an elliptical Gaussian surface-density. With that, our method also clears the final hurdle to be efficient. Next in Section 6.3, we summarize the kinematic analysis for the Gaussian components from Cappellari (2008). Then

in Section 6.4, we describe the lensing analysis for the Gaussian components and complete the unification of lensing and kinematic descriptions.

6.3 Kinematics of Gaussian components

Cappellari (2008) presents the Jeans anisotropic modelling of kinematics for a mass profile decomposed into concentric Gaussian components. We summarize the analysis here to complete our unified framework. The kinematic observable is the luminosity-weighted, line-of-sight velocity dispersion. The velocity dispersion can be an integrated measurement within a single aperture or it can be spatially resolved on the plane of the sky. To compute this quantity for a combination of mass and light profiles, we need to solve the Jeans equations. We can decompose the surface mass-density profile into concentric Gaussian components as

$$\Sigma(x, y) \approx \sum_{j=1}^J \Sigma_{0j} \exp\left(-\frac{q_j^2 x^2 + y^2}{2\sigma_j^2}\right), \quad (6.15)$$

and decompose the surface brightness profile into concentric Gaussian components as

$$I(x, y) \approx \sum_{k=1}^K I_{0k} \exp\left(-\frac{q_k^2 x^2 + y^2}{2\sigma_k^2}\right). \quad (6.16)$$

Here, we use different subscript letters to make the context of the Gaussian decomposition clear: we use the subscript j for a component of the mass profile and the subscript k for a component of the light profile. We have also allowed different ellipticity for each Gaussian component represented by q_j or q_k . This is the most general case, for example, when structures with different ellipticities constitute the total mass or light distribution. We first need to deproject these two-dimensional profiles into three-dimension as the kinematic quantities depend on the three-dimensional distributions of mass and light. We assume axisymmetry or spherical symmetry for the deprojected three-dimensional structure to circumvent the infinite degeneracy in deprojection. First, we provide the kinematic analysis for the axisymmetric case in Section 6.3.1; then we do the same for the simpler case of spherical symmetry in Section 6.3.2.

6.3.1 Axisymmetric case

For an axisymmetric system, the cylindrical coordinates (R', z', ϕ') are the most suitable to express the Jeans equations. We use the prime symbol to denote the coordinates in the system's *symmetry-frame*, where the z' -axis aligns with the axis of symmetry. We assign (x, y, z) coordinates to the *sky frame*, where the z -axis aligns with the line of sight and the x -axis aligns with the projected major axis. If the galaxy is inclined by an angle ι , then the (x', y', z') coordinates in the symmetry frame relate to the (x, y, z) coordinates in the sky frame as

$$\begin{pmatrix} x' \\ y' \\ z' \end{pmatrix} = \begin{pmatrix} 1 & 0 & 0 \\ 0 & \cos \iota & -\sin \iota \\ 0 & \sin \iota & \cos \iota \end{pmatrix} \begin{pmatrix} x \\ y \\ z \end{pmatrix}. \quad (6.17)$$

In the symmetry frame, equation (6.15) deprojects into the mass density profile ρ as

$$\rho(R', z') = \sum_{j=1}^J \frac{q_j'^2 \Sigma_{0j}}{\sqrt{2\pi} \sigma_j q_j} \exp \left(-\frac{q_j'^2 R'^2 + z'^2}{2\sigma_j^2} \right), \quad (6.18)$$

and equation (6.16) deprojects into the light density profile l as

$$l(R', z') = \sum_{k=1}^K \frac{q_k'^2 I_{0k}}{\sqrt{2\pi} \sigma_k q_k} \exp \left(-\frac{q_k'^2 R'^2 + z'^2}{2\sigma_k^2} \right). \quad (6.19)$$

Here, the intrinsic axis ratio q' relates to the projected axis ratio q as

$$q' = \frac{\sqrt{q^2 - \cos^2 \iota}}{\sin \iota}. \quad (6.20)$$

We can first solve the Jeans equations for these mass and light density profiles in the symmetry frame to get the intrinsic velocity dispersions and then integrate along the line of sight to obtain the line-of-sight velocity dispersion.

The Jeans equations to solve for an axisymmetric system are

$$\begin{aligned} \frac{b \overline{l v_{z'}^2} - l \overline{v_{\phi'}^2}}{R'} + \frac{\partial (b l \overline{v_{z'}^2})}{\partial R'} &= -l \frac{\partial \Phi}{\partial R'}, \\ \frac{\partial (l \overline{v_{z'}^2})}{\partial z'} &= -l \frac{\partial \Phi}{\partial z'}. \end{aligned} \quad (6.21)$$

Here, the gravitational potential Φ relates to the three-dimensional mass density ρ by $\nabla^2\Phi = \rho$, and b represents the anisotropy as in $\overline{v_{R'}^2} = b\overline{v_{z'}^2}$. We can let b_k for each luminous Gaussian component have different values to approximate the luminosity-weighted anisotropy parameter as

$$\beta_{z'}(R', z') \equiv 1 - \frac{\overline{v_{z'}^2}}{\overline{v_{R'}^2}} \approx 1 - \frac{\sum_k l_k}{\sum_k b_k l_k} \quad (6.22)$$

(Binney & Mamon 1982; Cappellari 2008). The line-of-sight second velocity moment for total mass profile obtained from solving the Jeans equations is given by

$$\begin{aligned} \overline{v_{\text{los}}^2}(x, y) = & 2\sqrt{\pi}G \int_0^1 \sum_{j=1}^J \sum_{k=1}^K \frac{q_j'^3 q_k'^2 \Sigma_{0j} I_{0k} u^2}{\sigma_j q_j \sigma_k q_k} \\ & \times \frac{\sigma_k^2 (\cos^2 \iota + b_k \sin^2 \iota) + \mathcal{D} x^2 \sin^2 \iota}{(1 - \mathcal{C} u^2) \sqrt{(\mathcal{A} + \mathcal{B} \cos^2 \iota) [1 - (1 - q_j'^2) u^2]}} \\ & \times \exp \left(-\mathcal{A} \left[x^2 + \frac{(\mathcal{A} + \mathcal{B}) y^2}{\mathcal{A} + \mathcal{B} \cos^2 \iota} \right] \right) du, \end{aligned} \quad (6.23)$$

where G is the gravitational constant and

$$\begin{aligned} \mathcal{A} &= \frac{1}{2} \left(\frac{u^2 q_j'^2}{\sigma_j^2} + \frac{q_k'^2}{\sigma_k^2} \right), \\ \mathcal{B} &= \frac{1}{2} \left\{ \frac{1 - q_k'^2}{\sigma_k^2} + \frac{q_j'^2 (1 - q_j'^2) u^4}{\sigma_j^2 [1 - (1 - q_j'^2) u^2]} \right\}, \\ \mathcal{C} &= 1 - q_j'^2 - \frac{q_j'^2 \sigma_k^2}{\sigma_j^2}, \\ \mathcal{D} &= 1 - b_k q_k'^2 - \left[(1 - b_k) \mathcal{C} + (1 - q_j'^2) b_k \right] u^2 \end{aligned} \quad (6.24)$$

(Cappellari 2008). The line-of-sight velocity dispersion σ_{los} relates to the second velocity moment by $\overline{v_{\text{los}}^2} = v_{\text{mean}}^2 + \sigma_{\text{los}}^2$, where v_{mean} is the stellar mean velocity.

6.3.2 Spherical case

If we assume the system is spherically symmetric, then the spherical coordinates (r, ϕ, θ) are the most suitable to express the Jeans equations. In this coordinate system, the mass

density profile deprojected from equation (6.15) takes the form

$$\rho(r) = \sum_{j=1}^J \frac{\Sigma_{0j}}{\sqrt{2\pi}\sigma_j q_j} \exp\left(-\frac{r^2}{2\sigma_j^2}\right), \quad (6.25)$$

and the light density profile deprojected from equation (6.16) turns into

$$l(r) = \sum_{k=1}^K \frac{I_{0k}}{\sqrt{2\pi}\sigma_k q_k} \exp\left(-\frac{r^2}{2\sigma_k^2}\right). \quad (6.26)$$

The projected axis ratio q shows up in these equations to keep the total mass and luminosity conserved. We can express the three-dimensional enclosed mass for this density profile as

$$M(r) = \sum_{j=1}^J \frac{2\pi\sigma_j^2 \Sigma_{0j}}{q_j} \left[\operatorname{erf}\left(\frac{r}{\sqrt{2}\sigma_j}\right) - \sqrt{\frac{2}{\pi}} \frac{r}{\sigma_j} \exp\left(-\frac{r^2}{2\sigma_j^2}\right) \right], \quad (6.27)$$

where $\operatorname{erf}(x)$ is the error function. The spherical Jeans equation is

$$\frac{d\left(l \overline{v_r^2}\right)}{dr} + \frac{2\beta l \overline{v_r^2}}{r} = -l \frac{d\Phi}{dr}, \quad (6.28)$$

where $\beta(r)$ is the anisotropy parameter given by

$$\beta(r) = 1 - \overline{v_\theta^2}/\overline{v_r^2}. \quad (6.29)$$

Spherical symmetry imposes that $\overline{v_\theta^2} = \overline{v_\phi^2}$. By solving the Jeans equation for the spherically symmetric case, we can obtain the line-of-sight second velocity moment as

$$\overline{v_{\text{los}}^2}(x, y) = \frac{2G}{I(x, y)} \int_{\sqrt{x^2+y^2}}^\infty \mathcal{K}_\beta\left(\frac{r}{\sqrt{x^2+y^2}}\right) l(r) M(r) \frac{dr}{r} \quad (6.30)$$

(Mamon & Łokas 2005). Here, the function $\mathcal{K}_\beta(v)$ depends on the form of the anisotropy parameter $\beta(r)$. For the isotropic case with $\beta = 0$, the function \mathcal{K}_β shapes into

$$\mathcal{K}_\beta(v) = \sqrt{1 - \frac{1}{v^2}}. \quad (6.31)$$

For the Osipkov-Merritt parameterization $\beta(r) = r^2/(r^2 + r_{\text{ani}}^2)$, where r_{ani} is a scale radius, the function \mathcal{K}_β takes the form

$$\begin{aligned} \mathcal{K}_\beta(v) = & \frac{v_{\text{ani}}^2 + 1/2}{(v_{\text{ani}} + 1)^{3/2}} \left(\frac{v^2 + v_{\text{ani}}^2}{v} \right) \tan^{-1} \left(\sqrt{\frac{v^2 - 1}{v_{\text{ani}}^2 + 1}} \right) \\ & - \frac{1/2}{v_{\text{ani}}^2 + 1} \sqrt{1 - \frac{1}{v^2}} \end{aligned} \quad (6.32)$$

with $v_{\text{ani}} = r_{\text{ani}}/\sqrt{x^2 + y^2}$ (Osipkov 1979; Merritt 1985b,a). See equation (A16) of Mamon & Lokas (2005) for the form of \mathcal{K}_β corresponding to other parameterizations of $\beta(r)$. When assuming spherical symmetry is sufficient, we can use equation (6.30) to compute the line-of-sight velocity dispersion in a much simpler way than the axisymmetric case [cf. equation (6.23)].

The kinematic description of an elliptical mass distribution by decomposing it into concentric Gaussian components is thus well developed in the literature. In the next section, we unify the lensing description with the kinematic description under the same framework.

6.4 Lensing by Gaussian components

In this section, we present the lensing analysis for an elliptical surface-density profile decomposed into concentric Gaussian components. In Section 6.2, we introduced an integral transform that efficiently decomposes an elliptical surface-density profile into concentric Gaussian components as

$$\Sigma(x, y) \approx \sum_{j=1}^J \Sigma_{0j} \exp\left(-\frac{q_j^2 x^2 + y^2}{2\sigma_j^2}\right). \quad (6.33)$$

We can compute a lensing quantity for each individual Gaussian component, and then linearly add the contributions from all the components to obtain the total lensing quantity. For example, if $\alpha_j(x, y)$ is the deflection at position (x, y) for the j -th Gaussian component, then the total deflection is simply given by $\alpha(x, y) = \sum_{j=1}^J \alpha_j(x, y)$. Therefore, it is sufficient to analyze the lensing properties of one elliptical Gaussian component. We use the complex formulation of lensing to solve the deflection integral for an elliptical Gaussian surface-density profile. Below, we first lay out the complex formalism of lensing in Section 6.4.1; then we study the lensing properties of an elliptical Gaussian surface-density profile in Section 6.4.2.

6.4.1 Complex formulation of lensing

The strong lensing effect is usually described using the vector formulation on the two-dimensional image plane. We first define the lensing quantities in the familiar vector formulation, then we translate them to the complex formulation. The convergence κ is a dimensionless surface-density defined as $\kappa \equiv \Sigma/\Sigma_{\text{crit}}$, where the critical density Σ_{crit} is given by

$$\Sigma_{\text{crit}} = \frac{c^2 D_s}{4\pi G D_{\text{ds}} D_d}. \quad (6.34)$$

Here, c is the speed of light. The three angular diameter distances are D_d : between the observer and the deflector, D_s : between the observer and the source, and D_{ds} : between the deflector and the source. The convergence κ relates to the vector deflection angle $\boldsymbol{\alpha}$ as $\kappa = \nabla \cdot \boldsymbol{\alpha}/2$. The deflection angle $\boldsymbol{\alpha}$ is the gradient of the deflection potential as $\boldsymbol{\alpha} = \nabla\psi$, thus the convergence κ relates to the deflection potential ψ as $\kappa = \nabla^2\psi/2$. The Hessian of the deflection potential is

$$\mathbf{H} = \begin{pmatrix} \frac{\partial^2\psi}{\partial^2x} & \frac{\partial^2\psi}{\partial x\partial y} \\ \frac{\partial^2\psi}{\partial x\partial y} & \frac{\partial^2\psi}{\partial^2y} \end{pmatrix}. \quad (6.35)$$

The convergence κ , the shear parameters (γ_1, γ_2) , and the magnification μ relate to the Hessian, since we can express them as

$$\begin{aligned} \kappa &= \frac{1}{2} \left(\frac{\partial^2\psi}{\partial^2x} + \frac{\partial^2\psi}{\partial^2y} \right), \\ \gamma_1 &= \frac{1}{2} \left(\frac{\partial^2\psi}{\partial^2x} - \frac{\partial^2\psi}{\partial^2y} \right), \\ \gamma_2 &= \frac{\partial^2\psi}{\partial x\partial y}, \\ \mu &= \frac{1}{\det(\mathbf{I} - \mathbf{H})}, \end{aligned} \quad (6.36)$$

where \mathbf{I} is the identity matrix. Therefore, if we start with a convergence κ and derive the deflection $\boldsymbol{\alpha}$ and the shear parameters (γ_1, γ_2) , then we can obtain the gradient and the

Hessian of the deflection potential from them.

Now we reformulate the lensing quantities on the complex plane. Following Bourassa et al. (1973), we can express the deflection vector $\boldsymbol{\alpha}$ as a complex quantity

$$\alpha(z) \equiv \alpha_x + i\alpha_y, \quad (6.37)$$

where the complex quantity $z = x + iy$ corresponds to the position vector $\mathbf{r} = (x, y)$. We can define a complex deflection potential $\psi(z)$ with its real part equal to the usual deflection potential (Schramm 1990). Then, the complex deflection angle is the Wirtinger derivative of the deflection potential as

$$\alpha(z) = \frac{\partial\psi}{\partial x} + i\frac{\partial\psi}{\partial y} = 2\frac{\partial\psi}{\partial z^*}. \quad (6.38)$$

We can express the convergence κ as

$$\kappa = \frac{\partial\alpha^*}{\partial z^*}. \quad (6.39)$$

Furthermore, the complex shear $\gamma \equiv \gamma_1 + i\gamma_2$ satisfies the relation

$$\gamma^* = \frac{\partial\alpha^*}{\partial z}. \quad (6.40)$$

Using this complex formulation, we analyze the lensing properties of an elliptical Gaussian convergence next in Section 6.4.2.

6.4.2 Lensing by elliptical Gaussian convergence

We derive the deflection angle and shear for the elliptical Gaussian convergence

$$\kappa(R) = \kappa_0 \exp\left(-\frac{R^2}{2\sigma^2}\right), \quad (6.41)$$

where $R = \sqrt{q^2x^2 + y^2}$ is the elliptical radius. Using the complex formulation, the deflection angle for the elliptical convergence can be obtained from

$$\begin{aligned} \alpha^*(z) &= 2 \operatorname{sgn}(z) \int_0^{R(z)} d\zeta \frac{\zeta \kappa(\zeta)}{\sqrt{q^2z^2 - (1 - q^2)\zeta^2}} \\ &= \frac{2\kappa_0}{qz} \int_0^{R(z)} d\zeta \frac{\zeta \exp(-\zeta^2/2\sigma^2)}{\sqrt{1 - (1 - q^2)\zeta^2/q^2z^2}}, \end{aligned} \quad (6.42)$$

where $\text{sgn}(z) \equiv \sqrt{z^2}/z$ is the complex sign function, and $R(z) = \sqrt{q^2x^2 + y^2}$ is the semi-minor axis length for the ellipse with axis-ratio q that goes through the point $z = x + iy$ (Bourassa & Kantowski 1975; Bray 1984). With changes of variables $s = 1/2\sigma^2$, $t = (1 - q^2)/q^2z^2$, $\tau = \sqrt{1 - t\zeta^2}$, we can express equation (6.42) as

$$\begin{aligned}
\alpha^*(z) &= \frac{2\kappa_0 e^{-s/t}}{qzt} \int_{\sqrt{1-tR(z)^2}}^1 d\tau \exp\left(\frac{s}{t}\tau^2\right) \\
&= \frac{2\kappa_0 e^{-s/t}}{qzt} \left[\frac{1}{2} \sqrt{\frac{\pi t}{s}} \text{erfi}\left(\sqrt{\frac{s}{t}}\tau\right) \right]_{\sqrt{1-t(q^2x^2+y^2)}}^1 \\
&= \kappa_0 \sigma \sqrt{\frac{2\pi}{1-q^2}} \exp\left(-\frac{q^2z^2}{2\sigma^2(1-q^2)}\right) \left[\text{erfi}\left(\frac{qz}{\sigma\sqrt{2(1-q^2)}}\right) \right. \\
&\quad \left. - \text{erfi}\left(\frac{q^2x + iy}{\sigma\sqrt{2(1-q^2)}}\right) \right] \\
&= \kappa_0 \sigma \sqrt{\frac{2\pi}{1-q^2}} \varsigma(z; q),
\end{aligned} \tag{6.43}$$

where $\text{erfi}(z) \equiv -i \text{erf}(iz)$ and we have defined the function

$$\begin{aligned}
\varsigma(z; q) &\equiv \exp\left(-\frac{q^2z^2}{2\sigma^2(1-q^2)}\right) \left[\text{erfi}\left(\frac{qz}{\sigma\sqrt{2(1-q^2)}}\right) \right. \\
&\quad \left. - \text{erfi}\left(\frac{q^2x + iy}{\sigma\sqrt{2(1-q^2)}}\right) \right].
\end{aligned} \tag{6.44}$$

We obtain the complex conjugate of the complex shear from equation (6.40) as

$$\begin{aligned}
\gamma^*(z) &= -\frac{\kappa_0}{1-q^2} \left[(1+q^2) \exp\left(-\frac{q^2x^2+y^2}{2\sigma^2}\right) - 2q \right. \\
&\quad \left. + \frac{\sqrt{2\pi}q^2z}{\sigma\sqrt{1-q^2}} \exp\left(-\frac{q^2z^2}{2\sigma^2(1-q^2)}\right) \left\{ \text{erfi}\left(\frac{qz}{\sigma\sqrt{2(1-q^2)}}\right) \right. \right. \\
&\quad \left. \left. - \text{erfi}\left(\frac{q^2x + iy}{\sigma\sqrt{2(1-q^2)}}\right) \right\} \right] \\
&= -\frac{1}{1-q^2} \left[(1+q^2)\kappa(x, y) - 2q\kappa_0 + \frac{\sqrt{2\pi}q^2\kappa_0z}{\sigma\sqrt{1-q^2}} \varsigma(z; q) \right].
\end{aligned} \tag{6.45}$$

Both the deflection angle and the shear contain the function $\varsigma(z; q)$. This function relates to the Faddeeva function $w_F(z)$. First, we write the function $\varsigma(z; q)$ as

$$\varsigma(z; q) = \varpi \left(\frac{qz}{\sigma \sqrt{2(1-q^2)}}; 1 \right) - \varpi \left(\frac{qz}{\sigma \sqrt{2(1-q^2)}}; q \right), \quad (6.46)$$

where $\varpi(z; q) = \exp(-z^2) \operatorname{erfi}(qx + iy/q)$. We can express $\varpi(z; q)$ using the Faddeeva function $w_F(z)$ as

$$\begin{aligned} \varpi(z; q) = & e^{-x^2 - 2ixy} e^{y^2} - i \exp \left[-x^2(1-q^2) - y^2(1/q^2 - 1) \right] \\ & \times w_F(qx + iy/q). \end{aligned} \quad (6.47)$$

Thus, we can compute the deflection angle and the shear using the Faddeeva function (Fig. 6.5). Faddeeva function is a well-studied special function for its various applications in physics, for example, in radiative transfer and in plasma physics (e.g., Armstrong 1967; Jiménez-Domínguez et al. 1989). We can readily compute $w_F(z)$ in PYTHON using the `SCIPY.SPECIAL.WOFZ` function. For some other popular programming languages, code-packages to compute this function are available at the web-address <http://ab-initio.mit.edu/Faddeeva>. In this paper, we use the algorithm outlined by Zaghloul (2017) to compute $w_F(z)$ with relative error less than 4×10^{-5} over the whole complex plane. We state this algorithm in Appendix 6.B. A PYTHON implementation of this algorithm is approximately twice as fast as the function provided by SCIPY. As a result, we can efficiently compute the gradient and Hessian of the deflection potential for an elliptical Gaussian convergence using equations (6.43) and (6.45).

Now, we turn our attention to computing the deflection potential. The deflection potential $\psi(z)$ is given by

$$\psi(z) = \operatorname{Re} \left(\int_0^z \alpha^*(z') \, dz' \right), \quad (6.48)$$

where we set $\psi(0) = 0$. Often times we are interested in the potential difference between two points z_1 and z_2 given by

$$\Delta\psi = \psi(z_2) - \psi(z_1) = \operatorname{Re} \left(\int_{z_1}^{z_2} \alpha^*(z') \, dz' \right). \quad (6.49)$$

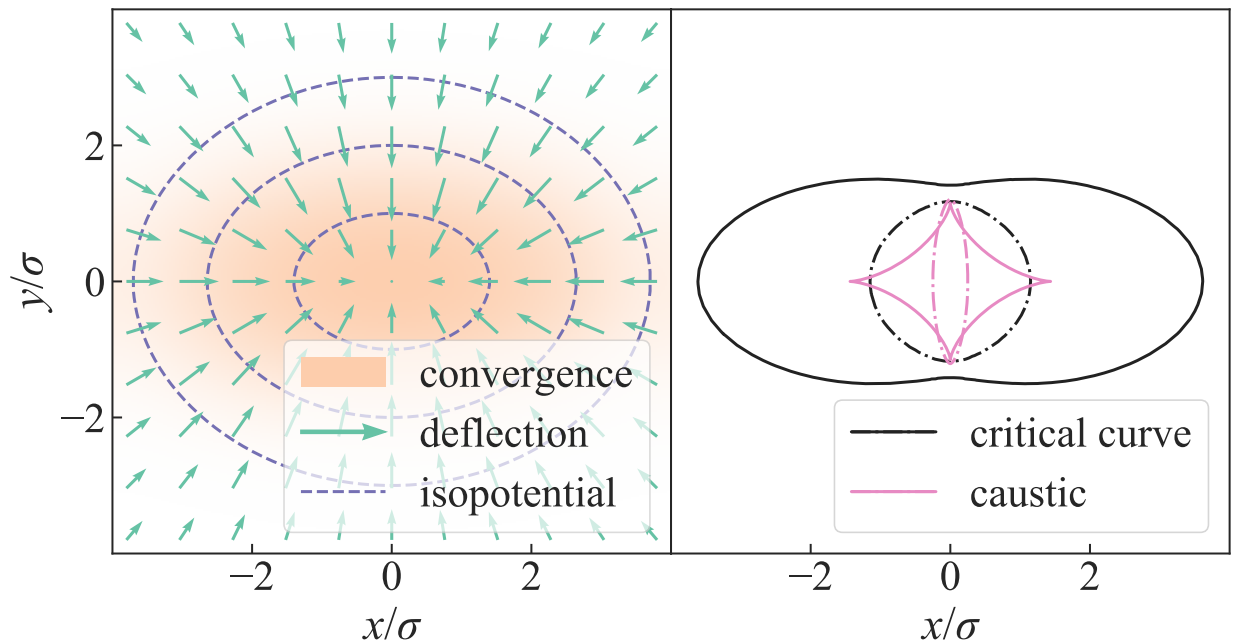


Figure 6.5: Lensing quantities for an elliptical Gaussian convergence profile. **Left:** convergence (orange shade), deflection field (green arrows), isopotential contours (blue, dashed contours). The arrow directions are for the negative of the deflection angles and the lengths are shrunk by a factor of 4 for nicer visualization. **Right:** Critical curves (black lines) and corresponding caustics (pink lines). The solid-contour caustic corresponds to the solid-contour critical curve, similarly dot-dashed contours correspond to each other. Here, we take the amplitude of the Gaussian convergence $\kappa_0 = 2$ and the axis ratio $q = 0.5$. We express the gradient and the Hessian of the deflection potential for an elliptical Gaussian convergence using the complex error function, as a result we can efficiently compute them.

This integral is independent of the choice of a contour. We have to carry out this integral numerically. However, the number of times we need to compute it in most applications, e.g., for computing time delays, is much fewer than that for $\alpha(z)$. We can also numerically solve the Poisson equation $\nabla^2\psi = 2\kappa$ using the Fourier transform of the deflection potential $\hat{\psi} \equiv \mathcal{F}[\psi]$ (van de Ven et al. 2009). This equation turns into $k^2\hat{\psi} = 2\hat{\kappa}$ in the Fourier domain. The solution of the Poisson equation is then $\psi = \mathcal{F}^{-1}(2\hat{\kappa}/k^2)$. We can analytically compute the forward Fourier transform because the convergence has the Gaussian form. Then, we need to compute only the inverse transform numerically. Although obtaining the deflection potential necessitates a numerical integration or a numerical Fourier transform, we can keep the computational burden under control in most applications by computing this quantity only for a feasible number of models sampled from the lens model posterior.

6.5 Adding it all together: proof of concept

In this section, we demonstrate the feasibility of our method to model lenses. We first simulate synthetic data of a mock lens and then model the lens using our method. We use the publicly available lens-modelling software LENSTRONOMY to simulate the synthetic data and perform the model-fitting (Birrer & Amara 2018). We added extra modules to LENSTRONOMY to implement the lensing analysis presented in Section 6.4.2.

For the mock strong lensing system, we adopt an elliptical NFW deflection potential for the dark component and an elliptical Chameleon convergence for the luminous component. We take realistic scale sizes and normalizations for these profiles. We choose the Chameleon profile for two reasons:

1. we can analytically simulate the data with ellipticity in the convergence, and
2. we know the Sérsic-profile parameters that approximates the chosen Chameleon profile *a priori*, so we can check the fidelity of our method.

We parameterize the scaling of the NFW profile with two parameters: scale radius r_s and the deflection angle α_s at r_s . For a spherical NFW profile given by

$$\rho_{\text{NFW}}(r) = \frac{\rho_s}{(r/r_s)(1 + r/r_s)^2}, \quad (6.50)$$

the normalization ρ_s relates to α_s as

$$\alpha_s = \frac{4\rho_s r_s^2}{D_d \Sigma_{\text{crit}}} (1 - \ln 2). \quad (6.51)$$

(Meneghetti et al. 2003). The elliptical Chameleon convergence is given by

$$\kappa_{\text{Chm}}(x, y) = \frac{\kappa_0}{1 + q} \left[\frac{1}{\sqrt{x^2 + y^2/q^2 + 4w_c^2/(1 + q^2)}} - \frac{1}{\sqrt{x^2 + y^2/q^2 + 4w_t^2/(1 + q^2)}} \right] \quad (6.52)$$

(Suyu et al. 2014). We also add external shear to the mass profiles. Therefore, our fiducial lens mass profile has three components in total: elliptical NFW deflection potential, elliptical Chameleon convergence, and external shear.

We simulate data for this fiducial lens system with image quality similar to the *Hubble Space Telescope (HST)* Wide-Field Camera 3 imaging in the F160W filter (see top-left panel of Fig. 6.6). We adopt 0.08 arcsec for the pixel size, 2197 s for exposure time, and a realistic point spread function (PSF) to achieve data quality similar to the lens sample presented by Shajib et al. (2019).

We fit the synthetic data with a model composed of elliptical NFW deflection potential, elliptical Sérsic convergence profile decomposed into concentric Gaussians, and external shear. Note that we take ellipticity in the deflection potential for the NFW profile due to a design restriction of LENSTRONOMY. However, we can also extend an elliptical NFW convergence into concentric Gaussians for lensing analysis in principle. For now, this limitation does not affect the point of this exercise to show that lensing analysis with Gaussian components is feasible. We take the PSF as known for simplicity when fitting a model.

We also separately model the lens with the fiducial mass profiles for comparison. In both cases, the parameters for the light and the luminous mass profiles are joint except for the amplitudes. We fit the model to the data by using the MCMC method. For every sample point in the parameter space, we first decompose the elliptical Sérsic profile into concentric Gaussian components using equations (6.5) and (6.7). Similar to the example in Section 6.2.1.2, we take 15 Gaussian components with logarithmically spaced σ 's between $0.02R_{\text{eff}}$ and $15R_{\text{eff}}$. These 15 Gaussian components approximate the Sérsic function well within the noise level for $0.1R_{\text{eff}} \leq R \leq 10R_{\text{eff}}$ (Fig. 6.3). We compute the gradient and the Hessian of the deflection potential for each Gaussian component. Finally, we add the contributions from all the individual components together to obtain these quantities for the total mass profile. These total quantities are used to compute the likelihood in the MCMC method for fitting the model to the data.

Our method fits the synthetic data very well (see the ‘Normalized Residuals’ plot in Fig. 6.6). The fiducial Sérsic profile parameters are also recovered with reasonable to high accuracies at the same time (Table 6.1). The total runtime is only approximately three times longer than using the fiducial model with the Chameleon profile. This loss in efficiency is a reasonable tradeoff for generality. Thus, we have demonstrated a feasible implementation of our lensing analysis in lens modelling.

6.6 Conclusion: precision is feasible.

In this paper, we present a general method for precise lensing analysis of any elliptical convergence profile. Our method follows a “divide and conquer” strategy. In our method, we first decompose an elliptical convergence profile into concentric Gaussian components as

$$\kappa(x, y) \approx \sum_{j=1}^J \kappa_{0j} \exp \left(-\frac{q^2 x^2 + y^2}{2\sigma_j^2} \right) \quad (6.53)$$

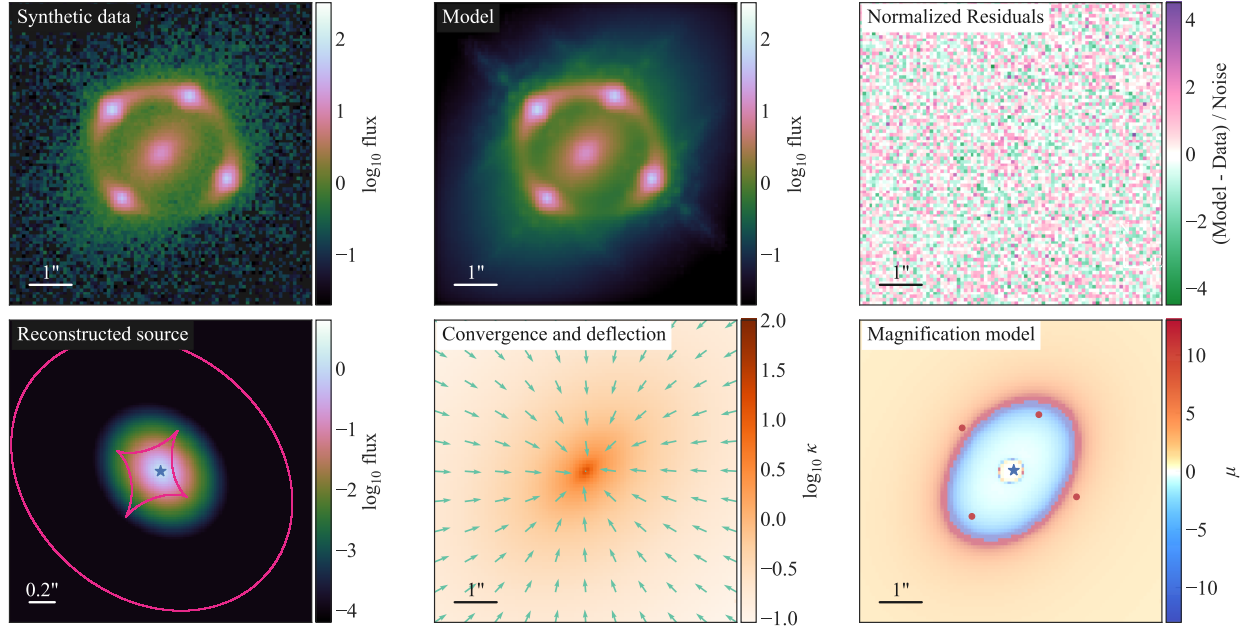


Figure 6.6: Fitting synthetic lensing data with concentric Gaussian components of an elliptical Sérsic profile for the luminous component. We fit the dark component with an elliptical NFW profile. The Sérsic parameters for the lens light are joint with the luminous mass distribution except for the amplitudes letting the global mass-to-light ratio be a free parameter. We generated the synthetic data for a composite model with elliptical NFW and elliptical Chameleon profiles. In the ‘Reconstructed source’ plot, the pink contours outline the caustics. The blue star indicates the point source position. The green arrows in the ‘Convergence and deflection’ plot represent negative deflection angles and they are shrunk by a factor of 4 for nicer visualization. The red dots in the ‘Magnification model’ plot point out the image positions. Our method of computing lensing quantities for the Sérsic profile with ellipticity in the convergence works well as evident from the ‘Normalized Residual’ plot. This method only takes approximately three times longer than using the fiducial model with the Chameleon profile. Unlike the Chameleon profile, however, our method is general.

Table 6.1: Fidelity of our lens modelling method. We simulate mock data with a fiducial model composed of elliptical Chameleon convergence, elliptical NFW deflection potential, and external shear. We test our method with the “Gaussian model”: elliptical Sérsic convergence decomposed into concentric Gaussians, elliptical NFW deflection potential, and external shear. The ‘True’ rows contain the mock values of the fiducial model parameters. The ‘Gaussian-fit’ rows contain the parameters of the “Gaussian model” fit to the data. Similarly, the ‘Fiducial-fit’ rows contain the parameters of the fiducial model fit to the data. We do not provide uncertainty for the values that are accurate up to the displayed decimal point. The accuracy of our computational method with Gaussian components is comparable to that using the fiducial model.

Mass Profile	Parameters			
Sérsic	R_{eff} (arcsec)	$n_{\text{Sérsic}}$	q	ϕ (deg)
True ^a	1.55	3.09	0.60	45
Gaussian-fit	1.51±0.02	3.04±0.03	0.61	45.1±0.3
Chameleon	w_t (arcsec)	w_c (arcsec)	q	ϕ (deg)
True	0.038	1.7	0.60	45
Fiducial-fit	0.038	1.7	0.60	45.0±0.2
NFW	r_s (arcsec)	α_s (arcsec)	q	ϕ (deg)
True	5	1	0.9	45
Gaussian-fit	5.0	0.99±0.03	0.87±0.02	44±2
Fiducial-fit	5.0	1.00±0.01	0.90±0.01	45±2
External shear	γ	ϕ (deg)	—	—
True	0.051	5.7	—	—
Gaussian-fit	0.056±0.002	9±3	—	—
Fiducial-fit	0.051±0.001	6±2	—	—

Notes. ^aThe true values of the Sérsic-profile parameters correspond to the true values of the Chameleon-profile parameters.

We then compute lensing quantities, e.g., the gradient and the Hessian of the deflection potential, for each Gaussian component. Finally, we add the lensing quantities from individual Gaussian components together to obtain these quantities for the total surface-density profile. Moreover, we can straightforwardly deproject a Gaussian component to obtain its corresponding three-dimensional density profile assuming either axisymmetry or spherical symmetry. Then, we can also compute the kinematic properties, such as the line-of-sight velocity dispersion, for each Gaussian component (Cappellari 2008). We can then add the velocity dispersions from individual Gaussians together to obtain the total line-of-sight velocity dispersion. In this way, we self-consistently unify the lensing and kinematic descriptions of any elliptical mass profile.

We introduce an integral transform with a Gaussian kernel that leads us to a general, precise, and fast algorithm for decomposing a surface density profile into concentric Gaussian components. Without such an algorithm, decomposing into Gaussians would end up as a bottleneck in the lens modelling efficiency. We obtain the algorithm by first inverting the integral transform as

$$f(\sigma) = \frac{1}{i\sigma^2} \sqrt{\frac{2}{\pi}} \int_C z F(z) \exp\left(\frac{z^2}{2\sigma^2}\right) dz. \quad (6.54)$$

Although this is an integral, we provide a straightforward formula to compute $f(\sigma)$. The computed values of $f(\sigma)$ then quantify the amplitudes κ_{0j} of the Gaussian components in equation (6.53). As a result, this integral transform fulfills the three requirements for a decomposition algorithm to be **(i)** general, **(ii)** precise, and **(iii)** fast. To be specific, this decomposition algorithm is $\sim 10^3$ times faster than the MGE algorithm from Cappellari (2002). Consequently, our lensing analysis requires the same order of CPU time as other methods currently in use to model a lens with a composite mass profile. Thus, the integral transform enables the lens modelling with the Gaussian components to be efficient and, in turn, makes our unified framework for lensing and kinematic analysis of an elliptical mass profile feasible.

Our method enables precise lens modelling with an elliptical mass profile for several astrophysical applications. Specifically, our method gives an efficient method to model composite mass profiles with separate components for the baryonic matter and the dark matter. For example, the usual choices for these components are the Sérsic and the NFW profiles; both are computationally difficult to directly implement in lens modelling for the elliptical case. Our method makes both of these profiles computationally tractable while achieving the required precision. Thus, our method will be useful in applications where a composite mass profile is essential for lens modelling, for example, in detecting dark-matter substructure, in measuring the Hubble constant, and in testing massive elliptical-galaxy formation theories (e.g., Vegetti et al. 2012; Wong et al. 2017; Nightingale et al. 2019).

Acknowledgements

AJS thanks Simon Birrer and Shouman Das for helpful discussions. AJS also thanks the anonymous referee for very useful suggestions that improved this paper. AJS expresses gratitude to Adriano Agnello, Simon Birrer, Xuheng Ding, Xinnan Du, Abhimat K. Gautam, Briley Lewis, Michael Topping, and Tommaso Treu for providing feedbacks that greatly improved the writing and the presentation of this paper. AJS acknowledges support by National Aeronautics and Space Administration (NASA) through Space Telescope Science Institute grant HST-GO-15320.

This research made use of LENSTRONOMY (Birrer & Amara 2018), NUMPY (Oliphant 2015), SCIPY (Jones et al. 2001), JUPYTER (Kluyver et al. 2016), and MATPLOTLIB (Hunter 2007).

6.A Properties of the Integral transform with a Gaussian Kernel

In this appendix, we prove some fundamental properties of the integral transform with a Gaussian kernel. In three theorems, we prove that

1. the integral transform exists for a function with certain characteristics,
2. the transform is unique for a continuous function, and
3. the transform is invertible.

First, we define the integral transform.

Definition 6.A.1. Define an integral transform \mathcal{T} that takes a function $f(\sigma) : \mathbb{R}_{\geq 0} \rightarrow \mathbb{R}$ to a function $F(z) : \mathbb{C} \rightarrow \mathbb{C}$ as

$$F(z) \equiv \mathcal{T}[f](z) \equiv \frac{1}{\sqrt{2\pi}} \int_0^\infty \frac{f(\sigma)}{\sigma} \exp\left(-\frac{z^2}{2\sigma^2}\right) d\sigma. \quad (6.55)$$

Next, we define a *transformable* function in the context of this paper.

Definition 6.A.2. A function $f(\sigma) : \mathbb{R}_{\geq 0} \rightarrow \mathbb{R}$ is said to be transformable, if it satisfies the following conditions:

1. the function $f(\sigma)$ is piecewise continuous,
2. the function $f(\sigma) = \mathcal{O}(\exp(c/2\sigma^2))$ as $\sigma \rightarrow 0$, where $c \in \mathbb{R}_{\geq 0}$,
3. the function $f(\sigma) = \mathcal{O}(\sigma^\lambda)$ with $\lambda < 0$ as $\sigma \rightarrow \infty$.

We refer to these three conditions as the transformability conditions. The namesake for the transformable function is made clear next in Theorem 6.A.3.

Theorem 6.A.3 (Existence). If $f(\sigma)$ is transformable, then its integral transform $F(z)$ exists in the region of convergence (ROC) $\text{Re}(z^2) > c$.

Proof. Divide the integral in equation (6.55) as

$$\begin{aligned} F(z) &= \frac{1}{\sqrt{2\pi}} \left(\int_0^a d\sigma + \int_a^b d\sigma + \int_b^\infty d\sigma \right) \frac{f(\sigma)}{\sigma} \exp\left(-\frac{z^2}{2\sigma^2}\right) \\ &= \frac{1}{\sqrt{2\pi}} (\mathcal{I}_1 + \mathcal{I}_2 + \mathcal{I}_3), \end{aligned} \quad (6.56)$$

where $0 < a < b < \infty$.

1. The integral \mathcal{I}_2 converges, as the integrand is piecewise continuous in $[a, b]$ according to transformability condition (i) in Definition 6.A.2.
2. According to transformability condition (ii), there exists $M_1 \in \mathbb{R}_{>0}$ such that $f(\sigma) \leq M_1 \exp(c/2\sigma^2)$ for $\sigma \leq a$. Then using Jensen's inequality, we have

$$\begin{aligned} |\mathcal{I}_1| &\leq \int_0^a \left| \frac{f(\sigma)}{\sigma} \exp\left(-\frac{z^2}{2\sigma^2}\right) \right| d\sigma \\ \Rightarrow |\mathcal{I}_1| &\leq \int_0^a \left| \frac{M_1}{\sigma} \exp\left(-\frac{z^2 - c}{2\sigma^2}\right) \right| d\sigma \\ \Rightarrow |\mathcal{I}_1| &\leq M_1 \int_0^a \frac{1}{\sigma} \exp\left(-\frac{\operatorname{Re}(z^2) - c}{2\sigma^2}\right) d\sigma. \end{aligned} \quad (6.57)$$

Therefore, the integral \mathcal{I}_1 converges in the region $\operatorname{Re}(z^2) = x^2 - y^2 > c$, where $z = x + iy$, $x \in \mathbb{R}, y \in \mathbb{R}$.

3. According to transformability condition (iii), there exists $M_2 \in \mathbb{R}_{>0}$ such that $f(\sigma) \leq M_2 \sigma^\lambda$ for $\sigma \geq b$. Then, we have

$$\begin{aligned} |\mathcal{I}_3| &\leq \int_b^\infty \left| \frac{f(\sigma)}{\sigma} \exp\left(-\frac{z^2}{2\sigma^2}\right) \right| d\sigma \\ \Rightarrow |\mathcal{I}_3| &\leq \int_b^\infty M_2 \sigma^{\lambda-1} \left| \exp\left(-\frac{z^2}{2\sigma^2}\right) \right| d\sigma \\ \Rightarrow |\mathcal{I}_3| &\leq M_2 \int_b^\infty \sigma^{\lambda-1} d\sigma = -M_2 \frac{b^\lambda}{\lambda} < \infty. \end{aligned} \quad (6.58)$$

Here, we applied the inequality $|\exp(-z^2/2\sigma^2)| \leq 1$ for $\operatorname{Re}(z^2) > c \geq 0$. As a result, the integral \mathcal{I}_3 converges.

Therefore, the transform $F(z)$ exists in the ROC $\operatorname{Re}(z^2) > c$. □

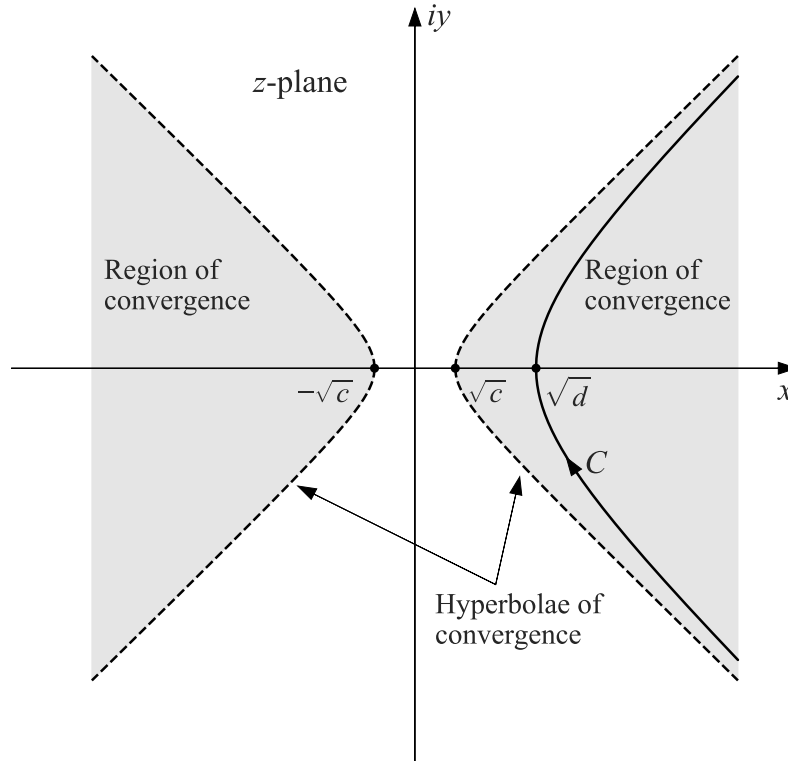


Figure 6.7: Region of convergence (shaded region) on the complex plane for the integral in equation (6.55). The hyperbolic contour C for the integral in equation (6.63) is shown with solid black hyperbola.

Fig. 6.7 shows the ROC for the integral in equation (6.55). We can extend the ROC by the following two corollaries.

Corollary 6.A.4. *If a transformable function $f(\sigma)$ additionally satisfies the condition $f(\sigma) = \mathcal{O}(\sigma^\beta \exp(c/2\sigma^2))$ with $\beta \geq 1$ as $\sigma \rightarrow 0$, then the integral in equation (6.55) converges in the ROC $\operatorname{Re}(z^2) \geq c$.*

Proof. According to the additional condition, there exists $M_3 \in \mathbb{R}_{>0}$ such that $f(\sigma) \leq$

$M_3\sigma^\beta \exp(c/2\sigma^2)$ for $\sigma \leq a$. Then, we can rewrite equation (6.57) as

$$\begin{aligned} |\mathcal{I}_1| &\leq \int_0^a \left| \frac{f(\sigma)}{\sigma} \exp\left(-\frac{z^2}{2\sigma^2}\right) \right| d\sigma \\ \Rightarrow |\mathcal{I}_1| &\leq \int_0^a \left| M_3\sigma^{\beta-1} \exp\left(-\frac{z^2-c}{2\sigma^2}\right) \right| d\sigma \\ \Rightarrow |\mathcal{I}_1| &\leq M_3 \int_0^a \sigma^{\beta-1} \exp\left(-\frac{\operatorname{Re}(z^2)-c}{2\sigma^2}\right) d\sigma. \end{aligned} \quad (6.59)$$

For $\operatorname{Re}(z^2) = c$, this becomes

$$|\mathcal{I}_1| \leq M_3 \int_0^a \sigma^{\beta-1} d\sigma = \frac{M_3 a^\beta}{\beta} < \infty. \quad (6.60)$$

Therefore, the ROC for the integral in equation (6.55) extends to $\operatorname{Re}(z^2) \geq c$. \square

Corollary 6.A.5. *If a transformable function $f(\sigma)$ additionally satisfies $f(\sigma) = \mathcal{O}(\sigma^\beta)$ with $\beta \geq 1$ as $\sigma \rightarrow 0$, then the integral in equation (6.55) converges in the ROC $\operatorname{Re}(z^2) \geq 0$.*

Proof. The proof is trivial with the substitution $c = 0$ in Corollary 6.A.4. \square

Next we prove the uniqueness theorem for the transform. First, we state a well-known proof of the following lemma for completeness.

Lemma 6.A.6. *If $f(x)$ is continuous in $[0, 1]$, and $\int_0^1 x^n f(x) dx = 0$ for $n = 0, 1, 2, \dots$, then $f(x) = 0$.*

Proof. From the Weierstrass approximation theorem, for any $\epsilon > 0$, there exists a polynomial $P_\epsilon(x)$ such that $|f(x) - P_\epsilon(x)| < \epsilon$ for all $x \in [0, 1]$. The hypothesis implies that $\int_0^1 P_\epsilon(x) f(x) dx = 0$. By taking the limit $\epsilon \rightarrow 0$, this equation becomes $\int_0^1 f(x) f(x) dx = 0$. As $f(x)^2 \geq 0$, we have $f(x) = 0$. \square

Theorem 6.A.7 (Uniqueness). *If $f(\sigma)$ and $g(\sigma)$ are continuous, and $\mathcal{T}[f](z) = \mathcal{T}[g](z)$ for all z in the ROC, then $f(\sigma) = g(\sigma)$.*

Proof. Due to linearity, it is sufficient to prove that if $\mathcal{T}[f](z) = 0$, then $f(\sigma) = 0$. Take d such that the contour $\text{Re}(z^2) = d$ lies in the ROC. By making the change of variables $s = \exp(-1/2\sigma^2)$, for $z^2 = d + n + 1$ with $n = 0, 1, 2, \dots$ we have

$$\begin{aligned}\mathcal{T}[f](z) &= \frac{1}{\sqrt{2\pi}} \int_0^\infty \frac{f(\sigma)}{\sigma} \exp\left(-\frac{d+n+1}{2\sigma^2}\right) d\sigma = 0 \\ \Rightarrow \int_0^1 \left[-\frac{s^d f(\sqrt{-1/2 \log s})}{2\sqrt{2\pi} \log s} \right] s^n ds &= 0.\end{aligned}\tag{6.61}$$

This integral exists as $s \rightarrow 0$, because

$$\lim_{s \rightarrow 0} \left[-\frac{s^d f(\sqrt{-1/2 \log s})}{2\sqrt{2\pi} \log s} \right] = \lim_{\sigma \rightarrow 0} \left[\frac{\sigma^2 f(\sigma)}{\sqrt{2\pi}} \exp\left(-\frac{d}{2\sigma^2}\right) \right] = 0.\tag{6.62}$$

Therefore, according to Lemma 6.A.6, we have $f(\sigma) = 0$. \square

Theorem 6.A.8 (Inversion). *If $F(z)$ is the transform of $f(\sigma)$, then $f(\sigma)$ is given by the inverse transform*

$$f(\sigma) = \mathcal{T}^{-1}[F](\sigma) = \frac{1}{i\sigma^2} \sqrt{\frac{2}{\pi}} \int_C z F(z) \exp\left(\frac{z^2}{2\sigma^2}\right) dz,\tag{6.63}$$

where the contour C is the hyperbola $\text{Re}(z^2) = d$ such that C lies in ROC of $F(z)$.

Proof. Write equation (6.55) for $z^2 = d$ as

$$F(\sqrt{d}) = \frac{1}{\sqrt{2\pi}} \int_0^\infty \frac{f(\sigma)}{\sigma} \exp\left(-\frac{d}{2\sigma^2}\right) d\sigma.\tag{6.64}$$

With the change of variables $p = 1/\sigma^2$, this equation transforms into

$$F(\sqrt{d}) = \int_0^\infty g(p) \exp\left(-\frac{dp}{2}\right) dp,\tag{6.65}$$

where

$$g(p) = \frac{\sigma^2 f(\sigma)}{2\sqrt{2\pi}}.\tag{6.66}$$

Define a new function

$$h(p) = \begin{cases} g(p) \exp\left(-\frac{dp}{2}\right), & p \geq 0, \\ 0, & p < 0. \end{cases}\tag{6.67}$$

Theorem 6.A.3 implies that $\int_{-\infty}^{\infty} |h(p)| dp < \infty$, thus $h(p)$ belongs to the Lebesgue space $L^1(\mathbb{R})$. Therefore, we can take the Fourier transform of $h(p)$ as

$$\begin{aligned}\hat{h}(\nu) &= \frac{1}{\sqrt{2\pi}} \int_{-\infty}^{\infty} h(p) e^{-ip\nu} dp \\ &= \frac{1}{\sqrt{2\pi}} \int_0^{\infty} g(p) \exp\left(-\frac{(d+2i\nu)p}{2}\right) dp \\ &= \frac{1}{\sqrt{2\pi}} F\left(\sqrt{d+2i\nu}\right),\end{aligned}\tag{6.68}$$

where we used equation (6.65) for the substitution in the last line. Now, take the inverse Fourier transform of $\hat{h}(\nu)$ as

$$\begin{aligned}h(p) &= \frac{1}{\sqrt{2\pi}} \int_{-\infty}^{\infty} \hat{h}(\nu) e^{ip\nu} d\nu \\ \Rightarrow g(p) \exp\left(-\frac{dp}{2}\right) &= \frac{1}{2\pi} \int_{-\infty}^{\infty} F\left(\sqrt{d+2i\nu}\right) e^{ip\nu} d\nu \\ \Rightarrow \frac{\sigma^2 f(\sigma)}{2\sqrt{2\pi}} &= \frac{1}{2\pi} \int_{-\infty}^{\infty} F\left(\sqrt{d+2i\nu}\right) \exp\left(\frac{d+2i\nu}{2\sigma^2}\right) d\nu \\ \Rightarrow f(\sigma) &= \frac{1}{i\sigma^2} \sqrt{\frac{2}{\pi}} \int_C z F(z) \exp\left(\frac{z^2}{2\sigma^2}\right) dz.\end{aligned}\tag{6.69}$$

Here, we used the substitution of variable $z^2 = d+2i\nu$ in the last line, which transforms the integral path to the hyperbolic contour C given by $\text{Re}(z^2) = d$. \square

Remark 6.A.9. Equation (6.65) has the form of a Laplace transform. Therefore, the integral transform with a Gaussian kernel for a transformable function can be converted into a Laplace transform by suitable change of variables.

6.B Efficient algorithm to compute the Faddeeva function

In this appendix, we state an efficient algorithm to compute the Faddeeva function $w_F(z)$ (Algorithm 1, for details see Zaghloul 2017). The relative error of this algorithm is less than 4×10^{-5} over the whole complex plane.

Algorithm 1 Compute $w_F(z)$

```
 $y \leftarrow \text{Im}(z)$   
if  $|z|^2 \geq 3.8 \times 10^4$  then  
     $w_F \leftarrow \frac{i}{z\sqrt{\pi}}$   
else if  $3.8 \times 10^4 > |z|^2 \geq 256$  then  
     $w_F \leftarrow \frac{iz}{\sqrt{\pi}(z^2 - 0.5)}$   
else if  $256 > |z|^2 \geq 62$  then  
     $w_F \leftarrow \frac{i(z^2 - 1)}{z\sqrt{\pi}(z^2 - 1.5)}$   
else if  $62 > |z|^2 \geq 30$  and  $y^2 \geq 10^{-13}$  then  
     $w_F \leftarrow \frac{iz(z^2 - 2.5)}{\sqrt{\pi}(z^2(z^2 - 3) + 0.75)}$   
else if  $(62 > |z|^2 \geq 30 \text{ and } y^2 < 10^{-13})$  or  $(30 > |z|^2 \geq 2.5 \text{ and } y^2 < 0.072)$  then  
     $U \leftarrow [1.320522, 35.7668, 219.031, 1540.787$   
         $3321.990, 36183.31]$   
     $V \leftarrow [1.841439, 61.57037, 364.2191, 2186.181$   
         $9022.228, 24322.84, 32066.6]$   
     $w_F \leftarrow \exp(-z^2) + iz \times (U[6] + z^2(U[5] + z^2(U[4] + z^2(U[3] +$   
         $z^2(U[2] + z^2(U[1] + z^2\sqrt{\pi})))))) / (V[7] + z^2(V[6] +$   
         $z^2(V[5] + z^2(V[4] + z^2(V[3] + z^2(V[2] + z^2(V[1]$   
         $+ z^2))))))$   
else  
     $U \leftarrow [5.9126262, 30.180142, 93.15558, 181.92853$   
         $214.38239, 122.60793]$   
     $V \leftarrow [10.479857, 53.992907, 170.35400, 348.70392$   
         $457.33448, 352.73063, 122.60793]$   
     $w_F \leftarrow (U[6] - iz(U[5] - iz(U[4] - iz(U[3] - iz(U[2] - iz(U[1]$   
         $- iz\sqrt{\pi})))))) / (V[7] - iz(V[6] - iz(V[5] - iz(V[4]$   
         $- iz(V[3] - iz(V[2] - iz(V[1] - iz))))))$   
end if
```

CHAPTER 7

Conclusion

7.1 Summaries

I present an evidence for the Λ CDM cosmology by detecting the integrated Sachs–Wolfe effect (Chapter 2). I perform a new measurement of the Hubble constant using time-delays of strongly lensed quasar system, which increases the tension between early-Universe and late-Universe measurements (Chapter 3). This increased tension can potentially point to new physics beyond the Λ CDM model. However, first we need to rule out the presence of systematics in various measurements including the time-delay cosmography. I develop several methodologies to improve the time-delay cosmography in the future to both improve the H_0 precision per system and to rapidly increase the sample size of analyzed systems (Chapters 4, 5, 6). I summarize the main results from the Chapters 2–7 below.

7.1.1 Chapter 2: An evidence of the Λ CDM cosmology: measuring the integrated Sachs–Wolfe effect

One of the physical features of a dark-energy-dominated universe is the integrated Sachs–Wolfe (ISW) effect on the cosmic microwave background (CMB) radiation, which gives us a direct observational window to detect and study dark energy. The AllWISE data release of the *Wide-field Infrared Survey Explorer* (*WISE*) has a large number of point sources, which span over a wide redshift range including where the ISW effect is maximized. AllWISE data is thus very well-suited for the ISW effect studies. In this study, we cross-correlate All-

WISE galaxy and active galactic nucleus (AGN) overdensities with the *Wilkinson Microwave Anisotropy Probe* CMB temperature maps to detect the ISW effect signal. We calibrate the biases for galaxies and AGNs by cross-correlating the galaxy and AGN overdensities with the *Planck* lensing convergence map. We measure the ISW effect signal amplitudes relative to the Λ CDM expectation of $A = 1$ to be $A = 1.18 \pm 0.36$ for galaxies and $A = 0.64 \pm 0.74$ for AGNs. The detection significances for the ISW effect signal are 3.3σ and 0.9σ for galaxies and AGNs respectively giving a combined significance of 3.4σ . Our result is in agreement with the Λ CDM model.

7.1.2 Chapter 3: Measurement of the Hubble constant from the strong lens system DES J0408–5354

We present a blind time-delay cosmographic analysis for the lens system DES J0408–5354. This system is extraordinary for the presence of two sets of multiple images at different redshifts, which provide the opportunity to obtain more information at the cost of increased modelling complexity with respect to previously analysed systems. We perform detailed modelling of the mass distribution for this lens system using three band *Hubble Space Telescope* imaging. We combine the measured time delays, line-of-sight central velocity dispersion of the deflector, and statistically constrained external convergence with our lens models to estimate two cosmological distances. We measure the “effective” time-delay distance corresponding to the redshifts of the deflector and the lensed quasar $D_{\Delta t}^{\text{eff}} = 3382_{-115}^{+146}$ Mpc and the angular diameter distance to the deflector $D_d = 1711_{-280}^{+376}$ Mpc, with covariance between the two distances. From these constraints on the cosmological distances, we infer the Hubble constant $H_0 = 74.2_{-3.0}^{+2.7}$ km s^{−1} Mpc^{−1} assuming a flat Λ CDM cosmology and a uniform prior for Ω_m as $\Omega_m \sim \mathcal{U}(0.05, 0.5)$. This measurement gives the most precise constraint on H_0 to date from a single lens. Our measurement is consistent with that obtained from the previous sample of six lenses analysed by the H_0 Lenses in COSMOGRAIL’s Wellspring (H0LiCOW) collaboration. It is also consistent with measurements of H_0 based on the local distance

ladder, reinforcing the tension with the inference from early Universe probes, for example, with 2.2σ discrepancy from the cosmic microwave background measurement.

7.1.3 Chapter 4: Improving time-delay cosmography with spatially resolved kinematics

Stellar kinematics of the deflector galaxy play an essential role in the measurement of the time-delay distance by: (i) helping break the mass-sheet degeneracy; (ii) determining in principle the angular diameter distance D_d to the deflector and thus further improving the cosmological constraints. In this paper we simulate observations of lensed quasars with integral field spectrographs and show that spatially resolved kinematics of the deflector enable further progress by helping break the mass-anisotropy degeneracy. Furthermore, we use our simulations to obtain realistic error estimates with current/upcoming instruments like OSIRIS on Keck and NIRSPEC on the *James Webb Space Telescope* for both distances (typically ~ 6 per cent on $D_{\Delta t}$ and ~ 10 per cent on D_d). We use the error estimates to compute cosmological forecasts for the sample of nine lenses that currently have well measured time delays and deep *Hubble Space Telescope* images and for a sample of 40 lenses that is projected to be available in a few years through follow-up of candidates found in ongoing wide field surveys. We find that H_0 can be measured with 2 per cent (1 per cent) precision from nine (40) lenses in a flat Λ cold dark matter cosmology. We study several other cosmological models beyond the flat Λ cold dark matter model and find that time-delay lenses with spatially resolved kinematics can greatly improve the precision of the cosmological parameters measured by cosmic microwave background data.

7.1.4 Chapter 5: Automated and uniform modelling of lensed quasars

Strong-gravitational lens systems with quadruply-imaged quasars (quads) are unique probes to address several fundamental problems in cosmology and astrophysics. Although they are

intrinsically very rare, ongoing and planned wide-field deep-sky surveys are set to discover thousands of such systems in the next decade. It is thus paramount to devise a general framework to model strong-lens systems to cope with this large influx without being limited by expert investigator time. We propose such a general modelling framework (implemented with the publicly available software `LENSTRONOMY`) and apply it to uniformly model three-band *Hubble Space Telescope* Wide Field Camera 3 images of 13 quads. This is the largest uniformly modelled sample of quads to date and paves the way for a variety of studies. To illustrate the scientific content of the sample, we investigate the alignment between the mass and light distribution in the deflectors. The position angles of these distributions are well-aligned, except when there is strong external shear. However, we find no correlation between the ellipticity of the light and mass distributions. We also show that the observed flux-ratios between the images depart significantly from the predictions of simple smooth models. The departures are strongest in the bluest band, consistent with microlensing being the dominant cause in addition to millilensing. Future papers will exploit this rich dataset in combination with ground based spectroscopy and time delays to determine quantities such as the Hubble constant, the free streaming length of dark matter, and the normalization of the initial stellar mass function.

7.1.5 Chapter 6: Unified lensing and kinematic analysis of elliptical mass profiles

We demonstrate an efficient method to compute the strong-gravitational-lensing deflection angle and magnification for any elliptical surface-density profile. This method solves a numerical hurdle in lens modelling that has lacked a general solution for nearly three decades. The hurdle emerges because it is prohibitive to derive analytic expressions of the lensing quantities for most elliptical mass profiles. In our method, we first decompose an elliptical mass profile into concentric Gaussian components. We introduce an integral transform that provides us with a fast and accurate algorithm for this Gaussian decomposition. We derive

analytic expressions of the lensing quantities for a Gaussian component. As a result, we can compute these quantities for the total mass profile by adding up the contributions from the individual components. This lensing analysis self-consistently completes the kinematic description in terms of Gaussian components presented by Cappellari (2008). Our method is general without extra computational burden unlike other methods currently in use.

7.2 Final remarks

Although the Λ CDM cosmology is tremendously successful in explaining a large number of observational results, the currently significant ($\gtrsim 5\sigma$) tension in H_0 can be a potential hint for new physics beyond the Λ CDM model. Future studies involving larger sample of lensed quasars and supernova will be independently able to resolve or confirm this tension, thanks to the methodologies developed in this dissertation in addition to the tremendous improvements this field of time-delay cosmography has experienced over the past decade. With several new space and ground based telescopes coming online within the next decade – such as the *James Webb Space Telescope*, the Vera Rubin Observatory Legacy Survey for Space and Time, the *Nancy Grace Roman Space Telescope* – thousands of new lensed quasars and galaxy–galaxy lenses will be discovered (Oguri & Marshall 2010; Collett 2015). These large datasets will provide us with sufficient number of lens systems to closely investigate the internal structure of lens galaxies to beat down systematics in the time-delay cosmography and help resolve the H_0 tension.

Bibliography

- Abate, J., G. L. Choudhury, & W. Whitt. 2000, An Introduction to Numerical Transform Inversion and Its Application to Probability Models, ed. W. K. Grassmann (Boston, MA: Springer US), 257–323
- Abate, J. & W. Whitt. 2006, *INFORMS Journal on Computing*, 18, 408
- Abazajian, K., J. K. Adelman-McCarthy, M. A. Agüeros, S. S. Allam, K. Anderson, S. F. Anderson, J. Annis, N. A. Bahcall, I. K. Baldry, S. Bastian, A. Berlind, M. Bernardi, M. R. Blanton, J. Bochanski, John J., W. N. Boroski, J. W. Briggs, J. Brinkmann, R. J. Brunner, T. Budavári, L. N. Carey, S. Carliles, F. J. Castander, A. J. Connolly, I. Csabai, M. Doi, F. Dong, D. J. Eisenstein, M. L. Evans, X. Fan, D. P. Finkbeiner, S. D. Friedman, J. A. Frieman, M. Fukugita, R. R. Gal, B. Gillespie, K. Glazebrook, J. Gray, E. K. Grebel, J. E. Gunn, V. K. Gurbani, P. B. Hall, M. Hamabe, F. H. Harris, H. C. Harris, M. Harvanek, T. M. Heckman, J. S. Hendry, G. S. Hennessy, R. B. Hindsley, C. J. Hogan, D. W. Hogg, D. J. Holmgren, S.-i. Ichikawa, T. Ichikawa, Ž. Ivezić, S. Jester, D. E. Johnston, A. M. Jorgensen, S. M. Kent, S. J. Kleinman, G. R. Knapp, A. Y. Kniazev, R. G. Kron, J. Krzesinski, P. Z. Kunszt, N. Kuropatkin, D. Q. Lamb, H. Lampeitl, B. C. Lee, R. F. Leger, N. Li, H. Lin, Y.-S. Loh, D. C. Long, J. Loveday, R. H. Lupton, T. Malik, B. Margon, T. Matsubara, P. M. McGehee, T. A. McKay, A. Meiksin, J. A. Munn, R. Nakajima, T. Nash, J. Neilsen, Eric H., H. J. Newberg, P. R. Newman, R. C. Nichol, T. Nicinski, M. Nieto-Santisteban, A. Nitta, S. Okamura, W. O’Mullane, J. P. Ostriker, R. Owen, N. Padmanabhan, J. Peoples, J. R. Pier, A. C. Pope, T. R. Quinn, G. T. Richards, M. W. Richmond, H.-W. Rix, C. M. Rockosi, D. J. Schlegel, D. P. Schneider, R. Scranton, M. Sekiguchi, U. Seljak, G. Sergey, B. Sesar, E. Sheldon, K. Shimasaku, W. A. Siegmund, N. M. Silvestri, J. A. Smith, V. Smolčić, S. A. Snedden, A. Stebbins, C. Stoughton, M. A. Strauss, M. SubbaRao, A. S. Szalay, I. Szapudi, P. Szkody, G. P. Szokoly, M. Tegmark, L. Teodoro, A. R. Thakar, C. Tremonti, D. L. Tucker, A. Uomoto,

D. E. Vanden Berk, J. Vandenberg, M. S. Vogeley, W. Voges, N. P. Vogt, L. M. Walkowicz, S.-i. Wang, D. H. Weinberg, A. A. West, S. D. M. White, B. C. Wilhite, Y. Xu, B. Yanny, N. Yasuda, C.-W. Yip, D. R. Yocum, D. G. York, I. Zehavi, S. Zibetti, & D. B. Zucker. 2004, *AJ*, 128, 502

Abbott, T. M. C., F. B. Abdalla, J. Annis, K. Bechtol, J. Blazek, B. A. Benson, R. A. Bernstein, G. M. Bernstein, E. Bertin, D. Brooks, D. L. Burke, A. Carnero Rosell, M. Carrasco Kind, J. Carretero, F. J. Castander, C. L. Chang, T. M. Crawford, C. E. Cunha, C. B. D’Andrea, L. N. da Costa, C. Davis, J. DeRose, S. Desai, H. T. Diehl, J. P. Dietrich, P. Doel, A. Drlica-Wagner, A. E. Evrard, E. Fernandez, B. Flaugher, P. Fosalba, J. Frieman, J. García-Bellido, E. Gaztanaga, D. W. Gerdes, T. Giannantonio, D. Gruen, R. A. Gruendl, J. Gschwend, G. Gutierrez, W. G. Hartley, J. W. Henning, K. Honscheid, B. Hoyle, D. Huterer, B. Jain, D. J. James, M. Jarvis, T. Jeltema, M. D. Johnson, M. W. G. Johnson, E. Krause, K. Kuehn, S. Kuhlmann, N. Kuropatkin, O. Lahav, A. R. Liddle, M. Lima, H. Lin, N. MacCrann, M. A. G. Maia, A. Manzotti, M. March, J. L. Marshall, R. Miquel, J. J. Mohr, T. Natoli, P. Nugent, R. L. C. Ogando, Y. Park, A. A. Plazas, C. L. Reichardt, K. Reil, A. Roodman, A. J. Ross, E. Roza, E. S. Rykoff, E. Sanchez, V. Scarpine, M. Schubnell, D. Scolnic, I. Sevilla-Noarbe, E. Sheldon, M. Smith, R. C. Smith, M. Soares-Santos, F. Sobreira, E. Suchyta, G. Tarle, D. Thomas, M. A. Troxel, A. R. Walker, R. H. Wechsler, J. Weller, W. Wester, W. L. K. Wu, & J. Zuntz. 2018a, *MNRAS*, 480, 3879

Abbott, T. M. C., F. B. Abdalla, A. Alarcon, J. Aleksić, S. Allam, S. Allen, A. Amara, J. Annis, J. Asorey, S. Avila, D. Bacon, E. Balbinot, M. Banerji, N. Banik, W. Barkhouse, M. Baumer, E. Baxter, K. Bechtol, M. R. Becker, A. Benoit-Lévy, B. A. Benson, G. M. Bernstein, E. Bertin, J. Blazek, S. L. Bridle, D. Brooks, D. Brout, E. Buckley-Geer, D. L. Burke, M. T. Busha, A. Campos, D. Capozzi, A. Carnero Rosell, M. Carrasco Kind, J. Carretero, F. J. Castander, R. Cawthon, C. Chang, N. Chen, M. Childress, A. Choi, C. Conselice, R. Crittenden, M. Crocce, C. E. Cunha, C. B. D’Andrea, L. N.

da Costa, R. Das, T. M. Davis, C. Davis, J. De Vicente, D. L. DePoy, J. DeRose, S. Desai, H. T. Diehl, J. P. Dietrich, S. Dodelson, P. Doel, A. Drlica-Wagner, T. F. Eifler, A. E. Elliott, F. Elsner, J. Elvin-Poole, J. Estrada, A. E. Evrard, Y. Fang, E. Fernandez, A. Ferté, D. A. Finley, B. Flaugher, P. Fosalba, O. Friedrich, J. Frieman, J. García-Bellido, M. Garcia-Fernandez, M. Gatti, E. Gaztanaga, D. W. Gerdes, T. Giannantonio, M. S. S. Gill, K. Glazebrook, D. A. Goldstein, D. Gruen, R. A. Gruendl, J. Gschwend, G. Gutierrez, S. Hamilton, W. G. Hartley, S. R. Hinton, K. Honscheid, B. Hoyle, D. Huterer, B. Jain, D. J. James, M. Jarvis, T. Jeltema, M. D. Johnson, M. W. G. Johnson, T. Kacprzak, S. Kent, A. G. Kim, A. King, D. Kirk, N. Kokron, A. Kovacs, E. Krause, C. Krawiec, A. Kremin, K. Kuehn, S. Kuhlmann, N. Kuropatkin, F. Lacasa, O. Lahav, T. S. Li, A. R. Liddle, C. Lidman, M. Lima, H. Lin, N. MacCrann, M. A. G. Maia, M. Makler, M. Manera, M. March, J. L. Marshall, P. Martini, R. G. McMahon, P. Melchior, F. Menanteau, R. Miquel, V. Miranda, D. Mudd, J. Muir, A. Möller, E. Neilsen, R. C. Nichol, B. Nord, P. Nugent, R. L. C. Ogando, A. Palmese, J. Peacock, H. V. Peiris, J. Peoples, W. J. Percival, D. Petravick, A. A. Plazas, A. Porredon, J. Prat, A. Pujol, M. M. Rau, A. Refregier, P. M. Ricker, N. Roe, R. P. Rollins, A. K. Romer, A. Roodman, R. Rosenfeld, A. J. Ross, E. Rozo, E. S. Rykoff, M. Sako, A. I. Salvador, S. Samuroff, C. Sánchez, E. Sanchez, B. Santiago, V. Scarpine, R. Schindler, D. Scolnic, L. F. Secco, S. Serrano, I. Sevilla-Noarbe, E. Sheldon, R. C. Smith, M. Smith, J. Smith, M. Soares-Santos, F. Sobreira, E. Suchyta, G. Tarle, D. Thomas, M. A. Troxel, D. L. Tucker, B. E. Tucker, S. A. Uddin, T. N. Varga, P. Vielzeuf, V. Vikram, A. K. Vivas, A. R. Walker, M. Wang, R. H. Wechsler, J. Weller, W. Wester, R. C. Wolf, B. Yanny, F. Yuan, A. Zenteno, B. Zhang, Y. Zhang, J. Zuntz, & Dark Energy Survey Collaboration. 2018b, *Phys. Rev. D*, 98, 043526

Adams, F. C., A. M. Bloch, S. C. Butler, J. M. Druce, & J. A. Ketchum. 2007, *ApJ*, 670, 1027

Afshordi, N. 2004, *Phys. Rev. D*, 70, 083536

- Afshordi, N., Y.-S. Loh, & M. A. Strauss. 2004, *Phys. Rev. D*, 69, 083524
- Agnello, A., M. W. Auger, & N. W. Evans. 2013, *MNRAS*, 429, L35
- Agnello, A., N. W. Evans, & A. J. Romanowsky. 2014, *MNRAS*, 442, 3284
- Agnello, A., C. Grillo, T. Jones, T. Treu, M. Bonamigo, & S. H. Suyu. 2018a, *MNRAS*, 474, 3391
- Agnello, A., B. C. Kelly, T. Treu, & P. J. Marshall. 2015a, *MNRAS*, 448, 1446
- Agnello, A., T. Treu, F. Ostrovski, P. L. Schechter, E. J. Buckley-Geer, H. Lin, M. W. Auger, F. Courbin, C. D. Fassnacht, J. Frieman, N. Kuropatkin, P. J. Marshall, R. G. McMahon, G. Meylan, A. More, S. H. Suyu, C. E. Rusu, D. Finley, T. Abbott, F. B. Abdalla, S. Allam, J. Annis, M. Banerji, A. Benoit-Lévy, E. Bertin, D. Brooks, D. L. Burke, A. Carnero Rosell, M. Carrasco Kind, J. Carretero, C. E. Cunha, C. B. D’Andrea, L. N. da Costa, S. Desai, H. T. Diehl, J. P. Dietrich, P. Doel, T. F. Eifler, J. Estrada, A. Fausti Neto, B. Flaugher, P. Fosalba, D. W. Gerdes, D. Gruen, G. Gutierrez, K. Honscheid, D. J. James, K. Kuehn, O. Lahav, M. Lima, M. A. G. Maia, M. March, J. L. Marshall, P. Martini, P. Melchior, C. J. Miller, R. Miquel, R. C. Nichol, R. Ogando, A. A. Plazas, K. Reil, A. K. Romer, A. Roodman, M. Sako, E. Sanchez, B. Santiago, V. Scarpine, M. Schubnell, I. Sevilla-Noarbe, R. C. Smith, M. Soares-Santos, F. Sobreira, E. Suchyta, M. E. C. Swanson, G. Tarle, J. Thaler, D. Tucker, A. R. Walker, R. H. Wechsler, & Y. Zhang. 2015b, *MNRAS*, 454, 1260
- Agnello, A., H. Lin, L. Buckley-Geer, T. Treu, V. Bonvin, F. Courbin, C. Lemon, T. Morishita, A. Amara, M. W. Auger, S. Birrer, J. Chan, T. Collett, A. More, C. D. Fassnacht, J. Frieman, P. J. Marshall, R. G. McMahon, G. Meylan, S. H. Suyu, F. Castander, D. Finley, A. Howell, C. Kochanek, M. Makler, P. Martini, N. Morgan, B. Nord, F. Ostrovski, P. Schechter, D. Tucker, R. Wechsler, T. M. C. Abbott, F. B. Abdalla, S. Allam,

A. Benoit-Lévy, E. Bertin, D. Brooks, D. L. Burke, A. C. Rosell, M. C. Kind, J. Carretero, M. Crocce, C. E. Cunha, C. B. D’Andrea, L. N. da Costa, S. Desai, J. P. Dietrich, T. F. Eifler, B. Flaughner, P. Fosalba, J. García-Bellido, E. Gaztanaga, M. S. Gill, D. A. Goldstein, D. Gruen, R. A. Gruendl, J. Gschwend, G. Gutierrez, K. Honscheid, D. J. James, K. Kuehn, N. Kuropatkin, T. S. Li, M. Lima, M. A. G. Maia, M. March, J. L. Marshall, P. Melchior, F. Menanteau, R. Miquel, R. L. C. Ogando, A. A. Plazas, A. K. Romer, E. Sanchez, R. Schindler, M. Schubnell, I. Sevilla-Noarbe, M. Smith, R. C. Smith, F. Sobreira, E. Suchyta, M. E. C. Swanson, G. Tarle, D. Thomas, & A. R. Walker. 2017, *MNRAS*, 472, 4038

Agnello, A., H. Lin, N. Kuropatkin, E. Buckley-Geer, T. Anguita, P. L. Schechter, T. Morishita, V. Motta, K. Rojas, T. Treu, A. Amara, M. W. Auger, F. Courbin, C. D. Fassnacht, J. Frieman, A. More, P. J. Marshall, R. G. McMahon, G. Meylan, S. H. Suyu, K. Glazebrook, N. Morgan, B. Nord, T. M. C. Abbott, F. B. Abdalla, J. Annis, K. Bechtol, A. Benoit-Lévy, E. Bertin, R. A. Bernstein, D. Brooks, D. L. Burke, A. C. Rosell, J. Carretero, C. E. Cunha, C. B. D’Andrea, L. N. da Costa, S. Desai, A. Drlica-Wagner, T. F. Eifler, B. Flaughner, J. García-Bellido, E. Gaztanaga, D. W. Gerdes, D. Gruen, R. A. Gruendl, J. Gschwend, G. Gutierrez, K. Honscheid, D. J. James, K. Kuehn, O. Lahav, M. Lima, M. A. G. Maia, M. March, F. Menanteau, R. Miquel, R. L. C. Ogando, A. A. Plazas, E. Sanchez, V. Scarpine, R. Schindler, M. Schubnell, I. Sevilla-Noarbe, M. Smith, M. Soares-Santos, F. Sobreira, E. Suchyta, M. E. C. Swanson, G. Tarle, D. Tucker, & R. Wechsler. 2018b, *MNRAS*, 479, 4345

Agnello, A., H. Lin, N. Kuropatkin, E. Buckley-Geer, T. Anguita, P. L. Schechter, T. Morishita, V. Motta, K. Rojas, T. Treu, A. Amara, M. W. Auger, F. Courbin, C. D. Fassnacht, J. Frieman, A. More, P. J. Marshall, R. G. McMahon, G. Meylan, S. H. Suyu, K. Glazebrook, N. Morgan, B. Nord, T. M. C. Abbott, F. B. Abdalla, J. Annis, K. Bechtol, A. Benoit-Lévy, E. Bertin, R. A. Bernstein, D. Brooks, D. L. Burke, A. Carnero Rosell, J. Carretero, C. E. Cunha, C. B. D’Andrea, L. N. da Costa, S. Desai, A. Drlica-Wagner,

- T. F. Eifler, B. Flaughe, J. García-Bellido, E. Gaztanaga, D. W. Gerdes, D. Gruen, R. A. Gruendl, J. Gschwend, G. Gutierrez, K. Honscheid, D. J. James, K. Kuehn, O. Lahav, M. Lima, M. A. G. Maia, M. March, F. Menanteau, R. Miquel, R. L. C. Ogando, A. A. Plazas, E. Sanchez, V. Scarpine, R. Schindler, M. Schubnel, I. Sevilla-Noarbe, M. Smith, M. Soares-Santos, F. Sobreira, E. Suchyta, M. E. C. Swanson, G. Tarle, D. Tucker, & R. Wechsler. 2018c, *MNRAS*, 479, 4345
- Agnello, A., P. L. Schechter, N. D. Morgan, T. Treu, C. Grillo, D. Malesani, T. Anguita, Y. Apostolovski, C. E. Rusu, V. Motta, K. Rojas, B. Chehade, & T. Shanks. 2018d, *MNRAS*, 475, 2086
- Akeret, J., S. Seehars, A. Amara, A. Refregier, & A. Csillaghy. 2013, *Astronomy and Computing*, 2, 27
- Alam, S., F. D. Albareti, C. Allende Prieto, F. Anders, S. F. Anderson, T. Anderton, B. H. Andrews, E. Armengaud, É. Aubourg, S. Bailey, & et al. 2015, *ApJS*, 219, 12
- Alam, S., M. Ata, S. Bailey, F. Beutler, D. Bizyaev, J. A. Blazek, A. S. Bolton, J. R. Brownstein, A. Burden, C.-H. Chuang, J. Comparat, A. J. Cuesta, K. S. Dawson, D. J. Eisenstein, S. Escoffier, H. Gil-Marín, J. N. Grieb, N. Hand, S. Ho, K. Kinemuchi, D. Kirkby, F. Kitaura, E. Malanushenko, V. Malanushenko, C. Maraston, C. K. McBride, R. C. Nichol, M. D. Olmstead, D. Oravetz, N. Padmanabhan, N. Palanque-Delabrouille, K. Pan, M. Pellejero-Ibanez, W. J. Percival, P. Petitjean, F. Prada, A. M. Price-Whelan, B. A. Reid, S. A. Rodríguez-Torres, N. A. Roe, A. J. Ross, N. P. Ross, G. Rossi, J. A. Rubiño-Martín, A. G. Sánchez, S. Saito, S. Salazar-Albornoz, L. Samushia, S. Satpathy, C. G. Scóccola, D. J. Schlegel, D. P. Schneider, H.-J. Seo, A. Simmons, A. Slosar, M. A. Strauss, M. E. C. Swanson, D. Thomas, J. L. Tinker, R. Tojeiro, M. Vargas Magaña, J. A. Vazquez, L. Verde, D. A. Wake, Y. Wang, D. H. Weinberg, M. White, W. M. Wood-Vasey, C. Yèche, I. Zehavi, Z. Zhai, & G.-B. Zhao. 2017, *MNRAS*, 470, 2617
- Amara, A., R. B. Metcalf, T. J. Cox, & J. P. Ostriker. 2006, *MNRAS*, 367, 1367

- Anguita, T., C. Faure, A. Yonehara, J. Wambsganss, J.-P. Kneib, G. Covone, & D. Alloin. 2008, *A&A*, 481, 615
- Anguita, T., P. L. Schechter, N. Kuropatkin, N. D. Morgan, F. Ostrovski, L. E. Abramson, A. Agnello, Y. Apostolovski, C. D. Fassnacht, J. W. Hsueh, V. Motta, K. Rojas, C. E. Rusu, T. Treu, P. Williams, M. Auger, E. Buckley-Geer, H. Lin, R. McMahon, T. M. C. Abbott, S. Allam, J. Annis, R. A. Bernstein, E. Bertin, D. Brooks, D. L. Burke, A. Carnero Rosell, M. Carrasco Kind, J. Carretero, C. E. Cunha, C. B. D’Andrea, J. De Vicente, D. L. DePoy, S. Desai, H. T. Diehl, P. Doel, B. Flaugher, J. García-Bellido, D. W. Gerdes, D. Gruen, R. A. Gruendl, J. Gschwend, W. G. Hartley, D. L. Hollowood, K. Honscheid, D. J. James, K. Kuehn, M. Lima, M. A. G. Maia, R. Miquel, A. A. Plazas, E. Sanchez, V. Scarpine, M. Smith, M. Soares-Santos, F. Sobreira, E. Suchyta, G. Tarle, & A. R. Walker. 2018, *MNRAS*, 480, 5017
- Armstrong, B. 1967, *J. Quant. Spec. Radiat. Transf.*, 7, 61
- Assef, R. J., D. Stern, C. S. Kochanek, A. W. Blain, M. Brodwin, M. J. I. Brown, E. Donoso, P. R. M. Eisenhardt, B. T. Jannuzi, T. H. Jarrett, S. A. Stanford, C.-W. Tsai, J. Wu, & L. Yan. 2013, *ApJ*, 772, 26
- Astropy Collaboration. 2013, *A&A*, 558, A33
- . 2018, *AJ*, 156, 123
- Auger, M. W., T. Treu, A. S. Bolton, R. Gavazzi, L. V. E. Koopmans, P. J. Marshall, L. A. Moustakas, & S. Burles. 2010a, *ApJ*, 724, 511
- Auger, M. W., T. Treu, R. Gavazzi, A. S. Bolton, L. V. E. Koopmans, & P. J. Marshall. 2010b, *ApJ*, 721, L163
- Avila, R. J., W. Hack, M. Cara, D. Borncamp, J. Mack, L. Smith, & L. Ubeda. 2015, in *Astronomical Society of the Pacific Conference Series*, Vol. 495, *Astronomical Data*

- Analysis Software and Systems XXIV (ADASS XXIV), ed. A. R. Taylor & E. Rosolowsky, 281
- Barkana, R. 1998, *ApJ*, 502, 531
- . 1999, FASTELL: Fast calculation of a family of elliptical mass gravitational lens models, Astrophysics Source Code Library, ascl:9910.003
- Barnabè, M., O. Czoske, L. V. E. Koopmans, T. Treu, & A. S. Bolton. 2011, *MNRAS*, 415, 2215
- Bartelmann, M. 1996, *A&A*, 313, 697
- Bartelmann, M. & M. Meneghetti. 2004, *A&A*, 418, 413
- Behroozi, P., R. H. Wechsler, A. P. Hearin, & C. Conroy. 2019, *MNRAS*, 488, 3143
- Bendinelli, O. 1991, *ApJ*, 366, 599
- Bennett, C. L., D. Larson, J. L. Weiland, N. Jarosik, G. Hinshaw, N. Odegard, K. M. Smith, R. S. Hill, B. Gold, M. Halpern, E. Komatsu, M. R. Nolta, L. Page, D. N. Spergel, E. Wollack, J. Dunkley, A. Kogut, M. Limon, S. S. Meyer, G. S. Tucker, & E. L. Wright. 2013, *ApJS*, 208, 20
- Berghea, C. T., G. J. Nelson, C. E. Rusu, C. R. Keeton, & R. P. Dudik. 2017, *ApJ*, 844, 90
- Bernal, J. L., L. Verde, & A. G. Riess. 2016, *J. Cosmology Astropart. Phys.*, 10, 019
- Bertin, E. & S. Arnouts. 1996, *A&AS*, 117, 393
- Bertin, G. & M. Lombardi. 2006, *ApJ*, 648, L17
- Binney, J. & G. A. Mamon. 1982, *MNRAS*, 200, 361
- Birrer, S. & A. Amara. 2018, *Physics of the Dark Universe*, 22, 189

- Birrer, S., A. Amara, & A. Refregier. 2015, *ApJ*, 813, 102
- . 2016, *J. Cosmology Astropart. Phys.*, 8, 020
- . 2017, *J. Cosmology Astropart. Phys.*, 5, 037
- Birrer, S. & T. Treu. 2019, *MNRAS*, 489, 2097
- Birrer, S., T. Treu, C. E. Rusu, V. Bonvin, C. D. Fassnacht, J. H. H. Chan, A. Agnello, A. J. Shajib, G. C.-F. Chen, M. Auger, F. Courbin, S. Hilbert, D. Sluse, S. H. Suyu, K. C. Wong, P. Marshall, B. C. Lemaux, & G. Meylan. 2019, *MNRAS*, 484, 4726
- Blandford, R. & R. Narayan. 1986, *ApJ*, 310, 568
- Blandford, R. D. & R. Narayan. 1992, *ARA&A*, 30, 311
- Bolton, A. S., S. Burles, L. V. E. Koopmans, T. Treu, & L. A. Moustakas. 2006, *ApJ*, 638, 703
- Bonvin, V., F. Courbin, S. H. Suyu, P. J. Marshall, C. E. Rusu, D. Sluse, M. Tewes, K. C. Wong, T. Collett, C. D. Fassnacht, T. Treu, M. W. Auger, S. Hilbert, L. V. E. Koopmans, G. Meylan, N. Rumbaugh, A. Sonnenfeld, & C. Spiniello. 2017, *MNRAS*, 465, 4914
- Bonvin, V., J. H. H. Chan, M. Millon, K. Rojas, F. Courbin, G. C.-F. Chen, C. D. Fassnacht, E. Paic, M. Tewes, D. C.-Y. Chao, M. Chijani, D. Gilman, K. Gilmore, P. Williams, E. Buckley-Geer, J. Frieman, P. J. Marshall, S. H. Suyu, T. Treu, A. Hempel, S. Kim, R. Lachaume, M. Rabus, T. Anguita, G. Meylan, V. Motta, & P. Magain. 2018, *A&A*, 616, A183
- Boughn, S. & R. Crittenden. 2004, *Nature*, 427, 45
- Bourassa, R. R. & R. Kantowski. 1975, *ApJ*, 195, 13
- Bourassa, R. R., R. Kantowski, & T. D. Norton. 1973, *ApJ*, 185, 747

- Boylan-Kolchin, M., J. S. Bullock, & M. Kaplinghat. 2011, MNRAS, 415, L40
- Bray, I. 1984, MNRAS, 208, 511
- Brewer, B. J., P. J. Marshall, M. W. Auger, T. Treu, A. A. Dutton, & M. Barnabè. 2014, MNRAS, 437, 1950
- Bruderer, C., J. I. Read, J. P. Coles, D. Leier, E. E. Falco, I. Ferreras, & P. Saha. 2016, MNRAS, 456, 870
- Buckley-Geer, E. J., H. Lin, C. Rusu, J. Poh, A. Palmese, A. Agnello, L. Christensen, J. Frieman, A. J. Shajib, T. Treu, T. Collett, S. Birrer, T. Anguita, C. D. Fassnacht, G. Meylan, S. Mukherjee, K. C. Wong, M. Aguena, S. Allam, S. Avila, E. Bertin, S. Bhargava, D. Brooks, A. Carnero Rosell, M. Carrasco Kind, J. Carretero, F. J. Castander, M. Costanzi, L. N. da Costa, J. De Vicente, S. Desai, H. T. Diehl, P. Doel, T. F. Eifler, S. Everett, B. Flaugher, P. Fosalba, J. García-Bellido, E. Gaztanaga, D. Gruen, R. A. Gruendl, J. Gschwend, G. Gutierrez, S. R. Hinton, K. Honscheid, D. J. James, K. Kuehn, N. Kuropatkin, M. A. G. Maia, J. L. Marshall, P. Melchior, F. Menanteau, R. Miquel, R. L. C. Ogando, F. Paz-Chinchón, A. A. Plazas, E. Sanchez, V. Scarpine, M. Schubnell, S. Serrano, I. Sevilla-Noarbe, M. Smith, M. Soares-Santos, E. Suchyta, M. E. C. Swanson, G. Tarle, D. L. Tucker, & T. N. Varga. 2020, arXiv e-prints, arXiv:2003.12117
- Cabass, G., M. Gerbino, E. Giusarma, A. Melchiorri, L. Pagano, & L. Salvati. 2015, Phys. Rev. D, 92, 063534
- Cappellari, M. 2002, MNRAS, 333, 400
- . 2008, MNRAS, 390, 71
- Cappellari, M., R. M. McDermid, K. Alatalo, L. Blitz, M. Bois, F. Bournaud, M. Bureau, A. F. Crocker, R. L. Davies, T. A. Davis, P. T. de Zeeuw, P.-A. Duc, E. Emself, S. Khochfar, D. Krajnović, H. Kuntschner, P.-Y. Lablanche, R. Morganti, T. Naab,

- T. Oosterloo, M. Sarzi, N. Scott, P. Serra, A.-M. Weijmans, & L. M. Young. 2012, *Nature*, 484, 485
- Cardelli, J. A., G. C. Clayton, & J. S. Mathis. 1989, *ApJ*, 345, 245
- Chen, G. C.-F., S. H. Suyu, K. C. Wong, C. D. Fassnacht, T. Chiueh, A. Halkola, I. S. Hu, M. W. Auger, L. V. E. Koopmans, D. J. Lagattuta, J. P. McKean, & S. Vegetti. 2016, *MNRAS*, 462, 3457
- Chen, G. C.-F., J. H. H. Chan, V. Bonvin, C. D. Fassnacht, K. Rojas, M. Millon, F. Courbin, S. H. Suyu, K. C. Wong, D. Sluse, T. Treu, A. J. Shajib, J.-W. Hsueh, D. J. Lagattuta, L. V. E. Koopmans, S. Vegetti, & J. P. McKean. 2018, *MNRAS*, 481, 1115
- Chen, G. C.-F., C. D. Fassnacht, S. H. Suyu, C. E. Rusu, J. H. H. Chan, K. C. Wong, M. W. Auger, S. Hilbert, V. Bonvin, S. Birrer, M. Millon, L. V. E. Koopmans, D. J. Lagattuta, J. P. McKean, S. Vegetti, F. Courbin, X. Ding, A. Halkola, I. Jee, A. J. Shajib, D. Sluse, A. Sonnenfeld, & T. Treu. 2019, *MNRAS*, arXiv:1907.02533
- Chevallier, M. & D. Polarski. 2001, *International Journal of Modern Physics D*, 10, 213
- Claeskens, J.-F., D. Sluse, P. Riaud, & J. Surdej. 2006, *A&A*, 451, 865
- Clowe, D., A. Gonzalez, & M. Markevitch. 2004, *ApJ*, 604, 596
- Collett, T. E. 2015, *ApJ*, 811, 20
- Collett, T. E. & M. W. Auger. 2014, *MNRAS*, 443, 969
- Collett, T. E., M. W. Auger, V. Belokurov, P. J. Marshall, & A. C. Hall. 2012, *MNRAS*, 424, 2864
- Collett, T. E., P. J. Marshall, M. W. Auger, S. Hilbert, S. H. Suyu, Z. Greene, T. Treu, C. D. Fassnacht, L. V. E. Koopmans, M. Bradač, & R. D. Blandford. 2013, *MNRAS*, 432, 679

Contopoulos, G. 1956, ZAp, 39, 126

Cooray, A. 2002, Phys. Rev. D, 65, 083518

Cooray, A. & W. Hu. 2000, ApJ, 534, 533

Courbin, F., V. Bonvin, E. Buckley-Geer, C. D. Fassnacht, J. Frieman, H. Lin, P. J. Marshall, S. H. Suyu, T. Treu, T. Anguita, V. Motta, G. Meylan, E. Paic, M. Tewes, A. Agnello, D. C.-Y. Chao, M. Chijani, D. Gilman, K. Rojas, P. Williams, A. Hempel, S. Kim, R. Lachaume, M. Rabus, T. M. C. Abbott, S. Allam, J. Annis, M. Banerji, K. Bechtol, A. Benoit-Lévy, D. Brooks, D. L. Burke, A. Carnero Rosell, M. Carrasco Kind, J. Carretero, C. B. D’Andrea, L. N. da Costa, C. Davis, D. L. DePoy, S. Desai, B. Flaugher, P. Fosalba, J. Garcia-Bellido, E. Gaztanaga, D. A. Goldstein, D. Gruen, R. A. Gruendl, J. Gschwend, G. Gutierrez, K. Honscheid, D. J. James, K. Kuehn, S. Kuhlmann, N. Kuropatkin, O. Lahav, M. Lima, M. A. G. Maia, M. March, J. L. Marshall, R. G. McMahon, F. Menanteau, R. Miquel, B. Nord, A. A. Plazas, E. Sanchez, V. Scarpine, R. Schindler, M. Schubnell, I. Sevilla-Noarbe, M. Smith, M. Soares-Santos, F. Sobreira, E. Suchyta, G. Tarle, D. L. Tucker, A. R. Walker, & W. Wester. 2018, A&A, 609, A71

Courteau, S., M. Cappellari, R. S. de Jong, A. A. Dutton, E. Emsellem, H. Hoekstra, L. V. E. Koopmans, G. A. Mamon, C. Maraston, T. Treu, & L. M. Widrow. 2014, Reviews of Modern Physics, 86, 47

Croom, S. M., B. J. Boyle, T. Shanks, R. J. Smith, L. Miller, P. J. Outram, N. S. Loaring, F. Hoyle, & J. da Ângela. 2005, MNRAS, 356, 415

Dalal, N. & C. S. Kochanek. 2002, ApJ, 572, 25

Dawson, K. S., D. J. Schlegel, C. P. Ahn, S. F. Anderson, É. Aubourg, S. Bailey, R. H. Barkhouser, J. E. Bautista, A. Beifiori, A. A. Berlind, V. Bhardwaj, D. Bizyaev, C. H. Blake, M. R. Blanton, M. Blomqvist, A. S. Bolton, A. Borde, J. Bovy, W. N. Brandt,

H. Brewington, J. Brinkmann, P. J. Brown, J. R. Brownstein, K. Bundy, N. G. Busca, W. Carithers, A. R. Carnero, M. A. Carr, Y. Chen, J. Comparat, N. Connolly, F. Cope, R. A. C. Croft, A. J. Cuesta, L. N. da Costa, J. R. A. Davenport, T. Delubac, R. de Putter, S. Dhital, A. Ealet, G. L. Ebelke, D. J. Eisenstein, S. Escoffier, X. Fan, N. Filiz Ak, H. Finley, A. Font-Ribera, R. Génova-Santos, J. E. Gunn, H. Guo, D. Haggard, P. B. Hall, J.-C. Hamilton, B. Harris, D. W. Harris, S. Ho, D. W. Hogg, D. Holder, K. Honscheid, J. Huehn-erhoff, B. Jordan, W. P. Jordan, G. Kauffmann, E. A. Kazin, D. Kirkby, M. A. Klaene, J.-P. Kneib, J.-M. Le Goff, K.-G. Lee, D. C. Long, C. P. Loomis, B. Lundgren, R. H. Lup-
ton, M. A. G. Maia, M. Makler, E. Malanushenko, V. Malanushenko, R. Mandelbaum, M. Manera, C. Maraston, D. Margala, K. L. Masters, C. K. McBride, P. McDonald, I. D. McGreer, R. G. McMahon, O. Mena, J. Miralda-Escudé, A. D. Montero-Dorta, F. Mon-tesano, D. Muna, A. D. Myers, T. Naugle, R. C. Nichol, P. Noterdaeme, S. E. Nuza, M. D. Olmstead, A. Oravetz, D. J. Oravetz, R. Owen, N. Padmanabhan, N. Palanque-
Delabrouille, K. Pan, J. K. Parejko, I. Pâris, W. J. Percival, I. Pérez-Fournon, I. Pérez-
Ràfols, P. Petitjean, R. Pfaffenberger, J. Pforr, M. M. Pieri, F. Prada, A. M. Price-Whelan, M. J. Raddick, R. Rebolo, J. Rich, G. T. Richards, C. M. Rockosi, N. A. Roe, A. J. Ross, N. P. Ross, G. Rossi, J. A. Rubiño-Martin, L. Samushia, A. G. Sánchez, C. Sayres, S. J. Schmidt, D. P. Schneider, C. G. Scóccola, H.-J. Seo, A. Sheldon, E. Sheldon, Y. Shen, Y. Shu, A. Slosar, S. A. Smee, S. A. Snedden, F. Stauffer, O. Steele, M. A. Strauss, A. Streblyanska, N. Suzuki, M. E. C. Swanson, T. Tal, M. Tanaka, D. Thomas, J. L. Tinker, R. Tojeiro, C. A. Tremonti, M. Vargas Magaña, L. Verde, M. Viel, D. A. Wake, M. Watson, B. A. Weaver, D. H. Weinberg, B. J. Weiner, A. A. West, M. White, W. M. Wood-Vasey, C. Yèche, I. Zehavi, G.-B. Zhao, & Z. Zheng. 2013, *AJ*, 145, 10

de Blok, W. J. G., F. Walter, E. Brinks, C. Trachternach, S. H. Oh, & J. Kennicutt, R. C. 2008, *AJ*, 136, 2648

Debattista, V. P., B. Moore, T. Quinn, S. Kazantzidis, R. Maas, L. Mayer, J. Read, & J. Stadel. 2008, *ApJ*, 681, 1076

- Debattista, V. P., F. C. van den Bosch, R. Roškar, T. Quinn, B. Moore, & D. R. Cole. 2015, *MNRAS*, 452, 4094
- Delchambre, L., A. Krone-Martins, O. Wertz, C. Ducourant, L. Galluccio, J. Klüter, F. Mignard, R. Teixeira, S. G. Djorgovski, D. P. Stern, M. J. Graham, U. Bastian, J. Surdej, J. Wambsganss, J.-F. Le Campion, & E. Slezak. 2018, ArXiv e-prints, arXiv:1807.02845
- Diehl, H. T., E. J. Buckley-Geer, K. A. Lindgren, B. Nord, H. Gaitsch, S. Gaitsch, H. Lin, S. Allam, T. E. Collett, C. Furlanetto, M. S. S. Gill, A. More, J. Nightingale, C. Odden, A. Pellico, D. L. Tucker, L. N. da Costa, A. Fausti Neto, N. Kuropatkin, M. Soares-Santos, B. Welch, Y. Zhang, J. A. Frieman, F. B. Abdalla, J. Annis, A. Benoit-Lévy, E. Bertin, D. Brooks, D. L. Burke, A. Carnero Rosell, M. Carrasco Kind, J. Carretero, C. E. Cunha, C. B. D’Andrea, S. Desai, J. P. Dietrich, A. Drlica-Wagner, A. E. Evrard, D. A. Finley, B. Flaugher, J. García-Bellido, D. W. Gerdes, D. A. Goldstein, D. Gruen, R. A. Gruendl, J. Gschwend, G. Gutierrez, D. J. James, K. Kuehn, S. Kuhlmann, O. Lahav, T. S. Li, M. Lima, M. A. G. Maia, J. L. Marshall, F. Menanteau, R. Miquel, R. C. Nichol, P. Nugent, R. L. C. Ogando, A. A. Plazas, K. Reil, A. K. Romer, M. Sako, E. Sanchez, B. Santiago, V. Scarpine, R. Schindler, M. Schubnell, I. Sevilla-Noarbe, E. Sheldon, M. Smith, F. Sobreira, E. Suchyta, M. E. C. Swanson, G. Tarle, D. Thomas, A. R. Walker, & DES Collaboration. 2017, *ApJS*, 232, 15
- Diemer, B. 2018, *ApJS*, 239, 35
- Diemer, B. & M. Joyce. 2019, *ApJ*, 871, 168
- D’Souza, R., G. Kauffman, J. Wang, & S. Vegetti. 2014, *MNRAS*, 443, 1433
- Dubinski, J. 1994, *ApJ*, 431, 617
- Dubinski, J. & R. G. Carlberg. 1991, *ApJ*, 378, 496

- Dutton, A. A. & T. Treu. 2014, MNRAS, 438, 3594
- Dutton, A. A., B. J. Brewer, P. J. Marshall, M. W. Auger, T. Treu, D. C. Koo, A. S. Bolton, B. P. Holden, & L. V. E. Koopmans. 2011, MNRAS, 417, 1621
- Eisenstein, D. J., I. Zehavi, D. W. Hogg, R. Scoccimarro, M. R. Blanton, R. C. Nichol, R. Scranton, H.-J. Seo, M. Tegmark, Z. Zheng, S. F. Anderson, J. Annis, N. Bahcall, J. Brinkmann, S. Burles, F. J. Castander, A. Connolly, I. Csabai, M. Doi, M. Fukugita, J. A. Frieman, K. Glazebrook, J. E. Gunn, J. S. Hendry, G. Hennessy, Z. Ivezić, S. Kent, G. R. Knapp, H. Lin, Y.-S. Loh, R. H. Lupton, B. Margon, T. A. McKay, A. Meiksin, J. A. Munn, A. Pope, M. W. Richmond, D. Schlegel, D. P. Schneider, K. Shimasaku, C. Stoughton, M. A. Strauss, M. SubbaRao, A. S. Szalay, I. Szapudi, D. L. Tucker, B. Yanny, & D. G. York. 2005, ApJ, 633, 560
- Emsellem, E., G. Monnet, R. Bacon, & J.-L. Nieto. 1994, A&A, 285, 739
- Ene, I., C.-P. Ma, M. Veale, J. E. Greene, J. Thomas, J. P. Blakeslee, C. Foster, J. L. Walsh, J. Ito, & A. D. Goulding. 2018, MNRAS, 479, 2810
- Falco, E. E., M. V. Gorenstein, & I. I. Shapiro. 1985, ApJ, 289, L1
- Falco, E. E., C. D. Impey, C. S. Kochanek, J. Lehar, B. A. McLeod, H.-W. Rix, C. R. Keeton, J. A. Muñoz, & C. Y. Peng. 1999, ApJ, 523, 617
- Fassnacht, C. D., E. Xanthopoulos, L. V. E. Koopmans, & D. Rusin. 2002, ApJ, 581, 823
- Ferraro, S., B. D. Sherwin, & D. N. Spergel. 2015, Phys. Rev. D, 91, 083533
- Ferreras, I., P. Saha, & S. Burles. 2008, MNRAS, 383, 857
- Foreman-Mackey, D. 2016, The Journal of Open Source Software, 24, doi:10.21105/joss.00024
- Foreman-Mackey, D., D. W. Hogg, D. Lang, & J. Goodman. 2013, PASP, 125, 306

- Fosalba, P. & E. Gaztañaga. 2004, MNRAS, 350, L37
- Fosalba, P., E. Gaztañaga, & F. J. Castander. 2003, ApJ, 597, L89
- Francis, C. L. & J. A. Peacock. 2010, MNRAS, 406, 2
- Freedman, W. L., B. F. Madore, D. Hatt, T. J. Hoyt, I.-S. Jang, R. L. Beaton, C. R. Burns, M. G. Lee, A. J. Monson, J. R. Neeley, M. M. Phillips, J. A. Rich, & M. Seibert. 2019, ApJ, 882, 34
- Gavazzi, R., T. Treu, L. V. E. Koopmans, A. S. Bolton, L. A. Moustakas, S. Burles, & P. J. Marshall. 2008, ApJ, 677, 1046
- Gavazzi, R., T. Treu, P. J. Marshall, F. Brault, & A. Ruff. 2012, ApJ, 761, 170
- Gavazzi, R., T. Treu, J. D. Rhodes, L. V. E. Koopmans, A. S. Bolton, S. Burles, R. J. Massey, & L. A. Moustakas. 2007, ApJ, 667, 176
- Geach, J. E., R. C. Hickox, L. E. Bleem, M. Brodwin, G. P. Holder, K. A. Aird, B. A. Benson, S. Bhattacharya, J. E. Carlstrom, C. L. Chang, H.-M. Cho, T. M. Crawford, A. T. Crites, T. de Haan, M. A. Dobbs, J. Dudley, E. M. George, K. N. Hainline, N. W. Halverson, W. L. Holzapfel, S. Hoover, Z. Hou, J. D. Hrubes, R. Keisler, L. Knox, A. T. Lee, E. M. Leitch, M. Lueker, D. Luong-Van, D. P. Marrone, J. J. McMahon, J. Mehl, S. S. Meyer, M. Millea, J. J. Mohr, T. E. Montroy, A. D. Myers, S. Padin, T. Plagge, C. Pryke, C. L. Reichardt, J. E. Ruhl, J. T. Sayre, K. K. Schaffer, L. Shaw, E. Shirokoff, H. G. Spieler, Z. Staniszewski, A. A. Stark, K. T. Story, A. van Engelen, K. Vanderlinde, J. D. Vieira, R. Williamson, & O. Zahn. 2013, ApJ, 776, L41
- Giannantonio, T., R. Scranton, R. G. Crittenden, R. C. Nichol, S. P. Boughn, A. D. Myers, & G. T. Richards. 2008, Phys. Rev. D, 77, 123520
- Gilman, D., A. Agnello, T. Treu, C. R. Keeton, & A. M. Nierenberg. 2017, MNRAS, 467, 3970

- Gilman, D., S. Birrer, T. Treu, C. R. Keeton, & A. Nierenberg. 2018, *MNRAS*, 481, 819
- Golse, G. & J.-P. Kneib. 2002, *A&A*, 390, 821
- Gomer, M. R. & L. L. R. Williams. 2018, *MNRAS*, 475, 1987
- Goobar, A., R. Amanullah, S. R. Kulkarni, P. E. Nugent, J. Johansson, C. Steidel, D. Law, E. Mörtzell, R. Quimby, N. Blagorodnova, A. Brandeker, Y. Cao, A. Cooray, R. Ferretti, C. Fremling, L. Hangard, M. Kasliwal, T. Kupfer, R. Lunnan, F. Masci, A. A. Miller, H. Nayyeri, J. D. Neill, E. O. Ofek, S. Papadogiannakis, T. Petrushevskaya, V. Ravi, J. Sollerman, M. Sullivan, F. Taddia, R. Walters, D. Wilson, L. Yan, & O. Yaron. 2017, *Science*, 356, 291
- Goodman, J. & J. Weare. 2010, *Communications in Applied Mathematics and Computational Science*, 5, 65
- Goodwin, E. T. 1949, *Mathematical Proceedings of the Cambridge Philosophical Society*, 45, 241–245
- Górski, K. M., E. Hivon, A. J. Banday, B. D. Wandelt, F. K. Hansen, M. Reinecke, & M. Bartelmann. 2005, *ApJ*, 622, 759
- Goto, T., I. Szapudi, & B. R. Granett. 2012, *MNRAS*, 422, L77
- Goullaud, C. F., J. B. Jensen, J. P. Blakeslee, C.-P. Ma, J. E. Greene, & J. Thomas. 2018, *ApJ*, 856, 11
- Granett, B. R., M. C. Neyrinck, & I. Szapudi. 2009, *ApJ*, 701, 414
- Greene, Z. S., S. H. Suyu, T. Treu, S. Hilbert, M. W. Auger, T. E. Collett, P. J. Marshall, C. D. Fassnacht, R. D. Blandford, M. Bradač, & L. V. E. Koopmans. 2013, *ApJ*, 768, 39
- Grillo, C., M. Lombardi, & G. Bertin. 2008, *A&A*, 477, 397

- Grillo, C., P. Rosati, S. H. Suyu, I. Balestra, G. B. Caminha, A. Halkola, P. L. Kelly, M. Lombardi, A. Mercurio, S. A. Rodney, & T. Treu. 2018, *ApJ*, 860, 94
- Gu  rou, A., D. Krajnovi  , B. Epinat, T. Contini, E. Emsellem, N. Bouch  , R. Bacon, L. Michel-Dansac, J. Richard, P. M. Weilbacher, J. Schaye, R. A. Marino, M. den Brok, & S. Erroz-Ferrer. 2017, *A&A*, 608, A5
- Hamilton, A. J. S. 2000, *MNRAS*, 312, 257
- Handley, W. J., M. P. Hobson, & A. N. Lasenby. 2015, *MNRAS*, 453, 4384
- Heiligman, G. & M. Schwarzschild. 1979, *ApJ*, 233, 872
- Heymans, C., E. Grocutt, A. Heavens, M. Kilbinger, T. D. Kitching, F. Simpson, J. Benjamin, T. Erben, H. Hildebrandt, H. Hoekstra, Y. Mellier, L. Miller, L. Van Waerbeke, M. L. Brown, J. Coupon, L. Fu, J. Harnois-D  raps, M. J. Hudson, K. Kuijken, B. Rowe, T. Schrabback, E. Semboloni, S. Vafaei, & M. Velander. 2013, *MNRAS*, 432, 2433
- Hezaveh, Y. D., L. P. Levasseur, & P. J. Marshall. 2017, *Nature*, 548, 555
- Hezaveh, Y. D., N. Dalal, D. P. Marrone, Y.-Y. Mao, W. Morningstar, D. Wen, R. D. Blandford, J. E. Carlstrom, C. D. Fassnacht, G. P. Holder, A. Kembell, P. J. Marshall, N. Murray, L. Perreault Levasseur, J. D. Vieira, & R. H. Wechsler. 2016, *ApJ*, 823, 37
- Higson, E. 2018, *Journal of Open Source Software*, 3, 916
- Higson, E., W. Handley, M. Hobson, & A. Lasenby. 2018, *Statistics and Computing*, doi:10.1007/s11222-018-9844-0
- Higson, E., W. Handley, M. Hobson, & A. Lasenby. 2019, dyPolyChord: Super fast dynamic nested sampling with PolyChord, *Astrophysics Source Code Library*, ascl:1902.010
- Hilbert, S., J. Hartlap, S. D. M. White, & P. Schneider. 2009, *A&A*, 499, 31

- Hinshaw, G., D. Larson, E. Komatsu, D. N. Spergel, C. L. Bennett, J. Dunkley, M. R. Nolte, M. Halpern, R. S. Hill, N. Odegard, L. Page, K. M. Smith, J. L. Weiland, B. Gold, N. Jarosik, A. Kogut, M. Limon, S. S. Meyer, G. S. Tucker, E. Wollack, & E. L. Wright. 2013, *ApJS*, 208, 19
- Hivon, E., K. M. Górski, C. B. Netterfield, B. P. Crill, S. Prunet, & F. Hansen. 2002, *ApJ*, 567, 2
- Ho, S., C. Hirata, N. Padmanabhan, U. Seljak, & N. Bahcall. 2008, *Phys. Rev. D*, 78, 043519
- Hoeting, J. A., D. Madigan, A. E. Raftery, & C. T. Volinsky. 1999, *Statist. Sci.*, 14, 382
- Hogg, D. W. & D. Lang. 2013, *PASP*, 125, 719
- Hsueh, J.-W., C. D. Fassnacht, S. Vegetti, J. P. McKean, C. Spingola, M. W. Auger, L. V. E. Koopmans, & D. J. Lagattuta. 2016, *MNRAS*, 463, L51
- Hsueh, J.-W., L. Oldham, C. Spingola, S. Vegetti, C. D. Fassnacht, M. W. Auger, L. V. E. Koopmans, J. P. McKean, & D. J. Lagattuta. 2017, *MNRAS*, 469, 3713
- Huang, C. D., A. G. Riess, W. Yuan, L. M. Macri, N. L. Zakamska, S. Casertano, P. A. Whitelock, S. L. Hoffmann, A. V. Filippenko, & D. Scolnic. 2020, *ApJ*, 889, 5
- Hunter, J. D. 2007, *Computing in Science and Engineering*, 9, 90
- Ibata, R., G. F. Lewis, M. Irwin, E. Totten, & T. Quinn. 2001, *ApJ*, 551, 294
- Inada, N., M. Oguri, M.-S. Shin, I. Kayo, M. A. Strauss, T. Morokuma, C. E. Rusu, M. Fukugita, C. S. Kochanek, G. T. Richards, D. P. Schneider, D. G. York, N. A. Bahcall, J. A. Frieman, P. B. Hall, & R. L. White. 2012, *AJ*, 143, 119
- Jaffe, W. 1983, *MNRAS*, 202, 995

- Jarrett, T. H., M. Cohen, F. Masci, E. Wright, D. Stern, D. Benford, A. Blain, S. Carey, R. M. Cutri, P. Eisenhardt, C. Lonsdale, A. Mainzer, K. Marsh, D. Padgett, S. Petty, M. Ressler, M. Skrutskie, S. Stanford, J. Surace, C. W. Tsai, S. Wheelock, & D. L. Yan. 2011, *ApJ*, 735, 112
- Jedrzejewski, R. I. 1987, *MNRAS*, 226, 747
- Jee, I., E. Komatsu, & S. H. Suyu. 2015, *J. Cosmology Astropart. Phys.*, 11, 033
- Jee, I., E. Komatsu, S. H. Suyu, & D. Huterer. 2016, *J. Cosmology Astropart. Phys.*, 4, 031
- Jiménez-Domínguez, H., H. Flores-Llamas, A. Cabral-Prieto, & A. Bravo-Ortega. 1989, *Nuclear Instruments and Methods in Physics Research A*, 278, 625
- Jing, Y. P. & Y. Suto. 2002, *ApJ*, 574, 538
- Jones, E., T. Oliphant, P. Peterson, & Others. 2001, *SciPy: Open source scientific tools for Python*
- Jorgensen, I., M. Franx, & P. Kjaergaard. 1995, *MNRAS*, 276, 1341
- Kaiser, N. 1992, *ApJ*, 388, 272
- Kassiola, A. & I. Kovner. 1993, *ApJ*, 417, 450
- Katz, N. & J. E. Gunn. 1991, *ApJ*, 377, 365
- Kauffmann, G., S. D. M. White, & B. Guiderdoni. 1993, *MNRAS*, 264, 201
- Kayo, I., N. Inada, M. Oguri, P. B. Hall, C. S. Kochanek, G. T. Richards, D. P. Schneider, D. G. York, & K. Pan. 2007, *AJ*, 134, 1515
- Kazantzidis, S., A. V. Kravtsov, A. R. Zentner, B. Allgood, D. Nagai, & B. Moore. 2004, *ApJ*, 611, L73
- Keeton, C. R. 2001, *ArXiv Astrophysics e-prints*, astro-ph/0102341

- Keeton, C. R., C. S. Kochanek, & E. E. Falco. 1998, *ApJ*, 509, 561
- Keeton, C. R. & L. A. Moustakas. 2009, *ApJ*, 699, 1720
- Kelly, P. L., S. A. Rodney, T. Treu, R. J. Foley, G. Brammer, K. B. Schmidt, A. Zitrin, A. Sonnenfeld, L.-G. Strolger, O. Graur, A. V. Filippenko, S. W. Jha, A. G. Riess, M. Bradac, B. J. Weiner, D. Scolnic, M. A. Malkan, A. von der Linden, M. Trenti, J. Hjorth, R. Gavazzi, A. Fontana, J. C. Merten, C. McCully, T. Jones, M. Postman, A. Dressler, B. Patel, S. B. Cenko, M. L. Graham, & B. E. Tucker. 2015, *Science*, 347, 1123
- Kennedy, J. & R. Eberhart. 1995, in *Proceedings of ICNN'95 - International Conference on Neural Networks* (IEEE)
- Kluyver, T., B. Ragan-Kelley, F. Pérez, B. Granger, M. Bussonnier, J. Frederic, K. Kelley, J. Hamrick, J. Grout, S. Corlay, P. Ivanov, D. Avila, S. Abdalla, & C. Willing. 2016, in *Positioning and Power in Academic Publishing: Players, Agents and Agendas*, ed. F. Loizides & B. Schmidt, IOS Press (IOS Press BV, Amsterdam, Netherlands), 87 – 90
- Klypin, A., A. V. Kravtsov, O. Valenzuela, & F. Prada. 1999, *ApJ*, 522, 82
- Kochanek, C. S. 2002, in *The Shapes of Galaxies and their Dark Halos*, ed. P. Natarajan (WORLD SCIENTIFIC), 62–71
- Kochanek, C. S. & N. Dalal. 2004, *ApJ*, 610, 69
- Koopmans, L. V. E. 2005, *MNRAS*, 363, 1136
- Koopmans, L. V. E. 2006, in *EAS Publications Series, Vol. 20*, *EAS Publications Series*, ed. G. A. Mamon, F. Combes, C. Deffayet, & B. Fort, 161–166
- Koopmans, L. V. E., T. Treu, C. D. Fassnacht, R. D. Blandford, & G. Surpi. 2003, *ApJ*, 599, 70

- Koopmans, L. V. E., A. Bolton, T. Treu, O. Czoske, M. W. Auger, M. Barnabè, S. Vegetti, R. Gavazzi, L. A. Moustakas, & S. Burles. 2009, *ApJ*, 703, L51
- Kormann, R., P. Schneider, & M. Bartelmann. 1994, *A&A*, 284, 285
- Kovács, A., I. Szapudi, B. R. Granett, & Z. Frei. 2013, *MNRAS*, 431, L28
- Kovner, I. 1987, *Nature*, 325, 507
- Kuntz, A. 2015, *A&A*, 584, A53
- Lackner, C. N. & J. E. Gunn. 2012, *MNRAS*, 421, 2277
- Lagattuta, D. J., S. Vegetti, C. D. Fassnacht, M. W. Auger, L. V. E. Koopmans, & J. P. McKean. 2012, *MNRAS*, 424, 2800
- Larkin, J., M. Barczys, A. Krabbe, S. Adkins, T. Aliado, P. Amico, G. Brims, R. Campbell, J. Canfield, T. Gasaway, A. Honey, C. Iserlohe, C. Johnson, E. Kress, D. LaFreniere, K. Magnone, N. Magnone, M. McElwain, J. Moon, A. Quirrenbach, G. Skulason, I. Song, M. Spencer, J. Weiss, & S. Wright. 2006, *New A Rev.*, 50, 362
- Lee, C.-H. 2017, *A&A*, 605, L8
- . 2018, *MNRAS*, 475, 3086
- Lemon, C., M. W. Auger, R. McMahon, T. Anguita, Y. Apostolovski, G. C. F. Chen, C. D. Fassnacht, A. Melo, V. Motta, A. Shajib, T. Treu, A. Agnello, E. Buckley-Geer, P. L. Schechter, S. Birrer, T. Collett, F. Courbin, C. E. Rusu, T. M. C. Abbott, S. Allam, J. Annis, S. Avila, E. Bertin, D. Brooks, D. L. Burke, A. Carnero Rosell, M. Carrasco Kind, J. Carretero, M. Costanzi, L. N. da Costa, J. De Vicente, S. Desai, T. F. Eifler, B. Flaugher, J. Frieman, J. García-Bellido, E. Gaztanaga, D. W. Gerdes, D. Gruen, R. A. Gruendl, J. Gschwend, G. Gutierrez, K. Honscheid, D. J. James, A. Kim, E. Krause, K. Kuehn, N. Kuropatkin, O. Lahav, M. Lima, H. Lin, M. A. G. Maia, M. March, J. L.

- Marshall, F. Menanteau, R. Miquel, A. Palmese, F. P. Chinchón, A. A. Plazas, A. Roodman, E. Sanchez, M. Schubnell, S. Serrano, M. Smith, M. Soares-Santos, E. Suchyta, G. Tarle, & A. R. Walker. 2019, arXiv e-prints, arXiv:1912.09133
- Lemon, C. A., M. W. Auger, R. G. McMahon, & F. Ostrovski. 2018, MNRAS, 479, 5060
- Lewis, A. & S. Bridle. 2002, Phys. Rev. D, 66, 103511
- Lewis, A., A. Challinor, & A. Lasenby. 2000, ApJ, 538, 473
- Limber, D. N. 1953, ApJ, 117, 134
- Lin, H., E. Buckley-Geer, A. Agnello, F. Ostrovski, R. G. McMahon, B. Nord, N. Kuropatkin, D. L. Tucker, T. Treu, J. H. H. Chan, S. H. Suyu, H. T. Diehl, T. Collett, M. S. S. Gill, A. More, A. Amara, M. W. Auger, F. Courbin, C. D. Fassnacht, J. Frieman, P. J. Marshall, G. Meylan, C. E. Rusu, T. M. C. Abbott, F. B. Abdalla, S. Allam, M. Banerji, K. Bechtol, A. Benoit-Lévy, E. Bertin, D. Brooks, D. L. Burke, A. Carnero Rosell, M. Carrasco Kind, J. Carretero, F. J. Castander, M. Crocce, C. B. D’Andrea, L. N. da Costa, S. Desai, J. P. Dietrich, T. F. Eifler, D. A. Finley, B. Flaugher, P. Fosalba, J. García-Bellido, E. Gaztanaga, D. W. Gerdes, D. A. Goldstein, D. Gruen, R. A. Gruendl, J. Gschwend, G. Gutierrez, K. Honscheid, D. J. James, K. Kuehn, O. Lahav, T. S. Li, M. Lima, M. A. G. Maia, M. March, J. L. Marshall, P. Martini, P. Melchior, F. Menanteau, R. Miquel, R. L. C. Ogando, A. A. Plazas, A. K. Romer, E. Sanchez, R. Schindler, M. Schubnell, I. Sevilla-Noarbe, M. Smith, R. C. Smith, F. Sobreira, E. Suchyta, M. E. C. Swanson, G. Tarle, D. Thomas, A. R. Walker, & DES Collaboration. 2017, ApJ, 838, L15
- Linder, E. V. 2003, Phys. Rev. Lett., 90, 091301
- . 2011, Phys. Rev. D, 84, 123529
- Lux, H., J. I. Read, G. Lake, & K. V. Johnston. 2012, MNRAS, 424, L16

- Macciò, A. V., A. A. Dutton, F. C. van den Bosch, B. Moore, D. Potter, & J. Stadel. 2007, *MNRAS*, 378, 55
- Madigan, D. & A. E. Raftery. 1994, *Journal of the American Statistical Association*, 89, 1535
- Mainzer, A., J. Bauer, T. Grav, J. Masiero, R. M. Cutri, J. Dailey, P. Eisenhardt, R. S. McMillan, E. Wright, R. Walker, R. Jedicke, T. Spahr, D. Tholen, R. Alles, R. Beck, H. Brandenburg, T. Conrow, T. Evans, J. Fowler, T. Jarrett, K. Marsh, F. Masci, H. McCallon, S. Wheelock, M. Wittman, P. Wyatt, E. DeBaun, G. Elliott, D. Elsbury, T. Gautier, IV, S. Gomillion, D. Leisawitz, C. Maleszewski, M. Micheli, & A. Wilkins. 2011, *ApJ*, 731, 53
- Mamon, G. A. & E. L. Lokas. 2005, *MNRAS*, 363, 705
- Martinet, L. & T. de Zeeuw. 1988, *A&A*, 206, 269
- McCully, C., C. R. Keeton, K. C. Wong, & A. I. Zabludoff. 2017, *ApJ*, 836, 141
- Meneghetti, M., M. Bartelmann, & L. Moscardini. 2003, *MNRAS*, 340, 105
- Meng, X.-L., T. Treu, A. Agnello, M. W. Auger, K. Liao, & P. J. Marshall. 2015, *J. Cosmology Astropart. Phys.*, 9, 059
- Merritt, D. 1985a, *MNRAS*, 214, 25P
- . 1985b, *AJ*, 90, 1027
- Metcalf, R. B. & A. Amara. 2012, *MNRAS*, 419, 3414
- Metcalf, R. B. & P. Madau. 2001, *ApJ*, 563, 9
- Metcalf, R. B. & H. Zhao. 2002, *ApJ*, 567, L5

- Millon, M., A. Galan, F. Courbin, T. Treu, S. H. Suyu, X. Ding, S. Birrer, G. C. F. Chen, A. J. Shajib, K. C. Wong, A. Agnello, M. W. Auger, E. J. Buckley-Geer, J. H. H. Chan, T. Collett, C. D. Fassnacht, S. Hilbert, L. V. E. Koopmans, V. Motta, S. Mukherjee, C. E. Rusu, D. Sluse, A. Sonnenfeld, C. Spiniello, & L. Van de Vyvere. 2019, arXiv e-prints, arXiv:1912.08027
- Moore, B., T. Quinn, F. Governato, J. Stadel, & G. Lake. 1999, MNRAS, 310, 1147
- Moustakas, L. A., K. Abazajian, A. Benson, A. S. Bolton, J. S. Bullock, J. Chen, E. Cheng, D. Coe, A. B. Congdon, N. Dalal, J. Diemand, B. M. Dobke, G. Dobler, O. Dore, A. Dutton, R. Ellis, C. D. Fassnacht, H. Ferguson, D. Finkbeiner, R. Gavassi, F. W. High, T. Jeltema, E. Jullo, M. Kaplinghat, C. R. Keeton, J.-P. Kneib, L. V. E. Koopmans, S. M. Koishiappas, M. Kuhlen, A. Kusenko, C. R. Lawrence, A. Loeb, P. Madae, P. Marshall, R. B. Metcalf, P. Natarajan, J. R. Primack, S. Profumo, M. D. Seiffert, J. Simon, D. Stern, L. Strigari, J. E. Taylor, R. Wayth, J. Wambsganss, R. Wechsler, & A. Zentner. 2009, in ArXiv Astrophysics e-prints, Vol. 2010, astro2010: The Astronomy and Astrophysics Decadal Survey
- Munari, E., A. Biviano, S. Borgani, G. Murante, & D. Fabjan. 2013, MNRAS, 430, 2638
- Navarro, J. F., C. S. Frenk, & S. D. M. White. 1996, ApJ, 462, 563
- . 1997, ApJ, 490, 493
- Nierenberg, A. M., T. Treu, S. A. Wright, C. D. Fassnacht, & M. W. Auger. 2014, MNRAS, 442, 2434
- Nierenberg, A. M., T. Treu, G. Brammer, A. H. G. Peter, C. D. Fassnacht, C. R. Keeton, C. S. Kochanek, K. B. Schmidt, D. Sluse, & S. A. Wright. 2017, MNRAS, 471, 2224
- Nightingale, J., S. Dye, & R. Massey. 2018, MNRAS, 478, 4738

- Nightingale, J. W., R. J. Massey, D. R. Harvey, A. P. Cooper, A. Etherington, S.-I. Tam, & R. G. Hayes. 2019, arXiv e-prints, arXiv:1901.07801
- Nolta, M. R., E. L. Wright, L. Page, C. L. Bennett, M. Halpern, G. Hinshaw, N. Jarosik, A. Kogut, M. Limon, S. S. Meyer, D. N. Spergel, G. S. Tucker, & E. Wollack. 2004, *ApJ*, 608, 10
- Nord, B., E. Buckley-Geer, H. Lin, H. T. Diehl, J. Helsby, N. Kuropatkin, A. Amara, T. Collett, S. Allam, G. B. Caminha, C. De Bom, S. Desai, H. Dúmet-Montoya, M. E. d. S. Pereira, D. A. Finley, B. Flaugher, C. Furlanetto, H. Gaitsch, M. Gill, K. W. Merritt, A. More, D. Tucker, A. Saro, E. S. Rykoff, E. Rozo, S. Birrer, F. B. Abdalla, A. Agnello, M. Auger, R. J. Brunner, M. Carrasco Kind, F. J. Castander, C. E. Cunha, L. N. da Costa, R. J. Foley, D. W. Gerdes, K. Glazebrook, J. Gschwend, W. Hartley, R. Kessler, D. Lagattuta, G. Lewis, M. A. G. Maia, M. Makler, F. Menanteau, A. Niernberg, D. Scolnic, J. D. Vieira, R. Gramillano, T. M. C. Abbott, M. Banerji, A. Benoit-Lévy, D. Brooks, D. L. Burke, D. Capozzi, A. Carnero Rosell, J. Carretero, C. B. D’Andrea, J. P. Dietrich, P. Doel, A. E. Evrard, J. Frieman, E. Gaztanaga, D. Gruen, K. Honscheid, D. J. James, K. Kuehn, T. S. Li, M. Lima, J. L. Marshall, P. Martini, P. Melchior, R. Miquel, E. Neilsen, R. C. Nichol, R. Ogando, A. A. Plazas, A. K. Romer, M. Sako, E. Sanchez, V. Scarpine, M. Schubnell, I. Sevilla-Noarbe, R. C. Smith, M. Soares-Santos, F. Sobreira, E. Suchyta, M. E. C. Swanson, G. Tarle, J. Thaler, A. R. Walker, W. Wester, Y. Zhang, & DES Collaboration. 2016, *ApJ*, 827, 51
- Oguri, M., N. Inada, J. A. Blackburne, M.-S. Shin, I. Kayo, M. A. Strauss, D. P. Schneider, & D. G. York. 2008, *MNRAS*, 391, 1973
- Oguri, M. & P. J. Marshall. 2010, *MNRAS*, 405, 2579
- Oguri, M., C. E. Rusu, & E. E. Falco. 2014, *MNRAS*, 439, 2494

- Oguri, M., N. Inada, B. Pindor, M. A. Strauss, G. T. Richards, J. F. Hennawi, E. L. Turner, R. H. Lupton, D. P. Schneider, M. Fukugita, & J. Brinkmann. 2006, *AJ*, 132, 999
- Oh, S., J. E. Greene, & C. N. Lackner. 2017, *ApJ*, 836, 115
- Oliphant, T. E. 2015, *Guide to NumPy*, 2nd edn. (USA: CreateSpace Independent Publishing Platform)
- Osipkov, L. P. 1979, *Pisma v Astronomicheskii Zhurnal*, 5, 77
- Ostrovski, F., R. G. McMahon, A. J. Connolly, C. A. Lemon, M. W. Auger, M. Banerji, J. M. Hung, S. E. Kopolov, C. E. Lidman, S. L. Reed, S. Allam, A. Benoit-Lévy, E. Bertin, D. Brooks, E. Buckley-Geer, A. Carnero Rosell, M. Carrasco Kind, J. Carretero, C. E. Cunha, L. N. da Costa, S. Desai, H. T. Diehl, J. P. Dietrich, A. E. Evrard, D. A. Finley, B. Flaugher, P. Fosalba, J. Frieman, D. W. Gerdes, D. A. Goldstein, D. Gruen, R. A. Gruendl, G. Gutierrez, K. Honscheid, D. J. James, K. Kuehn, N. Kuropatkin, M. Lima, H. Lin, M. A. G. Maia, J. L. Marshall, P. Martini, P. Melchior, R. Miquel, R. Ogando, A. Plazas Malagón, K. Reil, K. Romer, E. Sanchez, B. Santiago, V. Scarpine, I. Sevilla-Noarbe, M. Soares-Santos, F. Sobreira, E. Suchyta, G. Tarle, D. Thomas, D. L. Tucker, & A. R. Walker. 2017, *MNRAS*, 465, 4325
- Ostrovski, F., C. A. Lemon, M. W. Auger, R. G. McMahon, C. D. Fassnacht, G. C.-F. Chen, A. J. Connolly, S. E. Kopolov, E. Pons, S. L. Reed, & C. E. Rusu. 2018, *MNRAS*, 473, L116
- Padmanabhan, N., C. M. Hirata, U. Seljak, D. J. Schlegel, J. Brinkmann, & D. P. Schneider. 2005, *Phys. Rev. D*, 72, 043525
- Pápai, P., I. Szapudi, & B. R. Granett. 2011, *ApJ*, 732, 27
- Paraficz, D. & J. Hjorth. 2009, *A&A*, 507, L49
- Peacock, J. A. & S. J. Dodds. 1994, *MNRAS*, 267, 1020

- Peng, C. Y., C. D. Impey, H.-W. Rix, C. S. Kochanek, C. R. Keeton, E. E. Falco, J. Lehar, & B. A. McLeod. 2006, *ApJ*, 649, 616
- Perlmutter, S., G. Aldering, G. Goldhaber, R. A. Knop, P. Nugent, P. G. Castro, S. Deustua, S. Fabbro, A. Goobar, D. E. Groom, I. M. Hook, A. G. Kim, M. Y. Kim, J. C. Lee, N. J. Nunes, R. Pain, C. R. Pennypacker, R. Quimby, C. Lidman, R. S. Ellis, M. Irwin, R. G. McMahon, P. Ruiz-Lapuente, N. Walton, B. Schaefer, B. J. Boyle, A. V. Filippenko, T. Matheson, A. S. Fruchter, N. Panagia, H. J. M. Newberg, W. J. Couch, & T. S. C. Project. 1999, *ApJ*, 517, 565
- Perreault Levasseur, L., Y. D. Hezaveh, & R. H. Wechsler. 2017, *ApJ*, 850, L7
- Pesce, D. W., J. A. Braatz, M. J. Reid, A. G. Riess, D. Scolnic, J. J. Condon, F. Gao, C. Henkel, C. M. V. Impellizzeri, C. Y. Kuo, & K. Y. Lo. 2020, arXiv e-prints, arXiv:2001.09213
- Planck Collaboration. 2014, *A&A*, 571, A17
- . 2015, ArXiv e-prints, arXiv:1502.01595
- . 2016a, *A&A*, 594, A13
- . 2016b, *A&A*, 594, A15
- . 2018, arXiv e-prints, arXiv:1807.06209
- Raccanelli, A., A. Bonaldi, M. Negrello, S. Matarrese, G. Tormen, & G. de Zotti. 2008, *MNRAS*, 386, 2161
- Rassat, A., K. Land, O. Lahav, & F. B. Abdalla. 2007, *MNRAS*, 377, 1085
- Read, J. I. 2014, *Journal of Physics G Nuclear Physics*, 41, 063101
- Rees, M. J. & D. W. Sciama. 1968, *Nature*, 217, 511

Refregier, A. 2003, MNRAS, 338, 35

Refsdal, S. 1964, MNRAS, 128, 307

Reid, B. A., W. J. Percival, D. J. Eisenstein, L. Verde, D. N. Spergel, R. A. Skibba, N. A. Bahcall, T. Budavari, J. A. Frieman, M. Fukugita, J. R. Gott, J. E. Gunn, Ž. Ivezić, G. R. Knapp, R. G. Kron, R. H. Lupton, T. A. McKay, A. Meiksin, R. C. Nichol, A. C. Pope, D. J. Schlegel, D. P. Schneider, C. Stoughton, M. A. Strauss, A. S. Szalay, M. Tegmark, M. S. Vogeley, D. H. Weinberg, D. G. York, & I. Zehavi. 2010, MNRAS, 404, 60

Riess, A. G., S. Casertano, W. Yuan, L. M. Macri, & D. Scolnic. 2019, ApJ, 876, 85

Riess, A. G., A. V. Filippenko, P. Challis, A. Clocchiatti, A. Diercks, P. M. Garnavich, R. L. Gilliland, C. J. Hogan, S. Jha, R. P. Kirshner, B. Leibundgut, M. M. Phillips, D. Reiss, B. P. Schmidt, R. A. Schommer, R. C. Smith, J. Spyromilio, C. Stubbs, N. B. Suntzeff, & J. Tonry. 1998, AJ, 116, 1009

Riess, A. G., L. Macri, S. Casertano, M. Sosey, H. Lampeitl, H. C. Ferguson, A. V. Filippenko, S. W. Jha, W. Li, R. Chornock, & D. Sarkar. 2009, ApJ, 699, 539

Riess, A. G., L. M. Macri, S. L. Hoffmann, D. Scolnic, S. Casertano, A. V. Filippenko, B. E. Tucker, M. J. Reid, D. O. Jones, J. M. Silverman, R. Chornock, P. Challis, W. Yuan, P. J. Brown, & R. J. Foley. 2016, ApJ, 826, 56

Riess, A. G., S. Casertano, W. Yuan, L. Macri, B. Bucciarelli, M. G. Lattanzi, J. W. MacKenty, J. B. Bowers, W. Zheng, A. V. Filippenko, C. Huang, & R. I. Anderson. 2018, ApJ, 861, 126

Riess, A. G., S. Casertano, W. Yuan, L. Macri, J. Anderson, J. W. MacKenty, J. B. Bowers, K. I. Clubb, A. V. Filippenko, D. O. Jones, & B. E. Tucker. 2018, ApJ, 855, 136

Romanowsky, A. J. & C. S. Kochanek. 1998, ApJ, 493, 641

- Rusu, C. E., M. Oguri, Y. Minowa, M. Iye, N. Inada, S. Oya, I. Kayo, Y. Hayano, M. Hattori, Y. Saito, M. Ito, T.-S. Pyo, H. Terada, H. Takami, & M. Watanabe. 2016, MNRAS, 458, 2
- Rusu, C. E., C. D. Fassnacht, D. Sluse, S. Hilbert, K. C. Wong, K.-H. Huang, S. H. Suyu, T. E. Collett, P. J. Marshall, T. Treu, & L. V. E. Koopmans. 2017, MNRAS, 467, 4220
- Rusu, C. E., K. C. Wong, V. Bonvin, D. Sluse, S. H. Suyu, C. D. Fassnacht, J. H. H. Chan, S. Hilbert, M. W. Auger, A. Sonnenfeld, S. Birrer, F. Courbin, T. Treu, G. C.-F. Chen, A. Halkola, L. V. E. Koopmans, P. J. Marshall, & A. J. Shajib. 2019, arXiv e-prints, arXiv:1905.09338
- Sachs, R. K. & A. M. Wolfe. 1967, ApJ, 147, 73
- Schechter, P. L., T. Anguita, N. D. Morgan, M. Read, & T. Shanks. 2018, Research Notes of the AAS, 2, 21
- Schechter, P. L., N. D. Morgan, B. Chehade, N. Metcalfe, T. Shanks, & M. McDonald. 2017, AJ, 153, 219
- Schechter, P. L., D. Pooley, J. A. Blackburne, & J. Wambsganss. 2014, ApJ, 793, 96
- Schechter, P. L., C. D. Bailyn, R. Barr, R. Barvainis, C. M. Becker, G. M. Bernstein, J. P. Blakeslee, S. J. Bus, A. Dressler, E. E. Falco, R. A. Fesen, P. Fischer, K. Gebhardt, D. Harmer, J. N. Hewitt, J. Hjorth, T. Hurt, A. O. Jaunsen, M. Mateo, D. Mehlert, D. O. Richstone, L. S. Sparke, J. R. Thorstensen, J. L. Tonry, G. Wegner, D. W. Willmarth, & G. Worthey. 1997, ApJ, 475, L85
- Schneider, P., J. Ehlers, & E. E. Falco. 1992, Gravitational Lenses, 112, doi:10.1007/978-3-662-03758-4

- Schneider, P., C. S. Kochanek, & J. Wambsganss. 2006, *Saas-Fee Advanced Courses*, Vol. 33, *Gravitational Lensing: Strong, Weak and Micro*, ed. G. Meylan, P. Jetzer, P. North, P. Schneider, C. S. Kochanek, & J. Wambsganss (Springer), astro-ph/0407232
- Schneider, P. & D. Sluse. 2013, *A&A*, 559, A37
- . 2014, *A&A*, 564, A103
- Schramm, T. 1990, *A&A*, 231, 19
- Scolnic, D. M., D. O. Jones, A. Rest, Y. C. Pan, R. Chornock, R. J. Foley, M. E. Huber, R. Kessler, G. Narayan, A. G. Riess, S. Rodney, E. Berger, D. J. Brout, P. J. Challis, M. Drout, D. Finkbeiner, R. Lunnan, R. P. Kirshner, N. E. Sanders, E. Schlafly, S. Smartt, C. W. Stubbs, J. Tonry, W. M. Wood-Vasey, M. Foley, J. Hand, E. Johnson, W. S. Burgett, K. C. Chambers, P. W. Draper, K. W. Hodapp, N. Kaiser, R. P. Kudritzki, E. A. Magnier, N. Metcalfe, F. Bresolin, E. Gall, R. Kotak, M. McCrum, & K. W. Smith. 2018, *ApJ*, 859, 101
- Sérsic, J. L. 1968, *Atlas de Galaxias Australes*
- Shajib, A. J. 2019, *MNRAS*, 488, 1387
- Shajib, A. J., T. Treu, & A. Agnello. 2018, *MNRAS*, 473, 210
- Shajib, A. J. & E. L. Wright. 2016, *ApJ*, 827, 116
- Shajib, A. J., S. Birrer, T. Treu, M. W. Auger, A. Agnello, T. Anguita, E. J. Buckley-Geer, J. H. H. Chan, T. E. Collett, F. Courbin, C. D. Fassnacht, J. Frieman, I. Kayo, C. Lemon, H. Lin, P. J. Marshall, R. McMahon, A. More, N. D. Morgan, V. Motta, M. Oguri, F. Ostrovski, C. E. Rusu, P. L. Schechter, T. Shanks, S. H. Suyu, G. Meylan, T. M. C. Abbott, S. Allam, J. Annis, S. Avila, E. Bertin, D. Brooks, A. Carnero Rosell, M. Carrasco Kind, J. Carretero, C. E. Cunha, L. N. da Costa, J. De Vicente, S. Desai, P. Doel, B. Flaugher, P. Fosalba, J. García-Bellido, D. W. Gerdes, D. Gruen, R. A. Gruendl, G. Gutierrez,

- W. G. Hartley, D. L. Hollowood, B. Hoyle, D. J. James, K. Kuehn, N. Kuropatkin, O. Lahav, M. Lima, M. A. G. Maia, M. March, J. L. Marshall, P. Melchior, F. Menanteau, R. Miquel, A. A. Plazas, E. Sanchez, V. Scarpine, I. Sevilla-Noarbe, M. Smith, M. Soares-Santos, F. Sobreira, E. Suchyta, M. E. C. Swanson, G. Tarle, & A. R. Walker. 2019, *MNRAS*, 483, 5649
- Shajib, A. J., S. Birrer, T. Treu, A. Agnello, E. J. Buckley-Geer, J. H. H. Chan, L. Christensen, C. Lemon, H. Lin, M. Millon, J. Poh, C. E. Rusu, D. Sluse, C. Spiniello, G. C. F. Chen, T. Collett, F. Courbin, C. D. Fassnacht, J. Frieman, A. Galan, D. Gilman, A. More, T. Anguita, M. W. Auger, V. Bonvin, R. McMahon, G. Meylan, K. C. Wong, T. M. C. Abbott, J. Annis, S. Avila, K. Bechtol, D. Brooks, D. Brout, D. L. Burke, A. Carnero Rosell, M. Carrasco Kind, J. Carretero, F. J. Castander, M. Costanzi, L. N. da Costa, J. De Vicente, S. Desai, J. P. Dietrich, P. Doel, A. Drlica-Wagner, A. E. Evrard, D. A. Finley, B. Flaugher, P. Fosalba, J. García-Bellido, D. W. Gerdes, D. Gruen, R. A. Gruendl, J. Gschwend, G. Gutierrez, D. L. Hollowood, K. Honscheid, D. Huterer, D. J. James, T. Jeltema, E. Krause, N. Kuropatkin, T. S. Li, M. Lima, N. MacCrann, M. A. G. Maia, J. L. Marshall, P. Melchior, R. Miquel, R. L. C. Ogando, A. Palmese, F. Paz-Chinchón, A. A. Plazas, A. K. Romer, A. Roodman, M. Sako, E. Sanchez, B. Santiago, V. Scarpine, M. Schubnell, D. Scolnic, S. Serrano, I. Sevilla-Noarbe, M. Smith, M. Soares-Santos, E. Suchyta, G. Tarle, D. Thomas, A. R. Walker, & Y. Zhang. 2020, *MNRAS*, 494, 6072
- Shakura, N. I. & R. A. Sunyaev. 1973, *A&A*, 24, 337
- Shen, Y., G. T. Richards, M. A. Strauss, P. B. Hall, D. P. Schneider, S. Snedden, D. Bizyaev, H. Brewington, V. Malanushenko, E. Malanushenko, D. Oravetz, K. Pan, & A. Simmons. 2011, *ApJS*, 194, 45
- Skilling, J. 2004, in *American Institute of Physics Conference Series*, Vol. 735, American Institute of Physics Conference Series, ed. R. Fischer, R. Preuss, & U. V. Toussaint, 395–405

- Sluse, D., V. Chantry, P. Magain, F. Courbin, & G. Meylan. 2012a, *A&A*, 538, A99
- Sluse, D., D. Hutsemékers, F. Courbin, G. Meylan, & J. Wambsganss. 2012b, *A&A*, 544, A62
- Sluse, D., A. Sonnenfeld, N. Rumbaugh, C. E. Rusu, C. D. Fassnacht, T. Treu, S. H. Suyu, K. C. Wong, M. W. Auger, V. Bonvin, T. Collett, F. Courbin, S. Hilbert, L. V. E. Koopmans, P. J. Marshall, G. Meylan, C. Spiniello, & M. Tewes. 2017, *MNRAS*, submitted, 470, 4838
- Sluse, D., C. E. Rusu, C. D. Fassnacht, A. Sonnenfeld, J. Richard, M. W. Auger, L. Coccato, K. C. Wong, S. H. Suyu, T. Treu, A. Agnello, S. Birrer, V. Bonvin, T. Collett, F. Courbin, S. Hilbert, L. V. E. Koopmans, O. Tihhanova, P. J. Marshall, G. Meylan, A. J. Shajib, J. Annis, S. Avila, E. Bertin, D. Brooks, E. Buckley-Geer, D. L. Burke, A. Carnero Rosell, M. Carrasco Kind, J. Carretero, F. J. Castander, L. N. da Costa, J. De Vicente, S. Desai, P. Doel, A. E. Evrard, B. Flaugher, J. Frieman, J. García-Bellido, D. W. Gerdes, D. A. Goldstein, R. A. Gruendl, J. Gschwend, W. G. Hartley, D. L. Hollowood, K. Honscheid, D. J. James, A. G. Kim, E. Krause, K. Kuehn, N. Kuropatkin, M. Lima, H. Lin, M. A. G. Maia, J. L. Marshall, P. Melchior, F. Menanteau, R. Miquel, A. A. Plazas, E. Sanchez, S. Serrano, I. Sevilla-Noarbe, M. Smith, M. Soares-Santos, F. Sobreira, E. Suchyta, M. E. C. Swanson, & G. Tarle. 2019, *MNRAS*, arXiv:1905.08800
- Smith, R. E., J. A. Peacock, A. Jenkins, S. D. M. White, C. S. Frenk, F. R. Pearce, P. A. Thomas, G. Efstathiou, & H. M. P. Couchman. 2003, *MNRAS*, 341, 1311
- Sonnenfeld, A. 2018, *MNRAS*, 474, 4648
- Sonnenfeld, A., R. Gavazzi, S. H. Suyu, T. Treu, & P. J. Marshall. 2013, *ApJ*, 777, 97
- Sonnenfeld, A., A. Leauthaud, M. W. Auger, R. Gavazzi, T. Treu, S. More, & Y. Komiyama. 2018a, *MNRAS*, 481, 164

- Sonnenfeld, A., T. Treu, R. Gavazzi, P. J. Marshall, M. W. Auger, S. H. Suyu, L. V. E. Koopmans, & A. S. Bolton. 2012, *ApJ*, 752, 163
- Sonnenfeld, A., J. H. H. Chan, Y. Shu, A. More, M. Oguri, S. H. Suyu, K. C. Wong, C.-H. Lee, J. Coupon, A. Yonehara, A. S. Bolton, A. T. Jaelani, M. Tanaka, S. Miyazaki, & Y. Komiyama. 2018b, *PASJ*, 70, S29
- Soto, K. T., S. J. Lilly, R. Bacon, J. Richard, & S. Conseil. 2016, *MNRAS*, 458, 3210
- Spiniello, C., A. Agnello, N. R. Napolitano, A. V. Sergeyev, F. I. Getman, C. Tortora, M. Spavone, M. Bilicki, H. Buddelmeijer, L. V. E. Koopmans, K. Kuijken, G. Vernardos, E. Bannikova, & M. Capaccioli. 2018, *MNRAS*, 480, 1163
- Springel, V., S. D. M. White, A. Jenkins, C. S. Frenk, N. Yoshida, L. Gao, J. Navarro, R. Thacker, D. Croton, J. Helly, J. A. Peacock, S. Cole, P. Thomas, H. Couchman, A. Evrard, J. Colberg, & F. Pearce. 2005, *Nature*, 435, 629
- Stoughton, C., R. H. Lupton, M. Bernardi, M. R. Blanton, S. Burles, F. J. Castander, A. J. Connolly, D. J. Eisenstein, J. A. Frieman, G. S. Hennessy, R. B. Hindsley, Ž. Ivezić, S. Kent, P. Z. Kunszt, B. C. Lee, A. Meiksin, J. A. Munn, H. J. Newberg, R. C. Nichol, T. Nicinski, J. R. Pier, G. T. Richards, M. W. Richmond, D. J. Schlegel, J. A. Smith, M. A. Strauss, M. SubbaRao, A. S. Szalay, A. R. Thakar, D. L. Tucker, D. E. Vanden Berk, B. Yanny, J. K. Adelman, J. E. Anderson, Jr., S. F. Anderson, J. Annis, N. A. Bahcall, J. A. Bakken, M. Bartelmann, S. Bastian, A. Bauer, E. Berman, H. Böhringer, W. N. Boroski, S. Bracker, C. Briegel, J. W. Briggs, J. Brinkmann, R. Brunner, L. Carey, M. A. Carr, B. Chen, D. Christian, P. L. Colestock, J. H. Crocker, I. Csabai, P. C. Czarapata, J. Dalcanton, A. F. Davidsen, J. E. Davis, W. Dehnen, S. Dodelson, M. Doi, T. Dombeck, M. Donahue, N. Ellman, B. R. Elms, M. L. Evans, L. Eyer, X. Fan, G. R. Federwitz, S. Friedman, M. Fukugita, R. Gal, B. Gillespie, K. Glazebrook, J. Gray, E. K. Grebel, B. Greenawalt, G. Greene, J. E. Gunn, E. de Haas, Z. Haiman, M. Haldeman,

P. B. Hall, M. Hamabe, B. Hansen, F. H. Harris, H. Harris, M. Harvanek, S. L. Hawley, J. J. E. Hayes, T. M. Heckman, A. Helmi, A. Henden, C. J. Hogan, D. W. Hogg, D. J. Holmgren, J. Holtzman, C.-H. Huang, C. Hull, S.-I. Ichikawa, T. Ichikawa, D. E. Johnston, G. Kauffmann, R. S. J. Kim, T. Kimball, E. Kinney, M. Klaene, S. J. Kleinman, A. Klypin, G. R. Knapp, J. Korienek, J. Krolík, R. G. Kron, J. Krzesiński, D. Q. Lamb, R. F. Leger, S. Limmongkol, C. Lindenmeyer, D. C. Long, C. Loomis, J. Loveday, B. MacKinnon, E. J. Mannery, P. M. Mantsch, B. Margon, P. McGehee, T. A. McKay, B. McLean, K. Menou, A. Merelli, H. J. Mo, D. G. Monet, O. Nakamura, V. K. Narayanan, T. Nash, E. H. Neilsen, Jr., P. R. Newman, A. Nitta, M. Odenkirchen, N. Okada, S. Okamura, J. P. Ostriker, R. Owen, A. G. Pauls, J. Peoples, R. S. Peterson, D. Petravick, A. Pope, R. Pordes, M. Postman, A. Prosapio, T. R. Quinn, R. Rechenmacher, C. H. Rivetta, H.-W. Rix, C. M. Rockosi, R. Rosner, K. Ruthmansdorfer, D. Sandford, D. P. Schneider, R. Scranton, M. Sekiguchi, G. Sergey, R. Sheth, K. Shimasaku, S. Smee, S. A. Snedden, A. Stebbins, C. Stubbs, I. Szapudi, P. Szkody, G. P. Szokoly, S. Tabachnik, Z. Tsvetanov, A. Uomoto, M. S. Vogeley, W. Voges, P. Waddell, R. Walterbos, S.-i. Wang, M. Watanabe, D. H. Weinberg, R. L. White, S. D. M. White, B. Wilhite, D. Wolfe, N. Yasuda, D. G. York, I. Zehavi, & W. Zheng. 2002, *AJ*, 123, 485

Sunyaev, R. A. & Y. B. Zeldovich. 1972, *Comments on Astrophysics and Space Physics*, 4, 173

Suyu, S. H. & A. Halkola. 2010, *A&A*, 524, A94

Suyu, S. H., P. J. Marshall, M. W. Auger, S. Hilbert, R. D. Blandford, L. V. E. Koopmans, C. D. Fassnacht, & T. Treu. 2010, *ApJ*, 711, 201

Suyu, S. H., T. Treu, R. D. Blandford, W. L. Freedman, S. Hilbert, C. Blake, J. Braatz, F. Courbin, J. Dunkley, L. Greenhill, E. Humphreys, S. Jha, R. Kirshner, K. Y. Lo, L. Macri, B. F. Madore, P. J. Marshall, G. Meylan, J. Mould, B. Reid, M. Reid, A. Riess, D. Schlegel, V. Scowcroft, & L. Verde. 2012, *ArXiv e-prints*, arXiv:1202.4459

- Suyu, S. H., M. W. Auger, S. Hilbert, P. J. Marshall, M. Tewes, T. Treu, C. D. Fassnacht, L. V. E. Koopmans, D. Sluse, R. D. Blandford, F. Courbin, & G. Meylan. 2013, *ApJ*, 766, 70
- Suyu, S. H., T. Treu, S. Hilbert, A. Sonnenfeld, M. W. Auger, R. D. Blandford, T. Collett, F. Courbin, C. D. Fassnacht, L. V. E. Koopmans, P. J. Marshall, G. Meylan, C. Spiniello, & M. Tewes. 2014, *ApJ*, 788, L35
- Suyu, S. H., V. Bonvin, F. Courbin, C. D. Fassnacht, C. E. Rusu, D. Sluse, T. Treu, K. C. Wong, M. W. Auger, X. Ding, S. Hilbert, P. J. Marshall, N. Rumbaugh, A. Sonnenfeld, M. Tewes, O. Tihhonova, A. Agnello, R. D. Blandford, G. C.-F. Chen, T. Collett, L. V. E. Koopmans, K. Liao, G. Meylan, & C. Spiniello. 2017, *MNRAS*, 468, 2590
- Talman, J. D. 1978, *Journal of Computational Physics*, 29, 35
- Tessore, N. & R. B. Metcalf. 2015, *A&A*, 580, A79
- Tewes, M., F. Courbin, G. Meylan, C. S. Kochanek, E. Eulaers, N. Cantale, A. M. Mosquera, P. Magain, H. Van Winckel, D. Sluse, G. Cataldi, D. Vörös, & S. Dye. 2013, *A&A*, 556, A22
- Tie, S. S. & C. S. Kochanek. 2018, *MNRAS*, 473, 80
- Tihhonova, O., F. Courbin, D. Harvey, S. Hilbert, C. E. Rusu, C. D. Fassnacht, V. Bonvin, P. J. Marshall, G. Meylan, D. Sluse, S. H. Suyu, T. Treu, & K. C. Wong. 2018, *MNRAS*, 477, 5657
- Tinker, J., A. V. Kravtsov, A. Klypin, K. Abazajian, M. Warren, G. Yepes, S. Gottlöber, & D. E. Holz. 2008, *ApJ*, 688, 709
- Treu, T. 2010, *ARA&A*, 48, 87
- Treu, T., M. W. Auger, L. V. E. Koopmans, R. Gavazzi, P. J. Marshall, & A. S. Bolton. 2010, *ApJ*, 709, 1195

- Treu, T., R. Gavazzi, A. Gorecki, P. J. Marshall, L. V. E. Koopmans, A. S. Bolton, L. A. Moustakas, & S. Burles. 2009, *ApJ*, 690, 670
- Treu, T., L. V. Koopmans, A. S. Bolton, S. Burles, & L. A. Moustakas. 2006, *ApJ*, 640, 662
- Treu, T. & L. V. E. Koopmans. 2002a, *ApJ*, 575, 87
- . 2002b, *MNRAS*, 337, L6
- . 2004, *ApJ*, 611, 739
- Treu, T. & P. J. Marshall. 2016, *The Astronomy and Astrophysics Review*, 24, 11
- Treu, T., G. Brammer, J. M. Diego, C. Grillo, P. L. Kelly, M. Oguri, S. A. Rodney, P. Rosati, K. Sharon, A. Zitrin, I. Balestra, M. Bradač, T. Broadhurst, G. B. Caminha, A. Halkola, A. Hoag, M. Ishigaki, T. L. Johnson, W. Karman, R. Kawamata, A. Mercurio, K. B. Schmidt, L.-G. Strolger, S. H. Suyu, A. V. Filippenko, R. J. Foley, S. W. Jha, & B. Patel. 2016, *ApJ*, 817, 60
- Treu, T., A. Agnello, M. A. Baumer, S. Birrer, E. J. Buckley-Geer, F. Courbin, Y. J. Kim, H. Lin, P. J. Marshall, B. Nord, P. L. Schechter, P. R. Sivakumar, L. E. Abramson, T. Anguita, Y. Apostolovski, M. W. Auger, J. H. H. Chan, G. C. F. Chen, T. E. Collett, C. D. Fassnacht, J.-W. Hsueh, C. Lemon, R. G. McMahon, V. Motta, F. Ostrovski, K. Rojas, C. E. Rusu, P. Williams, J. Frieman, G. Meylan, S. H. Suyu, T. M. C. Abbott, F. B. Abdalla, S. Allam, J. Annis, S. Avila, M. Banerji, D. Brooks, A. Carnero Rosell, M. Carrasco Kind, J. Carretero, F. J. Castander, C. B. D’Andrea, L. N. da Costa, J. De Vicente, P. Doel, T. F. Eifler, B. Flaugher, P. Fosalba, J. García-Bellido, D. A. Goldstein, D. Gruen, R. A. Gruendl, G. Gutierrez, W. G. Hartley, D. Hollowood, K. Honscheid, D. J. James, K. Kuehn, N. Kuropatkin, M. Lima, M. A. G. Maia, P. Martini, F. Menanteau, R. Miquel, A. A. Plazas, A. K. Romer, E. Sanchez, V. Scarpine, R. Schindler, M. Schubnell, I. Sevilla-Noarbe, M. Smith, R. C. Smith, M. Soares-Santos, F. Sobreira, E. Suchyta,

- M. E. C. Swanson, G. Tarle, D. Thomas, D. L. Tucker, & A. R. Walker. 2018, MNRAS, 481, 1041
- van de Ven, G., R. Mandelbaum, & C. R. Keeton. 2009, MNRAS, 398, 607
- van der Marel, R. P. 1994, MNRAS, 270, 271
- van Dokkum, P. G. & C. Conroy. 2010, Nature, 468, 940
- Vegetti, S., G. Despali, M. R. Lovell, & W. Enzi. 2018, MNRAS, 481, 3661
- Vegetti, S. & L. V. E. Koopmans. 2009, MNRAS, 392, 945
- Vegetti, S., L. V. E. Koopmans, M. W. Auger, T. Treu, & A. S. Bolton. 2014, MNRAS, 442, 2017
- Vegetti, S., L. V. E. Koopmans, A. Bolton, T. Treu, & R. Gavazzi. 2010, MNRAS, 408, 1969
- Vegetti, S., D. J. Lagattuta, J. P. McKean, M. W. Auger, C. D. Fassnacht, & L. V. E. Koopmans. 2012, Nature, 481, 341
- Verde, L., T. Treu, & A. G. Riess. 2019, Nature Astronomy, 3, 891
- Vestergaard, M. & B. M. Peterson. 2006, ApJ, 641, 689
- Viel, M., G. D. Becker, J. S. Bolton, & M. G. Haehnelt. 2013, Phys. Rev. D, 88, 043502
- Vikhlinin, A., A. V. Kravtsov, R. A. Burenin, H. Ebeling, W. R. Forman, A. Hornstrup, C. Jones, S. S. Murray, D. Nagai, H. Quintana, & A. Voevodkin. 2009, ApJ, 692, 1060
- Warren, M. S., P. J. Quinn, J. K. Salmon, & W. H. Zurek. 1992, ApJ, 399, 405
- Waskom, M., O. Botvinnik, P. Hobson, J. B. Cole, Y. Halchenko, S. Hoyer, A. Miles, T. Augspurger, T. Yarkoni, T. Megies, L. P. Coelho, D. Wehner, cynddl, E. Ziegler, diego0020, Y. V. Zaytsev, T. Hoppe, S. Seabold, P. Cloud, M. Koskinen, K. Meyer, A. Qalieh, & D. Allan. 2014, seaborn: v0.5.0 (November 2014), doi:10.5281/zenodo.12710

- Weil, M. L. & L. Hernquist. 1996, *ApJ*, 460, 101
- Weinberg, D. H., M. J. Mortonson, D. J. Eisenstein, C. Hirata, A. G. Riess, & E. Rozo. 2013, *Phys. Rep.*, 530, 87
- Williams, P., A. Agnello, & T. Treu. 2017, *MNRAS*, 466, 3088
- Williams, P. R., A. Agnello, T. Treu, L. E. Abramson, T. Anguita, Y. Apostolovski, G. C.-F. Chen, C. D. Fassnacht, J.-W. Hsueh, B. C. Lemaux, V. Motta, L. Oldham, K. Rojas, C. E. Rusu, A. J. Shajib, & X. Wang. 2018, *MNRAS*, 477, L70
- Witt, H. J., S. Mao, & P. L. Schechter. 1995, *ApJ*, 443, 18
- Wong, K. C., S. H. Suyu, M. W. Auger, V. Bonvin, F. Courbin, C. D. Fassnacht, A. Halkola, C. E. Rusu, D. Sluse, A. Sonnenfeld, T. Treu, T. E. Collett, S. Hilbert, L. V. E. Koopmans, P. J. Marshall, & N. Rumbaugh. 2017, *MNRAS*, 465, 4895
- Wong, K. C., S. H. Suyu, G. C. F. Chen, C. E. Rusu, M. Millon, D. Sluse, V. Bonvin, C. D. Fassnacht, S. Taubenberger, M. W. Auger, S. Birrer, J. H. H. Chan, F. Courbin, S. Hilbert, O. Tihhonova, T. Treu, A. Agnello, X. Ding, I. Jee, E. Komatsu, A. J. Shajib, A. Sonnenfeld, R. D. Blandford, L. V. E. Koopmans, P. J. Marshall, & G. Meylan. 2019, *arXiv e-prints*, arXiv:1907.04869
- Woo, J.-H., H. A. N. Le, M. Karouzos, D. Park, D. Park, M. A. Malkan, T. Treu, & V. N. Bennert. 2018, *ApJ*, 859, 138
- Wright, E. L., P. R. M. Eisenhardt, A. K. Mainzer, M. E. Ressler, R. M. Cutri, T. Jarrett, J. D. Kirkpatrick, D. Padgett, R. S. McMillan, M. Skrutskie, S. A. Stanford, M. Cohen, R. G. Walker, J. C. Mather, D. Leisawitz, T. N. Gautier, III, I. McLean, D. Benford, C. J. Lonsdale, A. Blain, B. Mendez, W. R. Irace, V. Duval, F. Liu, D. Royer, I. Heinrichsen, J. Howard, M. Shannon, M. Kendall, A. L. Walsh, M. Larsen, J. G. Cardon, S. Schick, M. Schwalm, M. Abid, B. Fabinsky, L. Naes, & C.-W. Tsai. 2010, *AJ*, 140, 1868

- Wright, S. A., G. Walth, T. Do, D. Marshall, J. E. Larkin, A. M. Moore, M. Adamkovics, D. Andersen, L. Armus, A. Barth, P. Cote, J. Cooke, E. M. Chisholm, T. Davidge, J. S. Dunn, C. Dumas, B. L. Ellerbroek, A. M. Ghez, L. Hao, Y. Hayano, M. Liu, E. Lopez-Rodriguez, J. R. Lu, S. Mao, C. Marois, S. B. Pandey, A. C. Phillips, M. Schoeck, A. Subramaniam, S. Subramanian, R. Suzuki, J. C. Tan, T. Terai, T. Treu, L. Simard, J. L. Weiss, J. Wincentzen, M. Wong, & K. Zhang. 2016, in Proc. SPIE, Vol. 9909, Society of Photo-Optical Instrumentation Engineers (SPIE) Conference Series, ed. E. Marchetti, L. M. Close, & J.-P. Véran (SPIE), 990905
- Wucknitz, O. 2002, MNRAS, 332, 951
- Xu, D., D. Sluse, L. Gao, J. Wang, C. Frenk, S. Mao, P. Schneider, & V. Springel. 2015, MNRAS, 447, 3189
- Xu, D., D. Sluse, P. Schneider, V. Springel, M. Vogelsberger, D. Nelson, & L. Hernquist. 2016, MNRAS, 456, 739
- Yan, L., E. Donoso, C.-W. Tsai, D. Stern, R. J. Assef, P. Eisenhardt, A. W. Blain, R. Cutri, T. Jarrett, S. A. Stanford, E. Wright, C. Bridge, & D. A. Riechers. 2013, AJ, 145, 55
- Yildirim, A., S. H. Suyu, & A. Halkola. 2019, arXiv e-prints, arXiv:1904.07237
- Yonehara, A., H. Hirashita, & P. Richter. 2008, A&A, 478, 95
- Yoo, J., C. S. Kochanek, E. E. Falco, & B. A. McLeod. 2006, ApJ, 642, 22
- Yuan, W., A. G. Riess, L. M. Macri, S. Casertano, & D. Scolnic. 2019, arXiv e-prints, arXiv:1908.00993
- Zaghloul, M. R. 2017, ACM Trans. Math. Softw., 44, 22:1
- Zahid, H. J., M. J. Geller, D. G. Fabricant, & H. S. Hwang. 2016, ApJ, 832, 203
- Zhao, H. 1996, MNRAS, 278, 488